The Dissertation Committee for Thomas Alexander Ivanoff Certifies that this is the approved version of the following dissertation:

Reconstruction of Solidification History from Cast Microstructure in Remelted Nickel Alloy 718

Committee:

Eric Taleff, Supervisor

Desiderio Kovar

David Bourell

Michael Engelhardt

Trevor Watt

Reconstruction of Solidification History from Cast Microstructure in Remelted Nickel Alloy 718

by

Thomas Alexander Ivanoff

Dissertation

Presented to the Faculty of the Graduate School of

The University of Texas at Austin

in Partial Fulfillment

of the Requirements

for the Degree of

Doctor of Philosophy

The University of Texas at Austin

December 2017

Dedication

To my family

Acknowledgements

First, I would like to thank my advisor, Dr. Eric Taleff. His guidance has been insightful and his knowledge has been invaluable during this dissertation and the many other projects I have worked on. I am deeply appreciative of the time and effort he has taken to help me develop professionally. I have become a better engineer, a more astute researcher, and a not-so-terrible writer through his guidance. Thank you Dr. Taleff.

I would like to acknowledge my committee members, Dr. Desiderio Kovar, Dr. David Bourell, Dr. Michael Engelhardt, and Dr. Trevor Watt. Their feedback and advice has been constructive and most welcomed. I would like to specifically thank Dr. Trevor Watt for beginning this project and laying the foundations of the work presented in this dissertation.

I am beholden to my fellow lab members, even Dr. Phillip Noell, for their support and assistance during this dissertation. It has been a pleasure working with all of you.

Next, I want to acknowledge and thank all my family and friends for supporting me through my studies. They have never doubted me through this journey, and for that I am truly grateful.

Finally, I would like to acknowledge the US Air Force for supporting this work through the Metals Affordability Initiative (MAI) under contract number FA8650-11-2-5224-B. I gratefully acknowledge the support from everyone at Allegheny Technologies Incorporated, the Carpenter Technology Corporation, and the Special Metals Corporation who were involved with this study.

Reconstruction of Solidification History from Cast Microstructure in Remelted Nickel Alloy 718

Thomas Alexander Ivanoff, Ph.D.

The University of Texas at Austin, 2017

Supervisor: Eric Taleff

Digital image analysis techniques were developed to autonomously characterize dendritic solidification microstructures and estimate melt pool profiles and solidification rates in remelted nickel alloy 718 ingots. Automated macrophotography was used to image dendritic microstructures in etched ingot cross-sections and create large image montages. Two analysis techniques, particle identification and two-point correlation function analysis, were developed to measure primary dendrite arm orientation and secondary dendrite arm spacing from these digital image montages.

Particle identification techniques identified individual primary dendrite arms from the montage images. Primary dendrite arm orientations were measured from the geometry and location of the identified particles. A peak-counting technique was then implemented to measure secondary dendrite arm spacing after primary dendrite arms were identified.

Two-point correlation functions were used to measure average primary dendrite arm orientations and secondary dendrite arm spacings from controlled image areas. Fourier analysis was then used to measure the primary dendrite arm orientation from the two-point correlation function. A peak-counting technique was used to measure secondary dendrite arm spacing after primary dendrite arm orientation was measured.

The results produced using both analysis techniques were used to estimate melt pool profiles and solidification rates in a remelted alloy 718 ingot. Melt pool profile and solidification rate histories were calculated from primary dendrite arm orientations and secondary dendrite arm spacings, respectively. The techniques developed in this dissertation provide new technology and data needed by industry to validate computational process models of remelting processes such as electro-slag remelting (ESR) and vacuum-arc remelting (VAR).

Table of Contents

List of Tables

List of Figures

1. INTRODUCTION

1.1. BACKGROUND AND HISTORY

The need for high-temperature alloys began in earnest with the development of the gas-turbine engine near the turn of the 19th century. Operating conditions in gas turbines are unforgiving; components such as turbine blades, turbine disks, compressor disks, and power transmission shafts are required to operate at elevated temperatures and high pressures in corrosive and oxidizing environments [1, 2]. Turbine blades and disks experience the highest temperatures and harshest conditions, and the early gas-turbines relied on austenitic and martensitic steel alloys for these applications [3 – 5]. These first steel alloys, Stayblade and Rex 78 for example, typically contained high chromium and/or nickel alloying additions to provide resistance to oxidation and creep deformation [5, 6]. The nominal compositions of Stayblade and Rex 78 are provided in Table 1.1. Gas-turbine technologies rapidly progressed during the 1920's and 1930's, when turbine power and efficiency were increased by raising turbine inlet temperatures. The largest increase in turbine inlet temperatures occurred in the mid 1930's as development began on gas-turbine engines as a means for aircraft propulsion. Aviation applications demanded smaller, lighter, and higher performing gas turbines than those used for land based applications. Consequently, operating temperatures and pressures were significantly increased in these new gas-turbine engines to meet performance and efficiency requirements for aircraft. The increases in turbine inlet temperature and pressure drove the development of numerous new steel alloys with improved elevated-temperature performance. However, temperatures experienced by turbine blades and disks in the new gas-turbine engines quickly surpassed the capabilities of even these new steel alloys [6]. Scientists in Britain and Germany struggled to advance gas-turbine engine technologies because of shortcomings in the steel alloys available.

In Britain, Sir Frank Whittle lead the development of numerous gas-turbine engines between 1936 and 1948 that would power the Gloster E.28/39 and the Gloster Meteor, Britain's first gas-turbine powered aircraft [6]. The first Whittle engines built in 1936 used Stayblade, an austenitic stainless steel produced by Firth-Vickers, for turbine blades and disks [6]. In 1939, Whittle switched to Rex 78, another Firth-Vickers stainless steel alloy developed specifically for turbine blade applications, because turbine components manufactured from Stayblade began to fail as engine operating temperatures increased [6]. Rex 78 was used for turbine blades and disks until 1941 and was flown on the first British jet-engine aircraft [6]. After 1941, Rex 78 turbine components were replaced by Nimonic 80, a newly developed nickel-based alloy [2, 6]. Nickel alloys provided greater resistance to creep than any steel alloy available, which greatly improved reliability and reduced engine failures. The development of new high-temperature materials was essential to the success of Britain's gas-turbine engine program.

Table 1.1: The nominal compositions of steel alloys used in the first gas-turbine engines are provided in weight percent [5].

	Element (wt. %)								
Alloy	C	Mn	Si	Cr	Ni	Mo	Ti	Cu	Fe
Stayblade	0.22	0.6	1.0	20.0	8.5	-	1.2	-	Bal.
Rex 78	0.01	0.8	0.7	14.0	18.0	4.0	0.6	4.0	Bal.

In Germany, gas-turbine engines were developed concurrently by Junkers, Bayerische Motoren Werke AG (BMW), and Heinkel-Hirth. The Junkers Jumo 004 and BMW 003 engines both reached, or more descriptively were forced, into production near

the end of World War II and were used to power the Messerschmitt ME 262 and the Heinkel He 162, respectively [6]. These were the first aircraft powered by gas-turbine engines to be used in service. When their engines worked properly, they had performance superior to any aircraft powered by a rotary engine available at that time. However, both the ME 262 and HE 162 were plagued by reliability problems from their gas-turbine engines during service. These gas-turbine engines suffered from a comically-short service life, atrocious reliability, and frequent mechanical failures [6] because turbine components made from stainless steel alloys would fail quickly during service at normal operating temperatures. These failures were similar to those encountered by Whittle in engines that used Stayblade. Whittle was eventually able to overcome these issues by using high-nickel steel alloys and nickel-based alloys, but the Germans did not have access to enough nickel to develop more creep resistant alloys [6]. Consequently, Germany was unable to manufacture the high-temperature materials necessary to produce reliable gas-turbine engines. This is one minor factor of many that contributed to the final outcome of World War II.

After World War II, it was clear that jet aircraft were here to stay, and more capable high-temperature materials were required to withstand their extreme operating conditions. New high-temperature materials were needed to provide a greater resistance to oxidation and creep. Numerous alloy systems were studied, but the nickel-based alloys developed were the most successful among these and remain so today.

The first nickel-based alloys used for gas-turbine engines were developed in the United States and Britain in the early 1940's [5, 6]. Hastelloy B is a nickel-molybdenum alloy developed by Haynes International in the United States; the alloy composition is provided in Table 1.2 [2]. The high molybdenum content provides exceptional resistance to oxidation and solid-solution strengthening against creep at elevated temperatures.

Hastelloy B was primarily used for static components, such as exhaust channels and combustor chambers [2]. At nearly the same time as Hastelloy B was introduced, the International Nickel Company (INCO) developed a new nickel-chrome alloy, Nimonic 80, which provided sufficient creep strength at elevated temperatures to be used in turbine blade and disk applications. The nominal composition of Nimonic 80A is provided in Table 1.2 [2]. Before the production of Nimonic 80, it was well understood that nickel-chrome alloys possessed excellent resistance to oxidation at elevated temperature but little resistance to creep. Creep strength was improved in Nimonic 80 by the addition of aluminum and titanium because these alloying elements promote the formation of γ' (Ni_3Al or $Ni_3[Al,Ti]$), an intermetallic precipitate that provides significant precipitation strengthening against creep. Nimonic 80 was used by Whittle to replace steel alloy components in his engines during the early 1940's.

Table 1.2: The nominal composition of the first nickel-based alloys used for gas-turbine engines are provided in weight percent [2].

Alloy	Element (wt. %)									
	Cr	Ni	Co	Mo	Ti	Al	Fe	C	V	Cu
Hastelloy B	< 1.0	63.0	< 2.5	28.0	-	-	5.0	< 0.05	0.03	-
Nimonic 80A	19.5	73.0	1.0	-	2.25	1.4	1.5	0.05	-	< 0.10

1.2. NICKEL-BASED SUPERALLOYS

Superalloys are essential for the operation of any modern jet aircraft. They alone exhibit the creep strength, resistance to oxidation and corrosion, and ductility necessary to survive operation within the hottest sections of a modern gas-turbine engine. Today's

superalloys are nearly all derived from the precipitation hardening nickel-chromium alloy system. Most, like Nimonic 80 in the 1940's, use chromium to achieve a high resistance to oxidation and aluminum and titanium to form γ′ precipitates for creep strengthening [1, 2, 5, 6]. Many additional elements are added to these alloys for specific reasons, and a list of these elements and their effects on material behavior is provided in Table 1.3 [1, 2]. Processing of these alloys has been developed to produce a highly engineered microstructure that achieves great resistance to creep. The γ - γ′ microstructure consists of coherent intermetallic γ′ precipitates (Ni_3Al or $Ni_3[Al,Ti]$) with an ordered $L1_2$ crystal structure distributed throughout the face-centered-cubic γ lattice of Ni [1, 2]. The γ′ precipitates typically exhibit a spheroidal or cuboidal morphology and have lattice parameter mismatches of less than 1% with γ. The lattice parameter of γ is 0.3517 nm, and γ′ is 0.3570 nm [1]. A high volume fraction of γ′, typically near 70 percent, is desired for modern alloys [1]. The microstructure created by heat treating contains small γ′ precipitates (tens to hundreds of nm) separated by thin channels of γ. Heat treatments vary significantly depending on the specific alloy, but generally follow this procedure: solution treating between 1000 and 1100 °C for 2 to 10 hours and aging between 600 and 900 °C for 4 to 20 hours [2].

Table 1.3: The common alloying additions used in nickel-based superalloys and their effects are listed [1, 2].

Aluminum:	provides precipitation strengthening; promotes the formation of γ′
Titanium:	provides precipitation strengthening; promotes the formation of γ′
Niobium:	provides precipitation strengthening; promotes the formation of γ″
Chromium:	improves resistance to corrosion; decreases solvus temperature of γ′
Molybdenum:	provides solid-solution strengthening
Tantalum:	improves resistance to creep; mechanisms unclear
Tungsten:	provides solid-solution strengthening
Cobalt:	increases solvus temperature of γ′
Iron:	cheaper than nickel, used as a filler material when permitted

The γ - γ′ superalloys provide a high tensile yield strength and resistance to creep by impeding dislocation motion and are used at temperatures from 760 °C and up to 1100 °C [1]. A brief discussion of the two primary strengthening mechanisms in the γ - γ′ alloys is useful here. A detailed examination of both room-temperature and elevated-temperature strengthening mechanisms in γ - γ′ nickel-based superalloys is presented by Roger Reed [1]. A single (a/2) <110> {111} dislocation in pure γ nickel is shown in Figure 1.1. If this dislocation were to enter a γ′ precipitate it would create an anti-phase boundary. Therefore, dislocations from γ nickel must enter the γ′ phase as pairs. The first dislocation creates an anti-phase boundary, and the second dislocation eliminates that anti-phase boundary to restore the ordered structure of the γ′ phase. This dislocation pair, shown in Figure 1.1, is referred to as a super dislocation. The ordered structure in the γ′ phase that creates super dislocations provides the most potent strengthening mechanism in γ - γ′ alloys. At elevated temperatures, γ - γ′ alloys maintain a high tensile yield strength and often exhibit an anomalous increase in tensile yield strength as temperature increase up to

800 °C. As temperature increases, cross-slip is activated along the {001} plane in super dislocation segments within the γ′ phase. This type of cross-slip causes the Kear-Wilsdorf lock [7] that effectively pins dislocations, which cannot move in the normal {111} slip plane without creating an anti-phase boundary. These strengthening mechanisms combined produce high tensile strengths and exceptional resistance to creep at elevated temperatures.

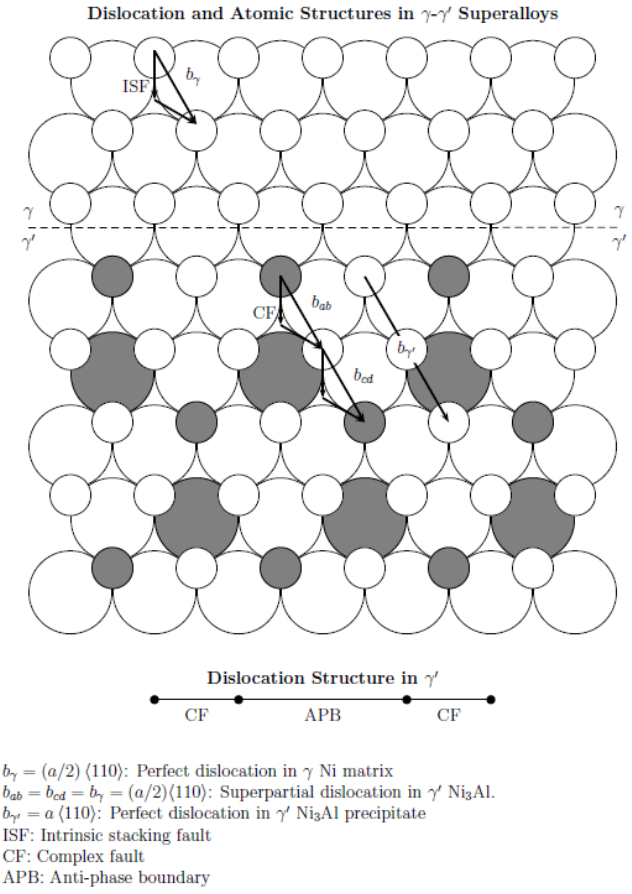

Figure 1.1: This schematic demonstrates the effect of (a/2) <110> {111} dislocations in γ and γ′ nickel. This figure was reproduced with permission from Dr. Eric Taleff.

The γ - γ′ superalloys exhibit remarkable properties but still suffer from some problems present since their initial development. First, the γ - γ′ superalloys are expensive to produce. Both the raw material and processing costs are high because many modern superalloys use rare-earth metals to improve performance and require extensive material processing to produce suitable microstructures [8]. Casting, forging, and heat treatment processes are often time consuming and must be closely monitored to ensure microstructural defects are not formed. Any defect within a component could result in catastrophic failure during service and cannot be tolerated. The γ - γ′ superalloys also exhibit poor notch sensitivity and weldability, which can make repairs and joining processes costly or ineffective. Additionally, it is difficult to manufacture large components from γ - γ′ superalloys because they are sensitive to aging heat treatments and segregation during casting [1, 2, 5].

In the 1950's, the problems associated with the γ – γ′ superalloys began to hinder the efforts of both General Electric and Pratt and Whitney to develop larger and more complex gas-turbine engines with improved serviceability [9 – 11]. A new alloy with elevated-temperature capabilities similar to that of the γ – γ′ superalloys and a more favorable manufacturability was needed. This led directly to the development of nickel alloy 718 and a new class of nickel-based superalloys, the γ - γ″ alloys.

1.3. NICKEL ALLOY 718

Nickel alloy 718, the subject of this dissertation, was developed in 1959 by Herbert Eiselstein at the Huntington Alloy Properties Division of the International Nickel Company (INCO) specifically for use in gas-turbine engines [12]. Alloy 718 demonstrates good creep strength, ductility, corrosion and oxidation resistance, microstructural stability, and fatigue

life up to 650 °C [1, 2, 8, 13 – 17]. The adequate high-temperature capability, relatively low cost, good manufacturability, and good weldability [18] compared to other nickel-based superalloys has made alloy 718 one of the most widely used and versatile superalloys of the last half century. Alloy 718 is used as wrought bar, sheet, castings, and forgings for both rotating (disks, shafts, and blades) and static (supports and casings) components in gas-turbine engines [9 – 11]. In 2001, alloy 718 accounted for 56 percent of the forged metal used by General Electric Aircraft Engines (GEAE), by weight [9, 11]. Over 40 percent of all the nickel-based material purchased by Pratt and Whitney in the mid 1990's was alloy 718. Over 4 million pounds were purchased in 1995 alone [10].

Alloy 718 derives its strength from coherent γ″ (Ni_3Nb) intermetallic precipitates distributed throughout the γ lattice, as opposed to most other nickel-based superalloys that are strengthened by γ′ precipitates (Ni_3Al or $Ni_3[Al,Ti]$) [1, 2, 8, 13, 19, 20]. Formation of the γ″ phase is promoted by niobium in alloy 718; the nominal composition of alloy 718 is provided in Table 1.4 [2]. The γ″ phase is a body-centered tetragonal phase with an ordered $D0_{22}$ crystal structure that forms as disk-like precipitates [1]. The γ″ precipitate has lattice parameters of a = 0.362 nm and c = 0.740 nm [1]. The width of the γ″ precipitate is similar to that of γ′, and the height is approximately double. Significant strength is achieved because of coherency strains introduced by the γ″ phase [1, 2]. The strengthening mechanisms present in the γ – γ′ microstructure previously discussed also provide similar strengthening benefits in alloy 718 [1, 2]. The γ′ phase can be precipitated simultaneously with the γ″ phase in alloy 718, but with a much smaller volume fraction. The γ′ phase does not contribute significantly to creep strengthening in alloy 718 [2].

Table 1.4: The nominal composition of alloy 718 in weight percent is provided [2].

Element	Ni	Cr	Fe	Nb	Mo	Ti	Al
Wt. %	50 – 55	17 – 21	Bal.	4.75 – 5.5	2.8 – 3.3	0.6 – 1.15	0.2 – 0.8

Element	Co	C	Mn	Si	P	S	B	Cu
Wt. %	< 1	< 0.08	< 0.35	< 0.35	< 0.015	< 0.015	< 0.006	< 0.3

Alloy 718 does not exhibit the same high-temperature capability of the γ - γ′ superalloys and can only be used at temperatures up to 650 °C [1, 2, 8]. At temperatures above 650 °C the γ″ phase will rapidly coarsen, reducing high-temperature performance. Consequently, alloy 718 cannot be used in the hottest sections of a gas-turbine engine; γ - γ′ superalloys are required for those components. Alloy 718 is ideal for use in the high-pressure compressor and low-pressure turbine stages, commonly called the "cold zones." Temperatures in the cold zones are high enough to require the use of nickel-based superalloys but low enough not to require a γ - γ′ superalloy; temperatures in the cold zones vary from 300 to 650 °C. Alloy 718 is preferred for components used in the cold zones because it possesses satisfactory mechanical properties and good manufacturability that make it easier and cheaper to produce than most γ - γ′ superalloys. Alloy 718 also demonstrates exceptional weldability compared to any other nickel-based superalloy. Literature demonstrates that the aging kinetics of the γ″ phase are sluggish compared to the γ′ phase, which improves manufacturability and weldability [9, 18]. Alloy 718 is also less sensitive to heat treatments. Large components, components with complex geometries, and welded assemblies not possible using γ – γ′ superalloys are produced in alloy 718 [15, 17]. Repairs by welding are also possible with alloy 718.

1.4. ALLOY 718 PRODUCTION

Like many segregation sensitive alloys, alloy 718 ingot production begins with double- or triple-melting during liquid metal processing (LMP) [21]. Following LMP, ingots are typically homogenized and hot forged to reduce chemical segregation and microstructural variation [21 – 24]. Alloy 718 is typically homogenized at 980 °C. Artificial aging at 720 °C for 8 hours and 620 °C for 10 hours then produces the desired, final microstructure in most wrought product [2, 22, 25]. LMP is important because the microstructure of the ingot determines the microstructure that can be developed in the wrought product, which then determines its mechanical properties [26 – 30]. Segregation defects and undesirable microstructural features, such as cavities, formed during LMP often cannot be remediated by homogenization heat treatments or hot forging [31]. Chemical segregation can cause non-uniform precipitation of γ″ during artificial aging, which creates regions with poor mechanical strength [31 – 33]. For critical applications, such as gas-turbine engine blades and shafts, these weak regions can result in catastrophic failures [1, 2], which cannot be tolerated. Consequently, inferior ingots must be again remelted, which is costly and time consuming.

Typical LMP of alloy 718 ingots includes vacuum-induction melting (VIM) followed by electro-slag remelting (ESR) and/or vacuum-arc remelting (VAR) [34 – 38]. Initial melting processes, like VIM, produce ingots with undesirable microstructural features that are used as feedstock for secondary remelting processes. Remelting reduces impurity content by removing undesirable oxides and volatile gases and refines the microstructure of the ingot [34]. Optimization of remelting can reduce manufacturing cost and improve material quality. This dissertation will primarily focus on data acquired from material produced by VAR, the process shown schematically in Figure 1.2. Material

produced by ESR, a process similar to VAR, was also investigated in this dissertation, and data acquired from ESR product will be presented.

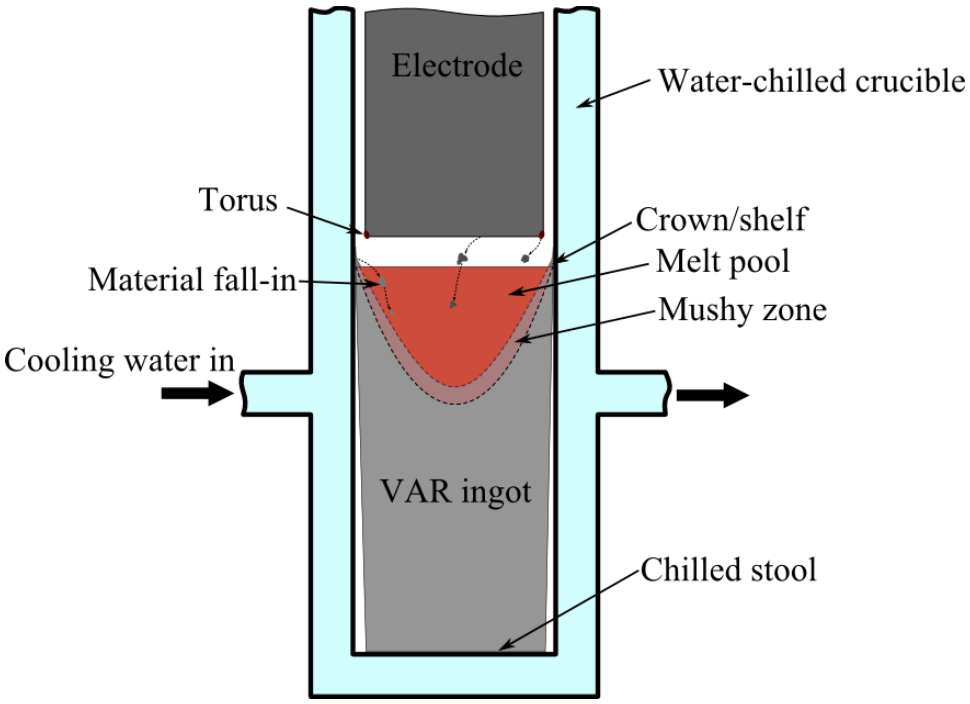

Figure 1.2: This schematic demonstrates the vacuum arc remelting (VAR) process. Regions of interest, such as the melt pool profile, are noted.

VAR uses a direct current to melt an electrode, typically an ingot produced by VIM or ESR, which then re-solidifies into a water-cooled crucible. As molten metal from the electrode falls into the crucible, a molten pool of metal, cleverly termed the melt pool, is formed. Solidification begins on the chilled stool at the bottom of the crucible. The size and geometry of the ingot, the electrode current, and the melt rate all influence the shape of the melt pool, the melt pool profile, and its solidification rate. VAR is performed under a vacuum to remove unwanted volatile elements and oxides [34]. ESR differs from VAR

by using a slag on top of the melt pool to remove undesirable elements instead of a vacuum. VAR produces exceptionally clean ingots, though it is susceptible to the formation of solidification defects such as freckle channels and white spots. These defects reduce tensile strength and low-cycle fatigue life in alloy 718 and can form when the melt pool is too shallow or too deep [17, 20, 38, 39]. Refinement and control of microstructure during VAR is essential to the production of a uniform defect-free ingot [34]. Detailed descriptions of VAR, the microstructures it produces, and the formation of common defects, such as freckle channels and white spots, can be found in the relevant literature [17, 20, 26 – 28, 31, 34, 36 – 49].

1.5. PROJECT MOTIVATION

Industry is very interested in optimizing alloy 718 ingot production because advances in ingot production technologies have the potential to reduce manufacturing cost and improve material quality [34, 39, 50]. Commercial computational process models are commonly used to improve and optimize remelting processes by simulating solidification [35, 51]. Manufacturers use these models in an attempt to control the microstructure produced in solidified ingots [50, 52 – 56]. To this end, manufacturers are interested in controlling two aspects of VAR: melt pool profile and solidification rate [50, 57]. The melt pool profile is defined as the shape of the solidification interface between the melt pool and the solidified material. Melt pool profile and solidification rate both influence the microstructure of the solidified ingot and the likelihood of defects forming during VAR [41, 44, 52, 57]. Computational process models such as the BAR, SIMCAST, and MESO codes predict melt pool behavior and solidification rate in order to simulate solidification behavior during remelting processes, including VAR [52 – 56]. However, limited

experimental data exists to validate the results of these simulations. Consequently, manufacturers seek new methods to acquire experimental data for the validation of process models. Currently, measuring melt pool profile and solidification rate during VAR is not feasible. Therefore, experimental measurements must be performed on the solidified ingot after VAR is completed.

This dissertation develops the new instrumentation and techniques necessary to acquire images of and quantitatively analyze the cast microstructure of slabs extracted from alloy 718 ingots produced by VAR and ESR. The dendritic microstructures of the solidified ingots are imaged with optical macrophotography, and the optical data is quantitatively analyzed. The data produced is used to calculate melt pool profiles and solidification rates. These techniques and data were provided to several industrial partners to help them improve and validate process models. A review of the current techniques used in industry and academia to measure melt pool profile and solidification rate follows.

1.6. Measurement of Melt Pool Profile

Melt pool profile is currently measured by intentionally marking the melt pool at distinct locations within an ingot and then locating the markers within that ingot after solidification. Marking is accomplished by introducing features, called pool markers, during remelting to decorate the melt pool profile at distinct locations. Melt pool profiles are measured from markers identified in sections excised from solidified ingots produced by the remelting process. The following melt pool markers are cited in the literature: metal ball pool markers, tree ring pool markers, and radioactive isotope pool markers [52, 58 – 61].

Metal ball pool markers, usually nickel or another high melting point metal, are used to decorate the melt pool profile during remelting [50, 52]. These markers can be visually observed in sections cut from the solidified ingot. Pool marking is conducted by dropping the metal balls into a melt at specific times and locations. Once in the melt pool, it is generally accepted that the metal balls sink through the molten metal and settle along the solidification interface. As the melt continues, the mushy zone solidifies around the metal balls, freezing them in place; once remelting is complete, ingots are cut open in order to reveal the metal ball pool markers. This technique is simple to implement but has some limitations. The melt pool profile can only be marked at a few distinct locations within an ingot. Because of this, melt pool profiles cannot be continuously measured throughout an ingot. Additionally, it is not known with confidence whether or not the metal ball pool markers actually settle along the melt pool profile.

Tree ring pool markers, much like metal ball pool markers, are used to decorate the melt pool profile during remelting with features that can be visually observed in sections cut from the solidified ingot [58 – 60]. Tree ring pool markers are small clusters of equiaxed grains located within larger regions of columnar grains. Tree ring formation is caused by disturbances to the melt pool profile, as shown in Figure 1.3 [26, 27, 60]. These features resemble tree rings when longitudinal cross-sections of an ingot are etched to reveal grain boundaries, hence their name. Pool marking is conducted by locally disturbing the melt pool profile during remelting with electromagnetic stirrers placed outside of the melt chamber or by manipulating the electric current of the melt. It has been shown that local disturbances to the melt pool profile promote the formation of equiaxed grains over columnar grains [26, 27, 60]. After remelting is completed, ingots are cut open and etched to reveal grain boundaries; the melt pool profile is measured by visually locating each pool marker [62]. This technique allows manufacturers to mark the melt pool more often than

with metal ball pool markers, but it still does not allow for continuous measurement of the melt pool profile.

A less common marking technique uses radioactive isotope markers to decorate the melt pool profile [61]. Radioactive isotope markers are added to the melt during remelting at distinct locations. The melt pool profile is then measured by locating the position of each marker within sections cut from the solidified ingot. However, the use of radioactive isotopes in LMP is often prohibited and/or difficult to implement. Because of this, there are very few instances where radioactive isotope pool markers are used. Like the other marker techniques, melt pool profile cannot be continuously measured throughout the ingot by radioactive isotope marking.

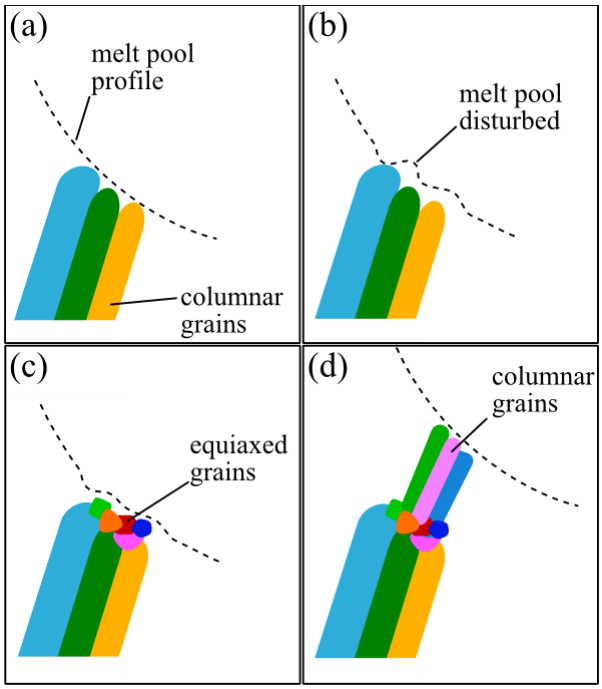

Figure 1.3: This schematic depicts the process of tree ring formation during VAR or ESR.

1.7. MEASUREMENT OF SOLIDIFICATION RATE

Solidification rate is calculated indirectly from measurements of secondary dendrite arm spacing in solidified ingots after remelting is completed [63]. An example of a typical dendrite that forms during solidification is depicted by the drawing in Figure 1.4. Secondary dendrite arm spacing is observed to be related to local solidification time by the following relationship [63],

$$\lambda = 5.5\left(Mt_f\right)^{1/3} \qquad (1)$$

where, λ is secondary dendrite arm spacing, M is a material dependent parameter, and t_f is local solidification time. According to this relationship, the cube root of local solidification time is proportional to secondary dendrite arm spacing and can be calculated if the appropriate material dependent parameter, M, is known. For alloy 718, the material dependent parameter, M, was calculated to be 2.74 μm^3 per second based on the data presented by Rappaz and Boettinger [64, 65]. The solidification parameters used to determine M are described in the literature [65] and could not be experimentally determined from solidification experiments using the equipment available for this study. Secondary dendrite arm spacing can be measured after remelting is completed from ingot cross-sections etched to reveal dendrites [62]. The dendritic microstructure is imaged at a resolution sufficient to resolve secondary dendrite arms. Secondary dendrite arm spacing is typically manually measured from these images. This technique is time consuming and often only used to provide measurements at a few locations within the ingot.

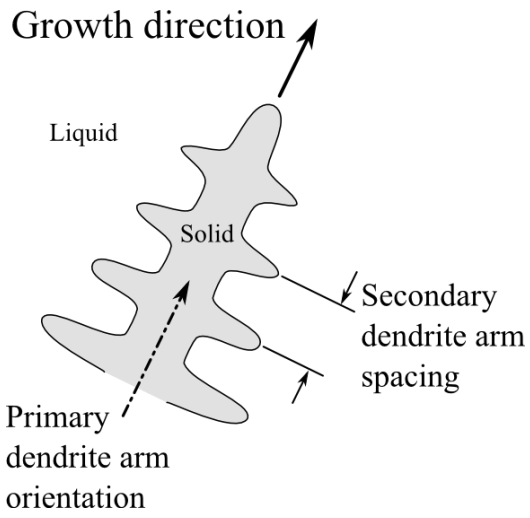

Figure 1.4: This schematic presents the basic features of a dendrite in a two-dimensional representation.

2. HYPOTHESIS AND RESEARCH GOALS

2.1. HYPOTHESIS

I hypothesize that solidification history, including melt pool profiles and local solidification rates, of remelted alloy 718 ingots can be reconstructed through characterization of solidification microstructures in ingot cross-sections. Melt pool profiles will be indicated by primary dendrite arm orientations. Local solidification rates will be calculated from secondary dendrite arm spacings. This hypothesis is based on an understanding of dendritic solidification. It uses solidification theory to describe the relationships between melt pool profile and primary dendrite arm orientation and between local solidification rate and secondary dendrite arm spacing. Kurz and Fisher provide an excellent review of solidification [63]. The aspects of solidification theory that pertain to this dissertation will be discussed in the following.

Highly alloyed systems, such as alloy 718, typically exhibit two types of dendritic solidification interfaces. Directional solidification occurs when heat flows from the melt to columnar dendrites. These dendrites grow opposite to the direction of heat flow, as shown in Figure 2.1 (a). During remelting processes, such as VAR, directional solidification occurs along the outer region of an ingot, near the crucible walls. Conditions along the sides of the ingot permit heat to flow from the molten liquid into the cooled crucible walls via the columnar dendrites. The second type of solidification, equiaxed solidification, occurs when the melt is undercooled. Heat must flow from dendrites into the undercooled melt. Newly formed dendrites grow radially in random directions, as shown in Figure 2.1 (b), until impeded by another dendrite or some other obstacle. There is no preferred growth direction, in contrast to directional solidification. During VAR, equiaxed solidification often occurs in the center of an ingot, where undercooling is likely.

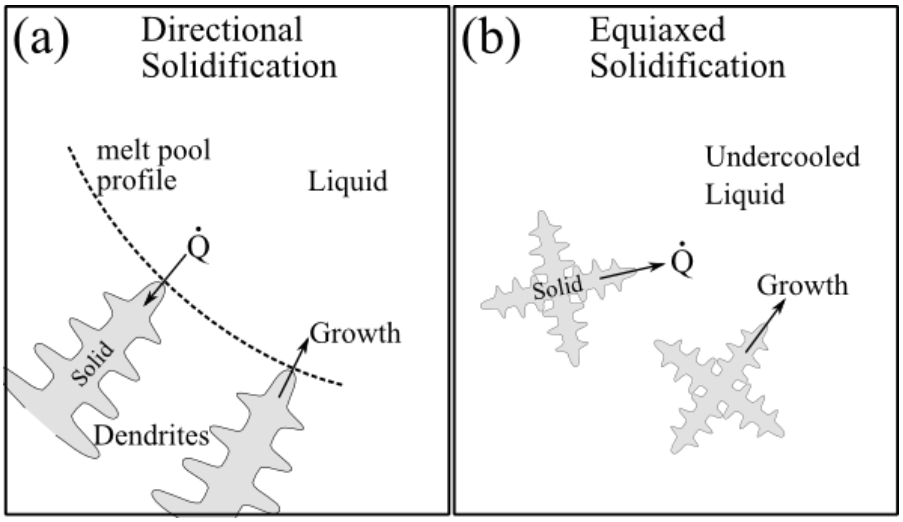

Figure 2.1: This schematic depicts (a) directional and (b) equiaxed dendritic solidification. $\dot{Q}$ indicates heat flow during solidification.

Melt pool profiles can be estimated from primary dendrite arm orientation in regions of directional solidification because primary dendrite arms grow opposite the direction of heat flow, which is typically orthogonal to the melt pool. In some cases, however, the orientation of a primary dendrite arm may not be orthogonal to the melt pool. For instance, if the melt pool profile is altered during the growth of a primary dendrite, the orientation of that primary dendrite cannot easily change because it is determined during the initial stages of growth. Additionally, small local perturbations to the melt pool profile may influence primary dendrite arm orientations. These issues are not expected to hinder melt pool profile estimations but will affect the uncertainty of this analysis technique. It is important to note that melt pool profiles cannot be estimated from primary dendrite arm orientations in regions of equiaxed solidification.

Local solidification rates can be calculated from secondary dendrite arm spacing in regions of directional and equiaxed solidification. Increasing solidification time increases

secondary dendrite arm thickness and spacing. Solidification rate can be calculated from secondary dendrite arm spacing using Equation 1.

2.2. RESEARCH GOALS

The first goal of this dissertation is to characterize solidification microstructures in cross-sectional slabs extracted from remelted alloy 718 ingot materials. The second goal is to use this microstructural data to produce new analyses of melt pool profiles and local solidification rates. These analyses will allow continuous measurement of melt pool profiles and local solidification rates throughout remelted alloy 718 ingots and provide manufacturers with new knowledge of solidification behavior during remelting processes. The steps necessary to successfully complete these goals are:

1) Develop new, automated instrumentation to acquire images of solidification microstructures from ingot slabs with large, somewhat uneven surfaces.
2) Assemble macrophotography equipment capable of resolving individual secondary dendrite arms. Build a fully automated linear XY stage to move the macrophotography equipment and image entire ingot slab surfaces. Incorporate auto-focus to account for surface roughness.
3) Develop a custom software program to link the control computer, linear XY stage, and macrophotography equipment.
4) Develop new procedures to perform automated image acquisition of large slab surfaces. Images must be acquired in such a manner that they can be stitched together to create a single montage image of the entire slab surface.
5) Acquire images of the VAR and ESR alloy 718 ingot slabs provided for this study.

6) Quantitatively characterize solidification microstructures using automated digital image analysis techniques. Use open source software when available.
7) Identify primary dendrite arm orientations and secondary dendrite arm spacings throughout ingot slabs.
8) Calculate melt pool profiles from primary dendrite arm orientations and local solidification rates from secondary dendrite arm spacing measurements.

3. MATERIALS

3.1. VACUUM-ARC REMELTED MATERIAL

A laboratory-scale vacuum-arc remelted (VAR) alloy 718 ingot, shown in Figure 3.1 before sectioning, was produced by Los Alamos National Laboratory for this study [66]. The ingot measured 212 mm in diameter and 406 mm in height. Two slabs were extracted from this ingot for characterization and microstructural analysis according to the diagram presented in Figure 3.2.

A single slab, approximately 28 mm thick, was sectioned 2.54 mm off center from the ingot along the casting direction; the slab was sectioned off center to preserve the centerline of the ingot within the slab for easy exposure after grinding. This slab was further sectioned in half, perpendicular to the casting direction, to facilitate handling. Each slab was precision ground to a 35 RA (μin) finish and a flatness tolerance of ± 0.1 in (0.254 mm) to reveal the ingot centerline and was then chemically etched to reveal the solidification microstructure. A segregation etch, Canada's etch (8 parts H_2O, 2 parts H_2SO_4, 2 parts HF, and 1 part HNO_3; etch at or above 70 °C) [62], was used to reveal solidification microstructures. Each slab was cleaned using soapy water and a stiff nylon brush prior to characterization. The ingot was sectioned, precision ground, and chemically etched by ATI Precision Finishing. The two prepared slabs, shown in Figure 3.3, were subsequently used to develop the techniques necessary to characterize solidification microstructures and measure melt pool profiles and local solidification rates in alloy 718 ingots. The noticeable "V-shape" and shrinkage cavity located at the top of the ingot were created at the end of the melt when the electrode current was stopped.

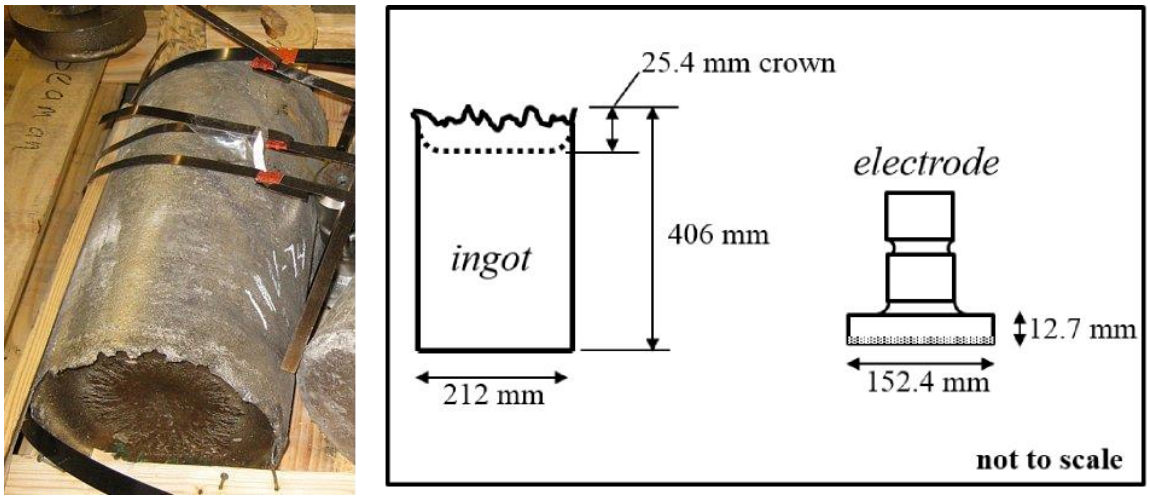

Figure 3.1: The vacuum-arc remelted (VAR) ingot produced by Los Alamos National Laboratories is presented. The dimensions of the ingot and electrode used to manufacture this ingot are provided.

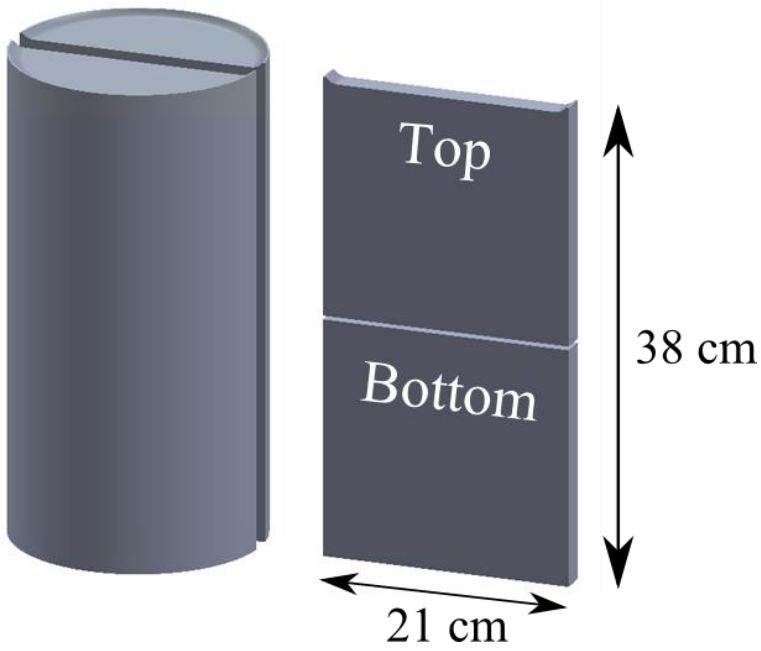

Figure 3.2: This schematic illustrates the locations within the VAR ingot from which the slabs were extracted.

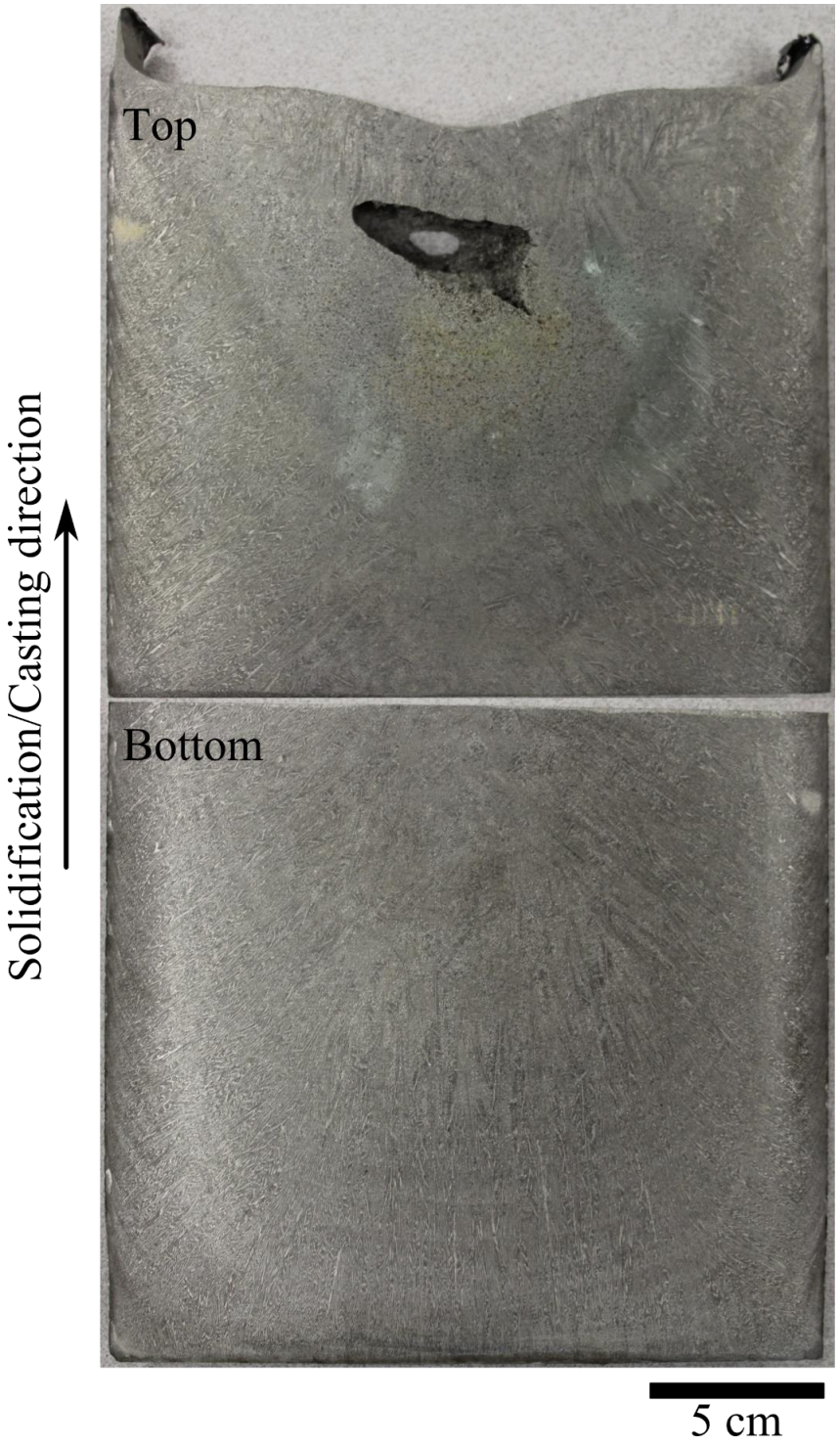

Figure 3.3: The surfaces of the slabs extracted from the VAR ingot are presented after precision grinding, chemical etching, and cleaning.

3.2. ELECTRO-SLAG REMELTED MATERIAL

Slabs from three industrial-scale electro-slag remelted (ESR) alloy 718 ingots were provided for characterization from three different suppliers: Allegheny Technologies Incorporated (ATI), Carpenter Technology Corporation (CarTech), and Special Metals Corporation (SMC) [50]. The ingot slabs supplied by ATI and CarTech were extracted from round ingots, each with a diameter of 430 mm. The slabs provided by SMC were extracted from a rectangular ingot with a width of 305 mm and a length of 1350 mm. The slabs characterized for each ingot are presented in Figure 3.4, Figure 3.5, and Figure 3.6. Each slab was prepared in a manner similar to that of the VAR ingot previously described. These ESR slabs were characterized using the same techniques applied to the VAR ingot. The data produced from the ESR slabs were supplied to each industrial partner for validation of computational process models of electro-slag remelting. Not all of the microstructural data and analysis from the ESR ingots could be included in this dissertation because these are the proprietary property of the industrial partners.

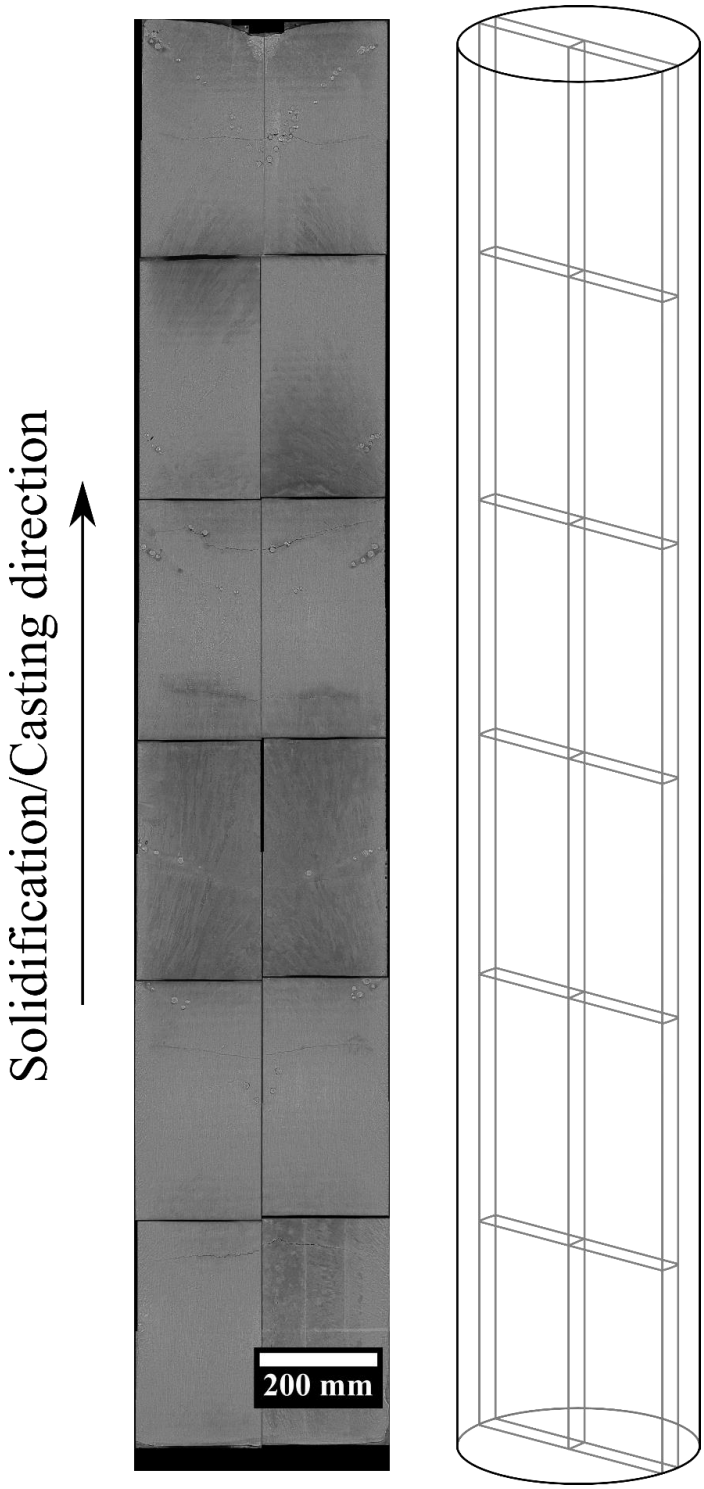

Figure 3.4: The slabs removed from the ESR ingot produced by ATI are presented. This figure is after that from [50].

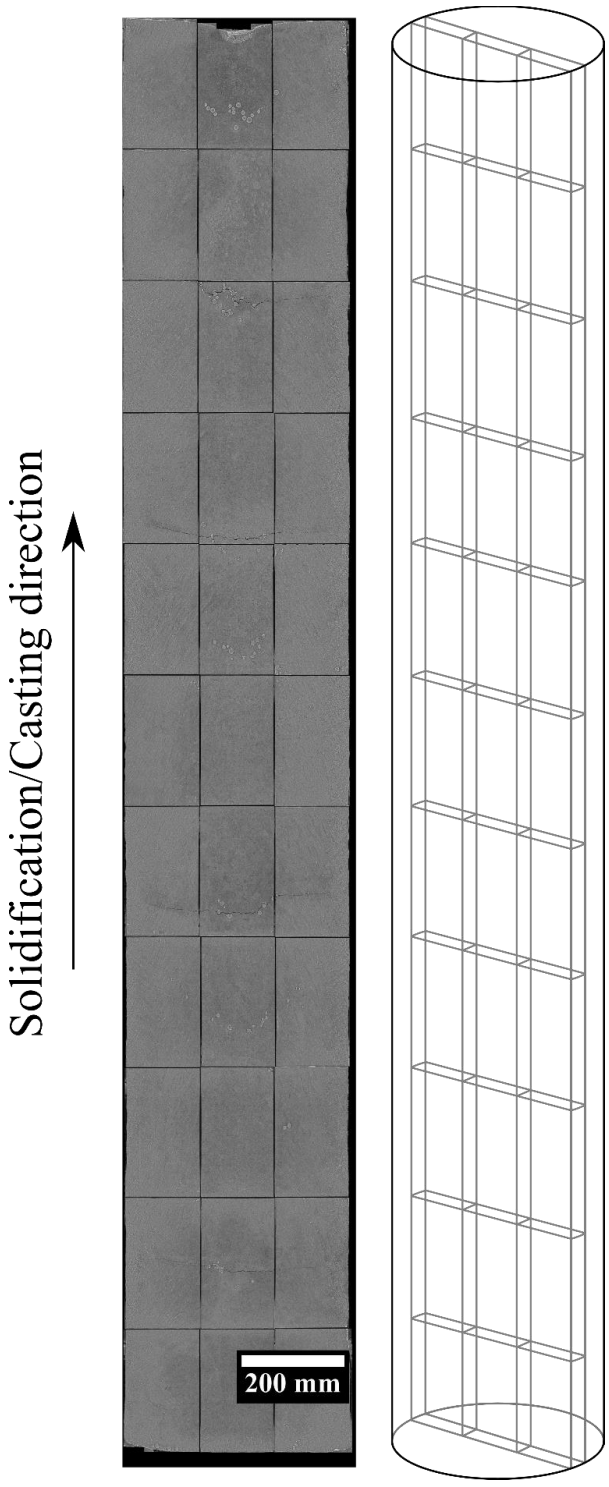

Figure 3.5: The slabs removed from the ESR ingot produced by CarTech are presented. This figure is after that from [50].

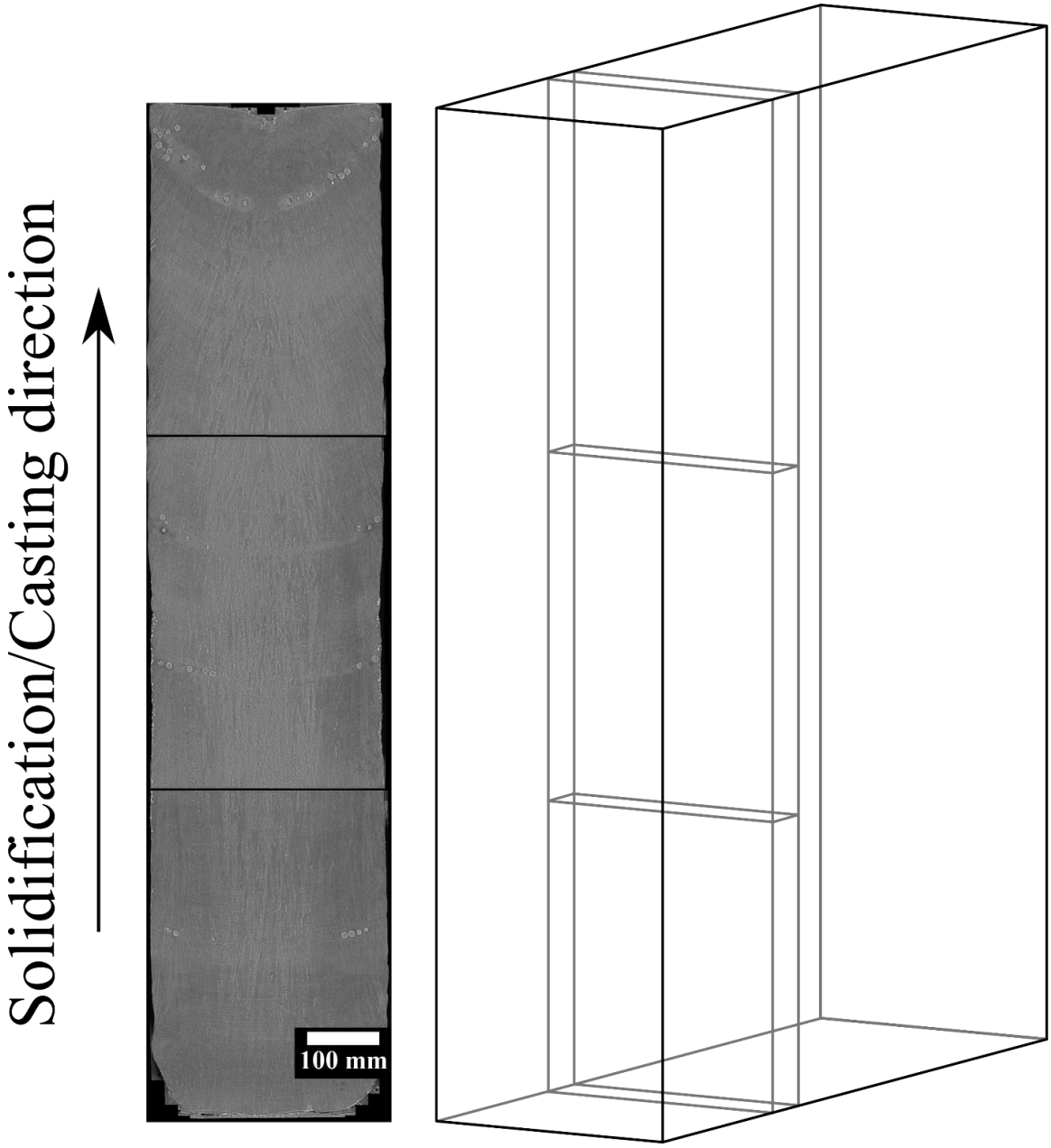

Figure 3.6: The slabs removed from the ESR ingot produced by SMC are presented. This figure is after that from [50].

4. IMAGING EQUIPMENT

4.1. DESIGN AND CONSTRUCTION OF IMAGING INSTRUMENTATION

Custom imaging instrumentation was used to image microstructures from the alloy 718 ingot slabs provided for this study. The design and selection of the imaging instrumentation was completed by two undergraduate students, Ms. Katie Adams and Mr. Mykal Madrid, under the supervision of Dr. Trevor Watt. I completed the construction of the imaging instrumentation with the help of Ms. Adams and Mr. Madrid. Mr. Madrid also assisted me with the acquisition of images from the alloy 718 slabs.

The imaging system used in this study was designed to: (1) provide a resolution sufficient to distinguish individual dendrites (tens to hundreds of μm), (2) acquire images from surface areas larger than 40,000 mm^2, and (3) operate autonomously. Macrophotography was chosen to acquire images because it provides ample resolution to identify dendrites and a reasonable imaging size. A Canon™ EOS 60D digital single-lens reflex camera equipped with a Sigma™ 105mm F2.8 EX DG OS HSM macro lens was used to acquire images. This macrophotography equipment provided 1:1 image magnification (the object being imaged is the same size as that seen by the optical sensor), autofocusing, and an image size of 22.3 by 14.9 mm at a 1:1 magnification. A maximum resolution of 4.3 μm per pixel was achieved with this equipment at a 1:1 magnification. Two Paul C. Bluff AlienBees™ B400 strobe units were used to provide uniform illumination across the entire surface of each slab during imaging. A Hoya™ circular polarizing filter was used to reduce glare from the specimen for improved image quality.

A custom built linear XY stage mounted to an optical breadboard, shown in Figure 4.1, was fabricated to hold the macrophotography equipment and raster it across the imaging area. The macrophotography equipment was attached to an adjustable mount that permitted motion along the z-axis; position on the z- axis was manually adjusted. This

mount was attached to a screw-driven linear actuator secured to a moving gantry beam. The screw-driven linear actuator allowed motion along the y-axis. The moving gantry beam was attached to a ball-screw driven linear actuator on one end and supported by a journal bearing riding on a stainless steel rod at the opposing end. The ball-screw actuator allowed motion along the x-axis, and the journal bearing supported the weight of the beam and allowed free motion along the x-axis. Motion of the XY stage in the x-y plane was controlled by two stepper motors, one for each direction. The strobe units were mounted to the XY stage. The alloy 718 slab specimens were supported within the imaging stage by three swivel leveling mounts.

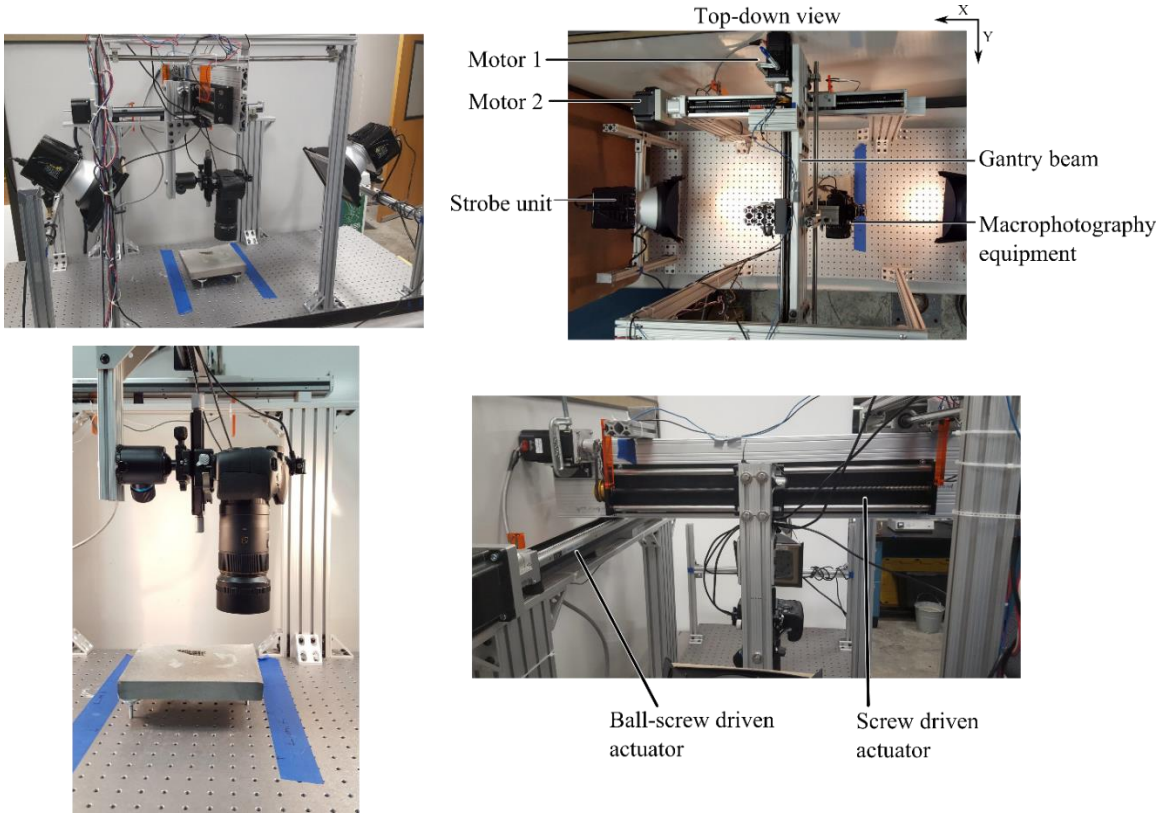

Figure 4.1: The imaging instrumentation used to acquire images of the alloy 718 ingot slabs is shown.

4.2. AUTOMATED CONTROL SYSTEM

Each component of the imaging instrumentation was controlled through a custom Labview™ software program I developed. This program used a single control computer to define the imaging area, control the macrophotography equipment, and control the motion of the XY stage. The macrophotography equipment was controlled using a National Instruments™ DAQ (data acquisition) board operated by the control program. This DAQ board was used to trigger autofocusing and camera shutter operation. The strobe units were activated directly from the camera. The stepper motors were controlled using a different National Instruments™ DAQ board operated by the control program. The stepper motors were controlled by sending commands to move either a desired number of individual steps or to move to a specific location within the XY stage.

4.3. IMAGE ACQUISITION

Two non-automated procedures were necessary prior to automated imaging: (1) alignment of the alloy 718 slab specimen to be imaged within the XY stage and (2) positioning of the macrophotography equipment on the z-axis. The slabs were manually positioned within the center of the imaging stage on three swivel leveling mounts, and the slab edges were aligned parallel to the x-axis and y-axis of the XY stage. The heights of the swivel mounts were adjusted independently until the surface of the slab was level with respect to the optical breadboard. This ensured the camera lens was perpendicular to the slab surface. Because macrophotography was always completed at approximately a 1:1 magnification, the image was focused by adjusting the distance between the lens and slab surface. After the slab was centered and leveled, the position of the macrophotography equipment in the z-axis was adjusted until a focused image was acquired at a 1:1 magnification.

Prior to automated imaging, the macrophotography equipment was positioned above the upper left corner of the slab in the x-y reference plane. Imaging was then completed in sequential steps along the snake-like pattern presented in Figure 4.2. An approximately 20 percent linear overlap between adjacent images was maintained to support subsequent digital stitching together of images into a montage for analysis. Image data in the raw CR2 native Canon^{TM} image format was transferred from the camera to the control computer through a USB connection after each acquisition event. The control program recorded the position within the XY stage where each macrophotograph was acquired. The automated imaging procedure is presented as a flowchart in Figure 4.3 and described in the following:

1) Immediately prior to acquiring an image, the position of the macrophotography equipment within the XY stage and time of acquisition are recorded in a text file generated by the control program.
2) With the macrophotography equipment in position, the control program triggers the phase detection auto focus functionality of the camera. The focusing point is determined by the camera software. Phase detection auto focusing was necessary to account for small height variations across the imaging surface.
3) After focusing, the control program triggers the camera to lock the mirror in the up position. A 1.5 second hold time is programmed into the imaging procedure to allow for any vibrations created by the mirror locking motion to dissipate before a macrophotograph is taken.
4) The shutter is triggered by the control program, and a macrophotograph is acquired. The two strobe units are triggered by the camera and arranged to provide uniform lighting across the image surface. An exposure time of 1/250 seconds was used

because it is the fastest possible speed at which the camera can be synced with the strobe units.

5) Image data in the raw CR2 format is transferred from the camera to the computer through a USB connection. Canon™ imaging software on the control computer automatically records each image.

6) The control program sends commands to each stepper motor to move the macrophotography equipment to the next position. The distance moved between photographs was pre-determined and hard-coded into the control program so that an approximately 20 percent linear overlap between adjacent images occurred in both the X and Y directions. The number of images taken is predetermined by the user based upon the size of the specimen.

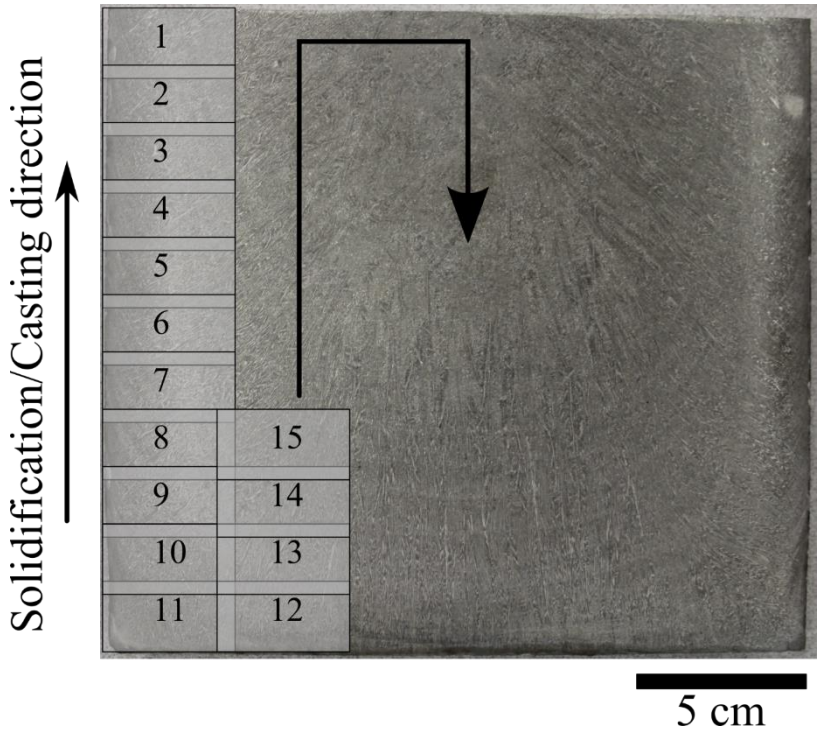

Figure 4.2: Individual macrophotographs were taken across the imaging surface using the snake-like pattern presented.

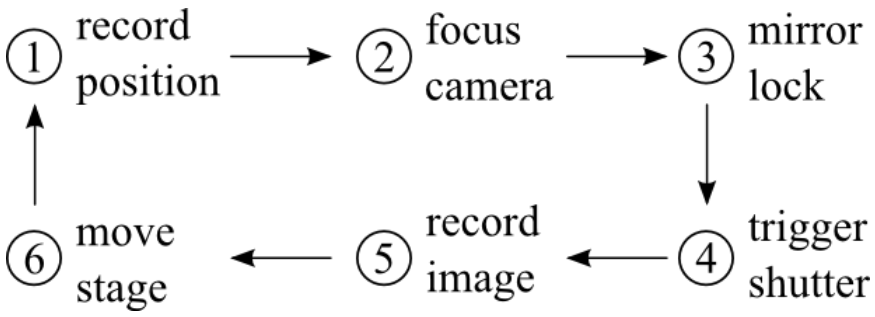

Figure 4.3: The image acquisition process is presented as a flowchart.

The macrophotography settings used to acquire images during this study were chosen to provide a balance of image clarity/sharpness and depth of focus. The macrophotography settings used are:

1) Camera: Canon™ EOS 60D
2) Lens: 105mm macro lens with a circular polarizer
3) F-stop: 8
4) Exposure time: 1/250 seconds
5) ISO number: 100
6) Strobes: Paul C. Bluff AlienBees™ B400 Flash Unit
   Strobe power: 3/8

After imaging, the magnification at each corner of the imaging area is acquired by photographing a machinist's ruler with markings every 100th of an inch. The values measured provide measurements of pixels per mm at each corner of the scan area. These values are later averaged together to produce a conversion value in pixels per mm for the entire scan area. The variation in magnification across the scan area for a single scan was typically less than 2 pixels per mm. For the top slab from the VAR ingot, the minimum and

maximum magnifications were 228.1 and 229.4 pixels per mm, respectively. For the bottom slab from the VAR ingot, the minimum and maximum magnifications were 223.4 and 225.2 pixels per mm, respectively. Similar behavior was observed for the ESR ingot material.

Note: A more detailed description of the image acquisition procedure is provided in Appendix A.

5. DATA ANALYSIS

5.1. DIGITAL IMAGE STITCHING

Individual macrophotographs acquired from each alloy 718 slab were digitally stitched together to create one montage image of each slab. Analysis of microstructure was then performed on these montage images. Digital image stitching was completed with superb help from Dr. Eric Taleff. The digital image stitching procedure is described in the following.

Images acquired from each slab were initially saved in the raw CR2 native Canon™ image format. Images saved in this file format do not suffer from any image compression losses but are large and are not recognized by many image viewing software programs. These raw images were converted to 8-bit grayscale TIFF (Tagged Image File Format) images, a smaller and more widely accepted image format. Compression was not used during this conversion. The TIFF files were manipulated as follows prior to stitching. First, a CLAHE (contrast limited adaptive histogram equalization) algorithm [67] was applied to the image to stretch its local contrast across the 8-bit file depth to improve feature recognition during stitching. Second, the image was reduced in size by 50 percent using bilinear scaling. This reduced the image resolution from approximately 4.3 μm per pixel to approximately 8.6 μm per pixel. The reduced image resolution is still sufficient for feature analysis and provides a manageable image size. These operations were accomplished using a Python script that calls the OpenCV [68] image function libraries to apply the CLAHE algorithm and reduce image size. Note that these steps were accomplished using the lossless PNG format, to avoid a bug in the Debian Linux TIFF libraries, and the final images were then converted back to uncompressed TIFF using the ImageMagick libraries [69]. (The OpenCV libraries did not have an option for producing uncompressed TIFF images.)

Montage images were created by stitching together the TIFF images acquired from each slab. Images were stitched using their locations from the XY stage, recorded during image acquisition. A "Scan" text file was generated to accompany the image files for each slab or each series of consecutively acquired images. The Scan file contains, on its first line, the average scaling of the images in pixels per mm. This measure is the average of measurements from separate photographs of a ruler lying flat upon the plate at the four corners of the scanned area. The remainder of the Scan file contains a list of image numbers, which correspond to the numbers of the named image files, and the position of the upper left corner of each image in native counts for the stepper motors and in units of millimeters. Date and time stamps are also included for each image listed in the Scan file. An example from the first few lines of a Scan file is shown in Table 5.1.

Table 5.1: Scan file example.

Conversion	227.3493251	pixels/mm			
Image	X	Y	X (mm)	Y (mm)	Time
001	-22500	-12000	-34.965	-29.2608	7/27/2015 21:43:10
002	-29900	-12000	-46.4646	-29.2608	7/27/2015 21:43:25
003	-37300	-12000	-57.9642	-29.2608	7/27/2015 21:43:39
004	-44700	-12000	-69.4638	-29.2608	7/27/2015 21:43:54
005	-52100	-12000	-80.9634	-29.2608	7/27/2015 21:44:09

Images were digitally stitched together using the grid/collection stitching plugin contained within the Fiji distribution of ImageJ, an open source image viewing and manipulating software package [70]. The algorithm used sequentially stitched images together based on their relative locations using a text file containing the image names and their corresponding spatial positions. This information was combined into a "Tile

Configuration" text file using the data from the Scan text file previously described. An example of the first several lines of a Tile Configuration file is shown in Table 5.2. Note that ImageJ was not able to stitch together files that would exceed a combined 1 GB in total size. For slab images that exceeded this practical software limit, the files were split into groups, each below this size limit, and then stitched separately. This workaround was applied on a case-by-case basis, but was only necessary for the large slabs from the industrial ingots. Because of an evident bug in the ImageJ program, the montage image would often be missing the first image file listed in the Tile Configuration file. A workaround to this bug was to copy this first file into two additional files and repeat these files at the position of the first file. ImageJ was then called in "headless" mode to stitch the individual images together, based on the Tile Configuration file used. The stitching algorithm applied translations, rotations, and affine scaling adjustments to each image to complete the stitching procedure.

Table 5.2: Tile configuration file example.

# Define the number of dimensions
dim = 2
# Define the image coordinates
IMG_1001.tiff; ; (0, 0)
IMG_1002.tiff; ; (0, 0)
IMG_0001.tiff; ; (0, 0)
IMG_0002.tiff; ; (0, 1307)
IMG_1003.tiff; ; (0, 2614)

5.2. DIGITAL IMAGE PROCESSING

After stitching, montage images were manually rotated and cropped to match to the overall ingot geometry. The rotation angle was determined by manually measuring the angle of the slab within each image. Images were rotated using a bilinear rotation algorithm in Matlab™ [71]. The angle of reorientation was recorded and used to calculate the correct placement of montage images relative to each other for subsequent analyses. Cropping was necessary after reorientation to remove regions along the sides of each image that did not contain any microstructural data; these featureless regions had the potential to negatively influence subsequent analyses. Cropping was manually performed using the Fiji distribution of ImageJ [70]. Scaling adjustments were performed after rotating and cropping. A consistent image resolution was necessary to compare data acquired from different montage images and combine them into a single, representative data set for the entire ingot. Each montage image was scaled to a resolution of 9 μm per pixel, a resolution sufficient for feature detection by the software used in this dissertation. This resolution was chosen because the resolution of each montage image is approximately 8.7 ± 0.2 μm per pixel and an image resolution of 9 μm per pixel is a convenient round number close to that value. The scaling factor used to adjust the resolution of each montage image was calculated from the conversion factor in pixels per mm contained in the Scan text file. A bilinear resizing algorithm was implemented in Matlab™ to scale each montage image [71]. The montage images of the two slabs sectioned from the VAR ingot are presented in Figure 5.1 and Figure 5.2 after reorientation, cropping, and scaling. Note that the montage images cannot be shown in this document at their full resolution. However, the slabs are presented together in Figure 5.3 with a small region enlarged to demonstrate the full image resolution.

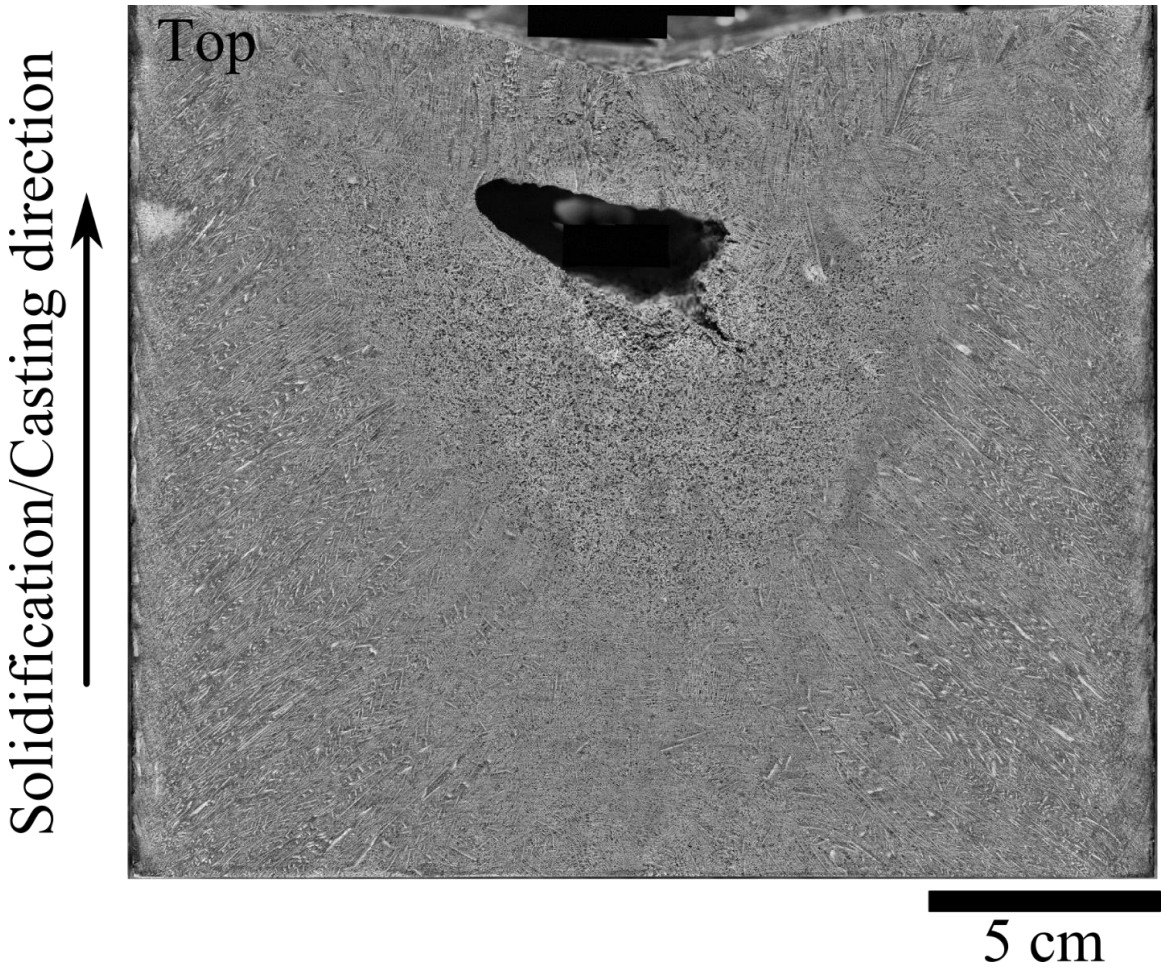

Figure 5.1: The montage image created from the top slab of the VAR ingot is presented.

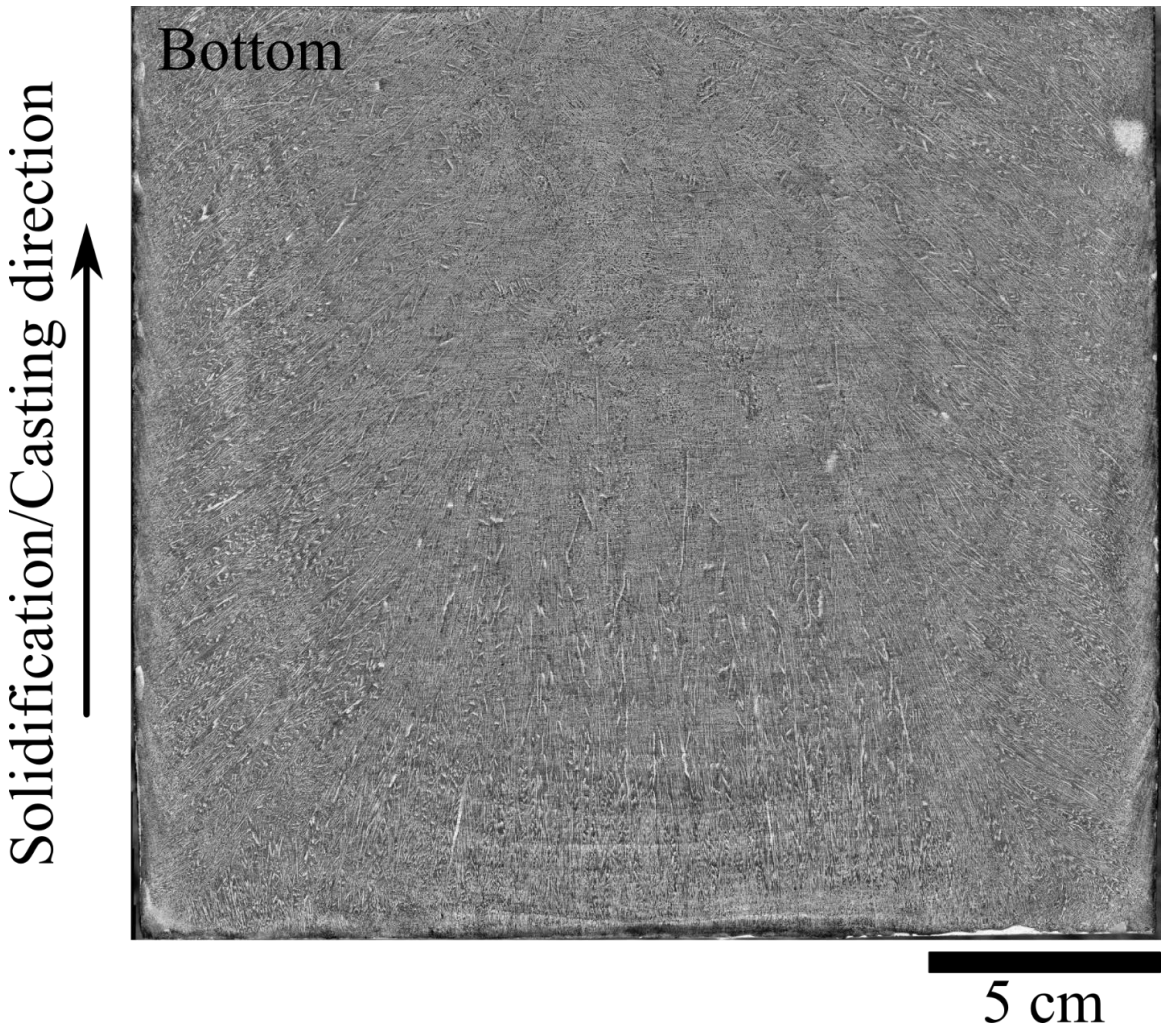

Figure 5.2: The montage image created from the bottom slab of the VAR ingot is presented.

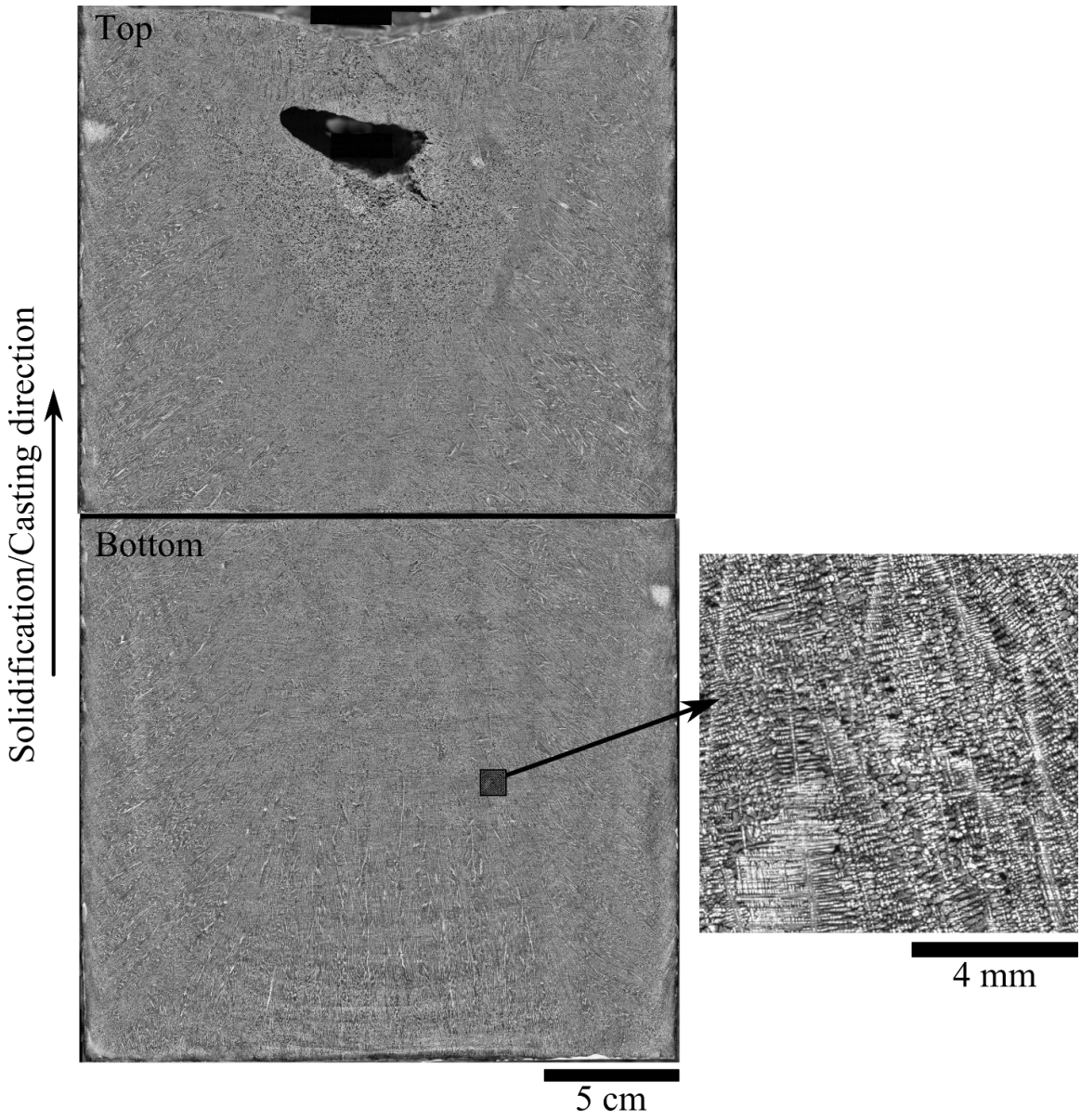

Figure 5.3: The montage images from the VAR ingot are presented. A small region has been enlarged to more closely demonstrate the true resolution of the montage images. Note that primary and secondary dendrite arms are clearly visible.

Primary and secondary dendrite arms were quantitatively analyzed in montage images using automated digital image analysis techniques. Automated analysis techniques were used because there were too many features to manually identify. Computerized image analysis software is not sophisticated enough to identify primary and secondary dendrite arms directly from grayscale montage images. Therefore, the grayscale images were processed into a binary image format prior to analysis. The binary conversion is necessary to transform the image data into a form that the computerized image analysis techniques are capable of handling.

A CLAHE algorithm was applied to each montage image prior to the binary conversion to stretch the local contrast across the 8-bit file depth and produce an image with uniform luminosity. Each image was then converted to a binary image by a threshold operation applied in Matlab^{TM} using a threshold value of 127 on an 8-bit scale [71]. Pixels with an intensity value below this threshold were converted to a value of 0 (black) and those above were converted to a value of 1 (white). With respect to the material microstructures, etching removed material within inter-dendritic regions, which created depressions that were processed into black pixels. The higher regions along dendrite arms appear lighter and were generally processed into white pixels. An example image of microstructure before and after binary processing is presented in Figure 5.4. This image was selected from the VAR ingot in the upper left corner of the bottom slab, assuming the casting direction is up.

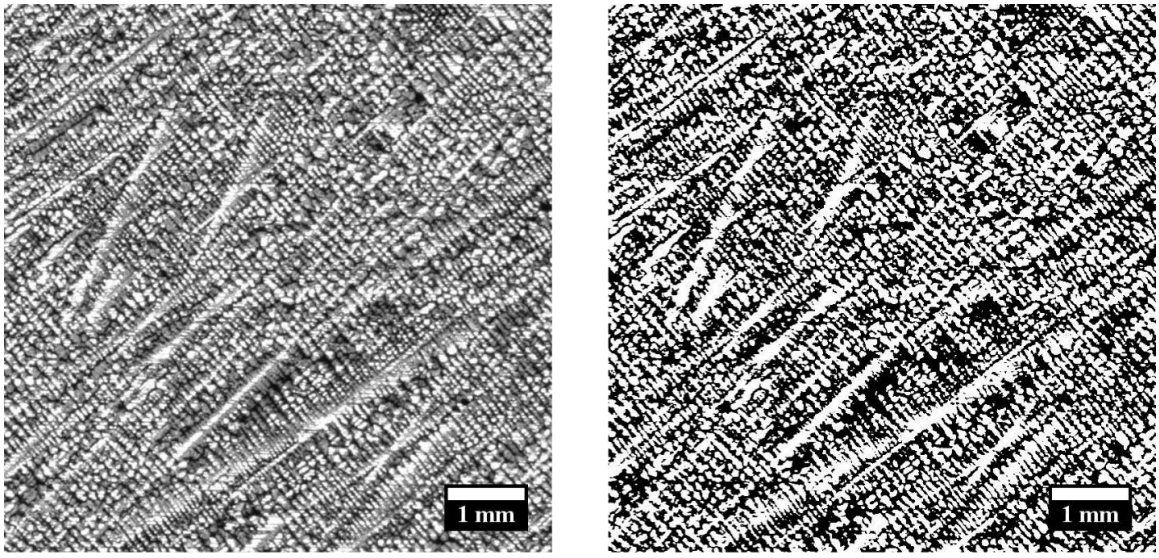

Figure 5.4: An example microstructure, from the VAR ingot in the upper left corner of the bottom slab, assuming the casting direction is up, is presented (a) before and (b) after binary processing.

5.3. MICROSTRUCTURAL ANALYSIS TECHNIQUES

Microstructures in the processed images were analyzed using two different techniques: (1) the particle identification technique and (2) the two-point correlation function technique. A brief introduction to each technique is presented in the following.

The particle identification algorithms and procedures used in this dissertation to characterize alloy 718 slabs were ingeniously developed by Dr. Trevor Watt [66]. This particle identification technique relies on the accurate identification of primary dendrite arms as individual particles to measure primary dendrite arm orientation and secondary dendrite arm spacing. Primary dendrite arms were identified as individual particles using software contained within the Fiji distribution of ImageJ and Matlab™ [70, 71]. Primary dendrite arm orientations were measured from the geometry and positon of each particle,

i.e. primary dendrite. Secondary dendrite arm spacing was measured from the change in image intensity along lines running parallel and directly adjacent to identified primary dendrite arms. The distance between peaks in image intensity is interpreted as the secondary dendrite arm spacing. There are two notable limitations to using the particle identification technique. First, some particles likely to represent primary dendrites are missed by the identification algorithm. It cannot easily identify overlapping dendrites or those obscured by artifacts from metallographic preparation. This leaves good data on the table without contributing to the analysis. Second, there is no clear methodology by which measurement uncertainty can be ascertained from individually identified particles. Despite these limitations, it was determined that a sufficient number of particles were correctly identified to analyze melt pool profiles and local solidification times throughout the alloy 718 slabs. The number of particles identified using this technique was deemed sufficient because the results produced qualitatively agreed with those observed from visual inspection of the prepared ingot cross-sections.

The second analysis technique used the two-point correlation function. The two-point correlation function algorithm used in this dissertation is based on that developed by Jung-Kuei Chang [72]. The two-point correlation function is useful for detecting microstructural trends and quantizing spatial relationships between microstructural features [73 – 75]. In this application, the two-point correlation function is used to determine the orientation and spacing of primary and secondary dendrite arms. This technique generates statistical arrays from regions of interest in an image which are used to detect trends in the data. One method of analyzing these arrays is to visualize them as 8-bit grayscale images and then interpret those images using digital image analysis techniques, such as Hough transforms and Fourier analysis. In contrast to the particle identification technique, this technique does not identify individual dendrites. Additionally,

every feature within an analysis region contributes to the two-point correlation function; no data are wasted, as are the missed particles in the particle identification technique.

These two analysis techniques complement each other. The two-point correlation function uses nearly all data from a region, even when particle identification is unsuccessful, to calculate average primary dendrite arm orientation and secondary dendrite arm spacing. The particle identification technique is useful for locating specific dendrites, especially outliers. Combined, these techniques provide a methodology to characterize average dendritic spatial relationships and to locate specific dendrites of interest. Nonetheless, it must be noted that the robustness of the data produced by these analysis techniques depends on the clarity of the microstructural image analyzed. Proper material preparation prior to imaging and analysis is critical to produce useful data.

5.4. PARTICLE IDENTIFICATION

The particle identification technique used in this dissertation to analyze binary montage images is described in the following. Additional discussion of the particle identification technique used is provided in Appendix B.

The particle identification algorithm contained within the Fiji distribution of ImageJ was used to identify particles from binary montage images [70]. This algorithm locates and identifies discrete areas of continuous white pixels and labels those areas as individual particles; it ignores regions of continuous black pixels. However, software identification of features, i.e. particles, from the as-converted binary image was poor because microstructural features often appear connected after the initial threshold operation. The binary image was further processed using morphological operations that grow and shrink regions of like-colored pixels to improve feature identification. Erosion

operations shrink regions of continuous white pixels, while dilation operations grow regions of continuous white pixels. These morphological operations improve feature identification by separating individual dendritic features from each other. Determining the processing steps necessary to improve feature recognition is somewhat of an art-form. For the material analyzed in this dissertation, experiments determined that two erosion operations were sufficient for the particle identification algorithm to operate effectively. The two erosion operations separate the individual primary dendrite arms connected by white pixels after the thresholding procedure, but do not shrink the primary dendrite arms enough to hinder their identification. It will be demonstrated later that this processing allows the particle identification algorithm used to detect many, but not all, primary dendrite arms. An individual image taken from the VAR ingot in the upper left corner of the bottom slab, assuming the casting direction is up, is presented in Figure 5.5 to demonstrate each image processing step. Figure 5.5 presents (a) the original grayscale image, (b) that image after CLAHE processing, (c) after binary conversion, and (d) after two erosion steps.

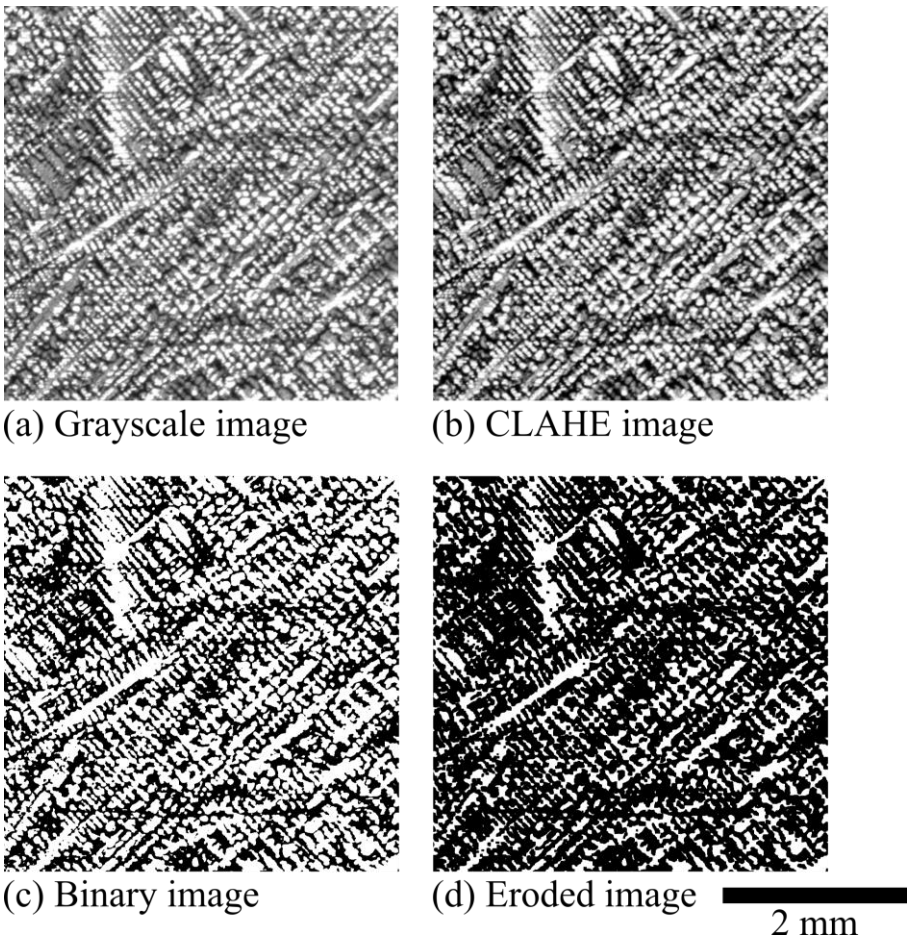

Figure 5.5: An image from the VAR ingot in the upper left corner of the bottom slab, assuming the casting direction is up, is presented to demonstrate each image processing step. (a) The original grayscale image, (b) that image after CLAHE processing, (c) after binary conversion, and (d) after two erosion steps are provided.

After particle identification was completed, each particle was fit with a bounding box and an ellipse to measure its shape and orientation. These particles were then filtered using a custom Matlab^{TM} program to remove particles not likely to represent primary dendrite arms [71]. Filtering was necessary because accurate identification of primary dendrite arms is critical to the measurement of both primary dendrite arm orientation and secondary dendrite arm spacing. Particles not likely to represent a primary dendrite arm,

which is long and slender, were removed from the data set by taking into account the size and shape of the particle. A particle may be filtered out for the following reasons:

1) Particles with an exceptionally small area may be removed. During this study, this filtering procedure was not deemed necessary, so a limit value of 0 pixels^2 was chosen.
2) Particles with low aspect ratios may be removed. The aspect ratio is calculated by dividing the length of the major axis of the ellipse fitted to the particle by the length of the minor axis of that ellipse. Particles with an aspect ratio below 5 were removed.
3) A particle may be removed if it was deemed too short or too long to represent a primary dendrite arm. This removed small image artifacts leftover from morphological processing and large artifacts present near the sides of the image. Particles shorter than 22 pixels and longer than 5000 pixels were removed.
4) A particle may be removed if the standard deviation of relative image intensity is large across that particle. This removes particles that do not correlate with the original image data. This is calculated by measuring the image intensity along the diagonal of the bounding box fit to that particle. If the standard deviation of this image intensity is large relative to the mean image intensity of the line, that particle may be removed. Particles with a relative standard (standard deviation/mean intensity) deviation above 0.5 were removed.

An individual image was taken from the VAR ingot in the upper left corner of the bottom slab to demonstrate the particle filtering process. Figure 5.6 presents (a) the original image, (b) the processed image, (c) all particles identified, (d) particles remaining after filtering, and (e) the particles after filtering overlaid on the original image.

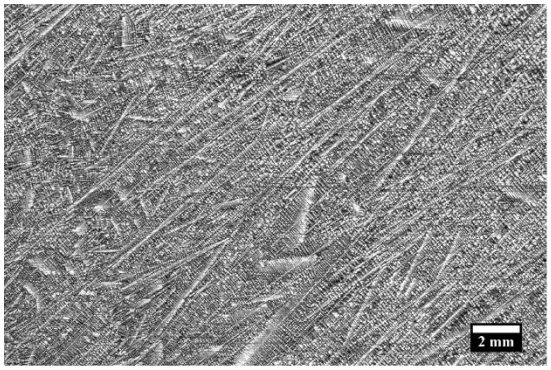

(a) Grayscale image

(b) Processed image

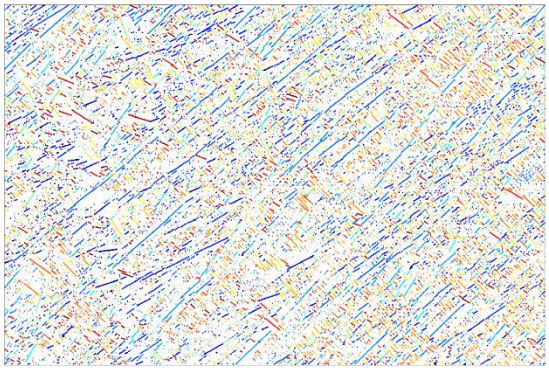

(c) Particles before filtering

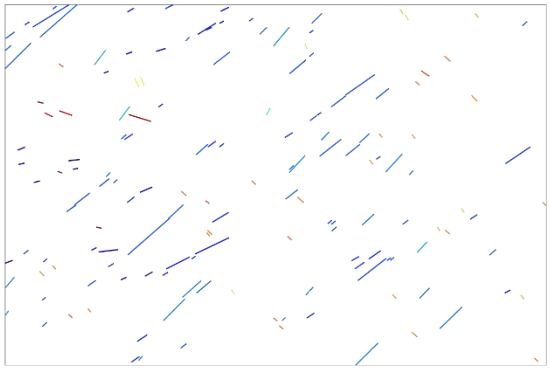

(d) Particles after filtering

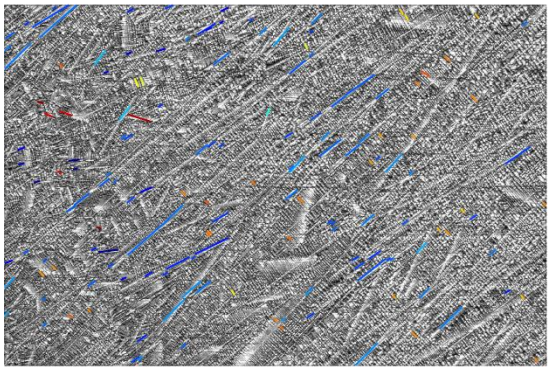

(e) Filtered particles overlay

Figure 5.6: An image from the VAR ingot in the upper left corner of the bottom slab, assuming the casting direction is up, is presented to illustrate the particle identification and particle filtering processes. Presented are (a) the grayscale image, (b) the processed image, (c) all particles identified, (d) the particles remaining after filtering, and (e) the filtered particles overlaid on the original grayscale image.

Two additional filtering steps were used to either modify or remove a particle previously identified as a primary dendrite arm. These considered the particle's relative orientation with respect to other particles within its immediate vicinity. These two final filters are now presented.

The first filter corrected for secondary dendrite arms misidentified as primary dendrite arms. Because secondary dendrite arms are expected to grow perpendicularly to primary dendrite arms, if a secondary dendrite arm was identified during particle identification, it can be rotated ± 90 degrees to create a "virtual" primary dendrite arm. A particle was determined to be a secondary dendrite arm if it was oriented 70 to 110 degrees from the average primary dendrite arm orientation in its region. This filter was applied in rectangular regions, 1000 pixels wide that spanned the height of the ingot along the casting direction. Particles that qualified for reorientation were rotated -90 degrees on the left side of the ingot and +90 degrees on the right side of the ingot. During this study, the filter was simultaneously run from both the left and the right sides of the ingot toward the center.

The second filter removed particles that were oriented at least two standard deviations from the mean particle orientation for a given region. For this filter, a circular region with a radius of 500 pixels was used. If a particle orientation inside this region was more than two standard deviations from the mean particle orientation within that region, it was removed. This filter reduced noise by removing particles that are poorly aligned with the other particles in its immediate vicinity. Because this filter uses the standard deviation across a given region to determine if a particle should be removed, it tends to filter out more objects from areas that have a well-defined particle orientation compared to areas that have a random distribution of orientations. This reduces noise in regions where primary dendrite arms are clearly identified without significantly affecting regions without a clear primary dendrite arm orientation.

An image from the VAR ingot in the upper left corner of the bottom slab is presented in Figure 5.7 to demonstrate the effects of the advanced particle filtering process. Figure 5.7 presents (a) the particles after initial filtering overlaid on the original image, (b) the particles after advanced filtering overlaid on the original image, (c) the particles before, and (d) after advanced filtering. Note the good agreement between the original image data and the particles after advanced filtering.

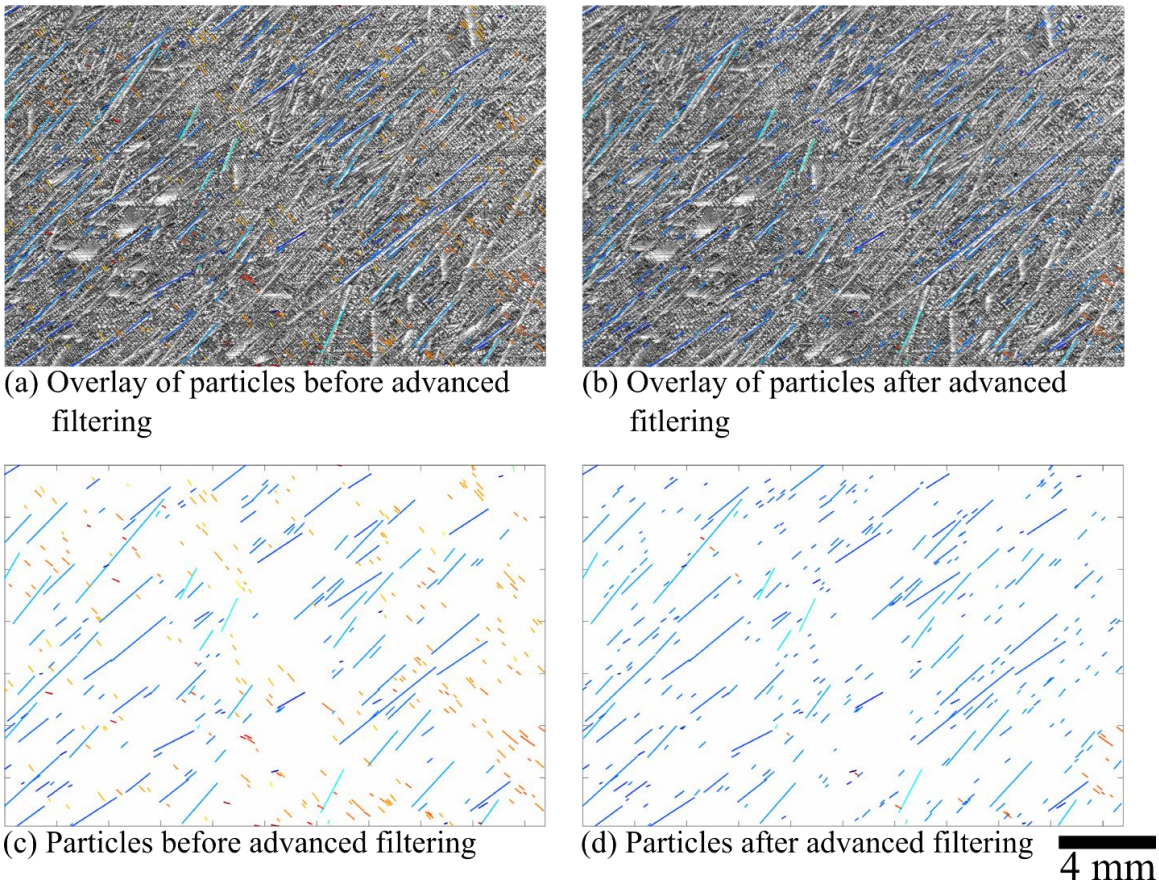

(a) Overlay of particles before advanced filtering

(b) Overlay of particles after advanced fitlering

(c) Particles before advanced filtering

(d) Particles after advanced filtering

Figure 5.7: The particles identified from an image taken from the VAR ingot are overlaid on the original image data (a) before and (b) after advanced filtering. The particles are shown alone (c) before and (d) after advanced filtering.

After primary dendrite arms were identified and filtered to reduce noise, secondary dendrite arm spacing was measured. Secondary dendrite arm spacing was measured from the change in image intensity along lines running parallel and directly adjacent to the identified primary dendrite arms. The distance between peaks in image intensity is interpreted as the secondary dendrite arm spacing. Figure 5.8 presents a single primary dendrite arm to illustrate how the lines for analysis of secondary dendrite arms were created. Figure 5.9 provides a measurement of image intensity along the secondary dendrite arm analysis lines in Figure 5.8. Secondary dendrite arms spacing was calculated in the following manner:

1) A single primary dendrite arm (PDA) is chosen for analysis.
2) The 8-bit grayscale TIFF image data from the alloy 718 slab where that primary dendrite arm is located is loaded into memory.
3) The PDA is defined as the line connecting the two points at the extreme ends of the particle bounding box. To measure secondary dendrite arm spacing (SDAS), additional lines are defined parallel to the PDA line, one on either side. These are termed the SDAS lines and are offset by 8 pixels from the PDA line.
4) The image intensity profile along the length of each SDAS line is measured. Each peak in the image intensity profile ideally represents a secondary dendrite. In this approach, the peaks are determined by using a local-maximum filter on the intensity profile. A window of a specified size is moved over the profile, and if the central pixel has the largest intensity within that window, it is set as a local maximum. This is subject to the additional constraints that it must not have a pixel intensity of zero and that it must not be neighboring another maximum.
5) SDAS is calculated by measuring the distance between peaks. The spatial position of the SDAS measurement is assigned to the geometric center of the PDA line.

a. If only one peak is identified, no SDAS value is recorded
b. If only two peaks are identified, the SDAS value is assigned the distance between the two peaks. The error associated with that measurement is calculated from the uncertainty of locating the center of each peak.
c. If more than two peaks are identified, the SDAS value is calculated as the mean of the distances between peaks. The error associated with that measurement is defined by the standard deviation of the distances between peaks.

6) The SDAS values are stored for the specific SDAS analysis line offset, initially 8 pixels.
7) Steps 3 through 6 are performed again for line offsets of 10, 12, 14, and 16 pixels.
8) The SDAS values for each offset line are compared, and the offset line with the smallest error in SDAS is retained. The rest are discarded.
9) The SDAS values are filtered to remove poor results. SDAS measurements with a relative standard deviation greater than or equal to 5 are discarded.

Two filters were applied to the automated secondary dendrite arm spacing measurements. The first filter removed secondary dendrite arm spacing measurements that were two standard deviations away from the mean secondary dendrite arm spacing value in the same region. During this study a circular region with a radius of 500 pixels was used for this filter. The second filter was used to remove secondary dendrite arm spacing measurements that were excessively large and not removed by the first filter.

Occasional regions produce large values for secondary dendrite arm spacing that were neither physically meaningful nor removed by the first filter. To remedy this problem, secondary dendrite arm spacing measurements greater than 270 μm were removed. To put

this in perspective, the average secondary dendrite arm spacing in the VAR ingot was manually measured as approximately 100 μm with a standard deviation of approximately 40 μm.

It is important to note that the automated secondary dendrite arm spacing measurement technique is prone to an error that increases the spacing measurement. This technique is expected to measure larger values for secondary dendrite arm spacing because it is susceptible to missing some secondary arms, which leads to an increase in the spacing measurement.

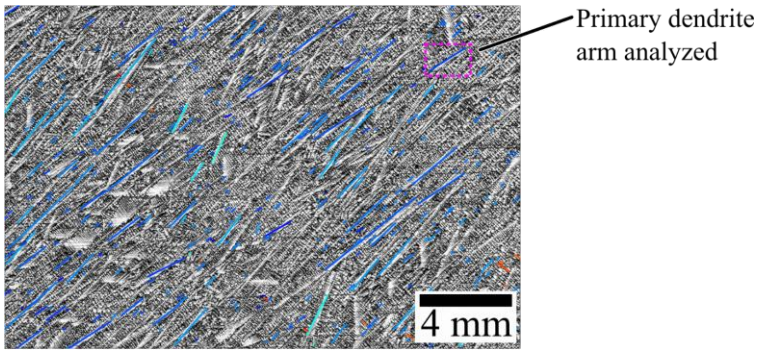

(a) Primary dendrtie arm is selected

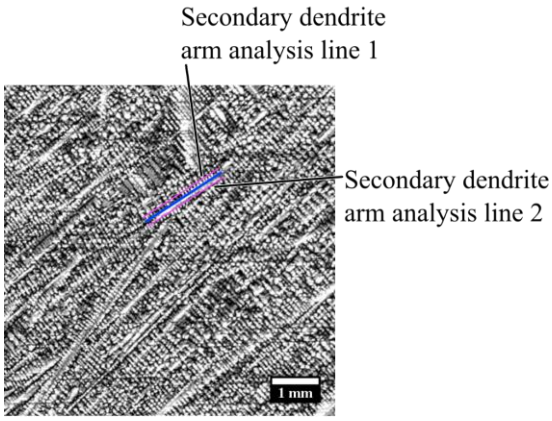

(b) Secondary dendrite arm analysis lines are created

Figure 5.8: An individual dendrite arm is highlighted in (a) and presented in (b) with the lines for secondary dendrite arm spacing analysis.

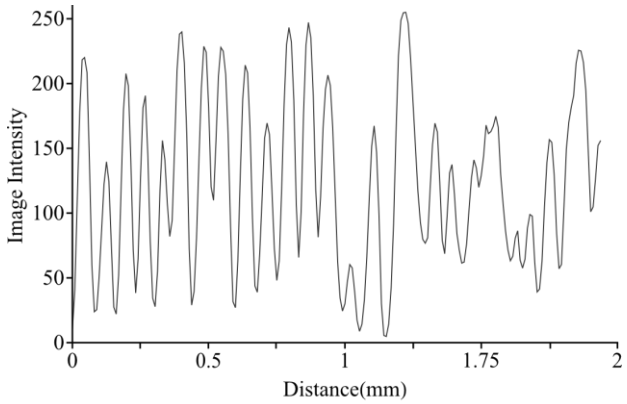

(a) Secondary dendrite arm line 1

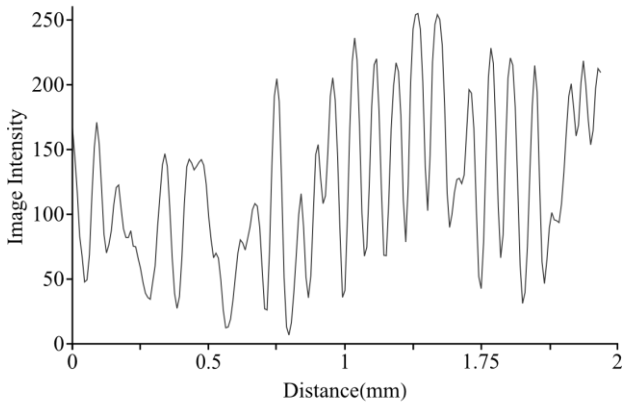

(b) Secondary dendrite arm line 2

Figure 5.9: The image intensity profiles along the lines used for secondary dendrite arm spacing analysis shown in Figure 5.8 are provided.

5.5. TWO-POINT CORRELATION FUNCTION

Correlation functions are used to describe the spatial relationships between features of interest in an image. They are often used in astronomy to determine the spacing of galaxies, for example [76]. For this dissertation, a two-point correlation function was used to measure the orientation and spacing of primary and secondary dendrite arms. The two-point correlation function is described in the following.

The two-point correlation function $P_{ij}(r,\theta)$ used in this dissertation is defined in cylindrical coordinates (r, θ) as the probability that a line with length r, orientation θ, and endpoints in phase i and phase j exists. This probability, $P_{ij}(r,\theta)$, is orientation dependent. The orientation-averaged probability function $\langle P_{ij}(r)\rangle$ is calculated in two dimensions as [72, 73, 77],

$$\langle P_{ij}(r)\rangle = \int_0^{\pi/2} P_{ij}(r,\theta)\sin\theta d\theta. \quad (2)$$

$\langle P_{ij}(r)\rangle$ is defined as the average probability that any line with length r and endpoints in phase i and phase j exists. For this study, only two phases exists in the microstructure. Dendrite arms are defined as phase 1 and inter-dendritic regions are defined as phase 2. The two-point correlation function is then defined by four probabilities: $\langle P_{11}(r)\rangle$, $\langle P_{12}(r)\rangle$, $\langle P_{21}(r)\rangle$, and $\langle P_{22}(r)\rangle$. Only one of these probabilities is independent according to the following relationships [72, 73, 77]:

$$\langle P_{11}(r)\rangle + \langle P_{12}(r)\rangle + \langle P_{21}(r)\rangle + \langle P_{22}(r)\rangle = 1 \quad (3)$$

$$\langle P_{12}(r)\rangle = \langle P_{21}(r)\rangle \quad (4)$$

$$\langle P_{11}(r)\rangle + \langle P_{12}(r)\rangle = f_1 \quad (5)$$

$$\langle P_{22}(r)\rangle + \langle P_{21}(r)\rangle = 1 - f_1 \quad (6)$$

Here f_1 is the volume fraction of phase 1 present in the microstructure.

5.6. IMPLEMENTATION OF THE TWO-POINT CORRELATION FUNCTION

Two-point correlation function analysis was performed on the as-converted binary montage images. No morphological processing was necessary prior to analysis, but the images were sometimes converted from the TIFF image format to the PGM image format using ImageJ. In the PGM format, dendrite arms were still represented by a pixel value of 1 (white), and inter-dendritic regions were represented by a pixel value of 0 (black).

Two-point correlation function analysis of microstructure was implemented in Mathematica™ using the process illustrated by Figure 5.10 to Figure 5.12 [78]. This implementation uses a moving window (transportable analysis window) to compute the two-point correlation function from a selected region of interest (analysis region) in the montage image. The analysis region is sequentially moved across the montage until the entire slab has been analyzed, as shown in Figure 5.10. The size of the analysis region was chosen based on the following criteria: (1) it must contain enough microstructural features to produce meaningful results, (2) primary dendrite arm orientation should be uniform in the region, (3) processing time to complete two-point correlation function analysis must be reasonable, and (4) it must be a square with dimensions equal to a power of two, i.e. images 2^n by 2^n large, where n is a positive integer, for compatibility with Fourier analysis. Using these constraints, an analysis region of 512 by 512 pixels was determined to be the best among those investigated for images with a resolution of approximately 9 μm per pixel. The process used to select this size for the analysis region is described later.

The calculation of the two-point correlation function within an individual analysis region is illustrated by Figure 5.11 and Figure 5.12. This calculation uses a transportable analysis window, a measurement frame describing the motion of the transportable analysis window, and the user-defined variable r_{max}. The transportable analysis window is used to calculate the two-point correlation function at individual steps in the analysis region. The

measurement frame defines the motion of the transportable analysis window. The variable r_{max}, determined by the user, defines the size of the transportable analysis window and the measurement frame. The measurement frame was positioned in the center of the analysis region a distance of r_{max} from the edges, as shown in Figure 5.11. The transportable analysis window is a square window with a width of $2r_{max}$. The center of the transportable analysis window is termed the "base point".

Figure 5.12 illustrates the calculation of the two-point correlation function from a two-phase microstructure; pixel values of 1 and 0 represent the two different phases. The transportable analysis window, the measurement frame, and the location of the first base point are noted in Figure 5.12 (a). Figure 5.12 (b) to (f) illustrate the calculation of the two-point correlation function in the transportable analysis window at individual locations in the measurement frame; note that only the $\langle P_{11}(r) \rangle$ calculation is presented. At each location in the measurement frame, the two-point correlation function, P_{ij}, is calculated by comparing the pixel value at the center of the transportable window, the base point, to all other pixel values in the transportable window. Positions in the transportable window are then assigned integer values of 1 or 0 depending on the correlation between their pixel value and that of the base point to create the P_{ij} array. Summing the individual P_{ij} arrays from each location in the measurement frame calculates the $\langle P_{ij} \rangle$ array, the two-point correlation function for the entire analysis region. The $\langle P_{11}(r) \rangle$ array was calculated at each location in the measurement frame using the following rules:

1) If the base point pixel value equals 1:
    a. Each position within the transportable array that has a pixel value of 1 is assigned a numerical value of 1. Each remaining position is assigned a numerical value of 0. This process is demonstrated by Figure 5.12 (b).
2) If the base point pixel value equals 0:

a. All positions in the transportable array are assigned a numerical value of 0. This process is demonstrated by Figure 5.12 (c)

3) The P_{ij} arrays calculated at each location in the measurement frame are summed to create $\langle P_{11}(r) \rangle$. This process is demonstrated in Figure 5.12 (f).

The $\langle P_{12}(r) \rangle$, $\langle P_{21}(r) \rangle$, and $\langle P_{22}(r) \rangle$ arrays are similarly calculated using analogous rules. The probability in percentage is found by dividing each value in the array by the maximum value in the array. This presents the probability of one point in the array being the same as the base point. These probability arrays can be visualized as 8-bit grayscale images; bright and dark regions represent high and low probabilities, respectively. These images were analyzed using digital image analysis techniques, such as Hough transforms and Fourier analysis, to determine the spatial relationships between microstructural features.

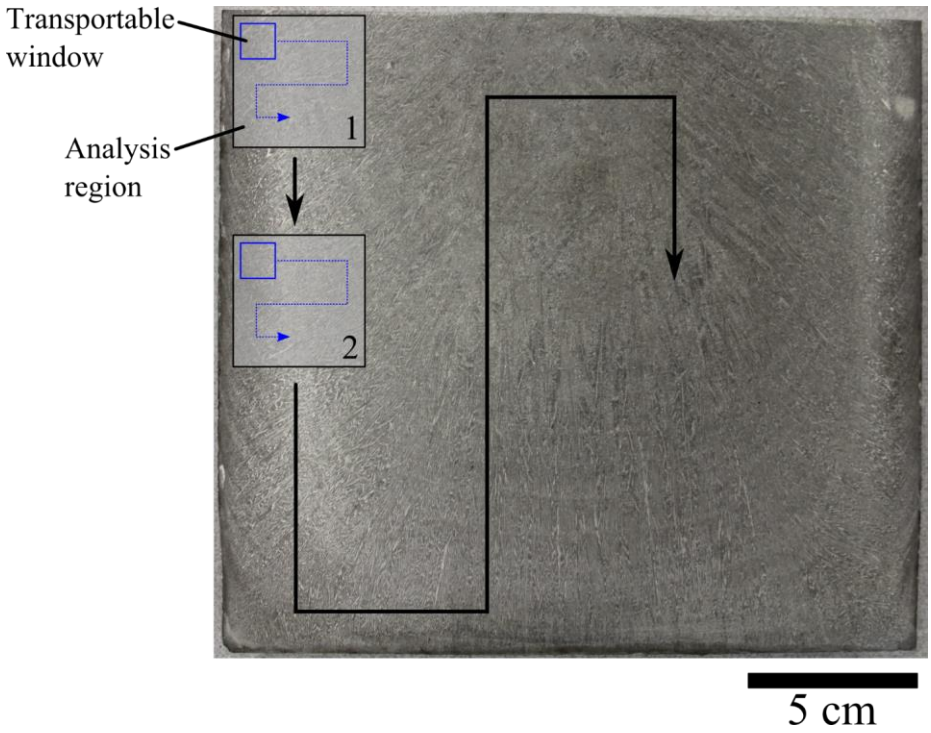

Figure 5.10: The sequential motion of the analysis region used for two-point correlation function calculations across a montage image is illustrated. The motion of the transportable analysis window within the analysis region is also illustrated.

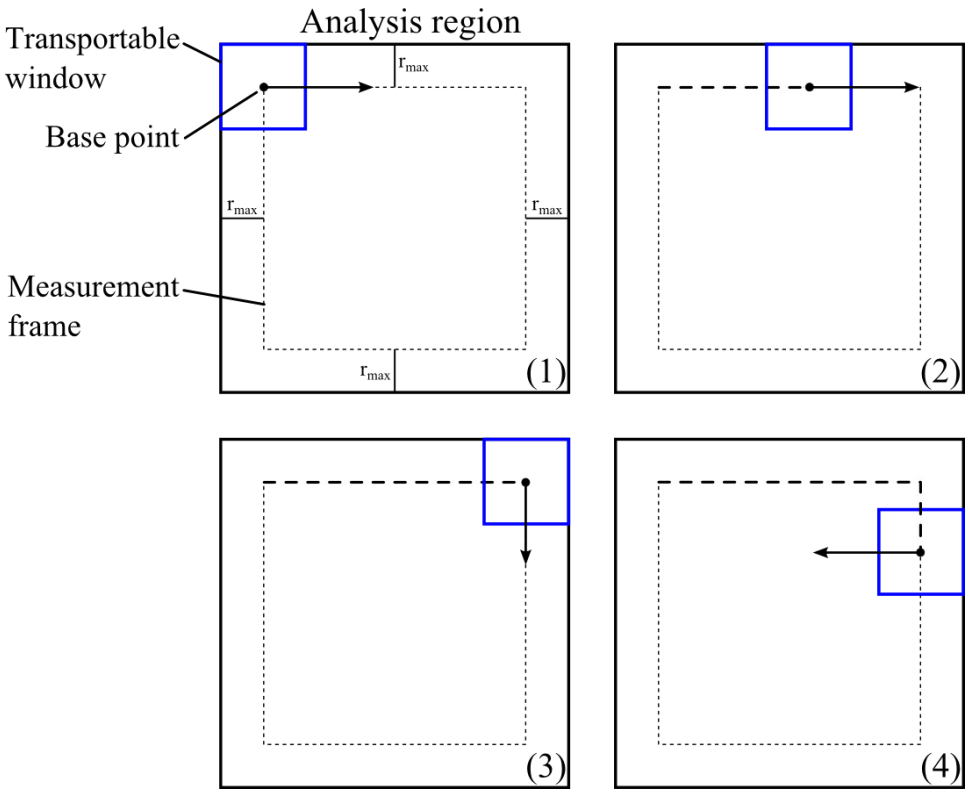

Figure 5.11: The calculation of the two-point correlation function within an individual analysis region is illustrated. The transportable analysis window is sequentially moved across the analysis region, as constrained by the measurement frame.

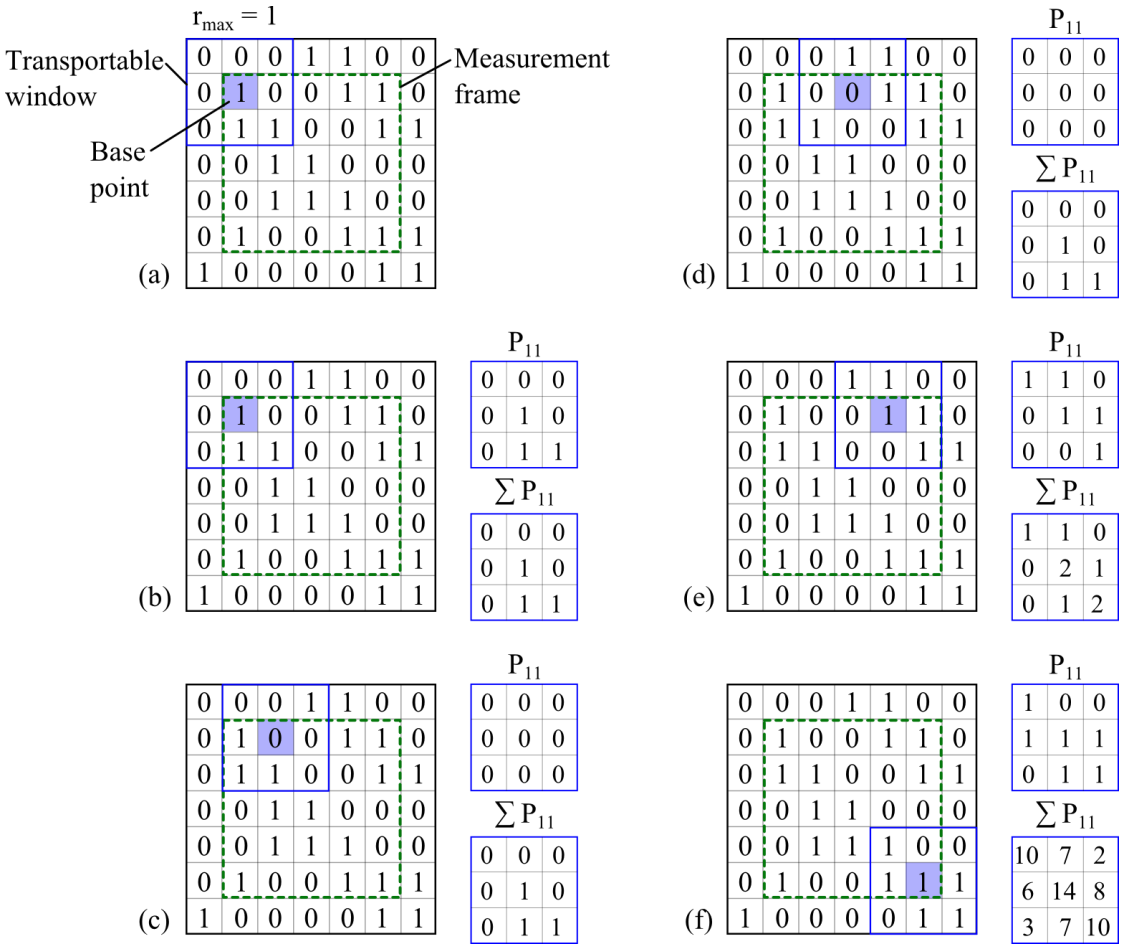

Figure 5.12: The calculation of P_{ij} arrays at individual positions within an analysis region are presented. A simulated two-phase microstructure, transportable analysis window, and measurement frame are presented in (a). P_{ij} arrays are calculated at different positions within the analysis region in (b) thru (f).

5.7. Two-point Correlation Function Tuning

The two-point correlation function technique is primarily controlled by adjusting the sizes of the analysis region and the transportable analysis window. These parameters must be tuned to the size of the microstructural features analyzed to provide the desired amount of data averaging and retention of fine feature detail. Tuning in this study was

accomplished using a single image taken from the VAR ingot in the upper left corner of the bottom slab. This image, presented in Figure 5.13, was chosen because both primary and secondary dendrite arms are visible in it. Square analysis regions 256, 512, and 1024 pixels wide were selected from the center of this image for tuning. These sizes were chosen because each contains enough microstructural features to produce meaningful results, and primary dendrite arm orientations are consistent in each region. The size of the analysis regions were limited to squares with dimensions equal to a power of two because of Fourier analysis considerations. The two-point correlation function was applied to each of these analysis regions using transportable analysis windows from 64 to 512 pixels wide. The analysis region and transportable analysis window sizes studied are summarized in Table 5.3. Each analysis region and the two-point correlation function data produced are presented in the following case descriptions.

Table 5.3: The analysis region and transportable analysis window sizes used for tuning are listed.

Analysis region size (pixels)	Transportable analysis window size (pixels)
256	64
	128
512	64
	128
	256
1024	128
	256
	512

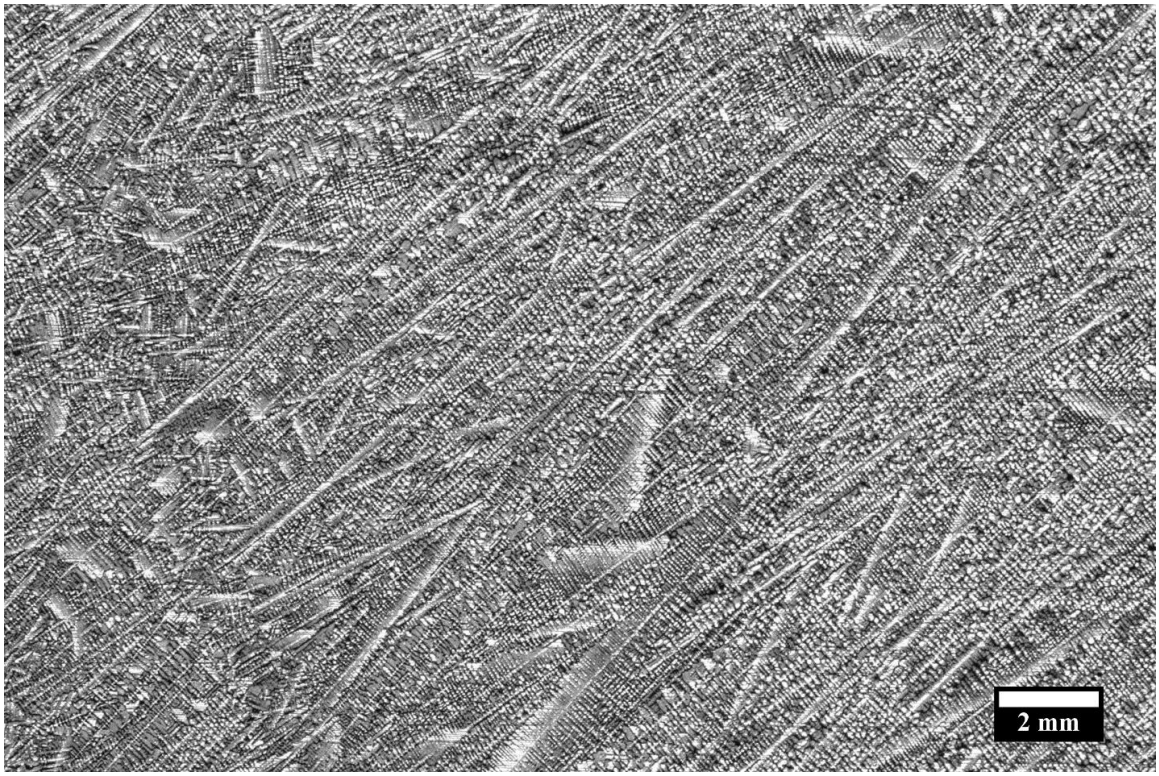

Figure 5.13: This image was used to tune the two-point correlation function operating parameters: analysis region size and transportable analysis region size. This image was taken from the upper left corner of the bottom slab from the VAR ingot. Analysis regions were taken from the center of this image to tune the two-point correlation function.

5.7.1. Case One: The 256 pixel analysis region

The 256 pixel analysis region is presented in Figure 5.14. This region contains approximately 5 primary dendrite arms, and there is a single primary dendrite arm orientation, which can be easily identified. Many secondary dendrite arms are visible within this region, and their orientations and spacings can be identified. At least one horizontal scratch from metallographic preparation is visible within the analysis region. Two 8-bit grayscale images are presented in Figure 5.15 to visualize the two-point correlation function outputs from the 256 pixel analysis region using the (a) 64 and (b) 128

pixel transportable analysis window sizes. Bright streaks are visible in both Figure 5.15 (a) and (b) along the primary and secondary dendrite arm orientations; the two highest intensity streaks run through the center of the data. These two streaks describe the average primary and secondary dendrite arm orientations in the analysis region. Additional streaks are along the secondary dendrite arm orientation and appear periodic in Figure 5.15 (b), repeating along the primary dendrite arm orientation. This periodicity can be measured and used to calculate secondary dendrite arm spacing. A horizontal streak is also visible in both Figure 5.15 (a) and (b) and is most likely produced by scratches evident in the analysis region.

The 128 pixel transportable window provides greater detail, i.e. more secondary dendrite arm streaks are discernable, than the 64 pixel transportable window for this analysis region. Conversely, the 64 pixel transportable window produces heavier averaging of the data.

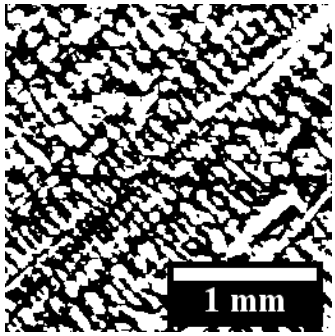

Figure 5.14: The 256 pixel wide analysis region selected from Figure 5.13 is provided after processing into a binary image format.

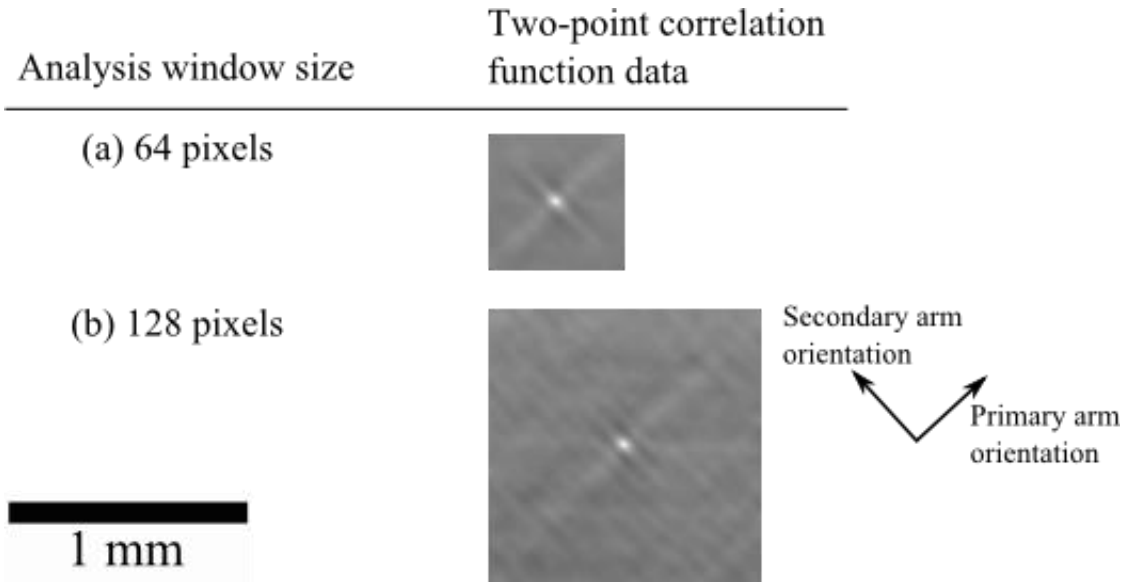

Figure 5.15: Outputs from two-point correlation function analysis on the 256 pixel analysis region are presented. Transportable analysis window sizes of (a) 64 and (b) 128 pixels were used.

5.7.2. Case Two: The 512 pixel analysis region

Figure 5.16 presents the 512 pixel analysis region. More than 5 primary dendrite arms are visible in this region. Their orientations are consistent throughout the analysis region. An abundance of secondary dendrite arms and two horizontal scratches are also present. Three 8-bit grayscale images are presented in Figure 5.17 to visualize the two-point correlation function outputs from the 512 pixel analysis region using the (a) 64, (b) 128, and (c) 256 pixel transportable analysis window sizes. Similar to the previous case, bright streaks are visible along the primary and secondary dendrite arm orientations in all of the two-point correlation function outputs. The two highest intensity streaks, again, pass through the center of the data. As demonstrated in Figure 5.17, the periodic streaks along the secondary dendrite arm orientation become less numerous and less defined as the

transportable window size decreases. But the two highest intensity streaks that pass through the center of the data, which represent the primary and secondary dendrite arms, are not strongly affected by the transportable window size. For this analysis region size, the 128 and 256 pixel transportable window sizes provide a useful balance between data averaging and the retention of fine feature details.

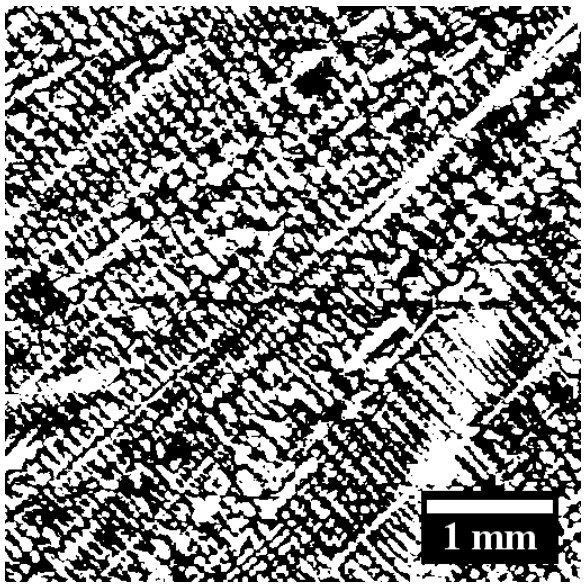

Figure 5.16: The 512 pixel wide analysis region selected from Figure 5.13 is provided after processing into a binary image format.

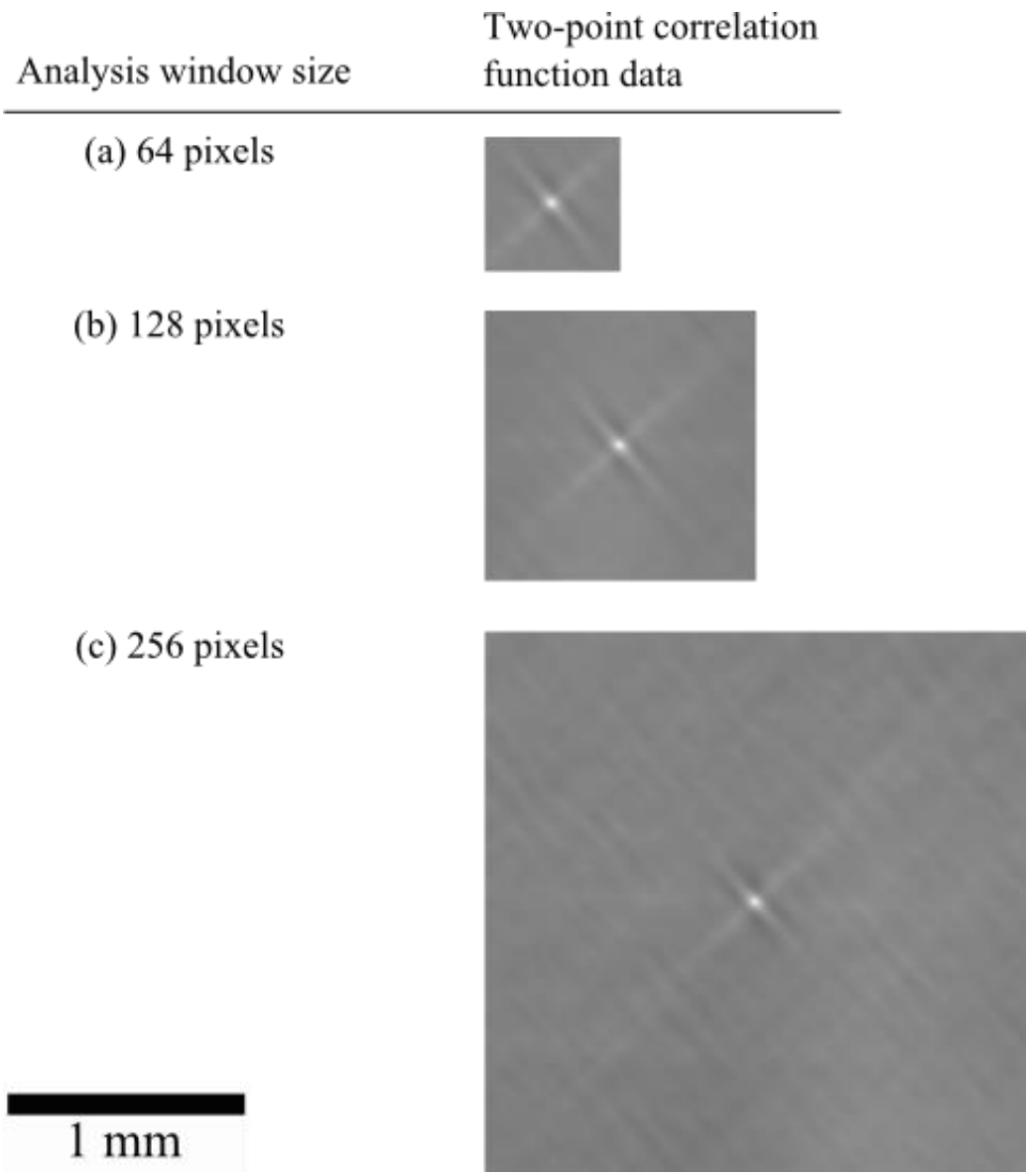

Figure 5.17: Outputs from two-point correlation function analysis on the 512 pixel analysis region are presented. Transportable analysis window sizes of (a) 64, (b) 128, and (c) 256 pixels were used.

5.7.3. Case Three: The 1024 pixel analysis region

The 1024 pixel analysis region is provided in Figure 5.18. Numerous primary dendrite arms and hundreds of secondary dendrite arms are visible in this analysis region. Individual primary dendrite arm orientations differ slightly across the region. Three 8-bit grayscale images are presented in Figure 5.19 to visualize the two-point correlation function outputs from the 1024 pixel analysis region using the (a) 128, (b) 256, and (c) 512 pixel transportable analysis window sizes. As for the two previous cases, two principle streaks, representing the primary and secondary dendrite arms, which run through the center of the data are produced using any transportable analysis window size. The smaller periodic streaks, which represent the secondary dendrite arm spacing, weaken as the transportable analysis window size is decreased. For this analysis region, the 256 and 512 pixel window sizes provide a suitable balance between data averaging and the retention of fine feature details.

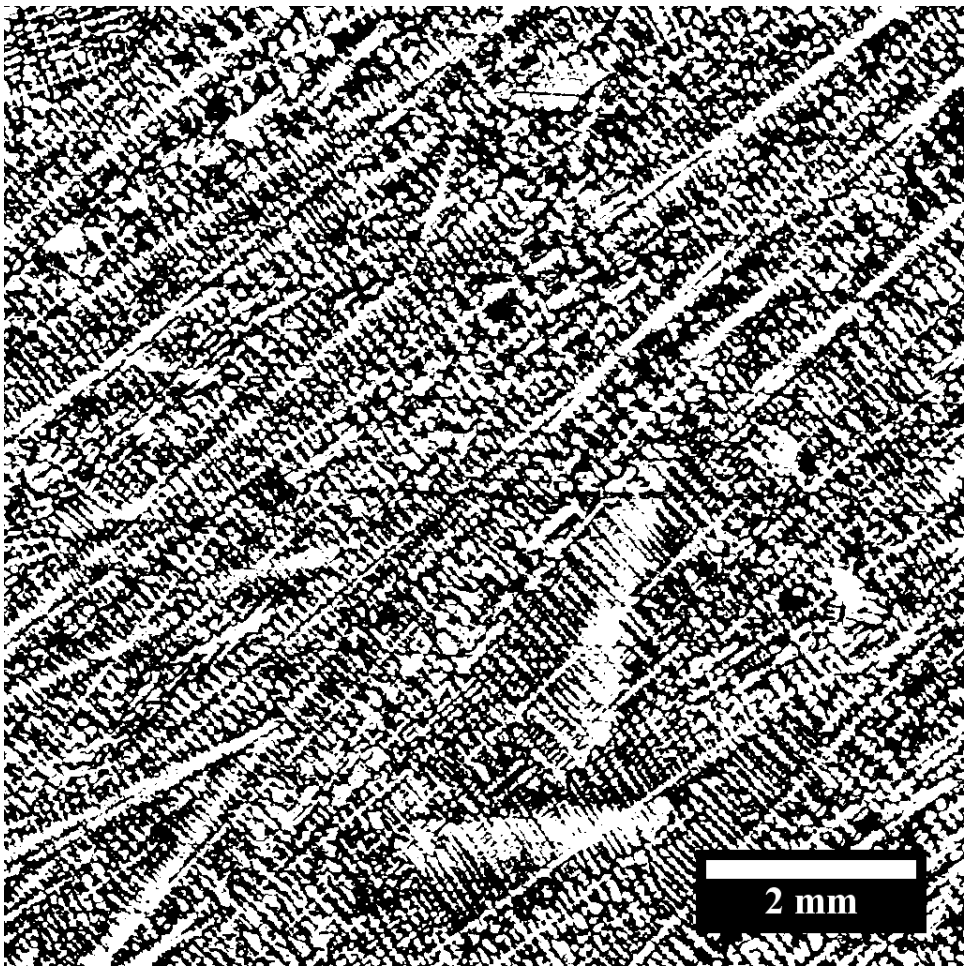

Figure 5.18: The 1024 pixel wide analysis region selected from Figure 5.13 is provided after processing into a binary image format.

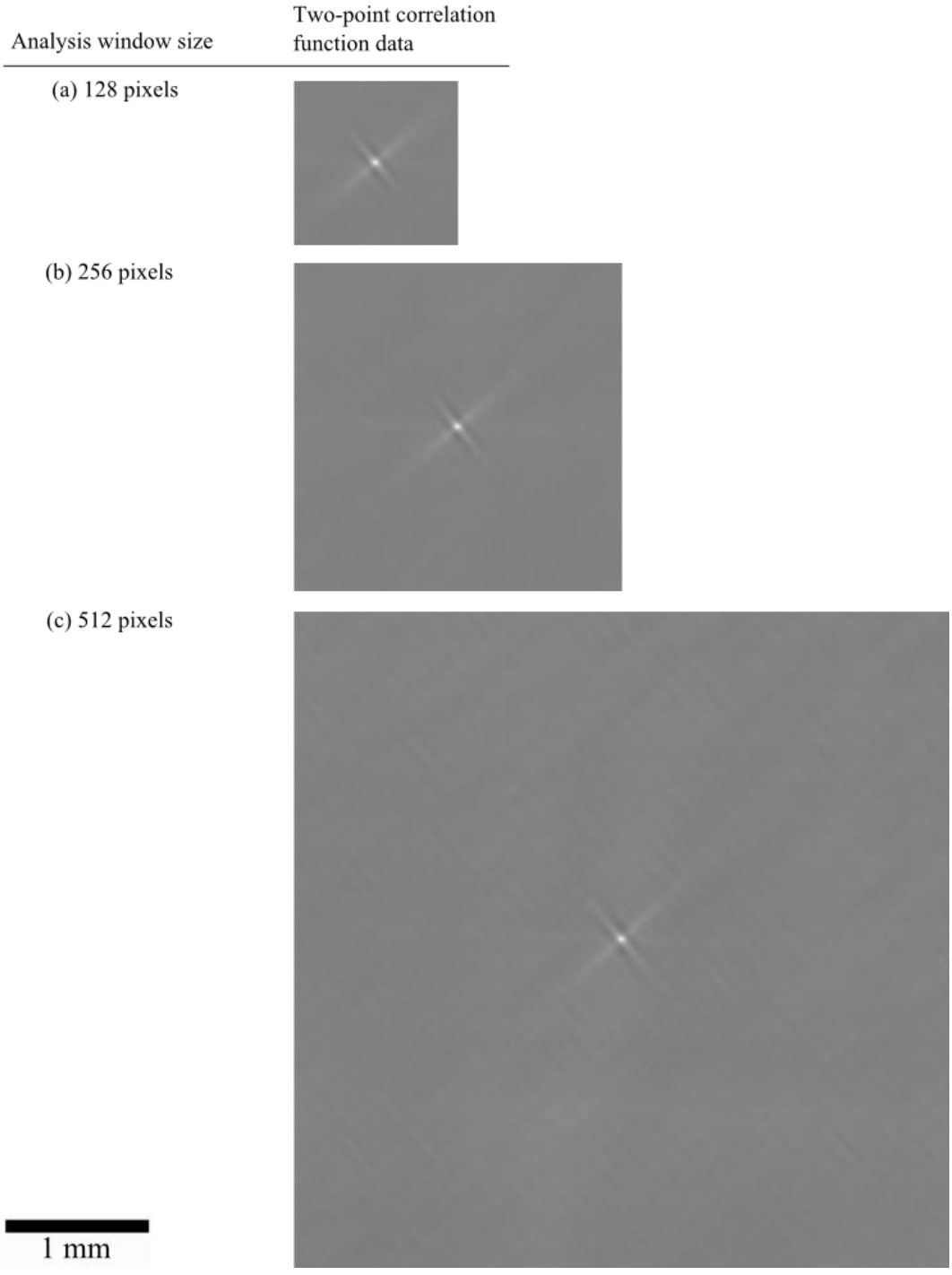

Figure 5.19: Outputs from two-point correlation function analysis on the 1024 pixel analysis region are presented. Transportable analysis window sizes of (a) 128, (b) 256, and (c) 512 pixels were used.

5.7.4. Computational Processing Time Considerations

Computational processing time was also considered during tuning of the two-point correlation function. Processing times for an individual two-point correlation function calculation of less than 300 seconds were considered reasonable for this study. Processing times for different analysis regions and transportable analysis window sizes are presented in Table 5.4. Computational times are based on a Dell™ Precision T3600 with an 8-core Intel™ Xeon™ E5-1620 @ 3.60 GHz processor and 32.0 GB of DDR3 RAM running Windows™ 7 Enterprise.

Table 5.4: Computational times to complete two-point correlation function analysis are presented for different analysis region and transportable analysis window sizes.

Analysis region size (pixels)	Transportable analysis window size (pixels)	Processing time (seconds)
256	64	0.60
	128	0.88
512	64	2.91
	128	5.78
	256	5.33
1024	128	32.4
	256	38.6
	512	159.0

5.7.5. Tuning summary

The best balance of data averaging, retention of fine feature detail, and computational processing time was achieved using the case with a 512 pixel analysis region and a 256 pixel transportable analysis window size. The 512 pixel analysis region contained a sufficient number of dendrites to analyze and provided a consistent primary dendrite arm orientation. As demonstrated by Table 5.4, this analysis case could be

calculated in a matter of seconds. The 512 pixel wide analysis region, paired with the 256 pixel transportable analysis window, was used to complete two-point correlation function analysis of the montage images from the VAR ingot.

The other cases were not used because of the following reasons. The 256 pixel analysis region was too small; not enough dendritic features were present within the region to reliably produce useful results. Additionally, the small size of the two-point correlation function output made further analysis difficult. The 1024 pixel analysis was considered too large because the orientation of primary dendrite arms varied across the region, and computational processing times were substantially greater than for any other case.

6. TWO-POINT CORRELATION FUNCTION OUTPUT ANALYSIS

6.1. ANALYSIS TECHNIQUES

Primary and secondary dendrite arm orientations and secondary dendrite arm spacing were measured from two-point correlation function outputs using digital image analysis techniques. Digital image analysis techniques are often used to detect lines, shapes, and patterns from images. In this dissertation, two-point correlation function outputs were analyzed as 8-bit grayscale images using Hough transforms, Radon transforms, and Fourier analysis. Each technique was implemented to measure primary dendrite arm orientation and secondary dendrite arm spacing. Determining secondary dendrite arm orientation, when possible, was also found to be useful. Of the three digital image analysis techniques used, Fourier analysis produced the most useful and consistent results. It was used to analyze the montage images acquired from the VAR ingot. The three digital image analysis techniques studied are now presented.

6.2. HOUGH TRANSFORM

The Hough transform was initially developed to detect lines in images [79, 80], but has since been modified to detect generalized shapes [81]. For this application, the Hough transform was used to detect the streaks, i.e. lines, in the two-point correlation function output. These lines typically describe the primary and secondary dendrite arm orientations.

The Hough transform uses the parametric representation of a line to transform image data described from the traditional two-dimensional coordinates (x, y) to the Hough space representation (ρ, θ) using the following relationship [80],

$$\rho = x\cos\theta + y\sin\theta. \qquad (7)$$

The relationship between (ρ, θ) and (x, y) is illustrated in Figure 6.1. The image data is transformed into Hough space using a binning technique. Bins are created for each (ρ, θ) combination possible in the image; the size of the bins determines the resolution of the image in Hough space. For each (x, y) location within the image, the corresponding (ρ, θ) values are calculated for θ between -90 and 90 degrees. The appropriate (ρ, θ) bins are then updated according to the pixel value at that (x, y) location. The transformed image data can then be viewed and analyzed as a grayscale image. The following points are useful to consider when analyzing an image in Hough space. First, a point in (x, y) space produces a sinusoidal curve in Hough space. Second, if points are aligned to form a line in (x, y) space, their corresponding sinusoids overlap in Hough space. Third, overlapping sinusoids in Hough space create points of high intensity. These points of high intensity in Hough space represent lines in traditional space.

An image taken from the VAR ingot in the center of the bottom slab, shown in Figure 6.2 (a), was analyzed with the two-point correlation function. The two-point correlation function output from this image is presented in Figure 6.2 (b). The Hough transform was applied to this two-point correlation function output and is presented in Figure 6.2 (c) as a grayscale image. The Hough transform was applied in Matlab^{TM} using bin sizes of one pixel for ρ and one degree for θ [71].

The Hough transform is dominated by two sinusoidal bands and two bright regions at -45 and 45 degrees from the overlap between these bands. Note that the θ location of these bright regions does not correspond with the angle of the dendrite arm directions visible in the two-point correlation function output. The sinusoidal bands in the Hough transform were not created by the dominant streaks in the two-point correlation function, but rather the background noise in the two-point correlation function output. This problem is common for images without well-defined lines and relatively low contrast, such as the

two-point correlation function output. Consequently, primary dendrite arm orientation could not be ascertained from the two-point correlation function output using the Hough transform.

Additionally, image artifacts, shown in Figure 6.2 (c), were created by the Hough transformation. These artifacts, which appear strongest at -45 and 45 degrees, arise from the binning process and are difficult to remove without discarding data. Furthermore, it is unclear how secondary dendrite arm spacing could be measured directly from Hough space. Secondary dendrite arm spacing could be measured from the change in image intensity along the primary dendrite arm orientation in the two-point correlation function output. But this would require an accurate measurement of primary dendrite arm orientation, currently unattainable using the Hough transform.

Several processes were studied to improve the detection of the primary dendrite arm orientation from two-point correlation function outputs using the Hough transform. First, multiple bin size combinations were used for ρ and θ, the parameters used to calculate the Hough transform. Bin sizes for ρ varied from 1 to 5 pixels in 1 pixel increments, and bin sizes for θ varied from 0.2 to 2 degrees in 0.1 degree increments. No combination of ρ and θ bin sizes used produced an accurate measurement of the primary dendrite arm orientation or eliminated the image artifacts created by the Hough transformation. Second, a CLAHE algorithm was applied to the two-point correlation function output prior to Hough analysis. This procedure did not improve the detection of dendritic arm orientations because it did not accentuate the dominant streaks that represent dendrite arm orientations or increase the contrast of the two-point correlation function output. Third, a threshold procedure was applied to the CLAHE processed two-point correlation function output to remove background noise and isolate the bright streaks that represent the dendritic arm orientations in the two-point correlation function output. The threshold process converted

all pixel values below 0.5 to 0, i.e. black. The threshold procedure slightly improved the detection of dendritic arm orientations, but produced inconsistent results across different images, generated large measurement uncertainty, and was difficult to automate. Fourth, a weighted calculation was used to emphasize data acquired from bright pixels over data from darker pixels in the two-point correlation function output. Several different weighting algorithms were tested, but none reliably improved detection of the primary dendrite arm orientation.

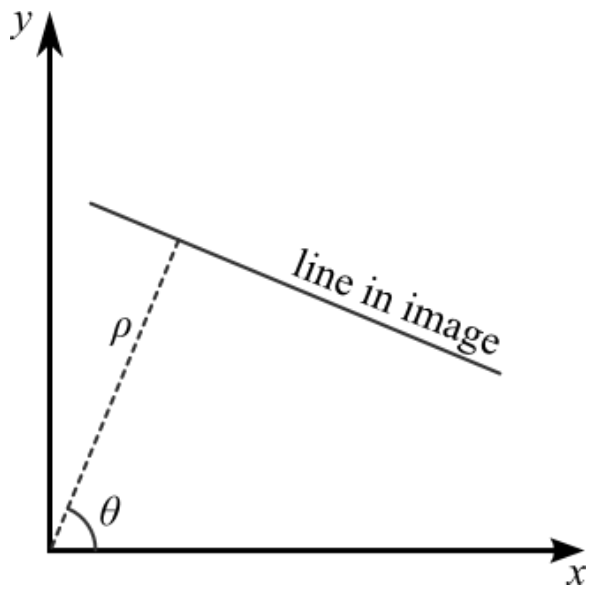

Figure 6.1: The relationship between (ρ, θ) and (x, y) used to calculate the Hough transform is presented.

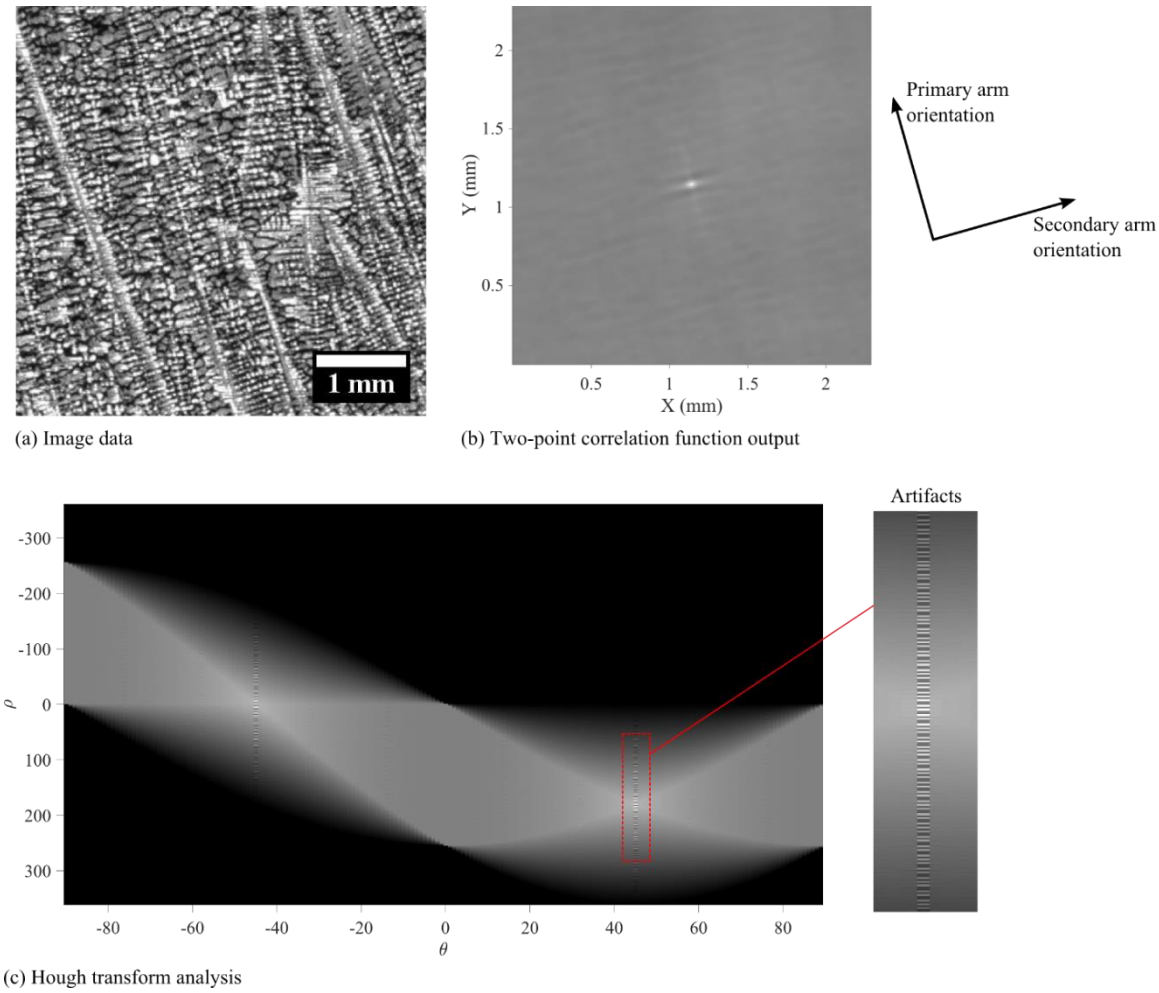

(a) Image data

(b) Two-point correlation function output

(c) Hough transform analysis

Figure 6.2: The Hough transformation process is illustrated by (a) an image taken from the VAR ingot in the center of the bottom slab, (b) the two-point correlation function output of that image, and (c) the Hough transform of the two-point correlation function output. The two-point correlation function was calculated from a 512 by 512 pixel analysis region using a transportable analysis window of 256 pixels. The Hough transform used bin sizes of one pixel for ρ and one degree for θ.

6.3. RADON TRANSFORM

The Radon transform [82] was studied as an alternative to the Hough transform because it is not as significantly affected by image artifacts. The Radon transform, similar to the Hough transform, uses the parametric notion of a line to transform image data, albeit in a different manner than the Hough transform. For a two-dimensional image, the Radon transform calculates image projections along planes rotated about the center of the image using a set of line integrals; this is illustrated in Figure 6.3 (a). The line integrals are calculated using the following relationships,

$$R_\theta(x') = \int_{-\infty}^{\infty} f(x'\cos\theta - y'\sin\theta,\ \ x'\sin\theta + y'\cos\theta)dy' \qquad (8)$$

$$x' = x\cos\theta + y\sin\theta \qquad (9)$$

$$y' = -x\sin\theta + y\cos\theta. \qquad (10)$$

The relationship between the (x, y) coordinate frame and the (x', y') coordinate frame used in the Radon transform is presented in Figure 6.3 (b). After the Radon transform is completed for each pixel in the image analyzed, the transforms are then summed. Regions of high intensity in the Radon transform represent lines from the original image.

The Radon transform was implemented in Matlab™ [71] to analyze the two-point correlation function output previously analyzed using the Hough transform. The two-point correlation function output, the image it was acquired from, and the Radon transform of the two-point correlation function output are presented in Figure 6.4. Similar to the Hough transform image, the Radon transform image is dominated by two sinusoidal bands and two bright regions created at 45 and 135 degrees. Once again, these bright regions do not correspond with the angle of the dendrite arm directions visible in the two-point correlation function output. It is concluded that the Radon transform, similar to the Hough transform,

is dominated by background noise in the two-point correlation function output and not the streaks representative of dendrite orientations.

Primary dendrite arm orientation could not be ascertained from the two-point correlation function output using the Radon transform. No clear methodology exists for determining secondary dendrite arm spacing using the Radon transform. Because the results produced by the Radon transform were similar to those produced using the Hough transform, the ineffective procedures studied to improve the Hough transform were not attempted to improve the Radon transform results.

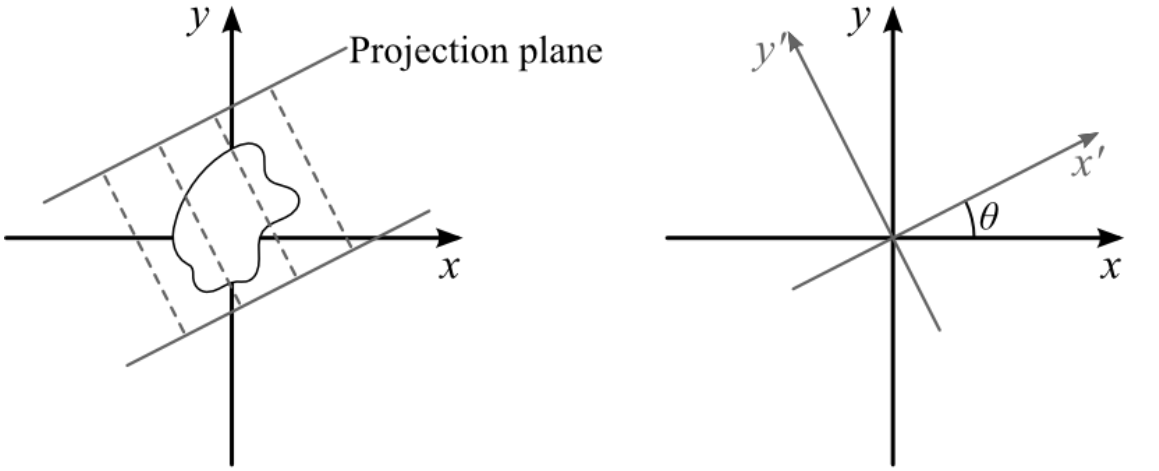

Figure 6.3: The Radon transform of a two-dimensional image is calculated using (a) the projections of that image along planes rotated about the center of the image, and (b) the (x', y') coordinate frame.

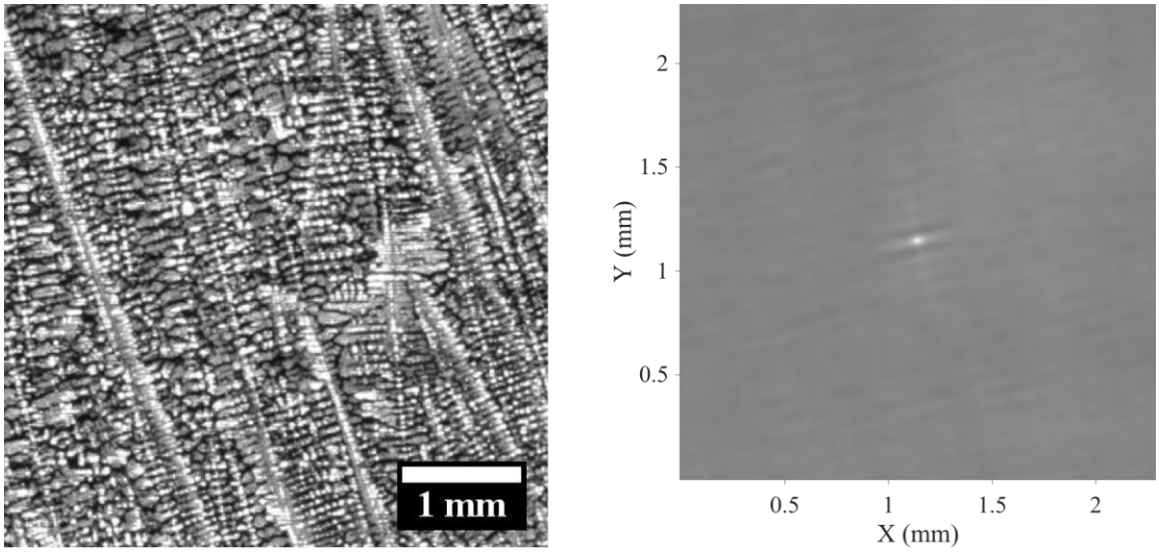

(a) Image data

(b) Two-point correlation function output

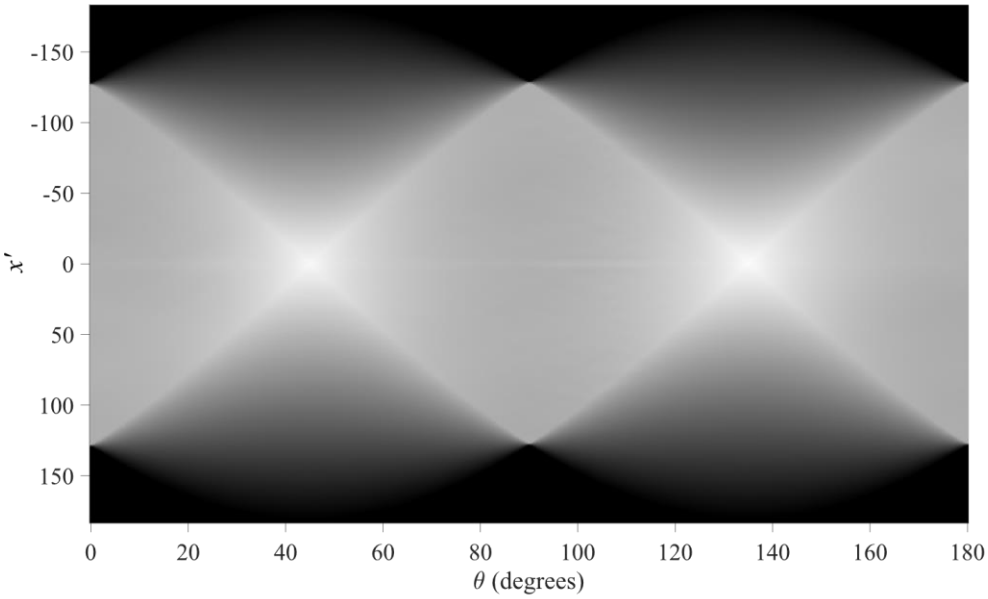

(c) Radon transform analysis

Figure 6.4: The Radon transformation is illustrated by (a) an image taken from the VAR ingot in the center of the bottom slab, (b) the two-point correlation function output of that image, and (c) the Radon transform of the two-point correlation function output. The two-point correlation function was calculated from a 512 by 512 pixel analysis region using a transportable analysis window of 256 pixels.

6.4. FOURIER ANALYSIS

This dissertation presents the successful implementation of Fourier analysis to measure primary dendrite arm orientation and secondary dendrite arm spacing from two-point correlation function outputs. Analysis was completed using a two-dimensional (*x, y*) Fast Fourier Transform (FFT) algorithm implemented in Matlab™ [71]. The development of the Fourier analysis used in this dissertation is now presented.

The two-dimensional FFT of an *N* by *N* image can be computed using the following relationships,

$$F(u,v) = \frac{1}{N} \sum_{x=0}^{N-1} \sum_{y=0}^{N-1} f(x,y)\, e^{\left[\frac{-2\pi j(ux+vy)}{N}\right]} \quad (11)$$

$$F(u,v) = R(u,v) + jI(u,v) = |F(u,v)|\, e^{[j\phi(u,v)]} \quad (12)$$

$$|F(u,v)| = \sqrt{R(u,v)^2 + I(u,v)^2} \quad (13)$$

$$\phi(u,v) = \tan^{-1}\left[I(u,v) \Big/ R(u,v)\right]. \quad (14)$$

Here, $f(x,y)$ is the image data, $F(u,v)$ is the Fourier transform, *j* is the imaginary unit, $R(u,v)$ is the real component of the Fourier transform, $I(u,v)$ is the imaginary component of the Fourier transform, $|F(u,v)|$ is the complex magnitude of the Fourier transform, and $\phi(u,v)$ is the phase of the Fourier transform. Note that the FFT algorithms are most effective at analyzing square images with dimensions equal to a power of two, i.e. images 2^n by 2^n large, where *n* is a positive integer.

The two-dimensional FFT can be visualized as an image using the square of $|F(u,v)|$; this is called the power spectrum. The power spectrum is then scaled using a logarithm to base 10 to stretch its range, which improves image contrast. This visualization technique is demonstrated using the images presented in Figure 6.5. The original image data, which consists of parallel lines oriented 114 degrees from the horizontal, is shown in

Figure 6.5 (a) along with the complex magnitude calculated from the two-dimensional FFT of this image on (b) linear and (c) logarithmic scales. Note that a Blackman function was used to window the image in Figure 6.5 (a) prior to Fourier analysis. Little information is visible in the power spectrum presented on a linear scale compared to the one presented on a base-10 logarithmic scale. During the FFT calculation, image data is rotated by 90 degrees. Thus, the power spectrum must be rotated by 90 degrees, as shown in Figure 6.5 (d), to align the FFT data with the orientation of the original image data. This power spectrum can now be analyzed.

Power spectra can be analyzed using individual vectors that originate at the center of the image. The direction of a vector represents the orientation of a feature in the original image. The magnitude of a vector represents the periodicity of that orientation in the original image; a large magnitude correlates to a high periodicity. Vectors that end on a position with a high pixel intensity represent a dominant feature in the original image. Thus, the directionality of features in the original image can be determined by locating positions of high intensity in the power spectrum. This is demonstrated in Figure 6.5, where the orientation of the lines in the original image (a) are determined from the highest intensity points in the rotated power spectrum (d).

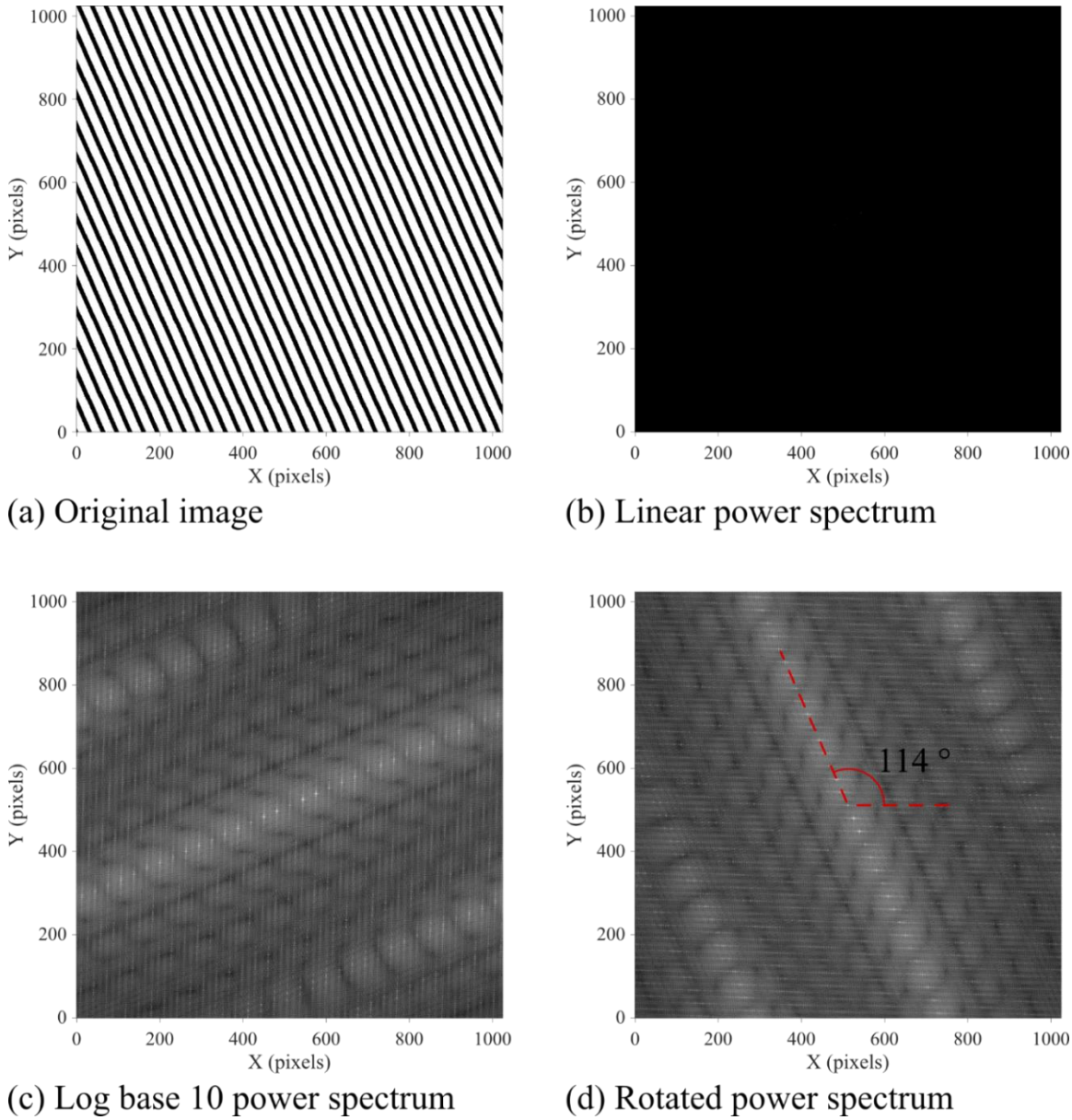

Figure 6.5: A two-dimensional FFT was applied to (a) a binary image consisting of parallel lines oriented 114 degrees from the horizontal. The power spectrum calculated from the FFT of this binary image is presented in (b) on a linear scale, (c) on a base-10 logarithmic scale, and (d) rotated 90 degrees on a base-10 logarithmic scale. Note that a Blackman function was used to window the binary image prior to Fourier analysis.

6.5. FOURIER ANALYSIS IMPLEMENTATION

Fourier analysis was used to measure primary dendrite arm orientation and secondary dendrite arm spacing from the VAR alloy 718 slabs. Power spectra calculated from the FFT of two-point correlation function outputs were analyzed using angular filters to determine primary dendrite arm orientations. Secondary dendrite arm spacings were measured directly from two-point correlation function outputs after primary dendrite arm orientations were determined. Secondary dendrite arm spacing was measured from the periodicity of streaks along the primary dendrite arm orientation in the two-point correlation function output. This FFT analysis procedure is now described.

A single image taken from the VAR ingot in the upper left corner of the bottom slab, presented in Figure 6.6, is used to demonstrate the Fourier analysis techniques of this dissertation. This is accomplished using a 512 by 512 pixel wide analysis region selected from the center of this image. Figure 6.7 presents this analysis region as (a) an 8-bit grayscale and (b) a binary image created after CLAHE processing of the grayscale image. Prior to Fourier analysis, two-point correlation function analysis was completed on this region using a 256 pixel transportable analysis window. The 512 pixel analysis region and 256 pixel transportable window were previously shown to provide the best analysis of this microstructure. A two-dimensional FFT implemented in Matlab™ analyzed the two-point correlation function output [71]. Figure 6.8 presents (a) the two-point correlation function output and (b) the power spectrum calculated from the FFT.

Note that two primary directions, most likely the primary and secondary dendrite arm orientations, are evident in Figure 6.8 (b), but these directions are obscured by a cross-shaped artifact. This artifact is created because the FFT assumes the image being analyzed repeats infinitely in space. Windowing functions can be used to smooth image edges and eliminate this artifact. During this study, a Hann function [83] was used to window the

two-point correlation function outputs. The windowed two-point correlation function output and the resulting power spectrum are presented in Figure 6.9. Note that no artifacts are present in the power spectrum calculated from the FFT of the windowed two-point correlation function output. The dominant directions noted in Figure 6.9 (b) correspond with the primary and secondary dendrite arm orientations visible in Figure 6.7 (a), the original image data. Even the orientation of scratches visible in the original image are detected using the FFT. This effectively demonstrates that the orientation of features, especially primary and secondary dendritic arms, can be measured from FFT data.

Primary and secondary dendrite arm orientations were measured from the FFT data. This was accomplished using a set of angular filters to measure the complex magnitudes of the FFT data along discrete orientations. The angular filter is equal in size to the FFT data and constructed from a zero valued background and a non-zero valued Gaussian distribution positioned near its center. The Gaussian distribution is symmetric along the x-axis and the y-axis. The filter values within the Gaussian distribution have a peak value of 1 and decline toward zero as described by the following,

$$G(x,y) = \left({}^{1}/_{2\pi\sigma_x\sigma_y}\right) e^{(-f(x,y))} \quad (15)$$

$$f(x,y) = \frac{(x-\mu_x)^2}{2{\sigma_x}^2} + \frac{(y-\mu_y)^2}{2{\sigma_y}^2}. \quad (16)$$

Here *G(x, y)* is the Gaussian distribution, σ_x is the standard deviation along the x-axis, σ_y is the standard deviation along the y-axis, μ_x is the mean along the x-axis, and μ_y is the mean along the y-axis. For this study, μ_x and μ_y were set to 0, σ_x was set to 2.5, and σ_y was set to 0.25. One angular filter, oriented at 0 degrees, is presented in Figure 6.10 (a); the Gaussian distribution is shown in white. The angular filter was designed to concentrate analysis

toward the center of the FFT data where feature orientations are most strongly represented. Angular filters were created with orientations of 0 to 179 degrees at 1 degree increments by rotating the horizontally oriented angular filter shown in Figure 6.10 (a).

Directional intensities were calculated by multiplying each angular filter with the complex magnitudes calculated from the FFT data, as demonstrated by Figure 6.10 (b). The resulting multiplication product is presented in Figure 6.10 (c). The total intensity of that direction is calculated by summing the intensity of all points in the multiplication product. This summed intensity describes the strength of a given direction in the two-point correlation function data. Implementation of the angular filter is summarized in the following:

1) Construct the angular filter.
2) Multiply the angular filter with the magnitudes calculated from the FFT; this is demonstrated in Figure 6.10 (b).
3) Sum the intensity values of the multiplication product; demonstrated in Figure 6.10 (c).
4) Rotate the angular filter counter-clockwise by 1 degree.
5) Repeat steps 1 thru 4 until the angular filter has been rotated 179 degrees.

After the angular filters were applied, a summed intensity value was calculated for each orientation of the filter. These summed intensity values describe the strength of each direction in the two-point correlation function data. This directionality data set can be viewed by plotting the summed intensity values against each direction, as shown in Figure 6.11. Peaks in the directionality data describe the prominent orientations of the microstructural features within the image analyzed and were located.

First the minimum summed intensity value from the directionality data was removed to eliminate background noise. Second, local maximums were identified in the directionality data using Matlab^{TM} [71], and these were labeled as peaks. For the algorithm implemented, peaks required a prominence with a minimum summed intensity of 10 to be measured, and no two peaks could be located within 10 degrees of each other. For this study, only large peaks were considered likely to describe the primary or secondary dendrite arm orientations. Therefore, a low-pass filter was used to discard any directionality data set that did not contain a local maximum with a summed intensity of at least 400. This limit was determined through experimentation. For directionality data sets that contained two large peaks separated by approximately 90 degrees, these likely represented the primary and secondary dendrite arm orientations. If only one large peak was identified, that peak likely represented either the primary or secondary dendrite arm orientation.

After the dominant peaks were identified, the peak most likely to represent the primary dendrite arm orientation was determined. If the peak associated with the primary dendrite arm orientation was identified, then that orientation was calculated. This was accomplished using the location within the ingot from which this data was acquired. Primary dendrite arms on the left side of the ingot are most likely oriented between 15 and 90 degrees. Those on the right side of the ingot are most likely oriented between 90 and 165 degrees. If a second peak was identified, it was then taken as the secondary dendrite arm orientation. If only one peak was identified, and if it represented the secondary dendrite arm orientation, the primary dendrite arm orientation was calculated as 90 degrees away.

Directionality calculated from two-point correlation function and Fourier analysis of the microstructure shown in Figure 6.7 is presented in Figure 6.11. Note that two large peaks are identified at 43 and 132 degrees. This is the ideal scenario because each peak

represents either the primary or the secondary dendrite arm orientation. Using the knowledge that this data was acquired from the left side of the VAR ingot, the primary and secondary dendrite arm orientations are determined to be 43 and 132 degrees, respectively.

After peak finding, Gaussian distributions were fit to the primary and secondary dendrite arm peaks if they exist. These fits provided a consistent method to measure peak location and uncertainty. This method was used because multiple small peaks often existed on top of the large identified peaks from small differences in dendrite arm orientations visible in the microstructural data. Since only one measure of dendrite orientation was reported, this fit provided a useful averaging for these small peaks. The peak location was then reported as the mean of the Gaussian distribution, and the standard deviation provided a measure of uncertainty. The Gaussian distributions to the peaks from Figure 6.11 are presented in Figure 6.12.

Fourier analysis was also applied directly to binary microstructural images. However, peak directions were not as pronounced or tight as those obtained from Fourier analysis of the two-point correlation function output. Filtering techniques could potentially improve results from Fourier analysis of microstructure, but none were investigated in this dissertation. Additionally, no clear methodology exists for measuring secondary dendrite arm spacing from Fourier analysis of microstructure. For these reasons, Fourier analysis directly of microstructural images was not pursued further.

The primary dendrite arm orientation identified using two-point correlation function and Fourier analysis was used to prepare the two-point correlation function output for secondary dendrite arm spacing analysis. The two-point correlation function output was rotated using a bilinear rotation algorithm until the primary dendrite arm orientation was horizontal. It was then cropped to a 128 pixel square. This was performed on the two-point correlation function output presented in Figure 6.8 (a), and the results are provided in

Figure 6.13. Secondary dendrite arm spacing was then measured from this image using two techniques. The first technique measured secondary dendrite arm spacing directly from the two-point correlation function output. The second technique measured secondary dendrite arm spacing using a one-dimensional FFT. The first technique is now described.

For the first technique, pixel intensity values were summed along the secondary dendrite arm orientation, i.e. along columns, in the rotated two-point correlation function output. The column sums produced a one-dimensional data vector of summed pixel intensity as a function of position. Peaks were then identified in this vector, and the distance between them was measured; a minimum of 4 peaks was stipulated to define a valid measurement. The summed secondary dendrite arm data from Figure 6.13 and the peaks identified are presented in Figure 6.14. The mean and standard deviation of the spacing between peaks were calculated. The mean is reported as the secondary dendrite arm spacing, and the standard deviation is reported as its uncertainty.

The second technique measured secondary dendrite arm spacing using a one-dimensional FFT. This technique measured wavenumber from the periodicity of the two-point correlation function output along the primary dendrite arm orientation. Like the first technique, pixel intensity values were summed along the secondary dendrite arm orientation. To impose the symmetry necessary for FFT analysis, the summed data set was then split in half at its center point, creating left-half and right-half data sets. Next, the right-half data set was flipped about the center point and added to the left-half data set. A result from this procedure is provided in Figure 6.15. This process was necessary to remove the large peak at the center of the summed data shown in Figure 6.14 because it created artifacts in the one-dimensional FFT. Next the large peak at the end of the halved data set, shown in Figure 6.15, was removed. This result was then returned to a power of 2 in length by mirroring data as shown in Figure 6.16. Finally, a one-dimensional FFT was

implemented in Matlab™ [71] to analyze this data, and the results are provided in Figure 6.17.

For the VAR ingot, secondary dendrite arm spacing was measured by identifying peaks in the FFT data located near a wavenumber of 10 cycles per mm. This wavenumber corresponds to a secondary dendrite arm spacing of 100 μm, the average secondary dendrite arm spacing calculated for the VAR ingot from manual measurements. This measurement technique is primarily limited by resolution. Because the data set used to calculate the secondary dendrite arm spacing is not very long, the resolution of the wavenumber is poor. The limited resolution only provides measurements in increments of approximately 2 cycles per mm, which corresponds to approximately 25 μm. This poor resolution also forces the wavenumber of interest, 10 cycles per mm for this material, toward the left end of the FFT data set, as shown in Figure 6.17. This locates the peaks of interest close to other peaks created from the gradual slope of the data that do not describe the secondary dendrite arm spacing. A larger data set would greatly improve the resolution and utility of this technique.

The subsequent chapter presents and discusses two-point correlation function and Fourier analysis of four different microstructures from the VAR ingot. These case studies are used to demonstrate the ability of the techniques developed to analyze different microstructures.

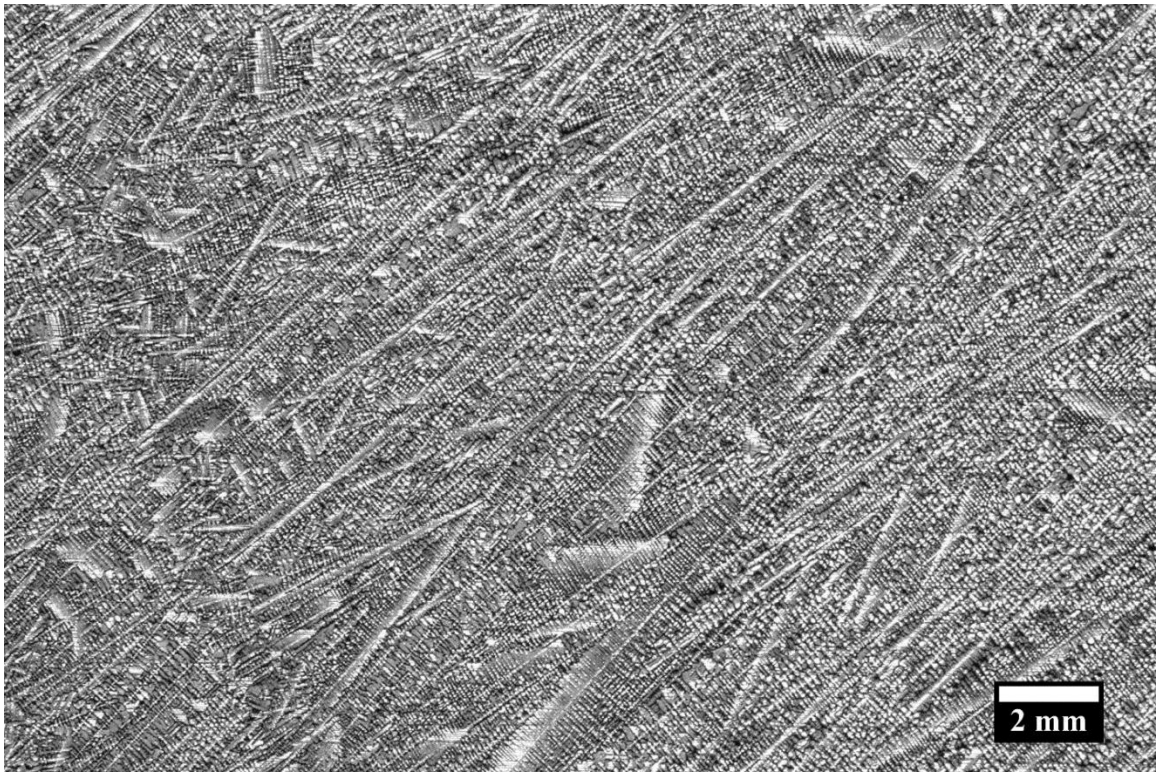

Figure 6.6: This image is used to demonstrate the Fourier analysis techniques. It was selected from the VAR ingot in the upper left corner of the bottom slab.

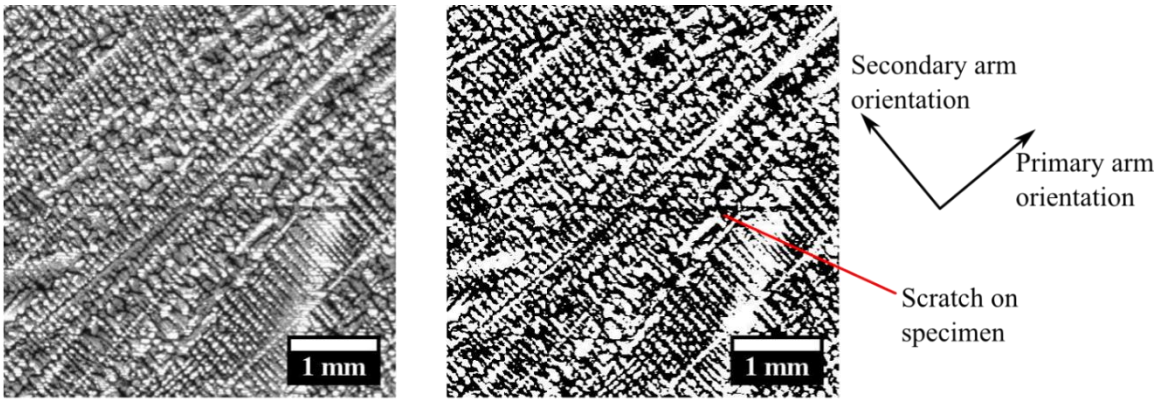

(a) Grayscale image of the analysis region

(b) Binary image of the analysis region

Figure 6.7: The analysis region selected from the center of Figure 6.6 is presented as (a) grayscale and (b) binary images. The primary and secondary dendrite arm orientations are noted.

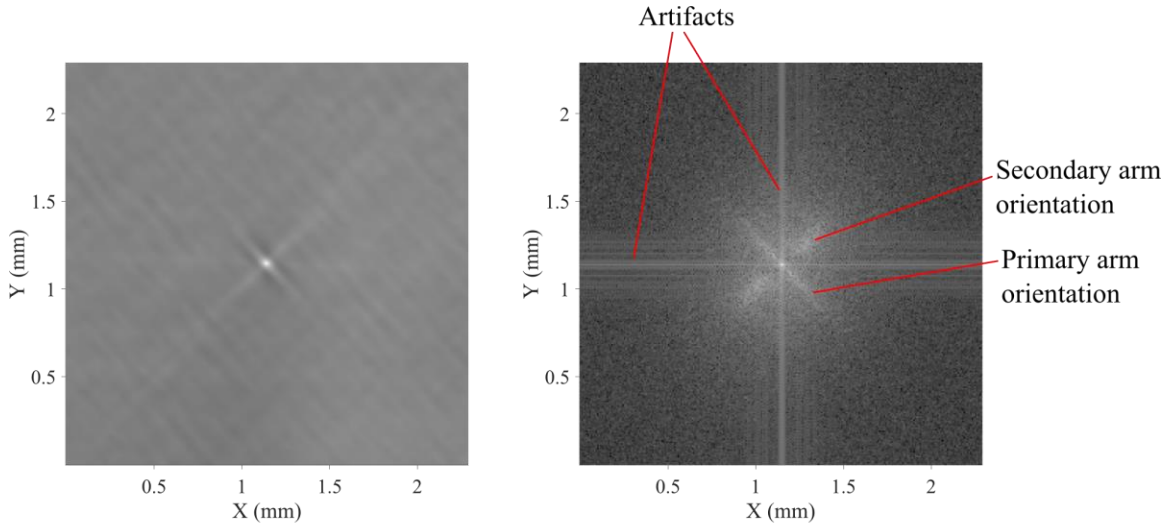

(a) Two-point correlation function output (b) Power spectrum

Figure 6.8: (a) The two-point correlation function output from analysis of Figure 6.7 (b) is presented. (b) The power spectrum calculated from the two-dimensional FFT of the two-point correlation function output is presented on a logarithmic scale for intensity. Dendritic arm orientations and image artifacts are noted.

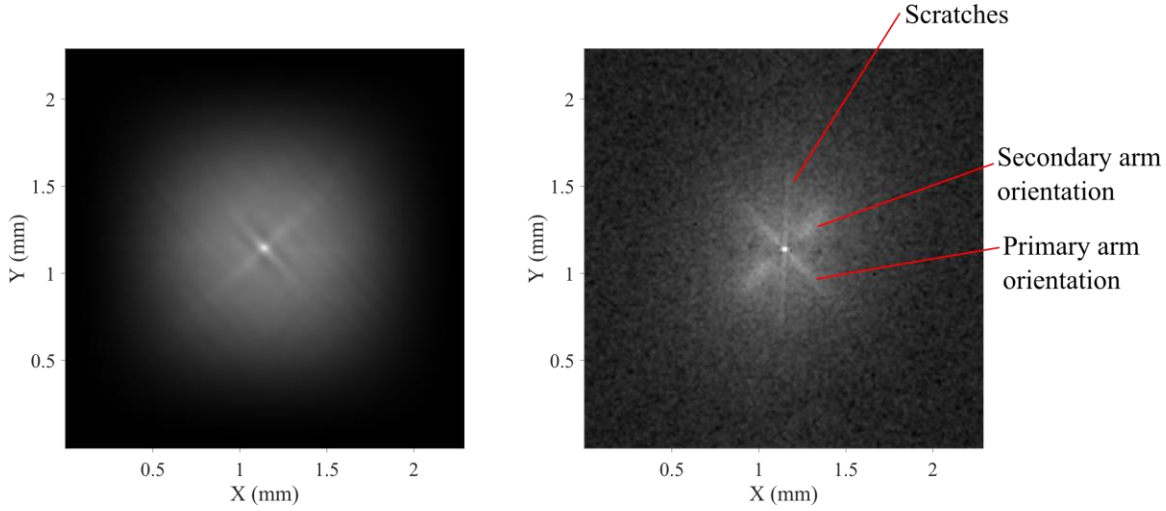

(a) Windowed two-point correlation function output (b) Power spectrum

Figure 6.9: (a) The windowed two-point correlation function output from analysis of Figure 6.7 (b) is presented. (b) The power spectrum calculated from the two-dimensional FFT of the windowed two-point correlation function output is presented on a logarithmic scale for intensity. Dendritic arm orientations and scratch orientations are noted.

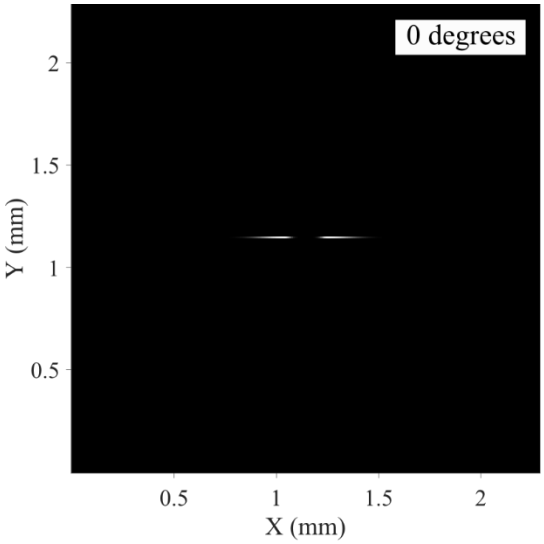

(a) Angular filter oriented at 0 degrees

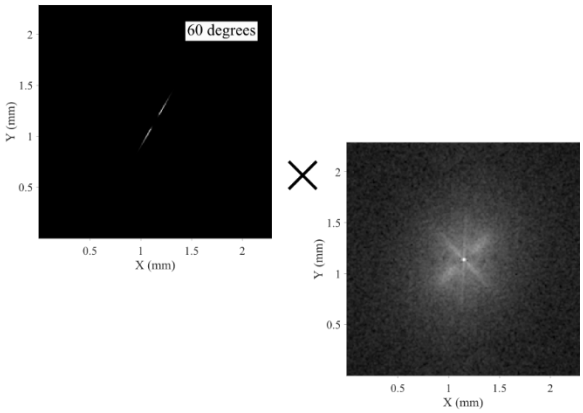

(b) Angular filter at 60 degrees multiplied with the power spectrum

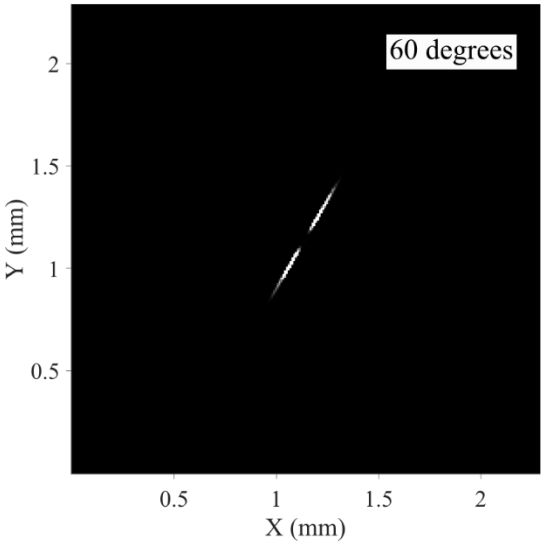

Intensity at 60 degrees:
∑ pixel intensity values = 255.1

(c) Multiplication product

Figure 6.10: This figure illustrates (a) the shape of the angular filter, (b) implementation of the angular filter, and (c) the product produced by application of the angular filter at 60° to the FFT data.

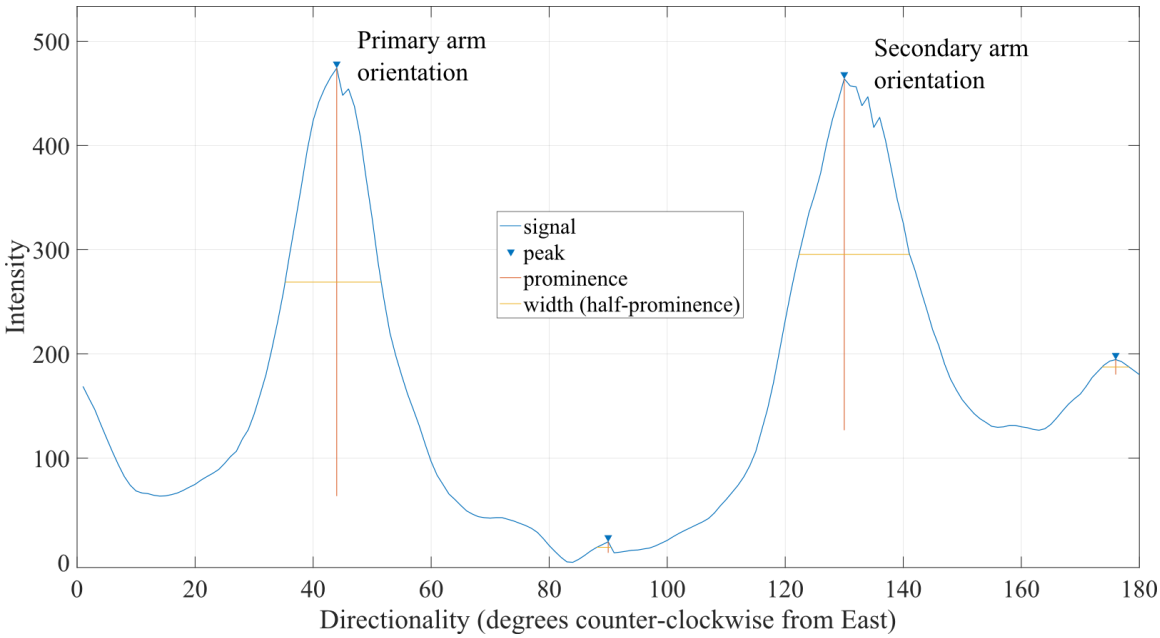

Figure 6.11: Directionality determined from Fourier analysis of the analysis region shown in Figure 6.7 is presented. The primary and secondary dendrite arm orientations are noted.

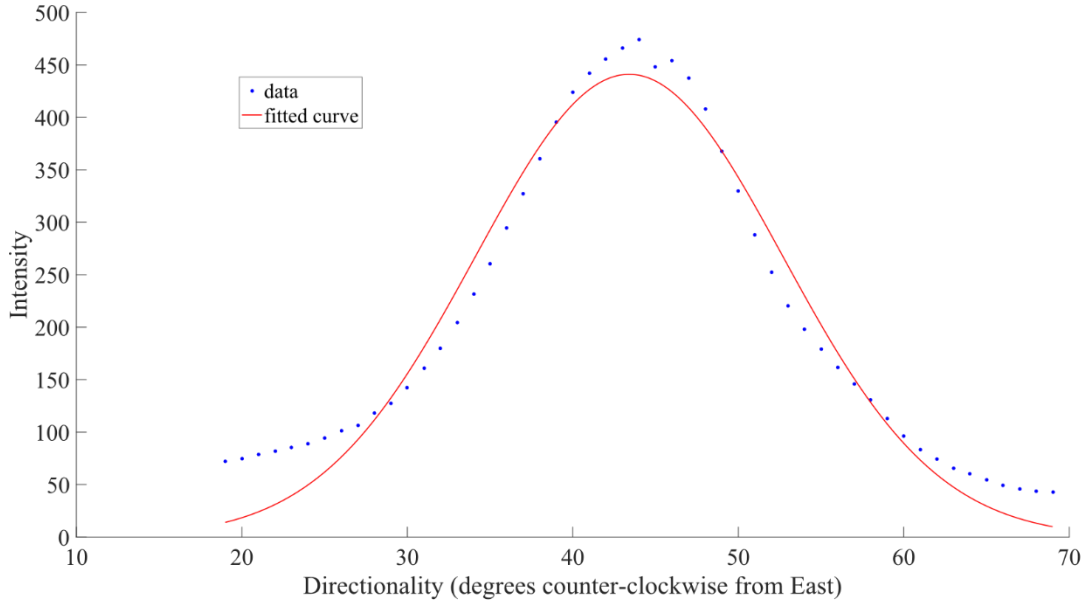

(a) Primary dendrite arm peak

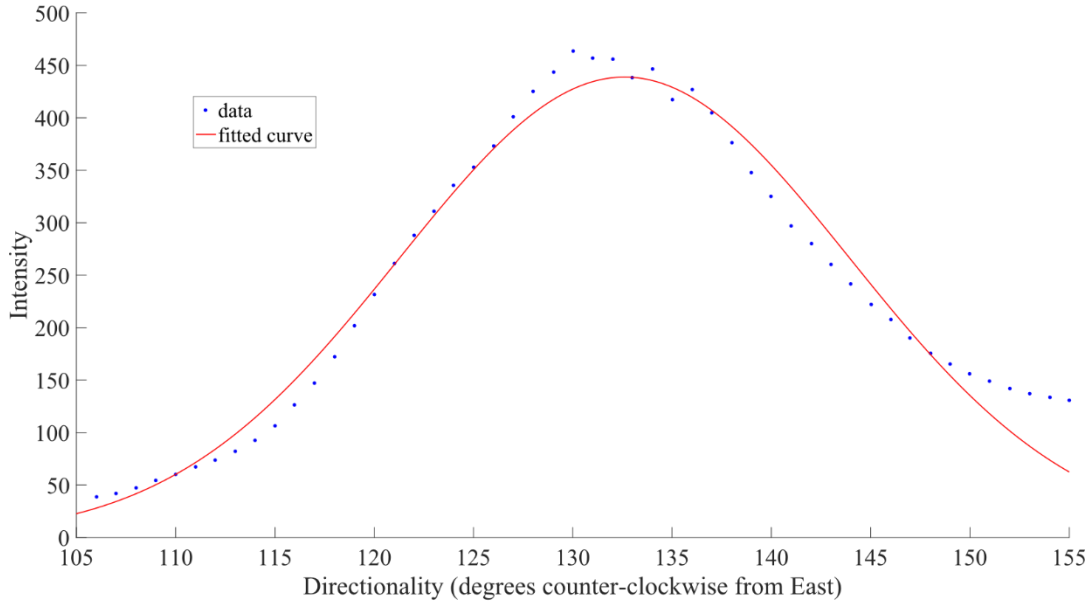

(b) Secondary dendrite arm peak

Figure 6.12: The Gaussian fits to the peaks that represent the (a) primary dendrite arm orientation and (b) secondary dendrite arm orientation are presented.

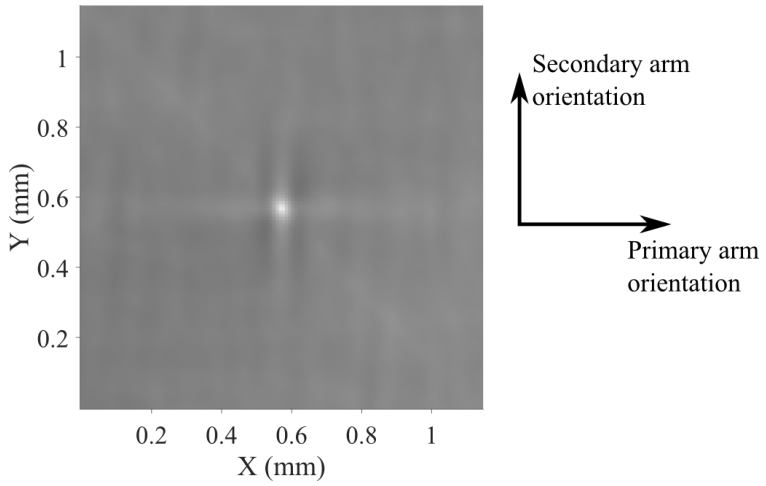

Figure 6.13: The rotated and cropped two-point correlation function output is presented.

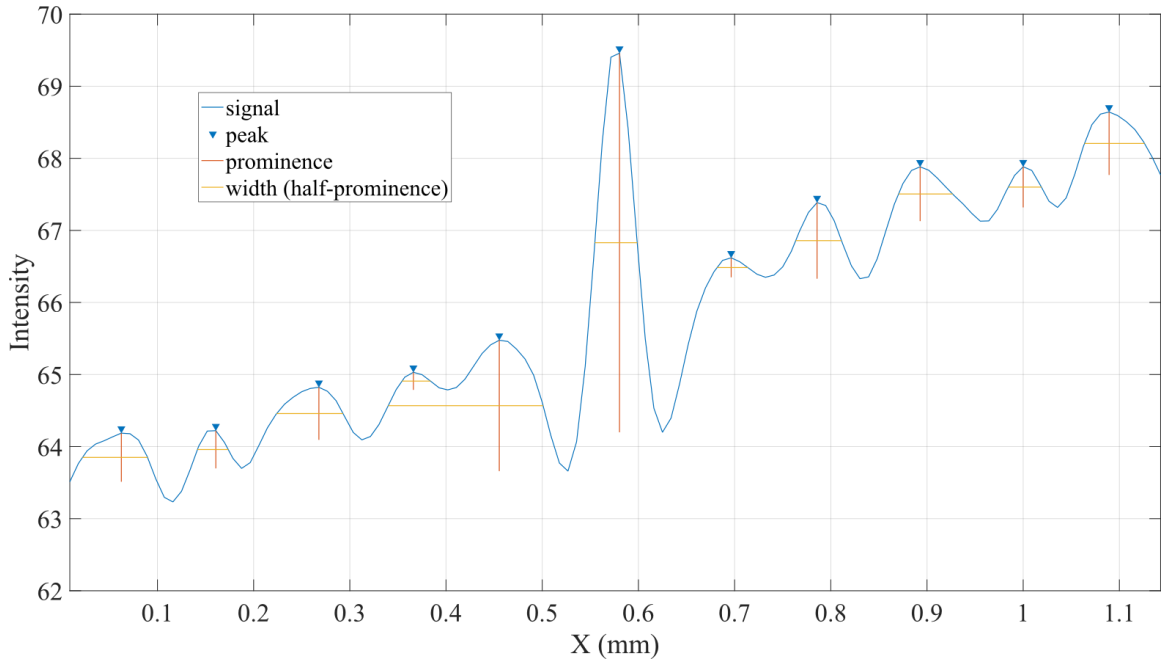

Figure 6.14: Intensity values calculated from Figure 6.13 by summing pixel intensities along the secondary dendrite arm orientation are provided. The peaks identified and their prominences and widths are noted.

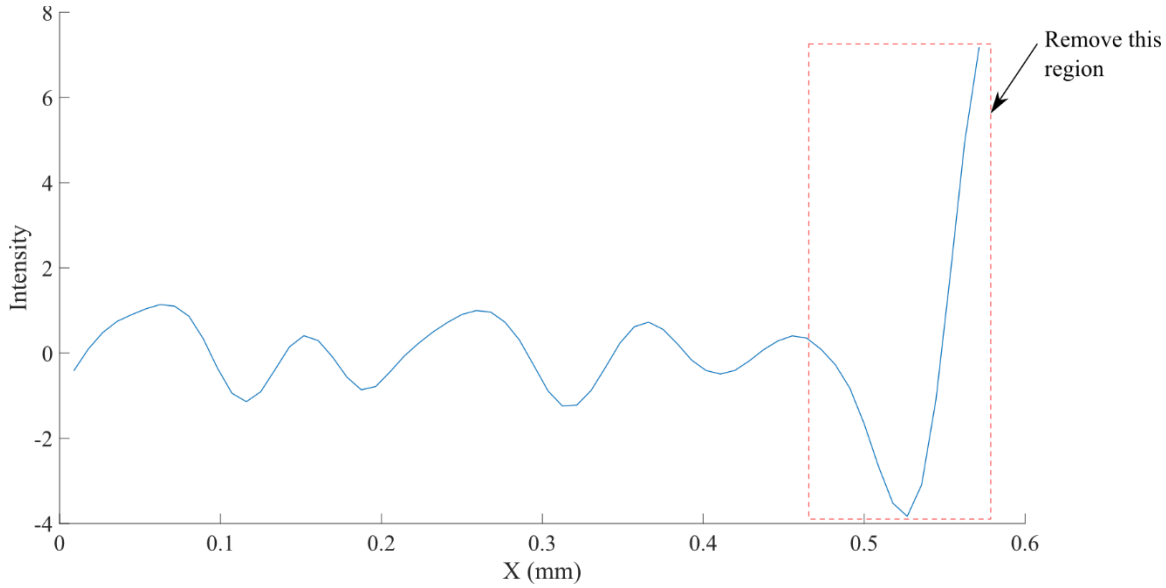

Figure 6.15: The sum of the pixel intensity halves presented in Figure 6.14 are provided. This was calculated by: (1) splitting the summed data in half at its center point, (2) then data in the right half was flipped about the center point and added to the left half. The large peak highlighted at the end of the data set was removed later in the analysis.

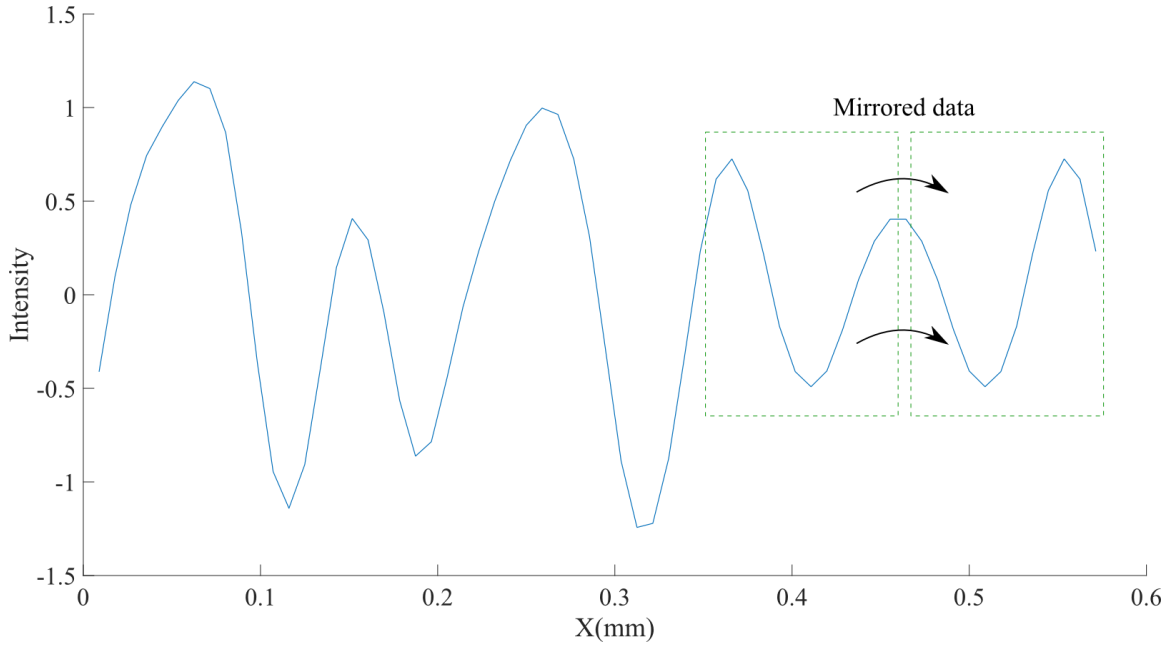

Figure 6.16: The data used to calculate secondary dendrite arm spacing using a one-dimension FFT is provided. This data was created after the large peak at the end of the halved data was removed. This data set was then returned to a power of 2 in length by mirroring data as shown.

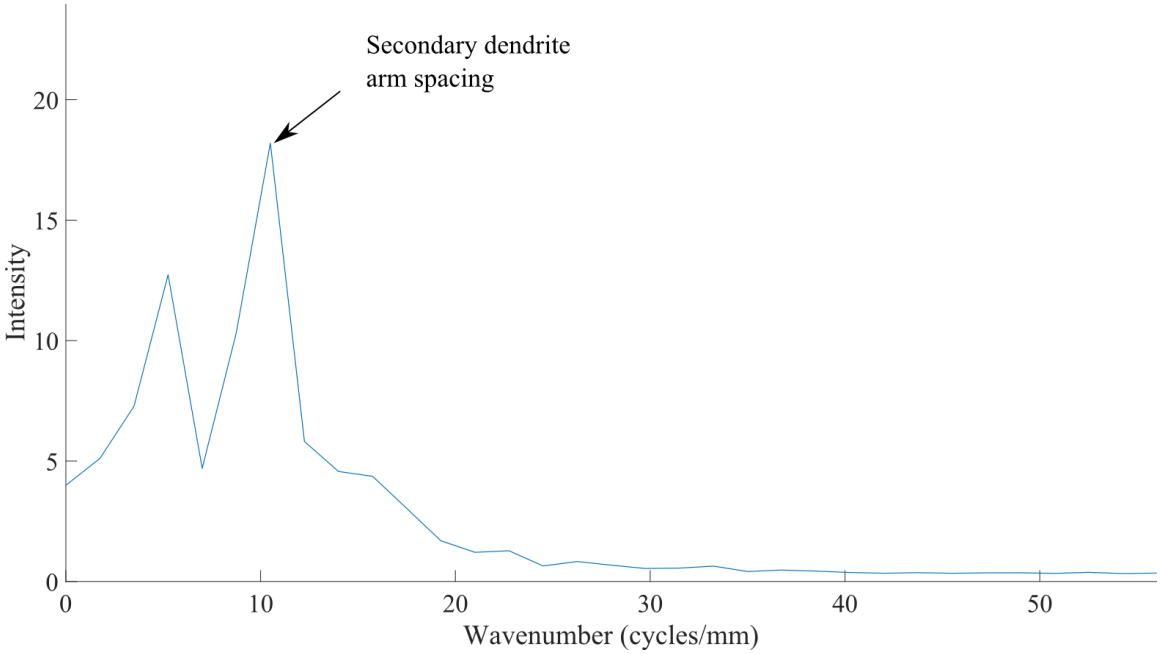

Figure 6.17: Results from the one-dimensional FFT of the secondary dendrite arm spacing data are provided. Intensity is plotted as a function of wavenumber. The peak likely to represent the secondary dendrite arm spacing of this region is noted. Note that this peak appears toward the left end of the data set.

7. FOURIER ANALYSIS CASE STUDIES

7.1. OVERVIEW

Two-point correlation function and Fourier analyses were performed on four different images acquired from the VAR ingot to demonstrate how these analysis techniques apply to different types of microstructures. Each image selected has a resolution of approximately 9.0 μm per pixel. Microstructural differences between these images include: (1) primary dendrite arm orientation, (2) secondary dendrite arm spacing, (3) secondary dendrite arm visibility, (3) the presence of scratches, (4) artifacts from metallographic preparation of the alloy 718 ingot slabs that appear as blob-like features, referred to herein as "blob-like artifacts," and (5) equiaxed or directional solidification characteristics.

Two-point correlation function analysis was performed on regions selected from the center of each image analyzed. The analysis regions measured 512 pixels (4.6 mm) square. The two-point correlation function analysis used a 256 pixel (2.3 mm) transportable analysis window. These parameters were previously determined to provide the best two-point correlation analysis of the VAR ingot. Fourier analysis was then performed on the two-point correlation function data produced from each image.

7.2. CASE ONE

The first microstructure, shown in Figure 7.1, was selected from the VAR ingot in the left side of the bottom slab. This microstructure demonstrates: (1) directional solidification, (2) well-defined primary dendrite arm orientations, (3) poor secondary dendrite arm distinction, and (4) blob-like artifacts. The analysis region selected from this image is presented in Figure 7.2. Two primary dendrite arm orientations are evident and

noted. Some secondary dendrite arms are visible in this region, but secondary dendrite arm spacing is expected to be difficult to measure. Blob-like artifacts are visible in the analysis region and noted in Figure 7.2. The two-point correlation function output from this region is provided in Figure 7.3 (a). Only a single streak direction is well-defined in the two-point correlation function output; it is suspected that this corresponds to the average primary dendrite arm orientation. This is expected because primary arms are clearly visible within the analysis region, and secondary dendrite arms are not. The windowed two-point correlation function data is provided in Figure 7.3 (b).

The power spectrum from the FFT of the windowed two-point correlation function data is presented in Figure 7.4. Like the two-point correlation function output, only one streak orientation, most likely the average primary dendrite arm orientation, is strongly represented in the FFT data. Directionality was then analyzed using angular filters, and the results are provided in Figure 7.5. A single large peak is identified at approximately 50 degrees. Because this data was acquired from the left side of the ingot, it is readily determined that this peak represents the primary dendrite arm orientation. Primary dendrite arms on the left side of the ingot are typically oriented between 15 and 90 degrees. A small peak was also identified at 145 degrees, approximately 90 degrees away from the primary peak. This small peak might be from secondary dendrite arms. However, this peak was too small to analyze. A Gaussian distribution was fit to the primary peak and is presented in Figure 7.6. The primary dendrite arm orientation was calculated to be 47.6 degrees with a 95 percent confidence interval of ± 1.5 degrees. The standard deviation was calculated as 18.5 degrees. This measure of primary dendrite arm orientation is consistent with the orientations visually identified in Figure 7.2. The asymmetry of the peak shown in Figure 7.5 and Figure 7.6 is qualitatively consistent with the range of primary dendrite arm orientations observed in Figure 7.2. The small peak at approximately 30 degrees may be

from the artifacts identified in Figure 7.2, and did not interfere significantly with this analysis.

The rotated two-point correlation function data used for secondary dendrite arm analysis is presented in Figure 7.7. Pixel intensity was summed along the secondary dendrite arm orientation and is presented in Figure 7.8. Because fewer than four peaks were identified in this data set, secondary dendrite arm spacing was deemed unmeasurable.

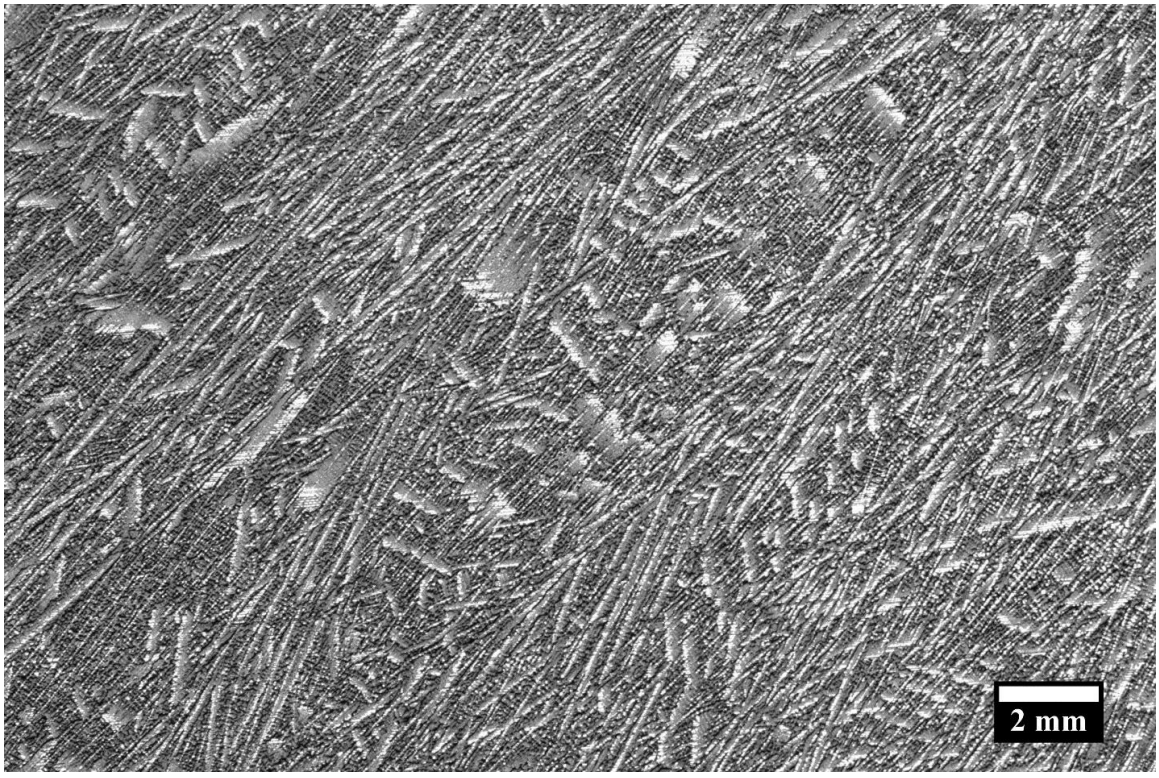

Figure 7.1: Microstructure from the VAR ingot in the left side of the bottom slab is presented as a grayscale image.

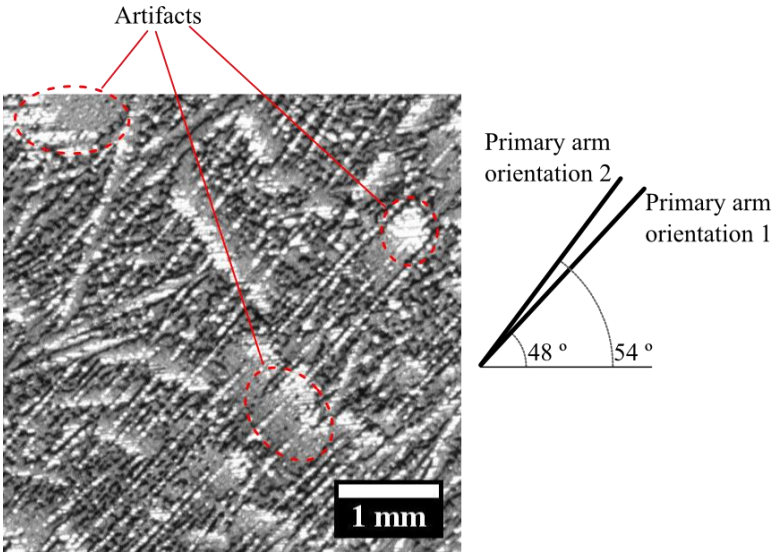

Figure 7.2: The analysis region is presented. The two primary dendrite arm orientations are noted.

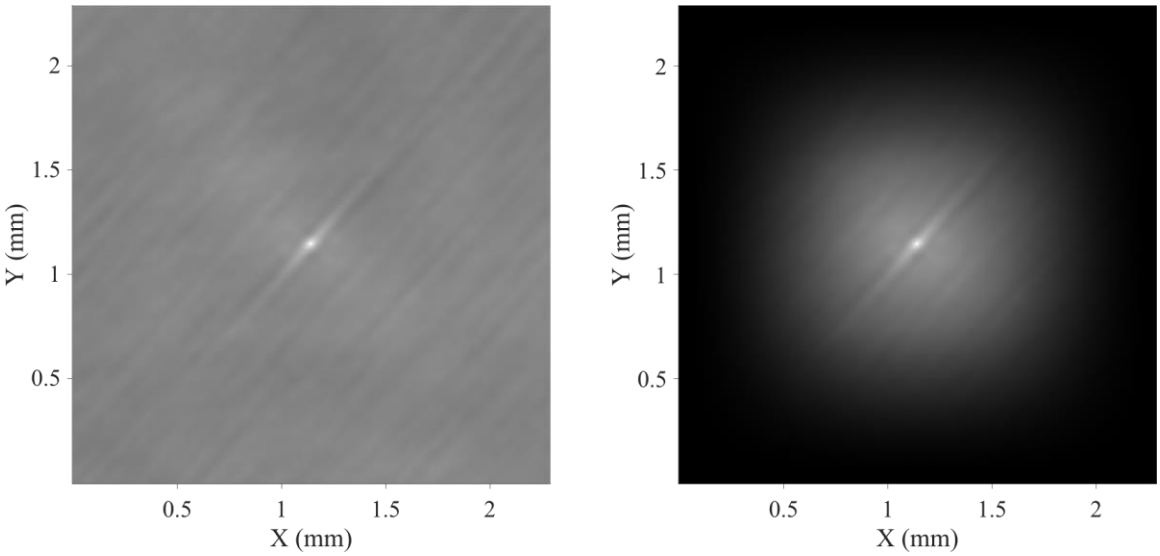

(a) Two-point correlation function output

(b) Windowed two-point correlation function output

Figure 7.3: The two-point correlation function output from the analysis region is presented (a) before and (b) after windowing. A Hann windowing function was used.

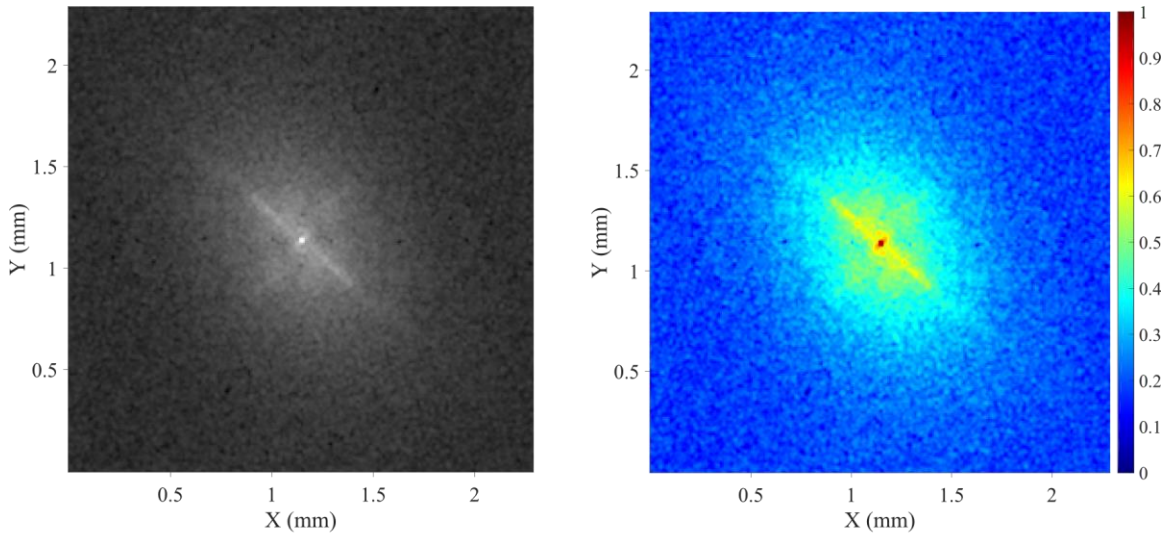

(a) Grayscale power spectrum (b) Color power spectrum

Figure 7.4: The power spectrum calculated from the FFT is presented on a base-10 logarithmic scale as (a) grayscale and (b) color images. Note that the FFT data is rotated 90 degrees with respect to the two-point correlation function output and original image data.

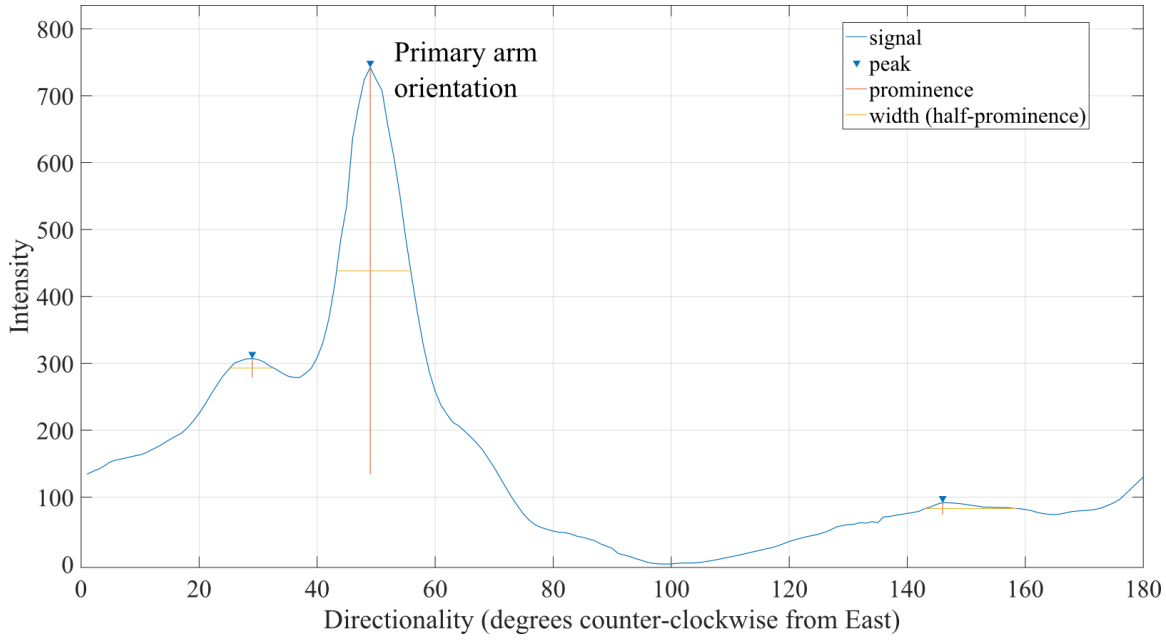

Figure 7.5: Directionality calculated from Fourier analysis is presented. The primary dendrite arm orientation is noted.

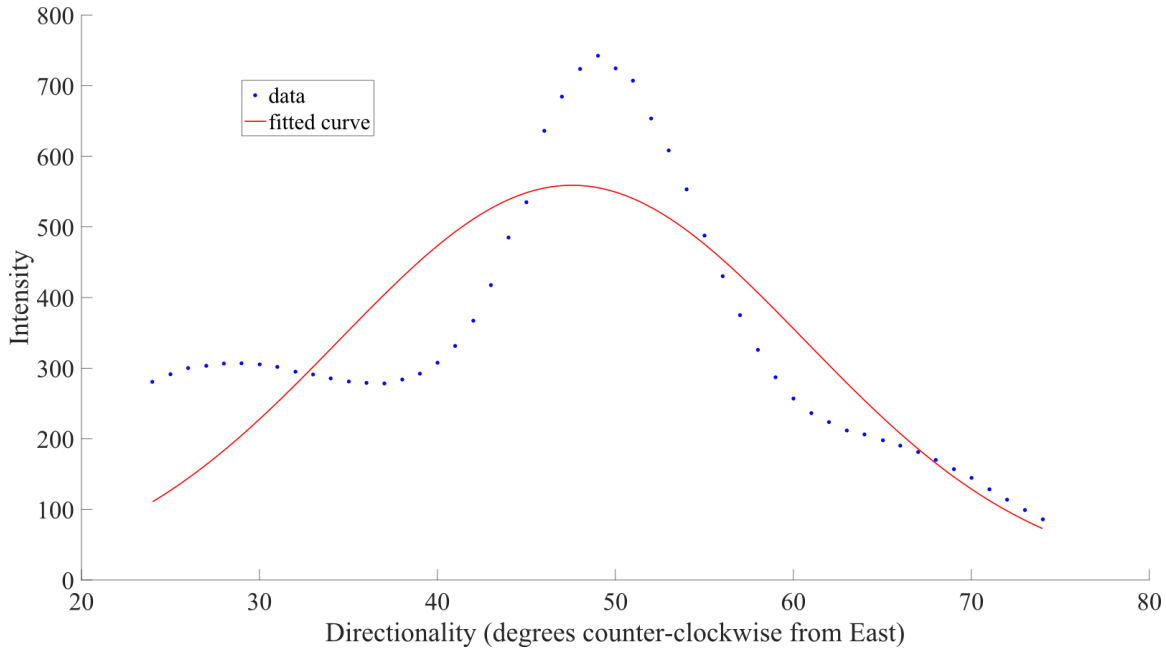

Figure 7.6: The Gaussian distribution fit to the primary dendrite arm peak is presented.

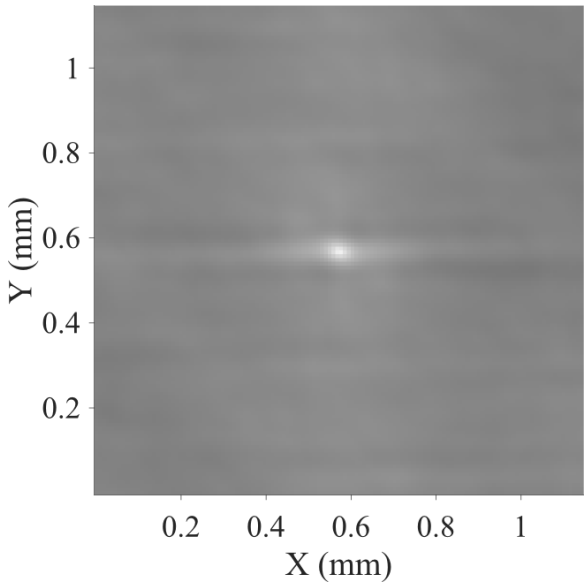

Figure 7.7: The rotated two-point correlation function data used for secondary dendrite arm analysis is presented. Rotation used the primary dendrite arm orientation identified from Fourier analysis.

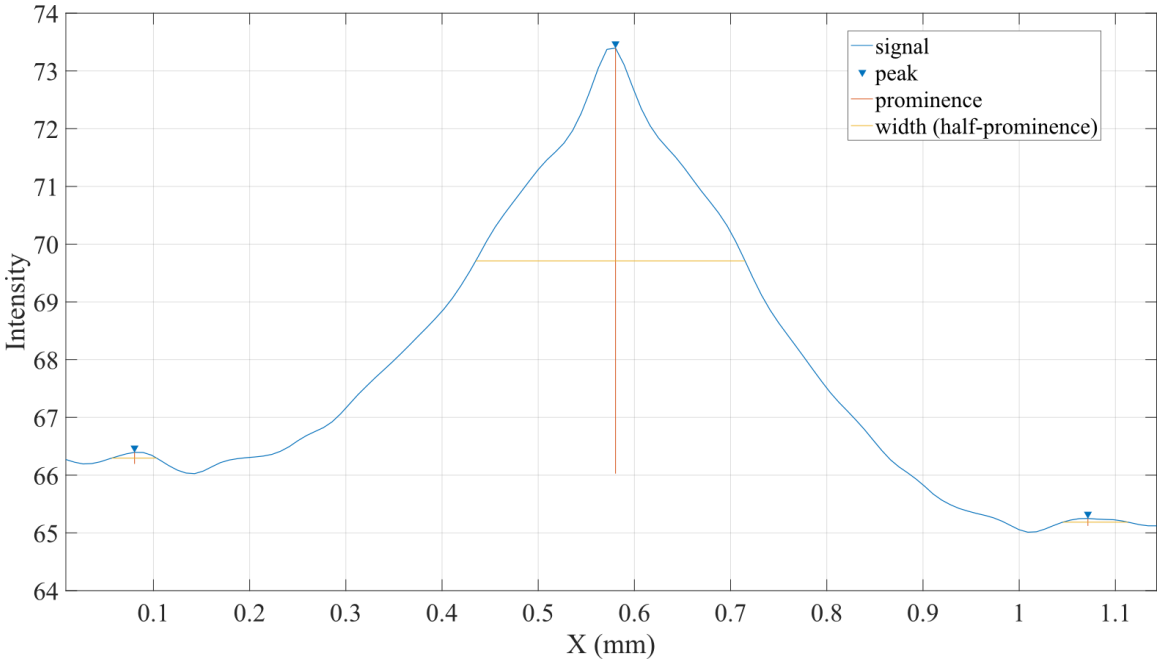

Figure 7.8: The image intensity summed along the secondary dendrite arm orientation is presented.

7.3. Case Two

The microstructure from the VAR ingot in the bottom left of the bottom slab is presented in Figure 7.9. This microstructure demonstrates: (1) directional solidification, (2) multiple primary dendrite arm orientations, (3) poor secondary dendrite arm distinction, and (4) small horizontal scratches. The analysis region selected from this image is presented in Figure 7.10, and the two visible primary dendrite arm orientations are noted. Secondary dendrite arms are visible intermittently throughout this region. Detection of the average primary dendrite arm orientation is expected, and measurement of secondary dendrite arm spacing may be possible.

The two-point correlation function output from this region is provided in Figure 7.11. A single streak direction is well-defined in the two-point correlation function

output, but this streak is more diffuse than the one identified in Case One. It is suspected that the 10 degree difference in primary dendrite arm orientations for this analysis region causes the diffuse nature of the streak.

The power spectrum from the FFT of the windowed two-point correlation function data is presented in Figure 7.12. Like the two-point correlation function output, only one streak orientation is identified, and it is slightly diffuse. Directionality was analyzed using angular filters, and the results are presented in Figure 7.13. One dominant peak is identified at 71 degrees. It was determined to represent the average primary dendrite arm orientation because this data was acquired from the left side of the ingot. The location of this peak is similar to the primary dendrite arm orientation of 73 degrees noted in Figure 7.10. A small peak was also identified at 60 degrees, which approximately corresponds with the other primary dendrite arm orientation noted in Figure 7.10. No peaks were identified that could reasonably represent the secondary dendrite arm orientation. The Gaussian distribution fit to the primary peak is presented in Figure 7.14. The primary dendrite arm orientation was calculated to be 72.7 degrees with a 95 percent confidence interval of ± 0.5 degrees. The standard deviation was calculated as 13.6 degrees. This result from the Gaussian fit indicated that the preponderance of primary dendrite arms are near the 73 degree orientation labeled in Figure 7.10 as “Primary arm orientation 2.”

The rotated two-point correlation function data used for secondary dendrite arm analysis is presented in Figure 7.15. Pixel intensity was summed along the secondary dendrite arm orientation and is presented in Figure 7.16. Enough peaks were identified to proceed with secondary dendrite arm analysis. Measuring the distance between peaks produced an average spacing of 102 μm and a standard deviation of 35 μm. Secondary dendrite arm spacing was also calculated from the data presented in Figure 7.17 using FFT analysis. This data was halved, summed, and mirrored as previously described. The results

are provided in Figure 7.18. Note that a peak is identified near a wavenumber of 10 cycles per mm, but it is obscured by other peaks at lower wavenumbers. Secondary dendrite arm spacing was calculated as 109 μm, but the resolution of this data only provides a measurement in increments of approximately 25 μm.

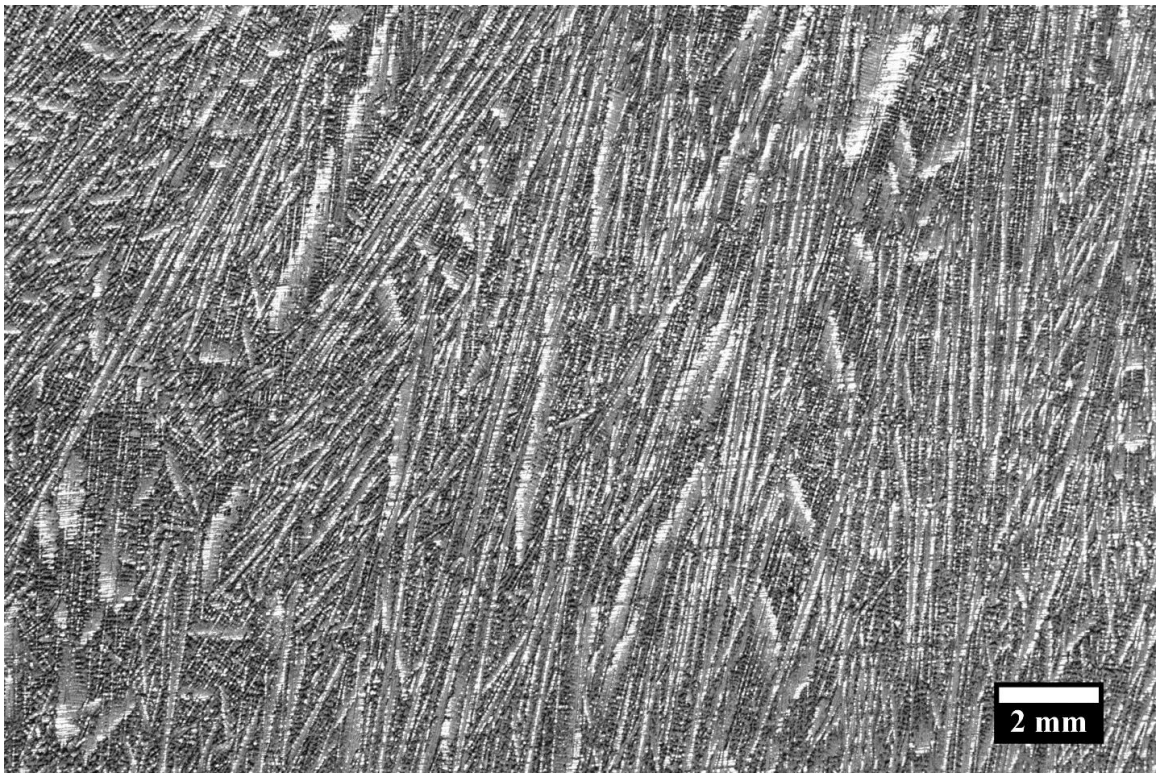

Figure 7.9: Microstructure from the VAR ingot in the bottom left of the bottom slab is presented as a grayscale image.

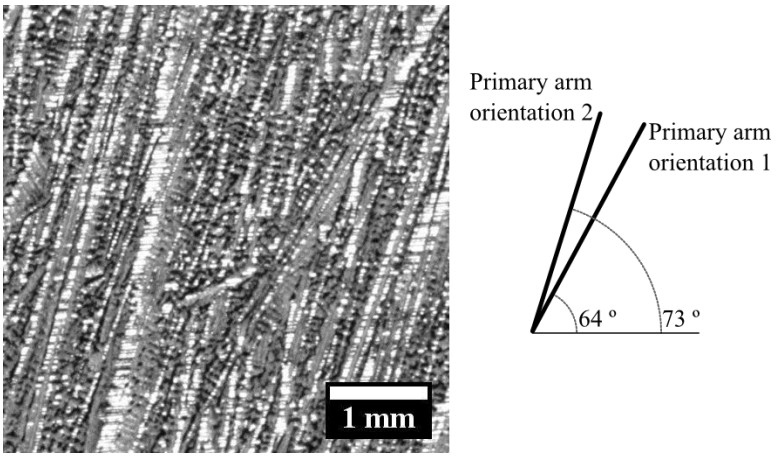

Figure 7.10: The analysis region is presented. The two primary dendrite arm orientations are noted.

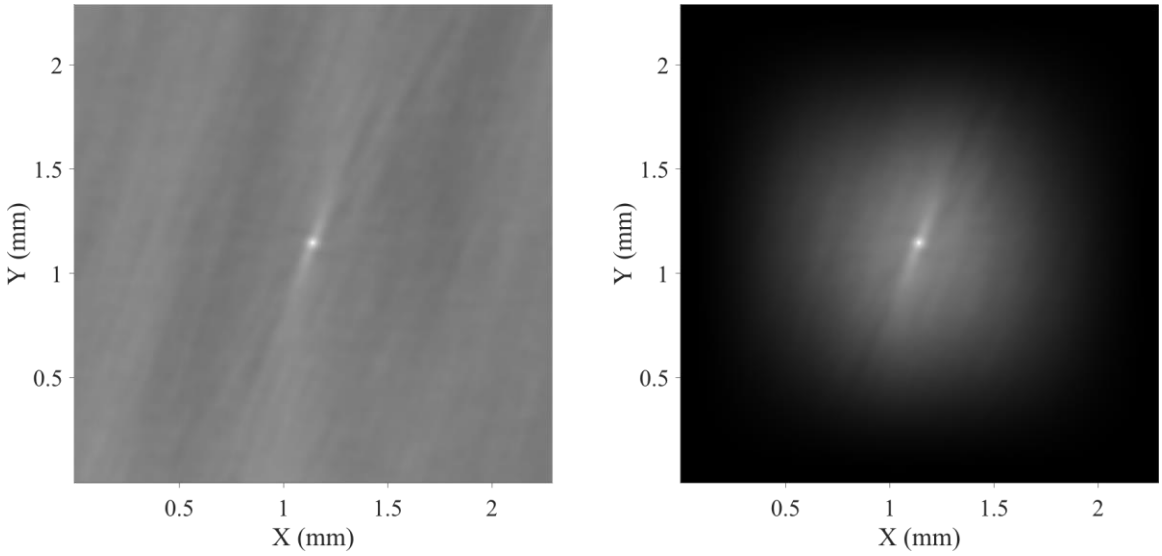

(a) Two-point correlation function output

(b) Windowed two-point correlation function output

Figure 7.11: The two-point correlation function output from the analysis region is presented (a) before and (b) after windowing. A Hann windowing function was used.

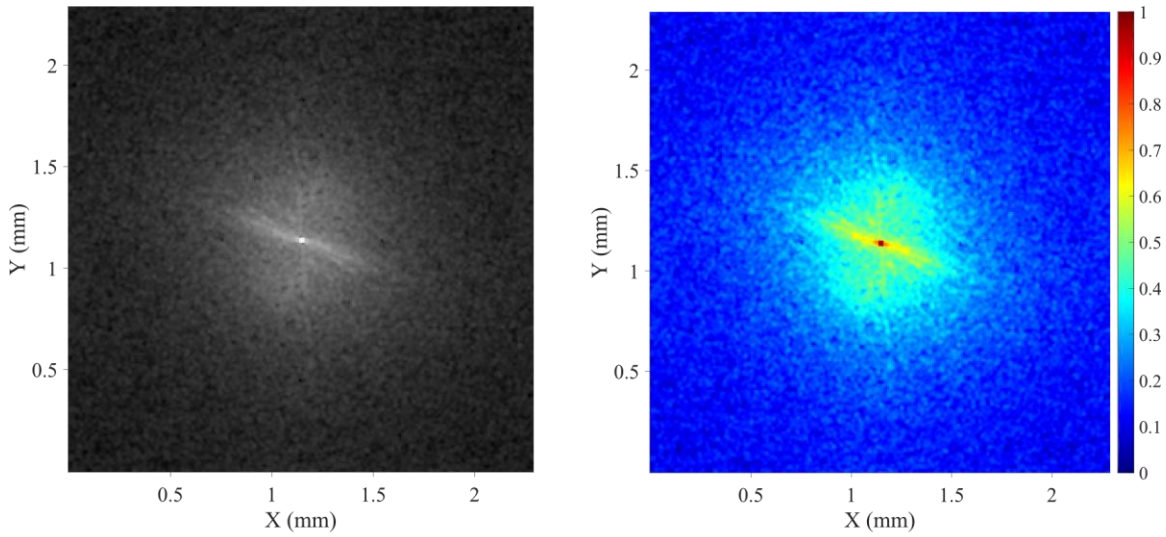

(a) Grayscale power spectrum (b) Color power spectrum

Figure 7.12: The power spectrum calculated from the FFT is presented on a base-10 logarithmic scale as (a) grayscale and (b) color images. Note that the FFT data is rotated 90 degrees with respect to the two-point correlation function output and original image data.

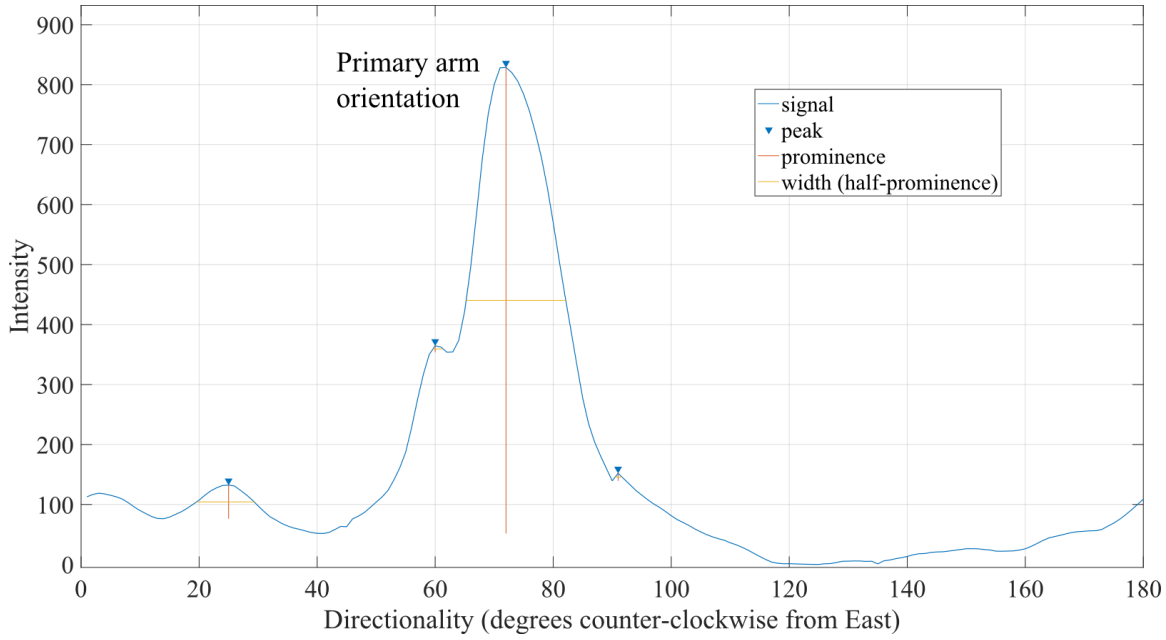

Figure 7.13: Directionality calculated from Fourier analysis is presented. The primary dendrite arm orientation is noted.

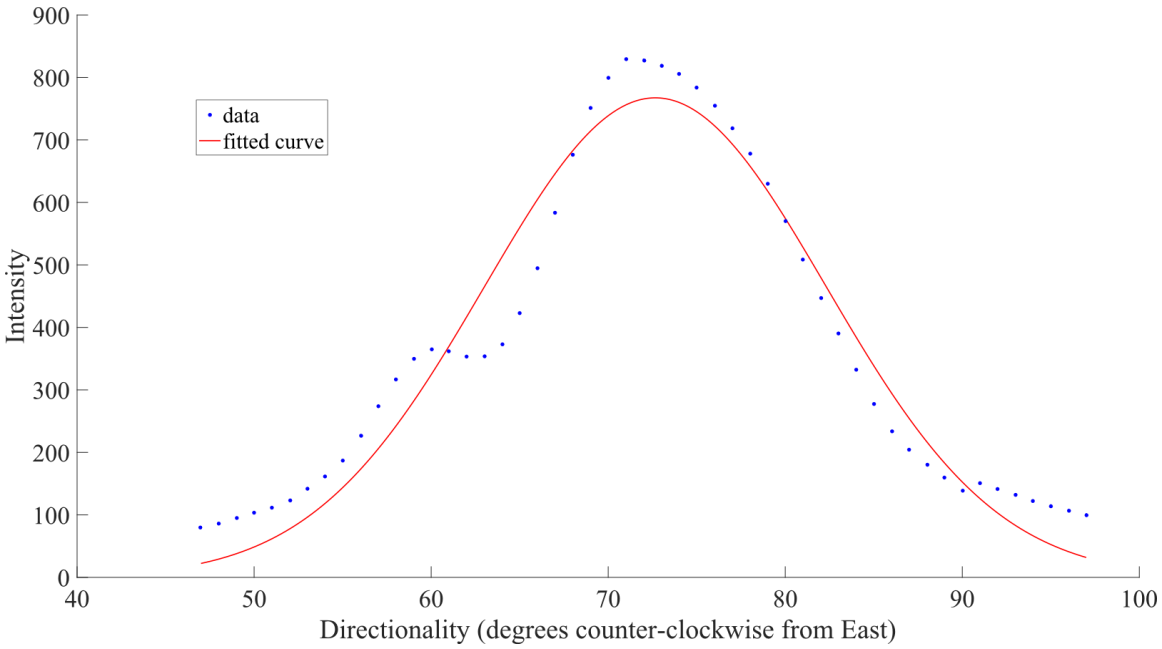

Figure 7.14: The Gaussian distribution fit to the primary dendrite arm peak is presented.

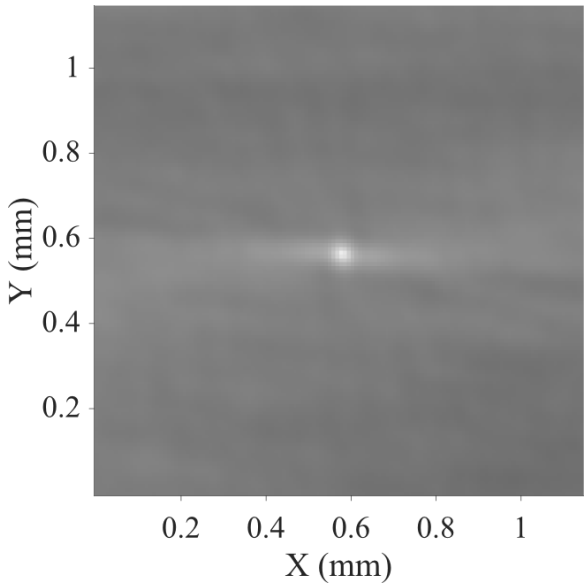

Figure 7.15: The rotated two-point correlation function data used for secondary dendrite arm analysis is presented. Rotation was completed using the primary dendrite arm orientation identified from Fourier analysis.

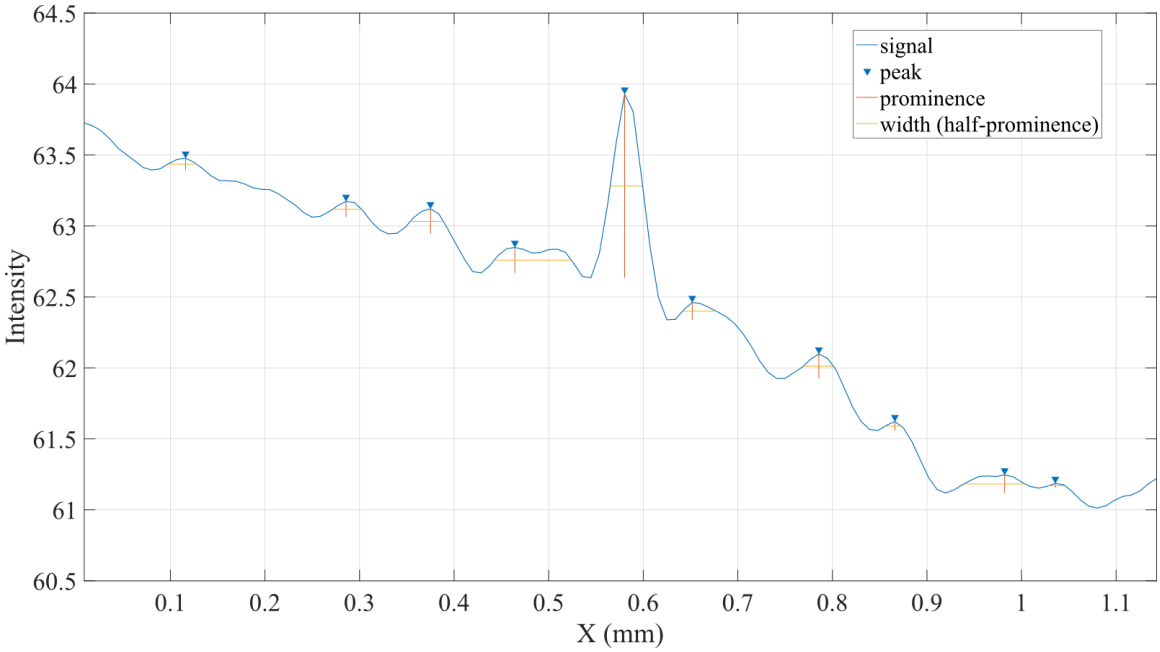

Figure 7.16: The image intensity summed along the secondary dendrite arm orientation is presented.

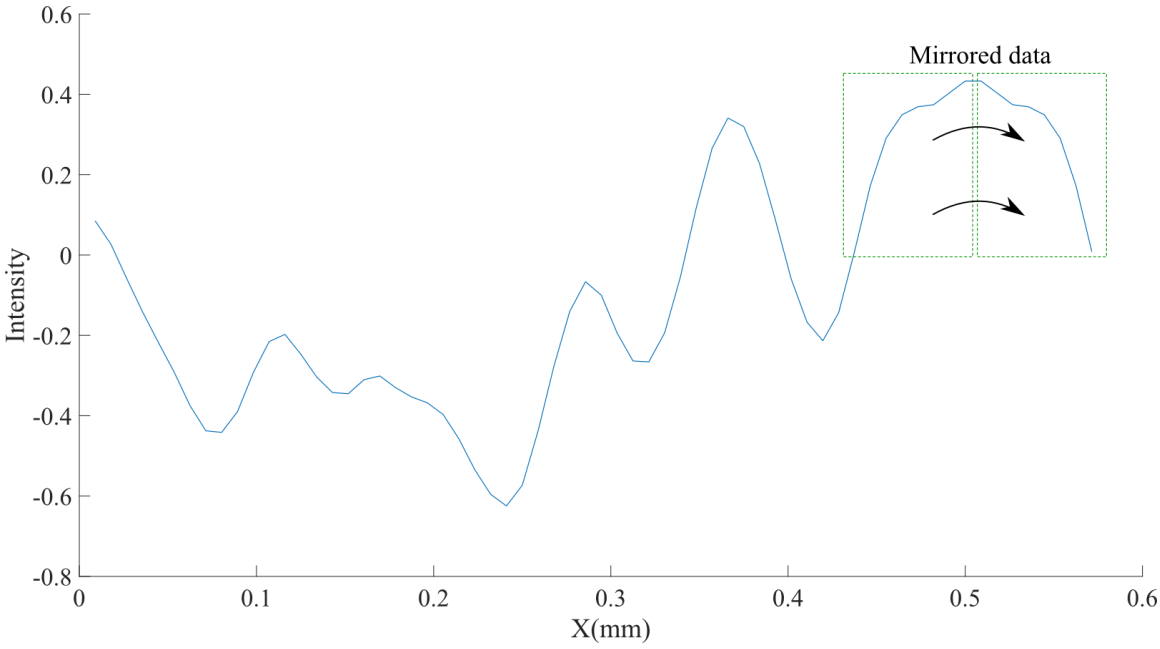

Figure 7.17: The data used to calculate secondary dendrite arm spacing with a one-dimensional FFT is provided.

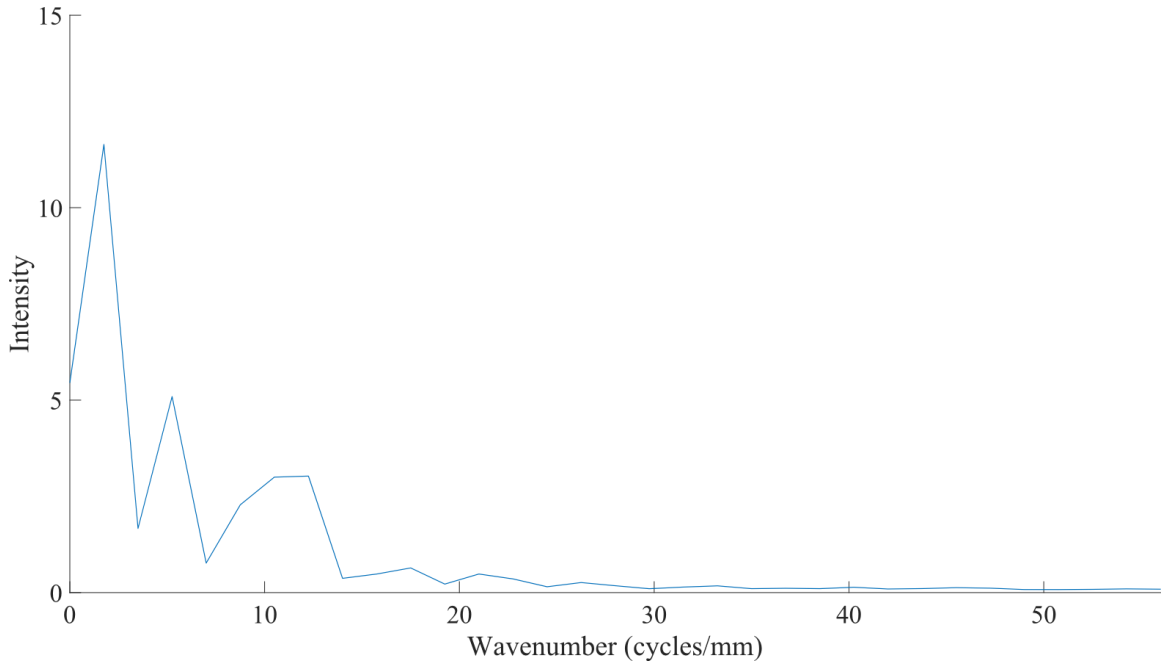

Figure 7.18: Results from the one-dimensional FFT of the secondary dendrite arm spacing data are provided. Intensity is plotted as a function of wavenumber.

7.4. Case Three

Microstructure from the VAR ingot in the bottom right of the bottom slab is presented in Figure 7.19. This microstructure demonstrates: (1) directional solidification, (2) distinct primary and secondary dendrite arms, (3) visible secondary dendrite arm spacing, and (4) a consistent primary dendrite arm orientation. The analysis region selected from this image is presented in Figure 7.20. In this analysis region, both primary and secondary dendrite arms are clearly evident. The primary dendrite arm orientation is consistent and nearly vertical. The secondary dendrite arm orientation is also consistent but nearly horizontal. This microstructure is ideal for measurement because both primary and secondary dendrite arms are visible, their orientations are consistent, and no scratches or blob-like artifacts are obvious.

The two-point correlation function output from this region is provided in Figure 7.21. Two distinct streak orientations are produced in the two-point correlation function output. Numerous small streaks are also visible and most likely describe the secondary dendrite arms. The power spectrum calculated from the FFT of the windowed data is presented in Figure 7.22. Two streak orientations are evident in the FFT result, with one slightly more diffuse than the other. Directionality was analyzed using angular filters, and the results are provided in Figure 7.23. The largest peak is identified at 11 degrees. This peak was determined to represent the secondary dendrite arm orientation because this data was acquired from the right side of the ingot. Another distinct peak was identified approximately 90 degrees from the dominant peak, at 106 degrees. This peak represents the primary dendrite arm orientation. As expected, peaks representing both the primary and secondary dendrite arm orientations were identified because these features are clearly visible in Figure 7.20.

Gaussian distributions fit to the peaks representing the primary and secondary dendrite arm orientations are presented in Figure 7.24 and Figure 7.25, respectively. The primary dendrite arm orientation was calculated as 106.4 degrees with a 95 percent confidence interval of ± 0.8 degrees and a standard deviation of 8.3 degrees. This correlates with the primary dendrite arm orientation observed in Figure 7.20. The secondary dendrite arm orientation was calculated as 11.6 degrees with a 95 percent confidence interval of ± 0.2 degrees and a standard deviation of 14.5 degrees.

The rotated two-point correlation function data used for secondary dendrite arm analysis is provided in Figure 7.26. Pixel intensity was summed along the secondary dendrite arm orientation and is presented in Figure 7.27. Enough peaks were identified to proceed with secondary dendrite arm analysis. Measuring the distance between peaks produced an average spacing of 79 μm and a standard deviation of 17 μm. FFT analysis

was used to calculate secondary dendrite arm spacing from the data presented in Figure 7.28. This data was halved, summed, and mirrored as described previously. The results are provided in Figure 7.29. As in Case Two, multiple peaks are located at low wavenumbers. Secondary dendrite arm spacing was calculated as 83 μm, but the resolution of this data only provides a measurement in increments of approximately 25 μm.

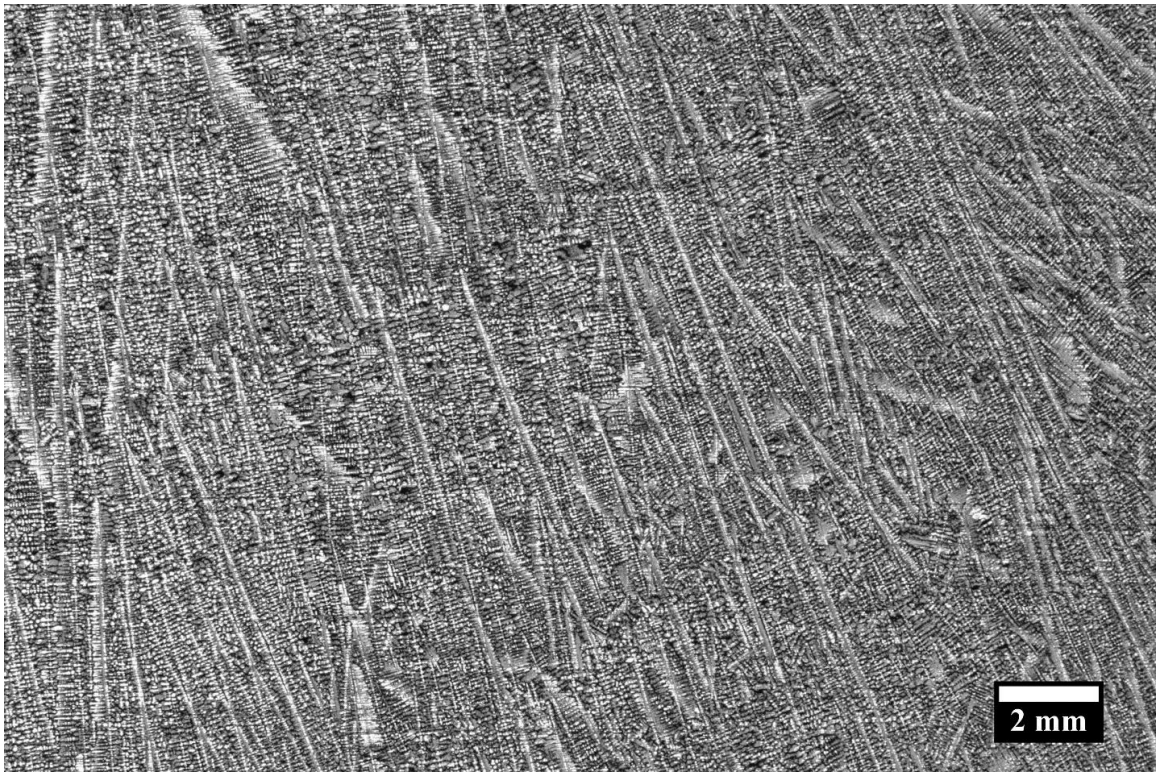

Figure 7.19: Microstructure from the VAR ingot in the bottom right of the bottom slab is presented as a grayscale image.

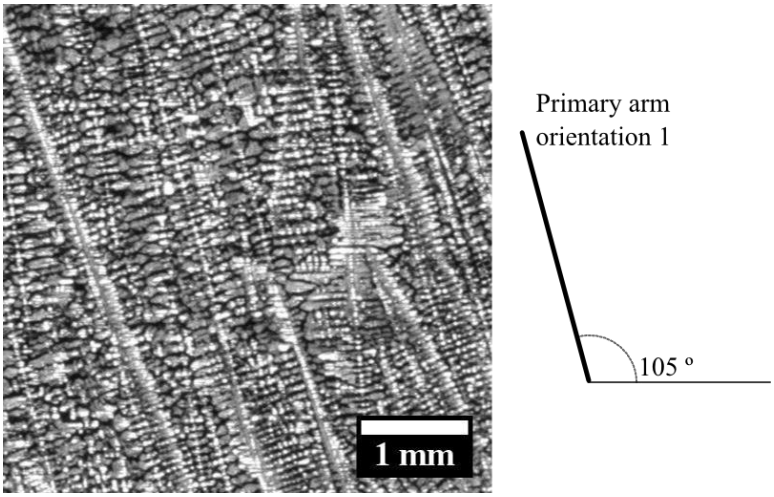

Figure 7.20: The analysis region is presented. The primary dendrite arm orientation is noted.

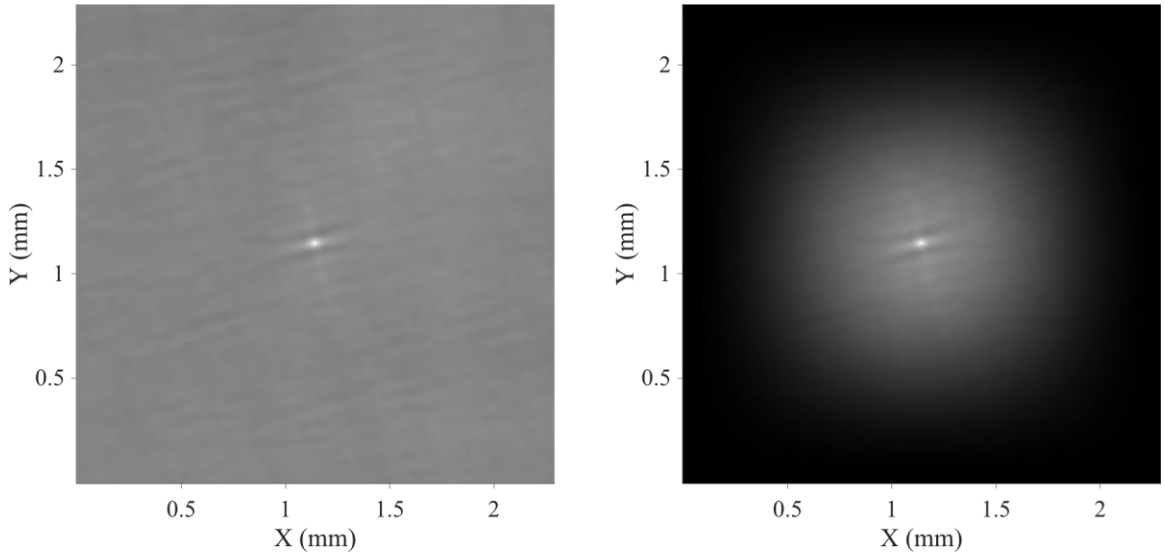

(a) Two-point correlation function output

(b) Windowed two-point correlation function output

Figure 7.21: The two-point correlation function output from the analysis region is presented (a) before and (b) after windowing. A Hann windowing function was used.

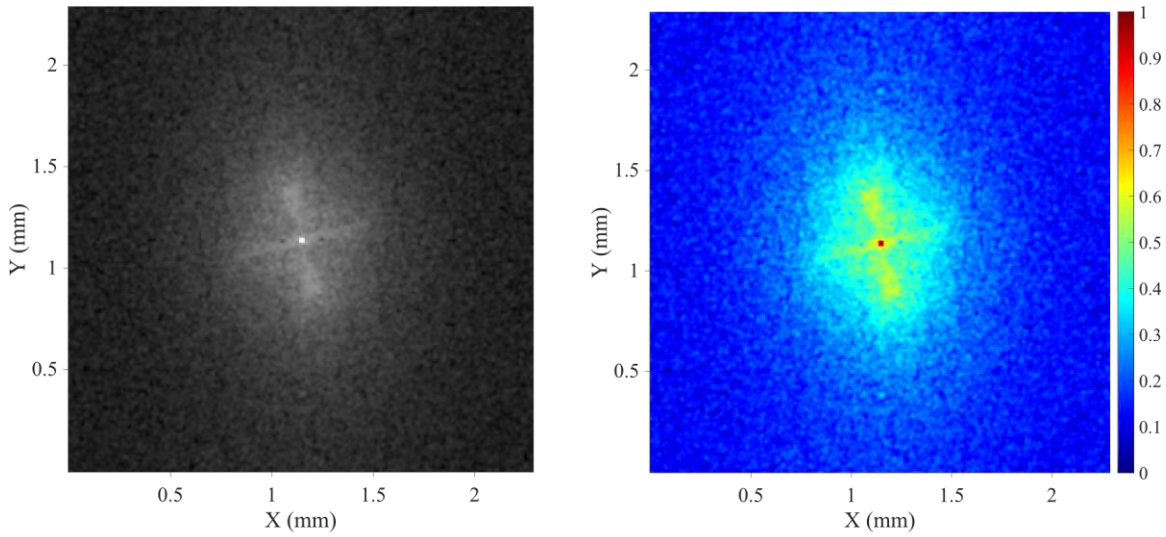

(a) Grayscale power spectrum (b) Color power spectrum

Figure 7.22: The power spectrum calculated from the FFT is presented on a base-10 logarithmic scale as (a) grayscale and (b) color images. Note that the FFT data is rotated 90 degrees with respect to the two-point correlation function output and original image data.

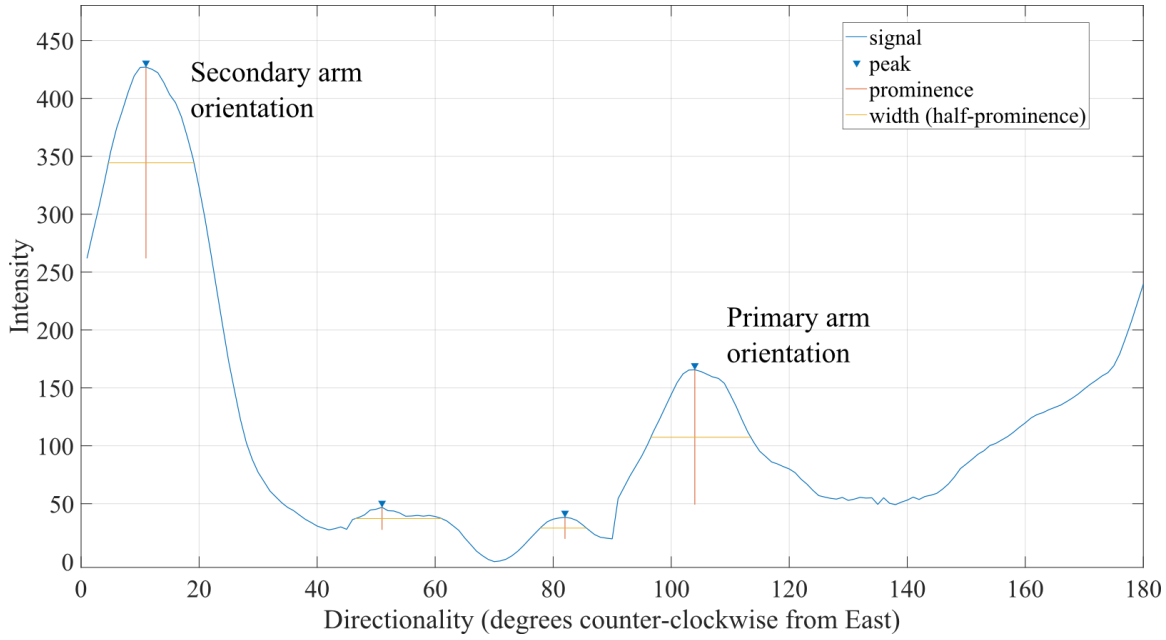

Figure 7.23: Directionality calculated from Fourier analysis is presented. The primary and secondary dendrite arm orientations are noted.

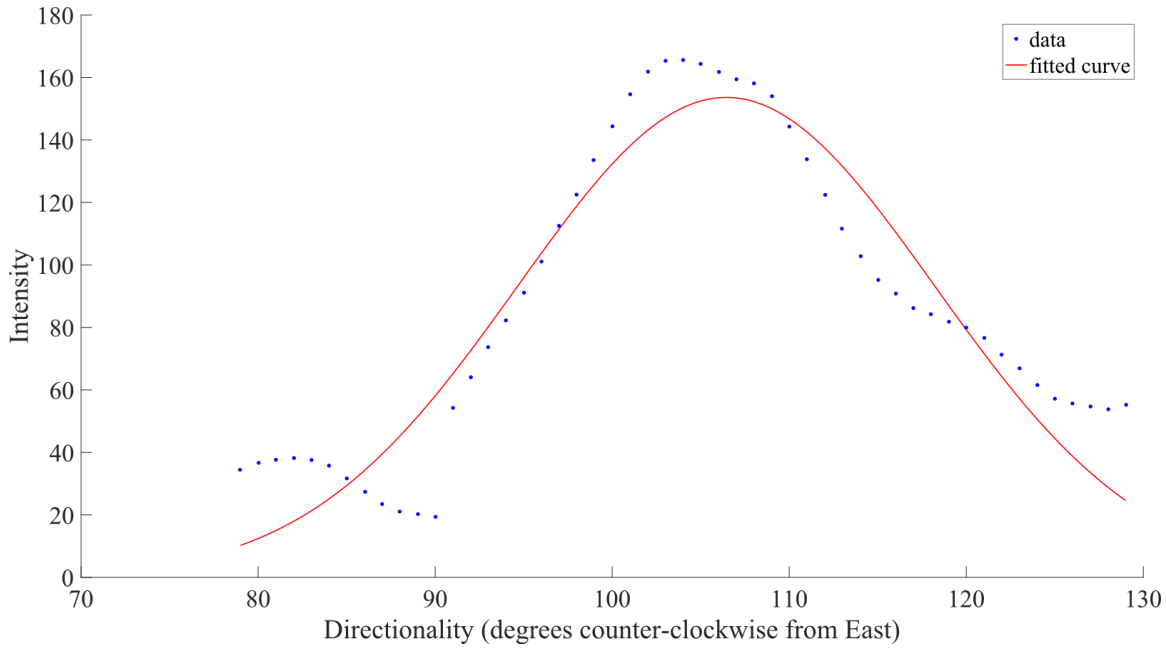

Figure 7.24: The Gaussian distribution fit to the primary dendrite arm peak is presented.

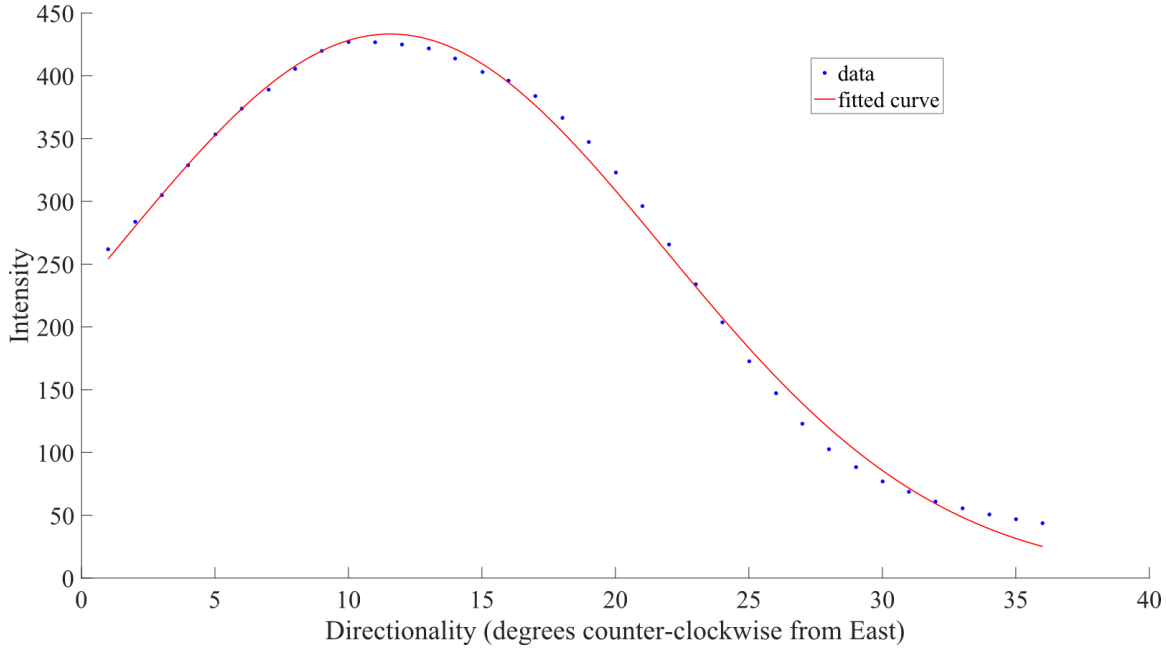

Figure 7.25: The Gaussian distribution fit to the secondary dendrite arm peak is presented.

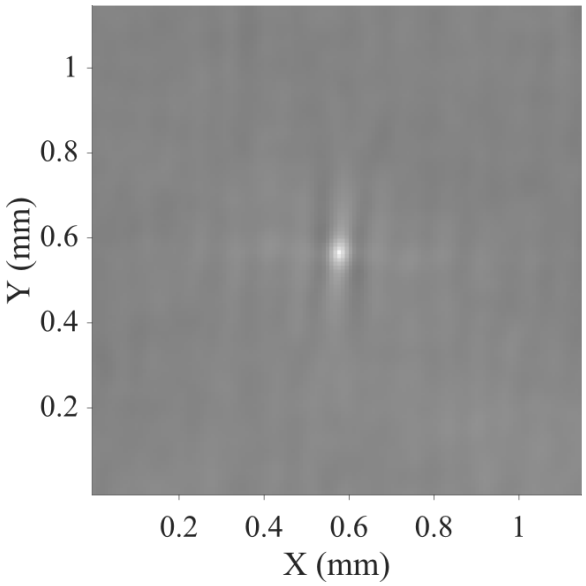

Figure 7.26: The rotated two-point correlation function data used for secondary dendrite arm analysis is presented. Rotation was completed using the primary dendrite arm orientation identified from Fourier analysis.

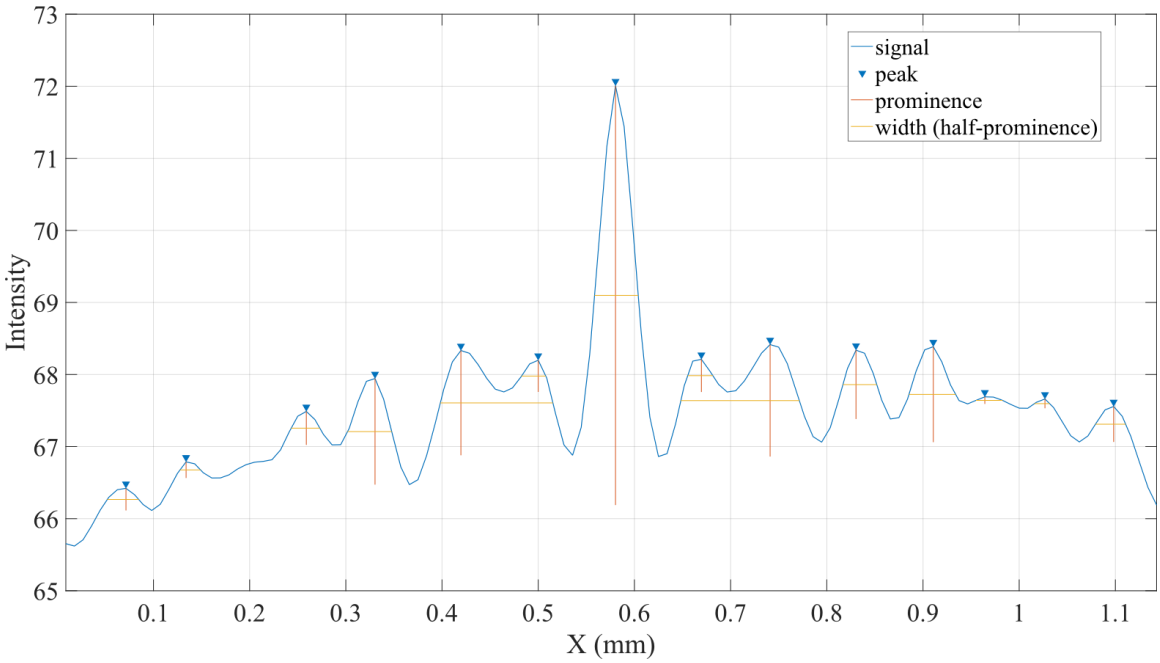

Figure 7.27: The image intensity summed along the secondary dendrite arm orientation is presented.

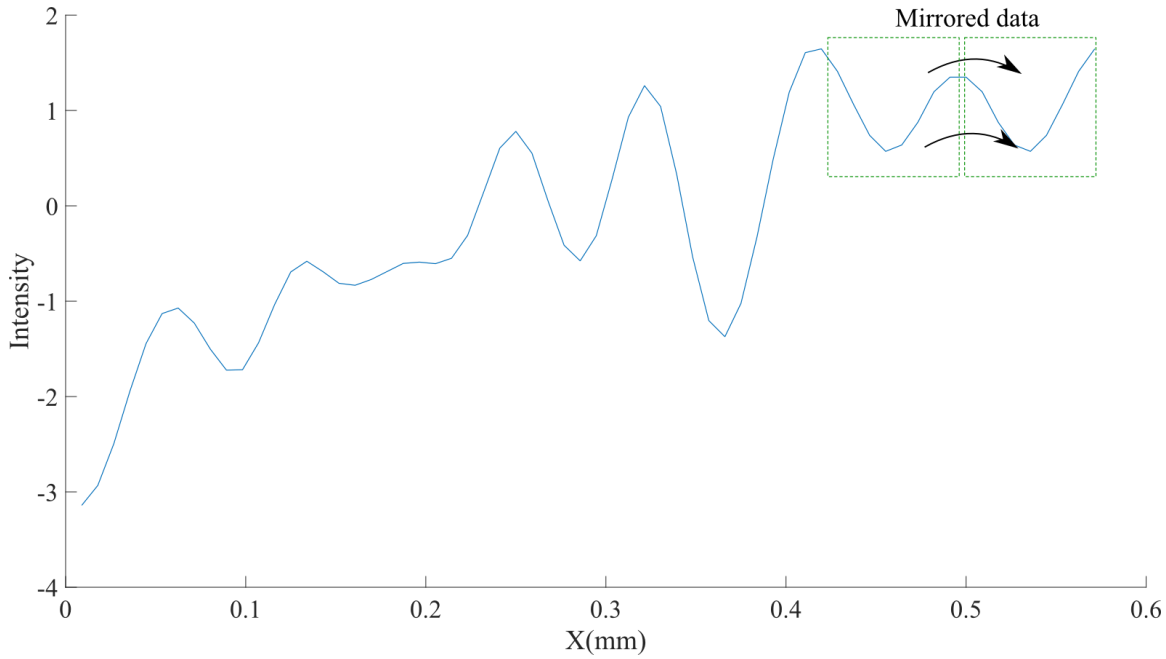

Figure 7.28: The data used to calculate secondary dendrite arm spacing using a one-dimension FFT is provided.

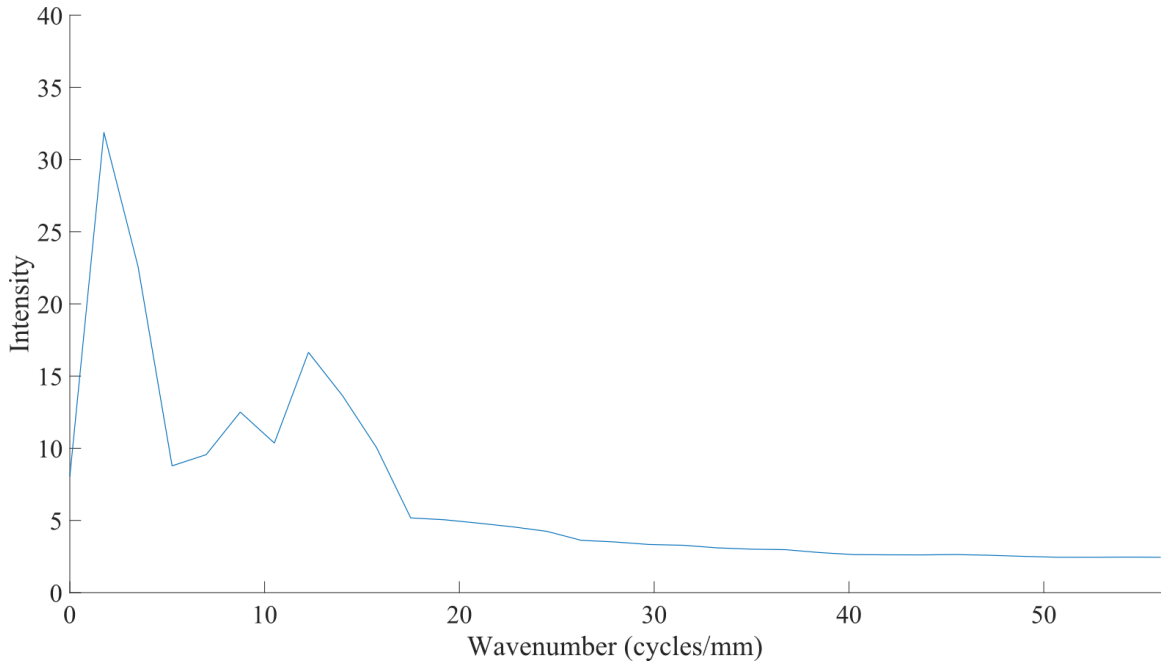

Figure 7.29: Results from the one-dimensional FFT of the secondary dendrite arm spacing data are provided. Intensity is plotted as a function of wavenumber.

7.5. CASE FOUR

The microstructure from the VAR ingot in the middle of the top slab is presented in Figure 7.30. This microstructure demonstrates: (1) equiaxed solidification, (2) no distinct primary dendrite arm orientation, and (3) visible primary and secondary dendrite arms. The analysis region selected from this image is presented in Figure 7.31. In this analysis region, both primary and secondary dendrite arms are observed, and primary dendrite arms are randomly orientated.

The two-point correlation function output from this region is provided in Figure 7.32. The power spectrum from the FFT of the windowed two-point correlation function data is presented in Figure 7.33. No distinct streak orientations are present in either the two-point correlation function output or the FFT data. Directionality was analyzed

using angular filters, and the results are presented in Figure 7.34. There were no peaks with a maximum intensity value of at least 400 units detected. Because of this, neither primary dendrite arm orientation nor secondary dendrite arm spacing were deemed measurable.

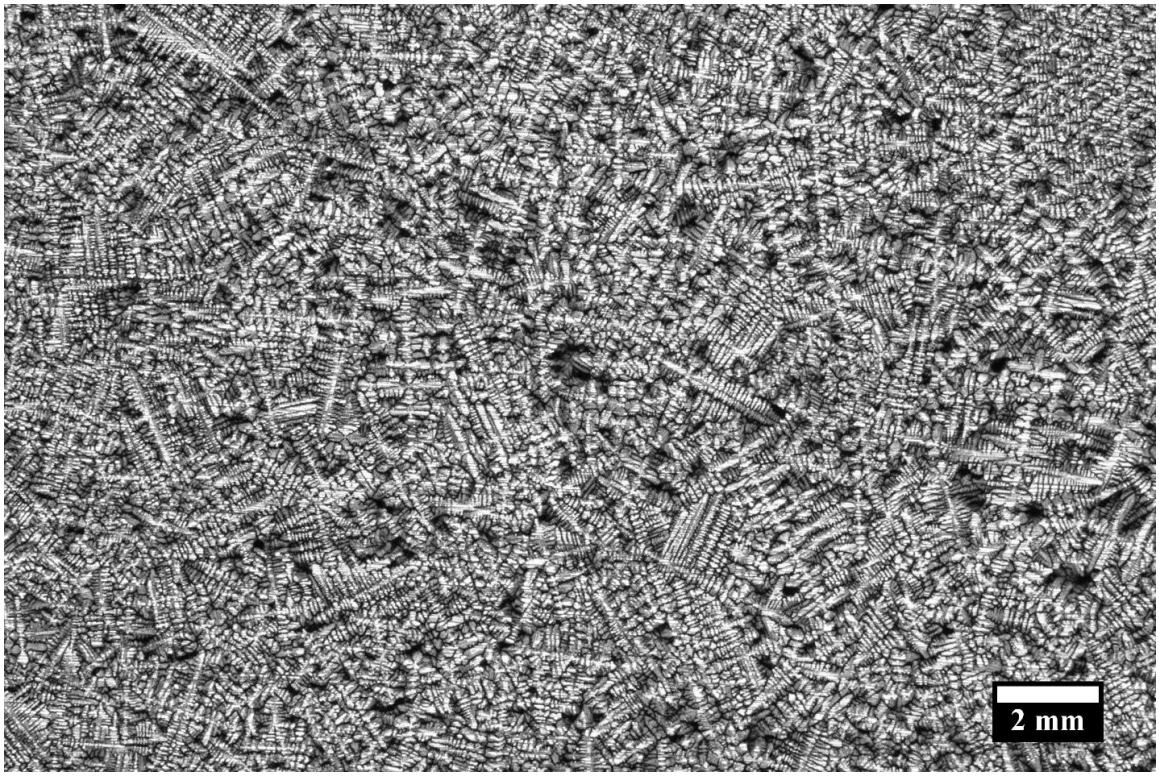

Figure 7.30: Microstructure from the VAR ingot in the middle of the top slab is presented as a grayscale image.

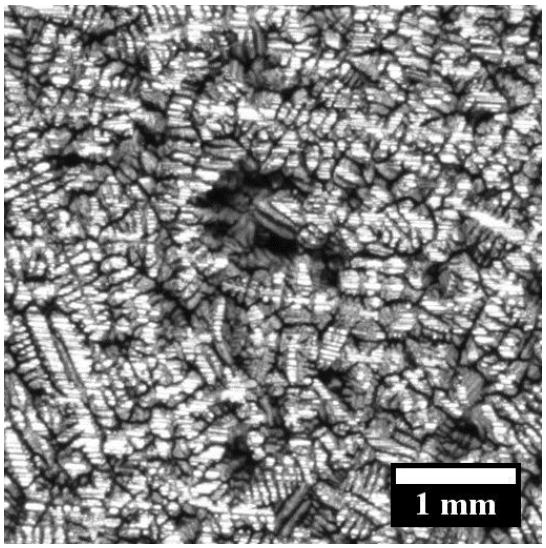

Figure 7.31: The analysis region is presented.

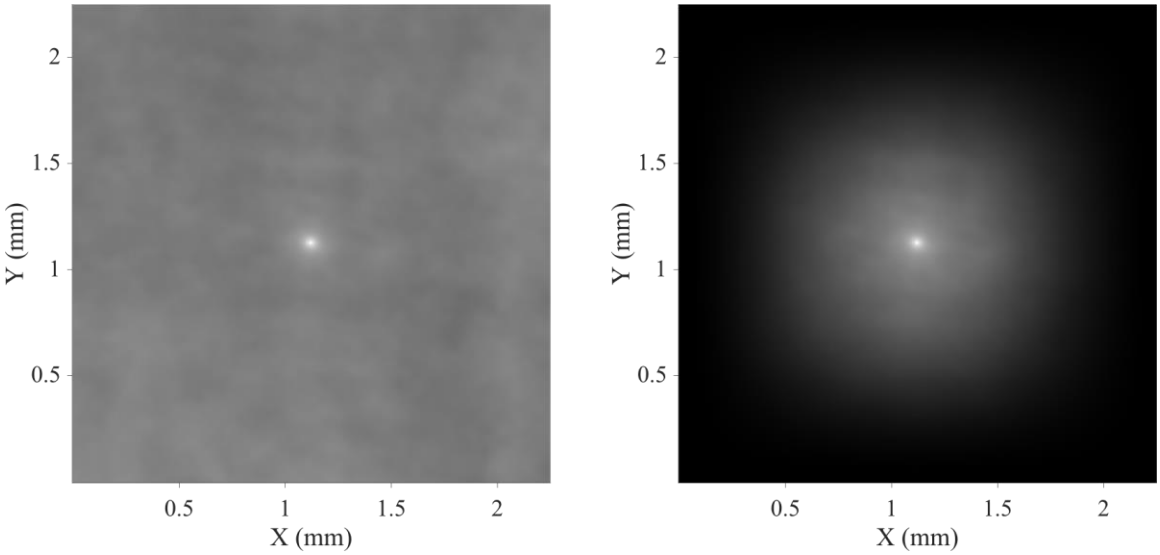

(a) Two-point correlation function output

(b) Windowed two-point correlation function output

Figure 7.32: The two-point correlation function output from the analysis region is presented (a) before and (b) after windowing. A Hann windowing function was used.

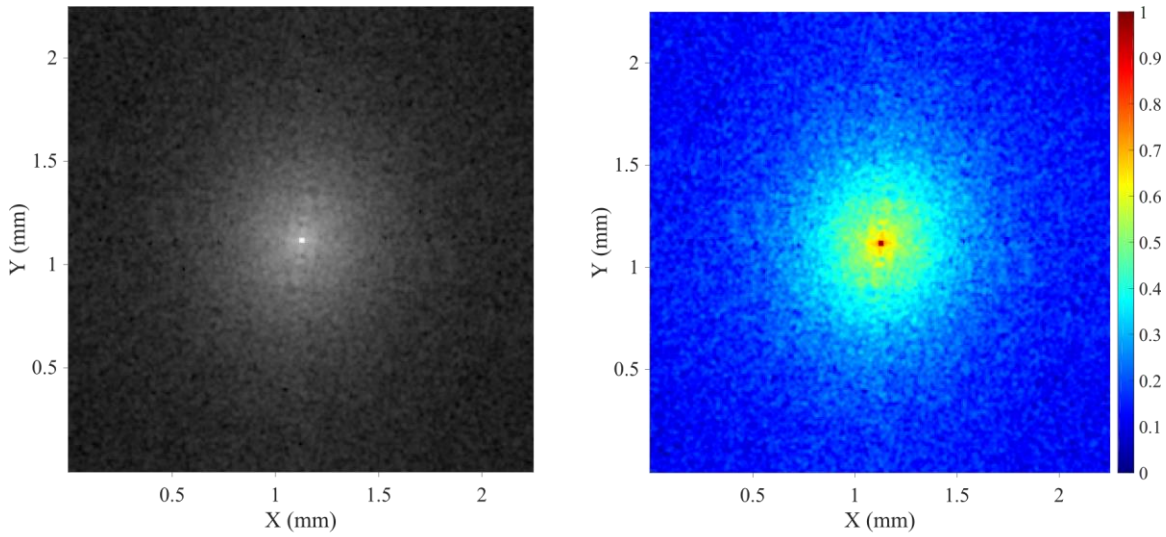

(a) Grayscale power spectrum (b) Color power spectrum

Figure 7.33: The power spectrum calculated from the FFT is presented on a base-10 logarithmic scale as (a) grayscale and (b) color images. Note that the FFT data is rotated 90 degrees with respect to the two-point correlation function output and original image data.

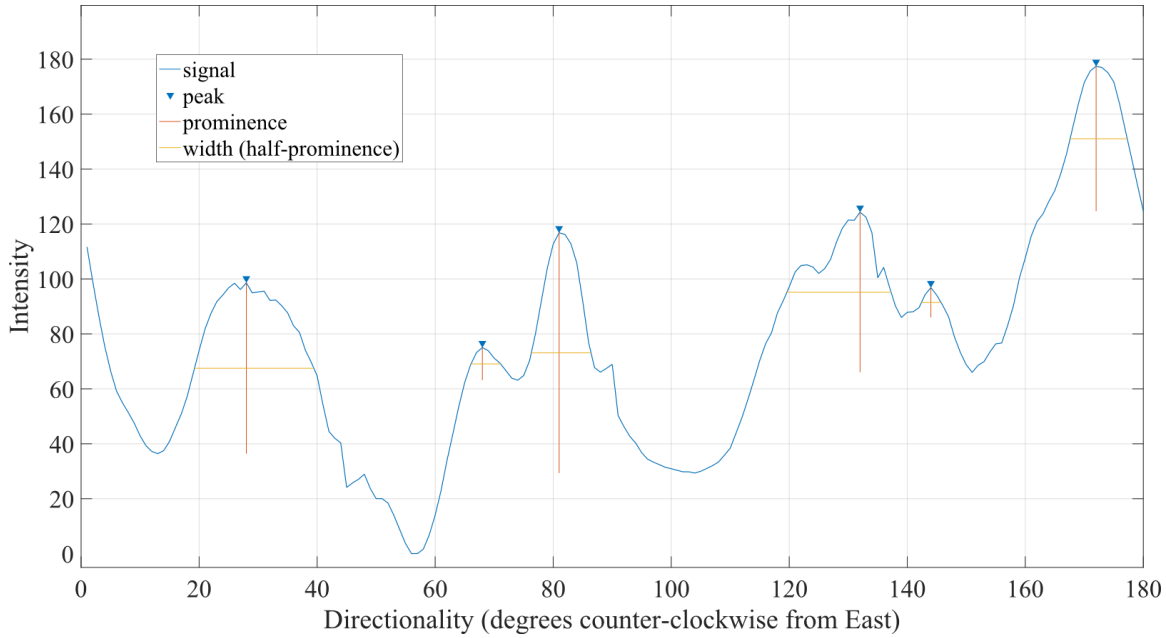

Figure 7.34: Directionality calculated from Fourier analysis is presented.

8. RESULTS FROM THE VAR INGOT

8.1. PARTICLE IDENTIFICATION

The particle identification technique was used to measure primary dendrite arm orientation and secondary dendrite arm spacing throughout the VAR ingot. Melt pool profiles were then estimated from primary dendrite arm orientations.

The 55,640 individual primary dendrite arms identified in the VAR ingot are presented in Figure 8.1; the color of each primary dendrite arm describes its orientation within the ingot. Primary dendrite arm density is high along the left, right, and bottom of the ingot. In these regions, directional solidification occurred, and the primary dendrites exhibit consistent orientations, as demonstrated in Figure 8.1. Primary dendrite arm orientations are consistent for a constant radial position across a wide range of heights. On the left side of the ingot, primary dendrite arms are oriented at approximately 25 degrees. This orientation increases to approximately 50 degrees at one-third of the diameter into the ingot. On the right side of the ingot, the average primary dendrite arm orientation decreases from approximately 156 degrees at the right surface to approximately 125 degrees at one-third of the diameter into the ingot. Along the bottom of the ingot, primary dendrite arms have a consistent orientation near 90 degrees. Because this ingot is small, the bottom region constitutes a large portion of the ingot.

At the center of the ingot, primary dendrite arms are randomly oriented. This is expected, because equiaxed solidification occurs in the center of the ingot. Furthermore, primary dendrite arms are sparsely identified at the center compared to the sides of the ingot. It is suspected that the geometry of the primary dendrite arms evident in the equiaxed region interferes with the particle identification methodology. For example, equiaxed solidification is expected to produce many primary dendrite arms that pass through the sectioning plane, instead of lying within that plane, preventing them from being identified.

Melt pool profiles were estimated from primary dendrite arm orientations. Figure 8.2 presents a montage image of the VAR ingot, the identified primary dendrite arms, and the melt pool profile estimates. These melt pool profiles are overlaid on the identified primary dendrite arms in Figure 8.3. Melt pool profiles were estimated using the streamline function in Matlab™ [71]. Profiles were started on the left and right surfaces of the ingot at several locations along the ingot height and were calculated toward the center of the ingot. As shown in Figure 8.2, the profile estimates were stopped 60 mm into the ingot, before they reached the equiaxed region. The profiles were halted before the equiaxed region because melt pool profiles cannot be acquired from the randomly oriented primary dendrite arms in the equiaxed region. Figure 8.3 includes manual approximations of melt pool profiles spanning the ingot diameter for comparison with the calculated estimates. Manual melt pool profiles were drawn by hand based on visual observations of the primary dendrite arm orientations from the particles identified.

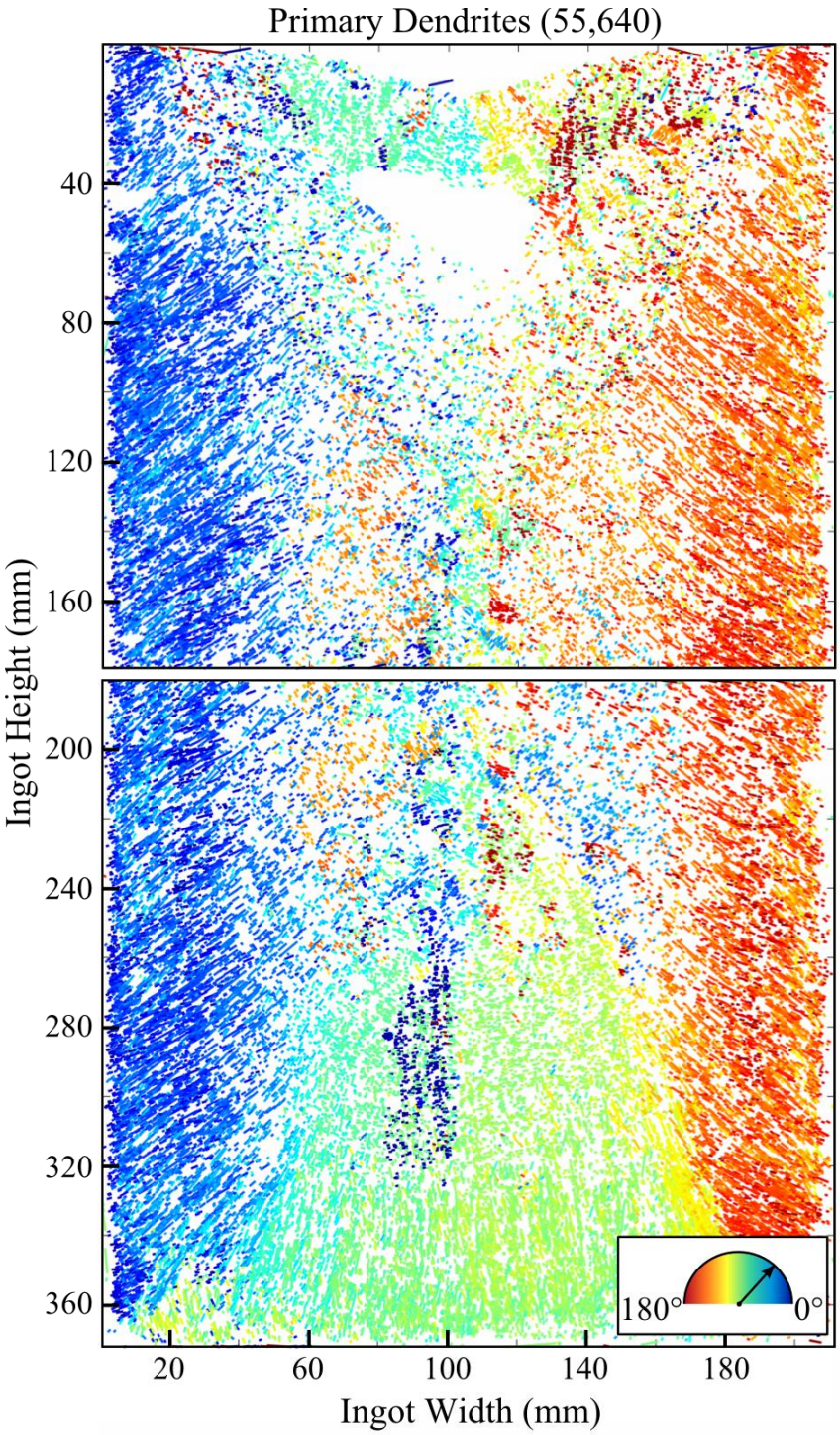

Figure 8.1: Primary dendrite arms identified from the VAR ingot using particle identification are presented. The color of each dendrite corresponds to its orientation within the ingot.

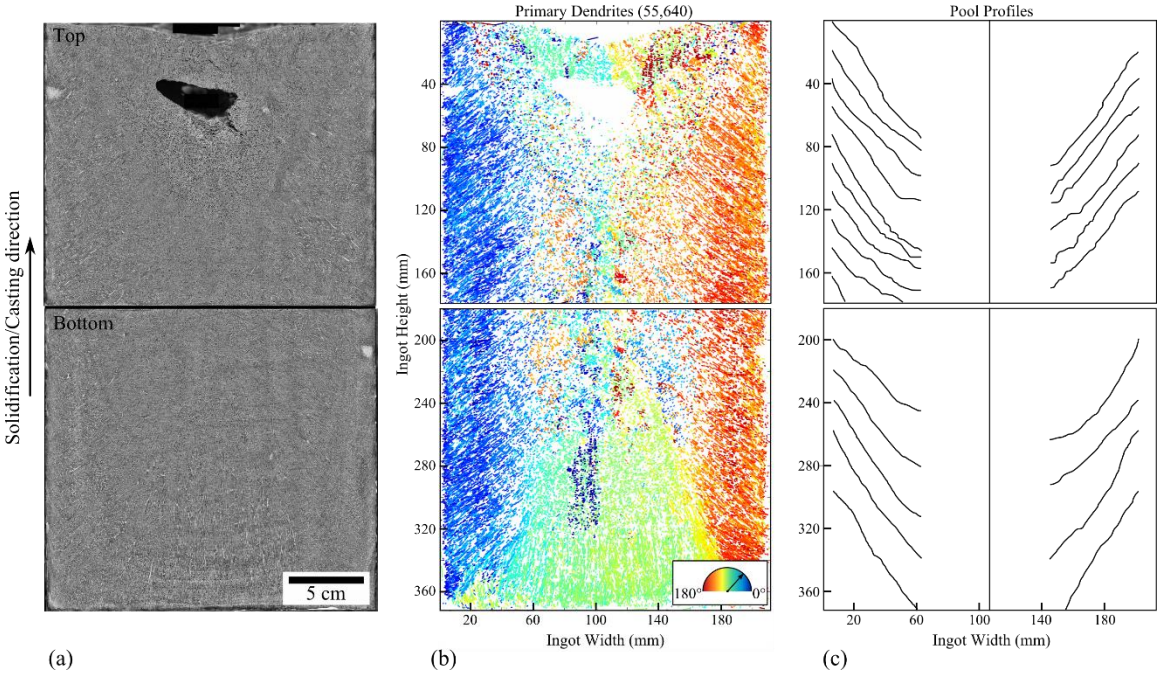

Figure 8.2: (a) The montage image of the VAR ingot is presented with (b) the primary dendrite arms identified and (c) the melt pool profiles calculated from primary dendrite arm orientations. These were calculated using particle identification.

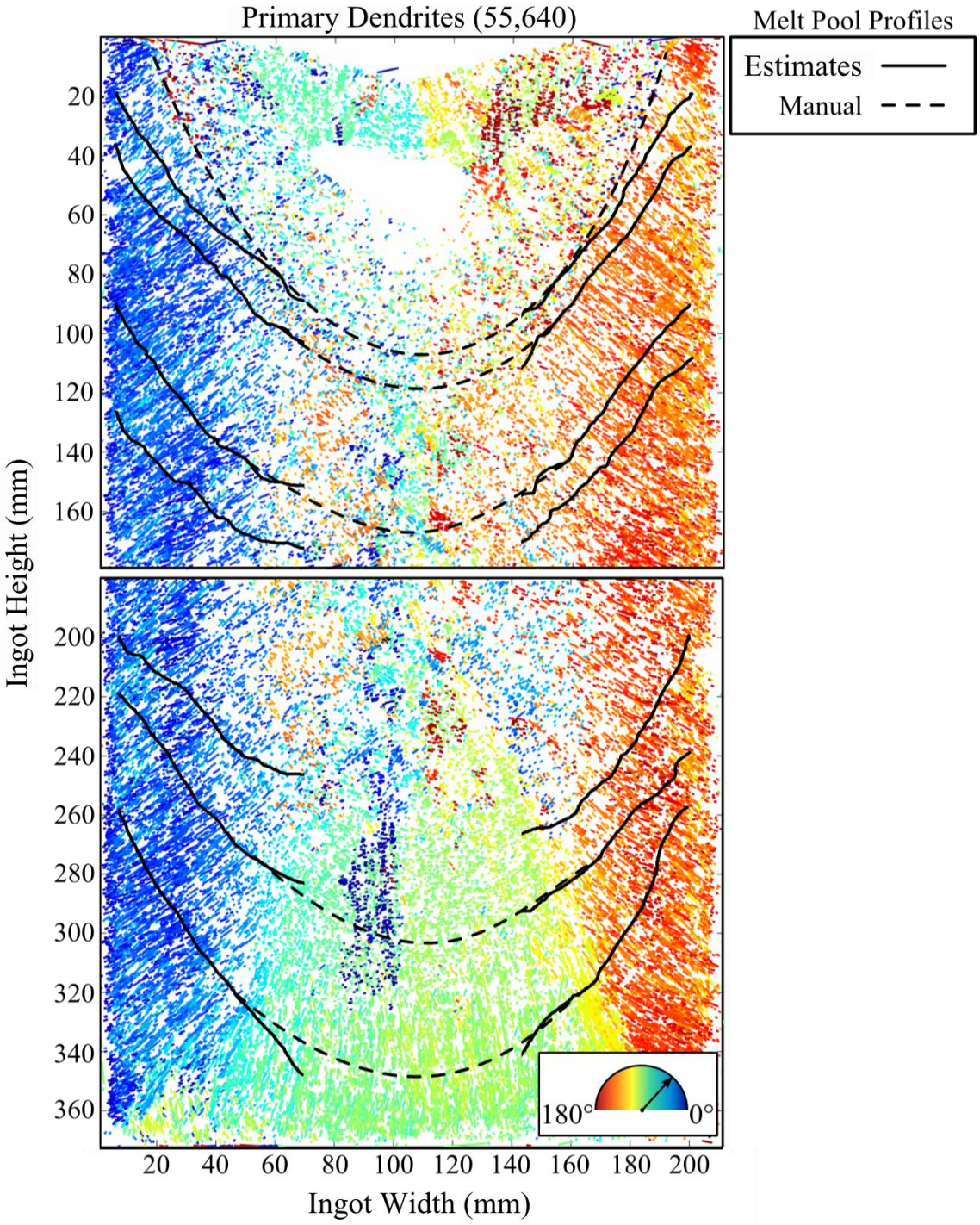

Figure 8.3: Automated melt pool profile estimates (solid lines) are combined with manual melt pool lines (dashed lines) drawn through the equiaxed region and overlaid on the primary dendrite arms identified from the VAR ingot. These profiles were calculated using particle identification.

Secondary dendrite arm spacing measurements are shown in Figure 8.4 using a Voronoi diagram. A Voronoi diagram represents data in space by forming a polygonal cell around each individual data point. The size and shape of a polygonal cell is chosen such that each position within that cell is located closer to the data point used to create that cell than any other data point. Figure 8.4 demonstrates that secondary dendrite arm spacing was successfully measured throughout the VAR ingot. No obvious trends in these measurements are observed. Instead, secondary dendrite arm spacing measurements vary throughout the ingot, and the majority of these measurements range from 100 to 180 μm.

Average secondary dendrite arm spacings were calculated from the left side of the VAR ingot using the automated technique and compared to manual measurements. Manual measurements were used to determine the accuracy of the automated measurement technique. Figure 8.5 presents the secondary dendrite arm spacing measurements from the left side of the VAR ingot and the average secondary dendrite arm spacings calculated at select locations along the ingot height. Secondary dendrite arm spacings were measured from the highlighted region in Figure 8.5 (a) manually and by using the automated technique. In Figure 8.5 (b), solid lines represent average secondary dendrite arm spacing measurements, and dashed lines represent the standard deviations of those measurements. Figure 8.5 (b) establishes that the automated secondary dendrite arm spacing measurements are consistently larger than manual measurements, and uncertainty in both the automated and manual measurements is large. The manual measurements typically fall within the uncertainty of the automated measurements. The average secondary dendrite arm spacing calculated from automated measurement is approximately 134 μm with a standard deviation of 42 μm. The average secondary dendrite arm spacing calculated from manual measurement is approximately 100 μm with a standard deviation of 23 μm. The automated technique is expected to produce a slightly larger secondary dendrite arm spacing

measurement because it is susceptible to missing some secondary arms, leading to an error that increases the spacing measurement.

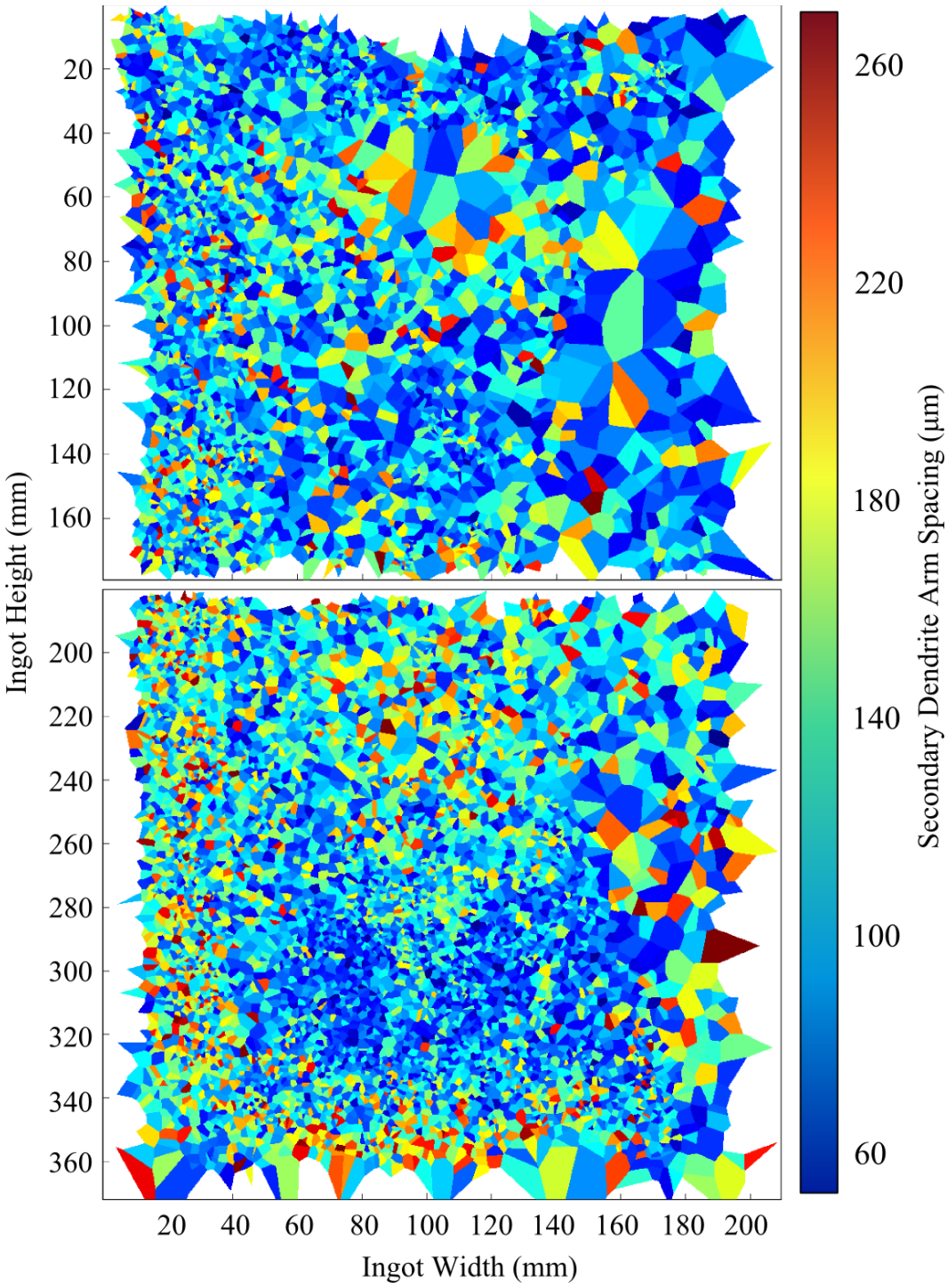

Figure 8.4: Secondary dendrite arm spacings measured from the VAR ingot are presented using a Voronoi diagram. These spacings were calculated using particle identification.

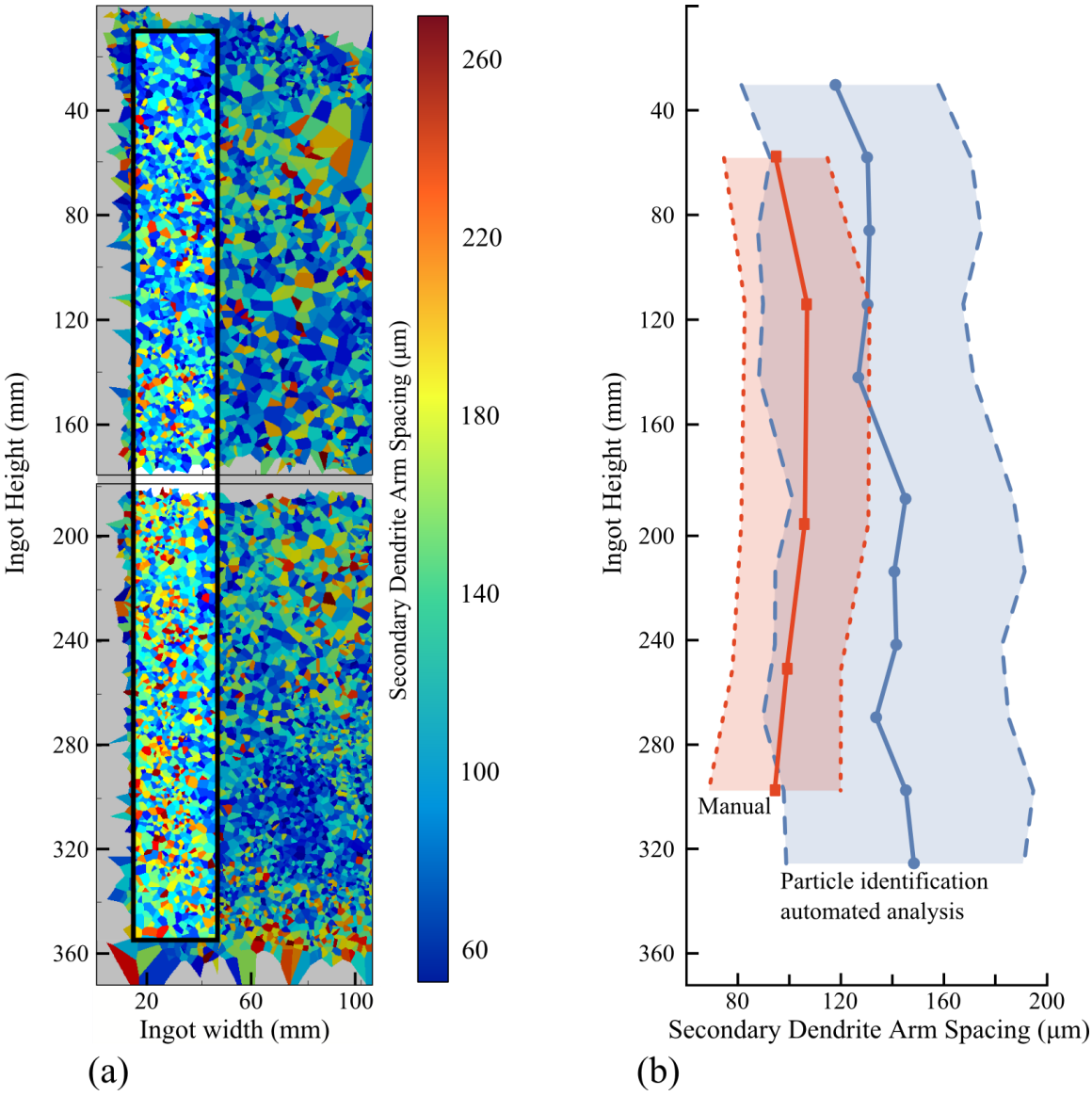

Figure 8.5: (a) Secondary dendrite arm spacing measurements from the left side of the VAR ingot are presented. (b) Average secondary dendrite arm spacings calculated from the highlighted region in (a) using automated and manual measurement techniques are presented. The automated spacings were calculated using particle identification.

8.2. TWO-POINT CORRELATION FUNCTION AND FOURIER ANALYSES

The VAR ingot was also analyzed using the two-point correlation function and Fourier analyses. Over 3,000 individual analysis regions were evaluated. Figure 8.6 presents the primary dendrite arm orientations calculated from each analysis region in the VAR ingot. These orientations are presented as lines located at the center of each analysis region. The color of each line describes its orientation within the ingot. White regions in Figure 8.6 represent analysis regions where no primary dendrite arm orientation was detected. Figure 8.6 demonstrates that primary dendrite arm orientations were successfully calculated throughout most of the VAR ingot; only the center of the top slab exhibited a large region were primary dendrite arm orientations could not be measured. Consistent primary dendrite arm orientations were measured along the left, right, and bottom of the ingot. On the left side of the ingot, the primary dendrite arm orientation does not significantly vary along most of the ingot height. Variation is slight along the ingot radius until near the center of the ingot. Similar behavior is observed on the right side of the ingot. Along the bottom of the ingot, primary dendrite arms are oriented near 90 degrees. Regions with random primary dendrite arm orientations are only observed within a narrow strip located in the center of the ingot.

Melt pool profiles in the VAR ingot were estimated from primary dendrite arm orientations calculated from each analysis region. Melt pools were estimated by rotating the primary dendrite arm orientations 90 degrees. Figure 8.7 presents these melt pool profile estimates, the primary dendrite arm orientations, and a montage image of the VAR ingot. The melt pool profile estimates break down in the center of the ingot where primary dendrite arms are randomly oriented, as illustrated by Figure 8.7.

It is important to note that not all of the information collected during the analysis of the VAR ingot was used to produce melt pool profile estimates. For example, only one

primary dendrite arm orientation is presented for each analysis region in Figure 8.6, yet in some instances, multiple orientations were detected. These secondary orientations were recorded but not used during analysis. For future analyses, this information may be useful for describing fine details in the melt pool profile or useful for qualifying the confidence of the melt pool profile estimates. The uncertainties associated with the primary dendrite arm orientations calculated from each analysis region were also estimated, but are not reported in this dissertation. The inclusion of these uncertainties during analysis of melt pool profiles may be useful, but is beyond the scope of this dissertation.

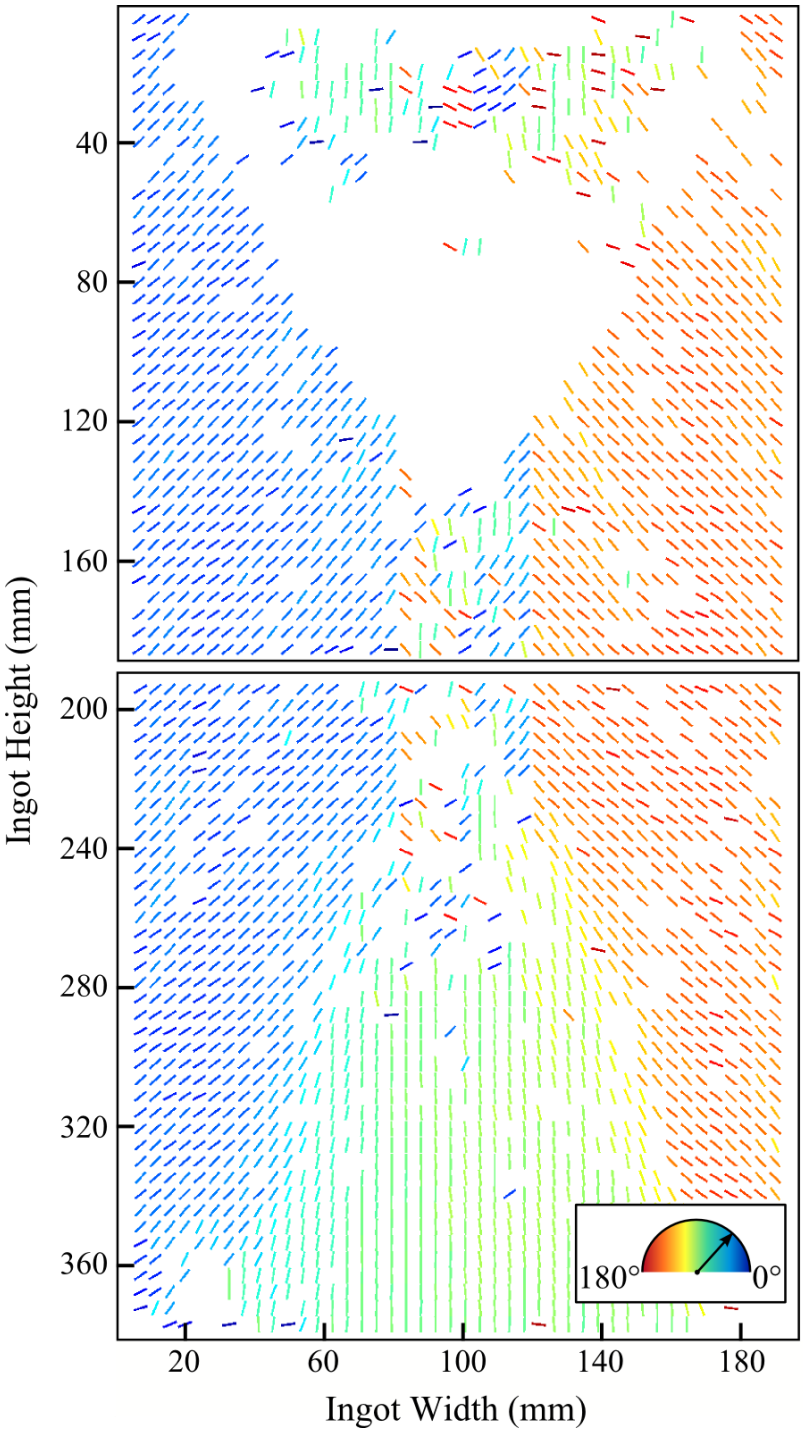

Figure 8.6: Primary dendrite arm orientations calculated from the VAR ingot for each analysis region are presented. These orientations calculated using two-point correlation function analysis.

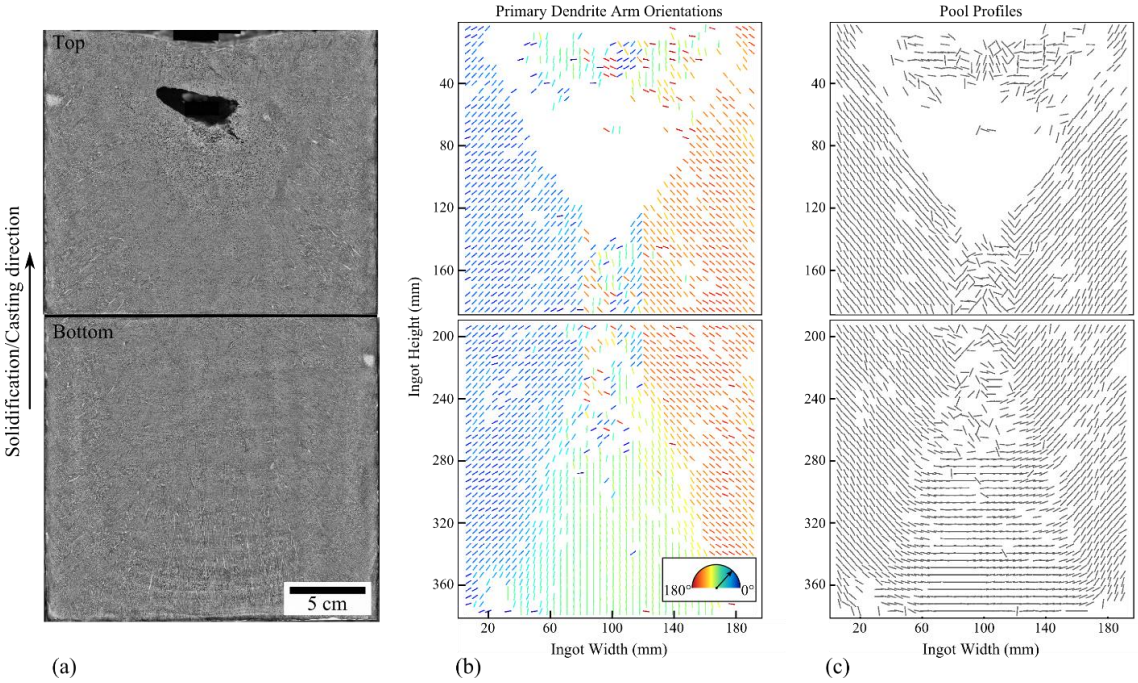

Figure 8.7: (a) The montage image of the VAR ingot is presented with (b) the primary dendrite arm orientations calculated from each analysis region and (c) the melt pool profiles calculated from these orientations. These were calculated using two-point correlation function analysis.

After primary dendrite arm orientations were calculated for each analysis region in the VAR ingot, secondary dendrite arm spacing was measured using two techniques. The first technique calculated secondary dendrite arm spacing by measuring peaks in image intensity along the primary dendrite arm orientation in the two-point correlation function output. The second technique used a one-dimensional FFT to analyze the two-point correlation function output along the primary dendrite arm orientation. Secondary dendrite arm spacing measurements calculated using both of these techniques are presented in Figure 8.8 and Figure 8.9. Data presented in Figure 8.8 was calculated using the peak-counting technique. Data in Figure 8.9 was calculated using the FFT technique. In both of these figures, secondary dendrite arm spacing measurements from each analysis region are

described by colored squares; the color of the square represents the value of the secondary dendrite arm spacing. White regions represent analysis regions where secondary dendrite arm spacing was unmeasurable using these techniques.

A trend is evident in the secondary dendrite arm spacing data acquired from the peak-counting technique; measurements are smaller along the sides of the ingot compared to its center. This trend is not observed in the data acquired from the FFT technique. It is suspected that the FFT technique does not demonstrate the resolution necessary to observe this trend.

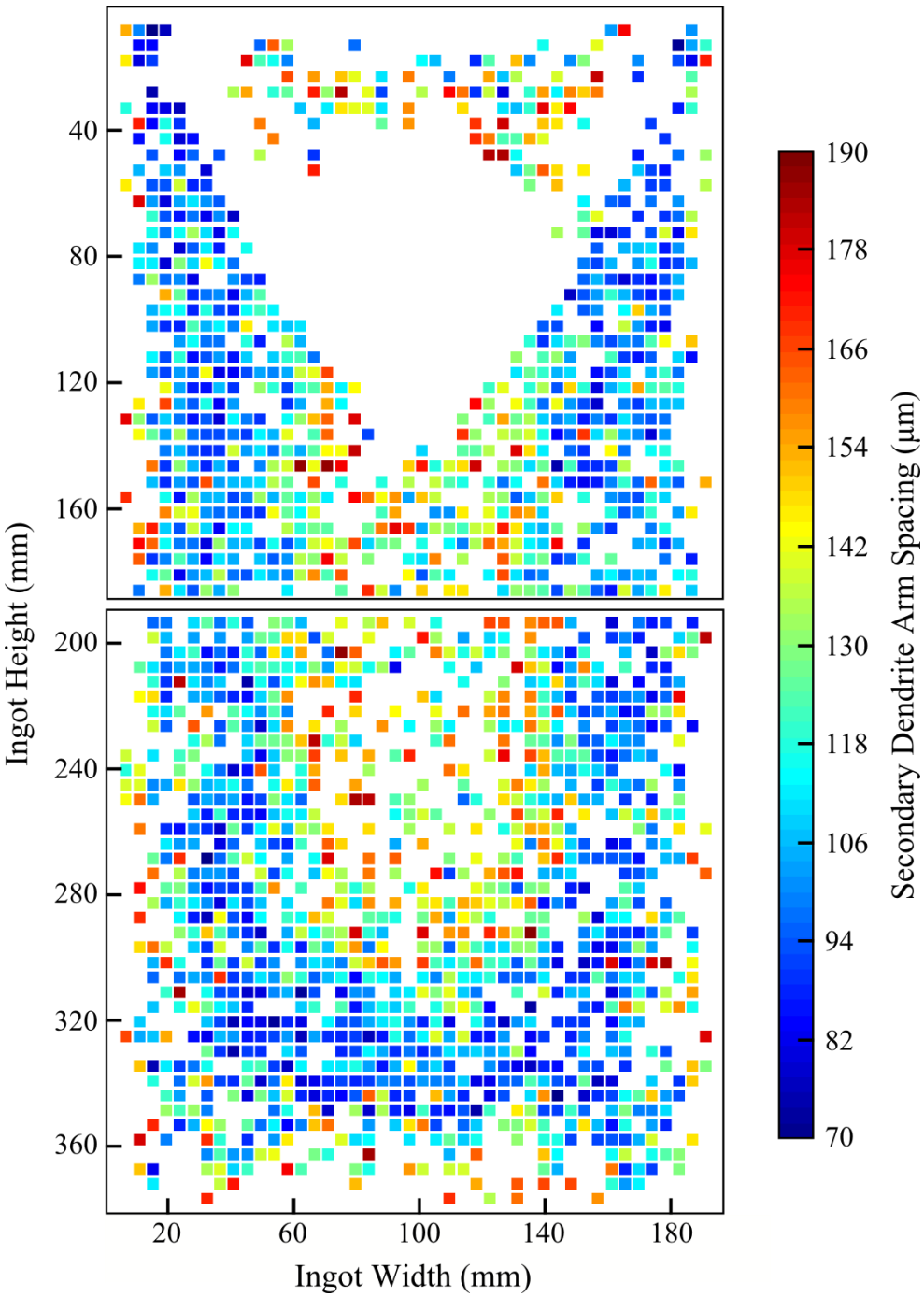

Figure 8.8: Secondary dendrite arm spacing measured from each analysis region in the VAR ingot is presented. Measurements were completed using the peak-counting technique for the two-point correlation function analysis. The color of each analysis region represents the value of the secondary dendrite arm spacing.

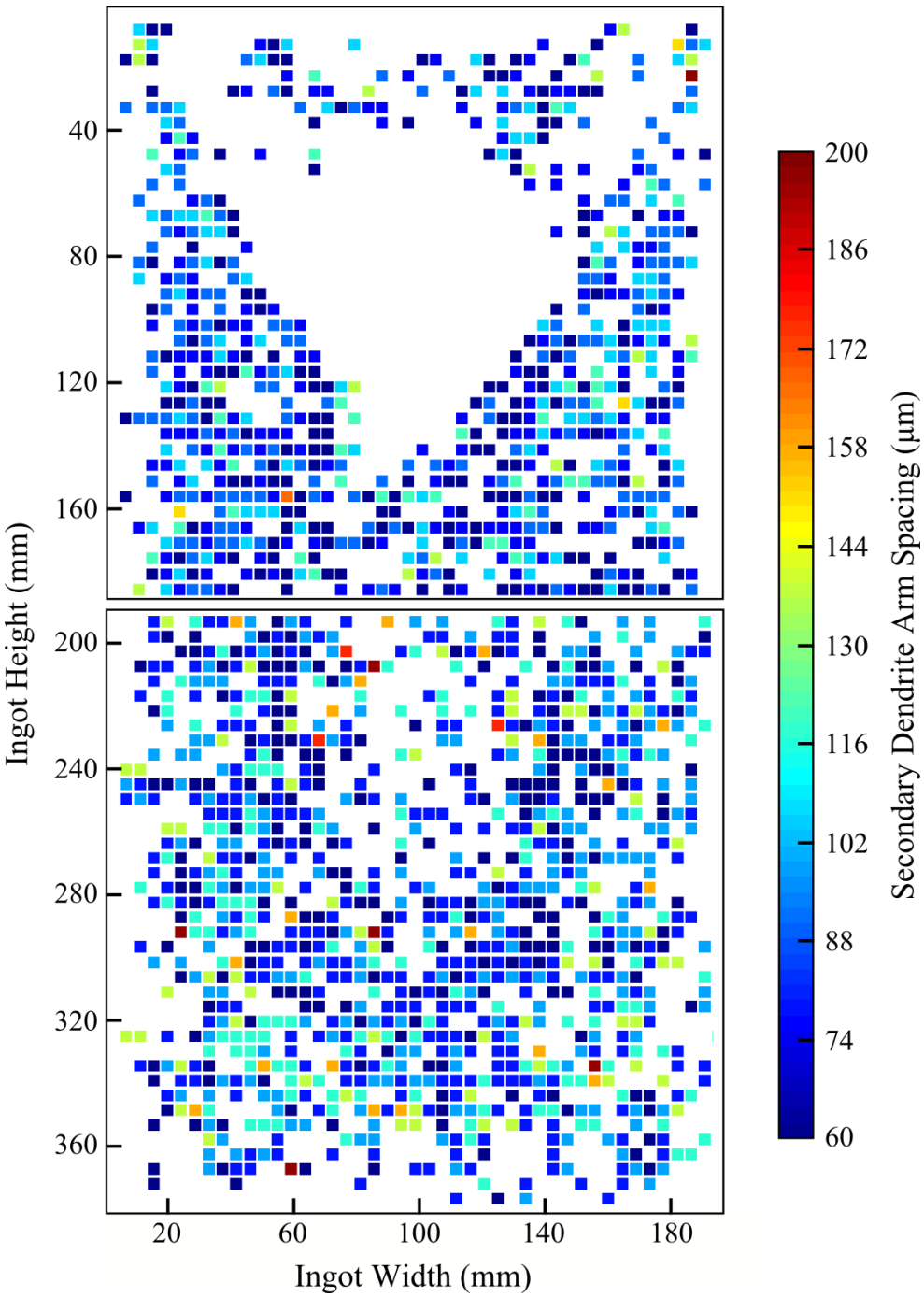

Figure 8.9: Secondary dendrite arm spacing measured from each analysis region in the VAR ingot is presented. Measurements were completed using the FFT technique for the two-point correlation function analysis. The color of each analysis region represents the value of the secondary dendrite arm spacing.

9. RESULTS FROM THE ESR INGOTS

9.1. PARTICLE IDENTIFICATION

All of the industrial ESR ingots provided for this dissertation were analyzed using the particle identification methodology. Unfortunately, not all of the results produced from these ingots can be presented in this dissertation. However, two examples are provided to demonstrate how some of the data produced was used by industry to develop computational process models for remelting. Figure 9.1 and Figure 9.2 demonstrate the comparison between measured primary dendrite arm orientations and those predicted through simulations of remelting. These figures were originally published in "Industrial-Scale Validation of a Transient Computational Model for Electro-Slag Remelting" from the *Liquid Metal Processing and Casting Conference 2017* [50] and are reproduced in this dissertation with permission.

Figure 9.1 and Figure 9.2 present the primary dendrite arm orientations measured from the ingots supplied by the Carpenter Technology Corporation and the Special Metals Corporation, respectively [50]. These measurements were acquired from the three-quarter radius or thickness position in both ingots. For both figures, the average primary dendrite arm orientation was calculated using a moving median, shown in blue, and the primary dendrite arm orientations predicted through simulation are shown in red. The moving median was used to reduce the influence of outliers in the primary dendrite arm orientation data. The moving median calculates the median value of the primary dendrite arm orientation using data from approximately the three-quarter radius position with a small window along the ingot length. The window is moved along the ingot length, and a median value is calculated at each position along that path. The predicted primary dendrite arm orientations were acquired using MeltFlow-ESR^{TM}; a commercially available two-

dimensional and transient model for ESR. The predictions for primary dendrite arm orientation were taken at a 0.95 liquid fraction.

These figures demonstrate a good agreement between prediction and measurement in both ingots; similar trends are observed in the predicted and measured primary dendrite arm orientations along the normalized ingot length. However, the predicted values for primary dendrite arm orientation are consistently larger than measurement in both ingots. Changes to the primary dendrite arm orientation appear at locations where steady-state changes to the melt rate occurred.

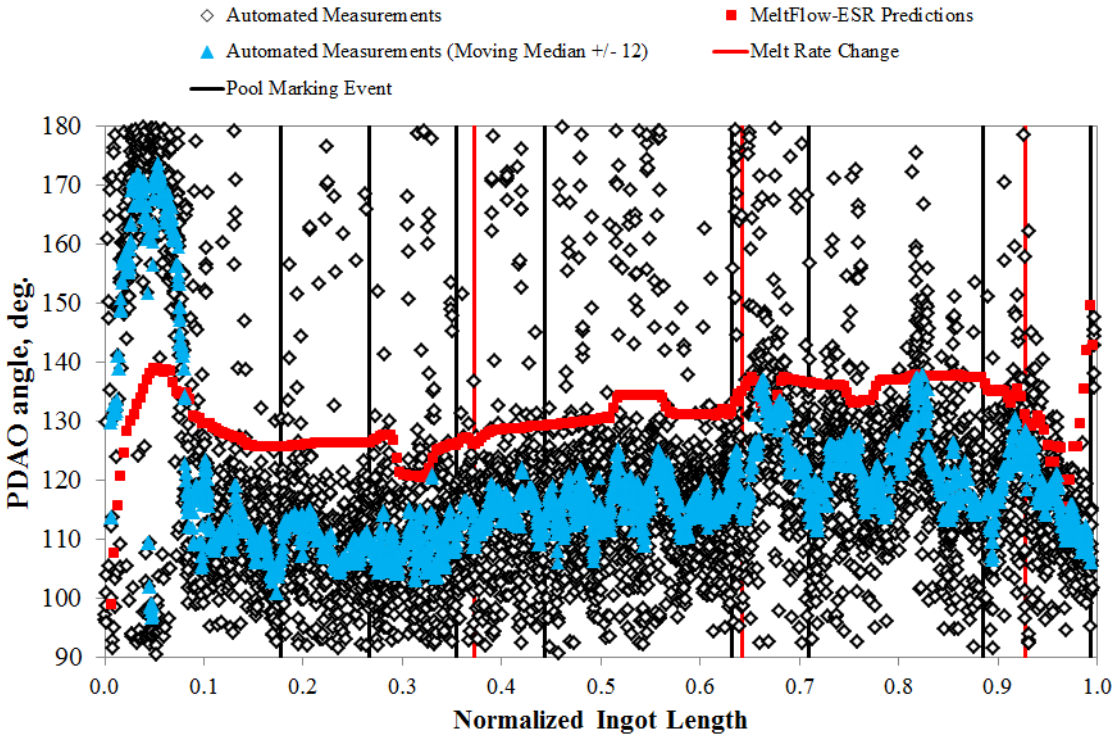

Figure 9.1: Primary dendrite arm orientations from the Carpenter Technology Corporation ingot are presented. These measurements were acquired from the 0.75 radius position using particle identification. Predicted primary dendrite arm orientations are shown for comparison. This figure was originally published in "Industrial-Scale Validation of a Transient Computational Model for Electro-Slag Remelting" from the *Liquid Metal Processing and Casting Conference 2017* [50] and is reproduced in this dissertation with permission.

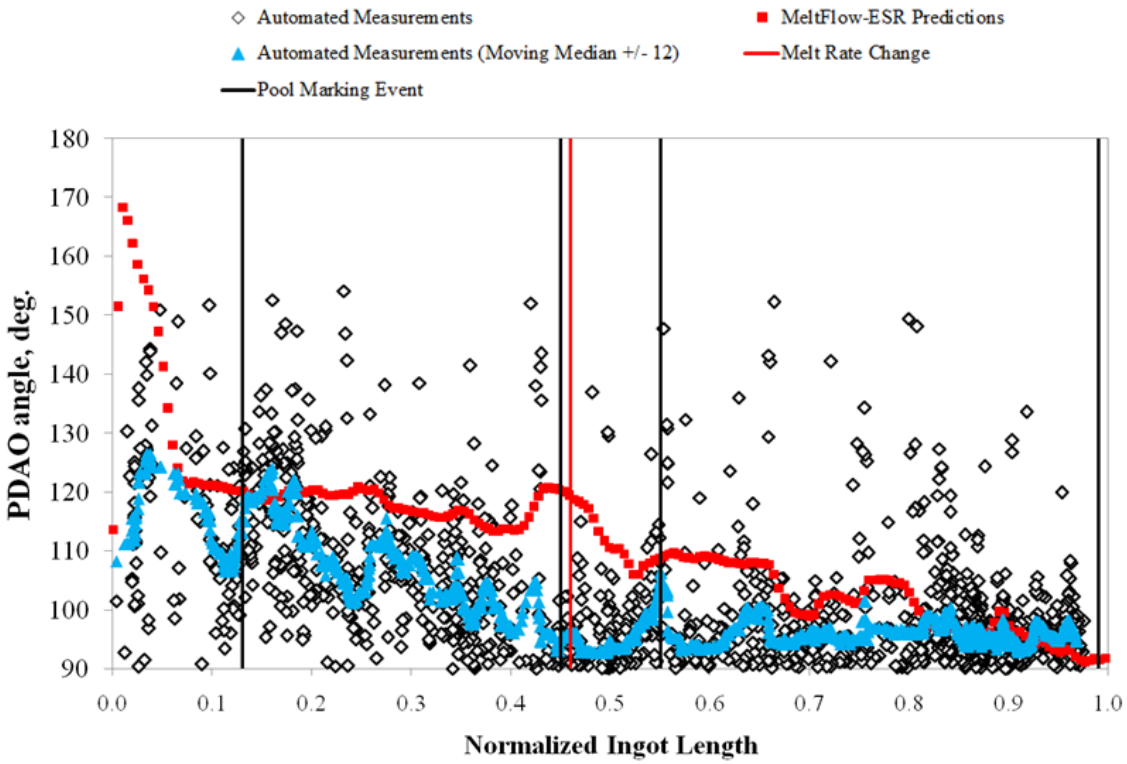

Figure 9.2: Primary dendrite arm orientations from the Special Metals Corporation ingot are presented. These measurements were acquired from the 0.75 thickness position using particle identification. Predicted primary dendrite arm orientations are shown for comparison. This figure was originally published in "Industrial-Scale Validation of a Transient Computational Model for Electro-Slag Remelting" from the *Liquid Metal Processing and Casting Conference 2017* [50] and is reproduced in this dissertation with permission.

Secondary dendrite arm spacing measurements were also used by industry to verify simulation predictions. Table 9.1 presents average secondary dendrite arm spacing measurements from the ingot supplied by the Carpenter Technology Corporation at three different melt rates. This data was originally published in "Industrial-Scale Validation of a Transient Computational Model for Electro-Slag Remelting" from the *Liquid Metal Processing and Casting Conference 2017* [50]. Measurements were acquired from both

manual and automated techniques along the ingot centerline. Predictions of secondary dendrite arm spacing along the ingot centerline are also presented in Table 9.1 at the different melt rates. Predictions were from MeltFlow-ESR™.

For each melt rate, manual measurements for secondary dendrite arm spacing were larger than those acquired using the automated analysis. The reasons for this disparity are not clear. The predicted measurements typically fell within the uncertainty of the automated and manual measurements. Though, both measurement techniques exhibit a large uncertainty. The simulations predicted a slight decrease in secondary dendrite arm spacing with decreasing melt rate. The opposite was generally observed for the manual and automated measurements.

Table 9.1: The secondary dendrite arm spacing measurements from the ingot supplied by the Carpenter Technology Corporation are provided. Data was acquired manually, from automated particle identification, and from simulations. Measurements were acquired from the centerline of the ingot. This table is after that previously published in "Industrial-Scale Validation of a Transient Computational Model for Electro-Slag Remelting" from the *Liquid Metal Processing and Casting Conference 2017* [50].

Melt Rate (lbs/hr)	Manual Measurements (μm)		Automated Measurements (μm)		Simulation (μm)
	Average	St. Dev.	Average	St. Dev.	Predicted
850	123	30	104	18	146
725	135	32	128	22	140
600	157	34	128	22	139

10. DISCUSSION

10.1. PARTICLE IDENTIFICATION

Figure 10.1 presents the primary dendrite arms determined using particle identification, the associated melt pool profile estimates, and the electrode current during remelting for the VAR ingot as a function of ingot height. Figure 10.1 (a) demonstrates that primary dendrite arms were successfully identified throughout the VAR ingot, even from the equiaxed microstructural region. Fewer primary dendrite arms were identified in the equiaxed region compared to the sides of the ingot, where directional solidification occured. Primary dendrite arms in the equiaxed region are randomly oriented and often pass through the sectioning plane, instead of lying in that plane, preventing them from being identified. Along the sides of the ingot, a large fraction of primary dendrite arms lie approximately within the sectioning plane, making them readily identifiable. The primary dendrite arm orientations measured qualitatively agree with the expected heat flow during solidification. Few outliers are identified in the regions where directional solidification occurred. This suggests that the techniques developed to remove erroneously identified primary dendrite arms were successful. Furthermore, a sufficient number of primary dendrite arms were accurately identified throughout the VAR ingot to produce a meaningful analysis of the melt pool profile, despite this technique not utilizing all of the microstructural data available.

It is useful to compare the primary dendrite arm orientations and the melt pool profiles to the electrode current during remelting because the electrode current influences the melt pool profile. The melt pool profile is expected to change with the electrode current, particularly for a large change in current held over a significant time. Figure 10.1 (b) and (c) present the melt pool profile estimates and the electrode current during remelting for the VAR ingot, respectively. Figure 10.1 (c) illustrates that the electrode current was

approximately steady at 3,000 amps during this melt. Some abrupt spikes in the electrode current are observed, but no large step changes occurred. Because the electrode current was approximately steady throughout the melt, no significant change in melt pool profile is expected along the ingot height past the bottom region near the cooled stool upon which solidification began. Figure 10.1 (b) demonstrates that the estimated melt pool profiles qualitatively appear similar throughout the top portion of the ingot and noticeably change only near the bottom the ingot. This is expected because the bottom of the ingot experiences transient conditions associated with the start of the melt on the water-cooled stool.

The slope and depth of the melt pool were quantified in the left side of the VAR ingot. Figure 10.2 presents the primary dendrite arms identified, the estimated melt pool profiles, and the slope and depth of each melt pool profile as a function of ingot height on the left side of the VAR ingot. The slope and depth of each melt pool estimate were calculated from the highlighted region in Figure 10.2 (a). Analysis was limited to this region because it is mostly unaffected by the surface of the ingot and the equiaxed center of the ingot, where melt pool profile estimates are rather difficult. Slopes and depths were calculated using the end points of each melt pool profile estimate contained within the highlighted region of Figure 10.2 (a). Slopes were calculated by measuring the angle of a straight line drawn between the first and last points of each melt pool estimate contained within the highlighted region in Figure 10.2 (a). Depths were calculated from the difference in height between the first and last points of each melt pool estimate contained within the highlighted region in Figure 10.2 (a)

Figure 10.2 (b) and (c) demonstrate that the characteristics of the melt pool profile change slightly along the ingot height. The slope of the melt pool is steepest near the top and bottom of the ingot and shallowest in the center. The depth of the melt pool behaves similarly. The cause of these changes in the slope and depth of the melt pool along the

ingot height is unclear. That said, it is unlikely that these changes are related to changes in the electrode current during melting. They may have been created from transient conditions at the top and bottom of the ingot. Because this ingot is quite small, transient conditions affect a large portion of the ingot. These results reflect one method of measuring the slope and the depth of the melt pool profile estimates; different measures may produce slightly different results.

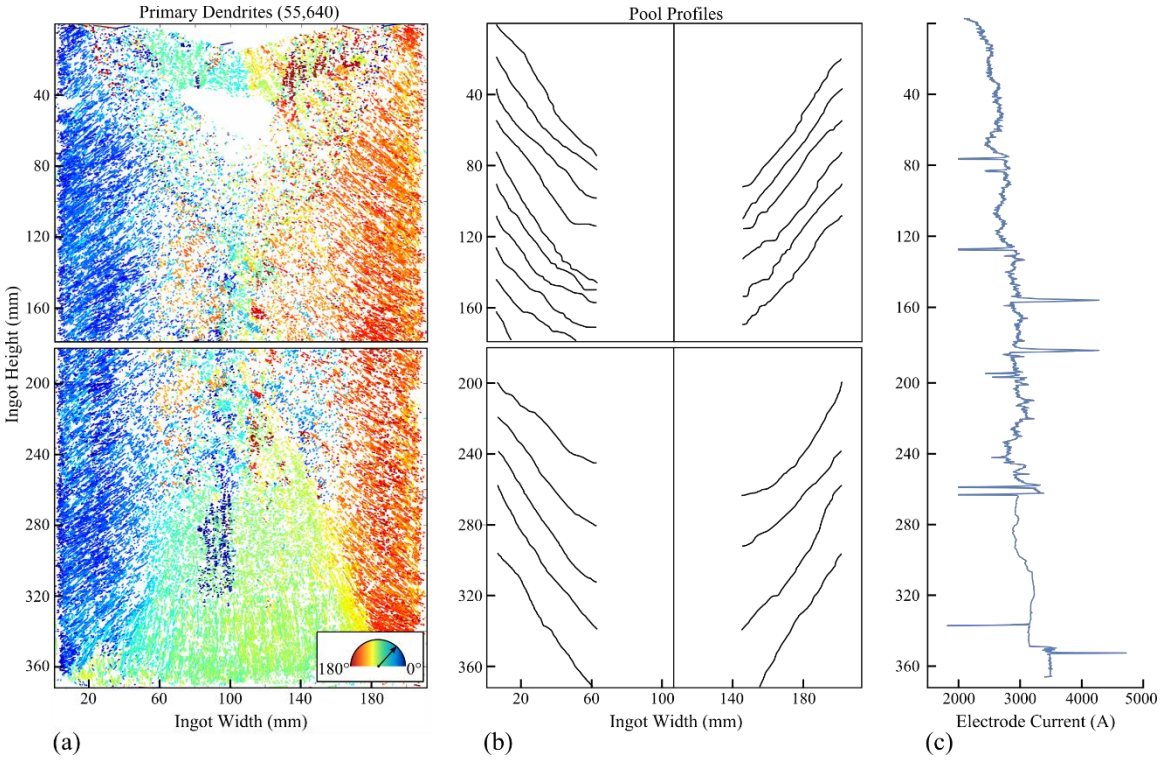

Figure 10.1: (a) The primary dendrite arms identified from the VAR ingot used to calculate (b) expected melt pool profiles from primary dendrite arm orientations are shown. These were calculated using particle identification. (c) The electrode current during melting is presented as a function of ingot height.

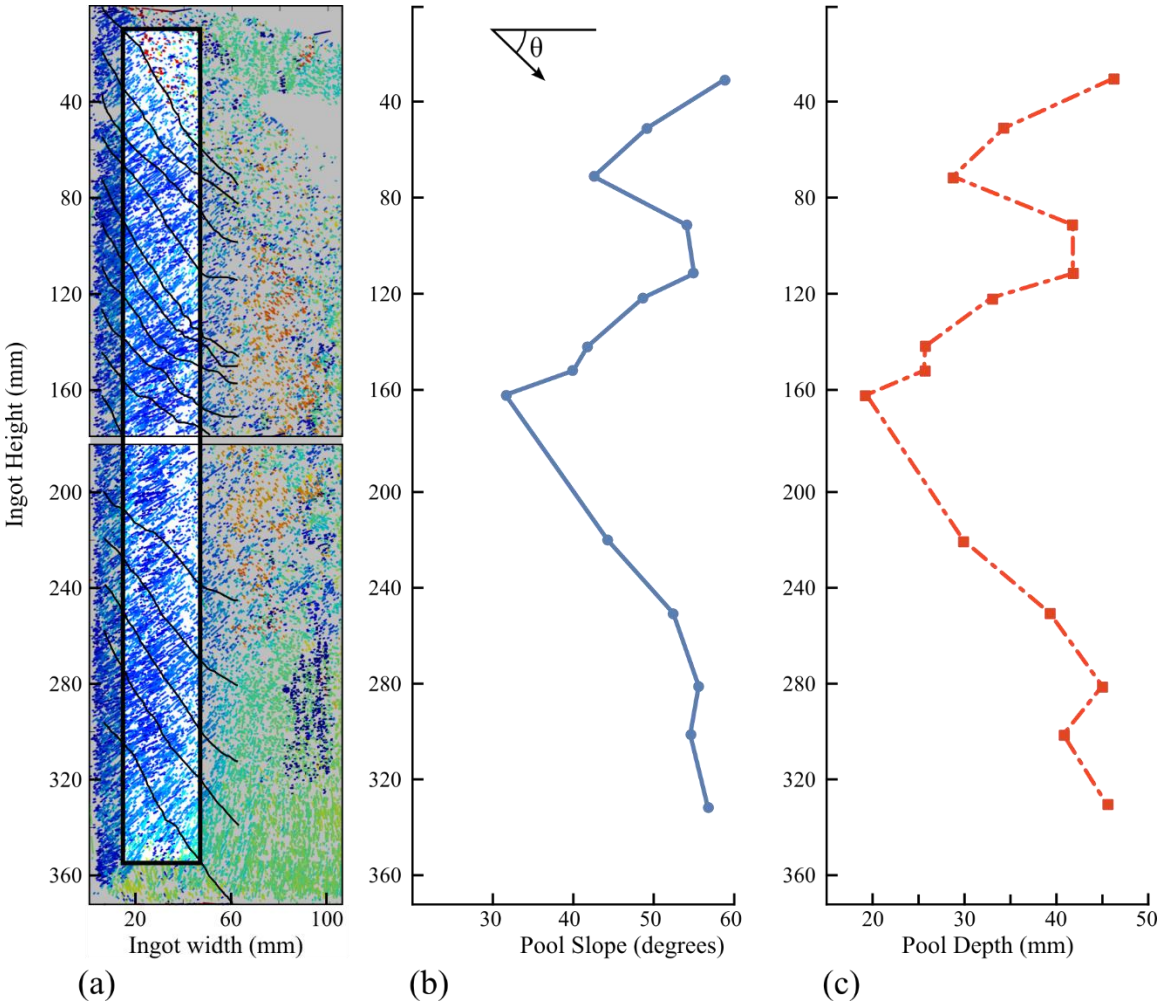

Figure 10.2: (a) Data from the left side of the VAR ingot is presented with (b) the slope of the melt pool and (c) the depth of the melt pool. These were calculated using particle identification. The highlighted region in (a) was used to calculate the slope and depth of the melt pool.

Secondary dendrite arm spacing measurements and local solidification times calculated from those measurements are provided in Figure 10.3. Local solidification times were calculated for the twelve 20 by 20 mm regions shown in Figure 10.3 (b). As mentioned previously, secondary dendrite arm spacing measurements varied significantly across the ingot. No obvious trends are apparent in the secondary dendrite arm spacing

data, as demonstrated by Figure 10.3 (a). Two plausible explanations for the lack of trends in secondary dendrite arm spacing values were identified. First, secondary dendrite arm spacing may indeed vary indiscriminately throughout the ingot. Second, the automated measurement technique may lack the sensitivity and robustness necessary to reveal any trends in this data. For example, if an identified particle is not precisely aligned with its primary dendrite arm, the secondary dendrite arm spacing measurement will be adversely affected. This often leads to a slightly larger secondary dendrite arm spacing measurement because some secondary arms are missed. These effects may lead to measurement uncertainties larger than the changes in secondary dendrite arm spacing between locations within the ingot, thus masking possible trends.

Solidification times, presented in Figure 10.3 (b), were calculated from secondary dendrite arm spacing measurements using Equation 1. Calculated solidification times are longest on the left side of the ingot and decrease toward the right side of the ingot. There is no clear explanation for this result, which is likely non-physical. It is probably an artifact of the large uncertainty associated with the automated secondary dendrite arm spacing measurements. It will be shown that the two-point correlation technique provides superior predictions.

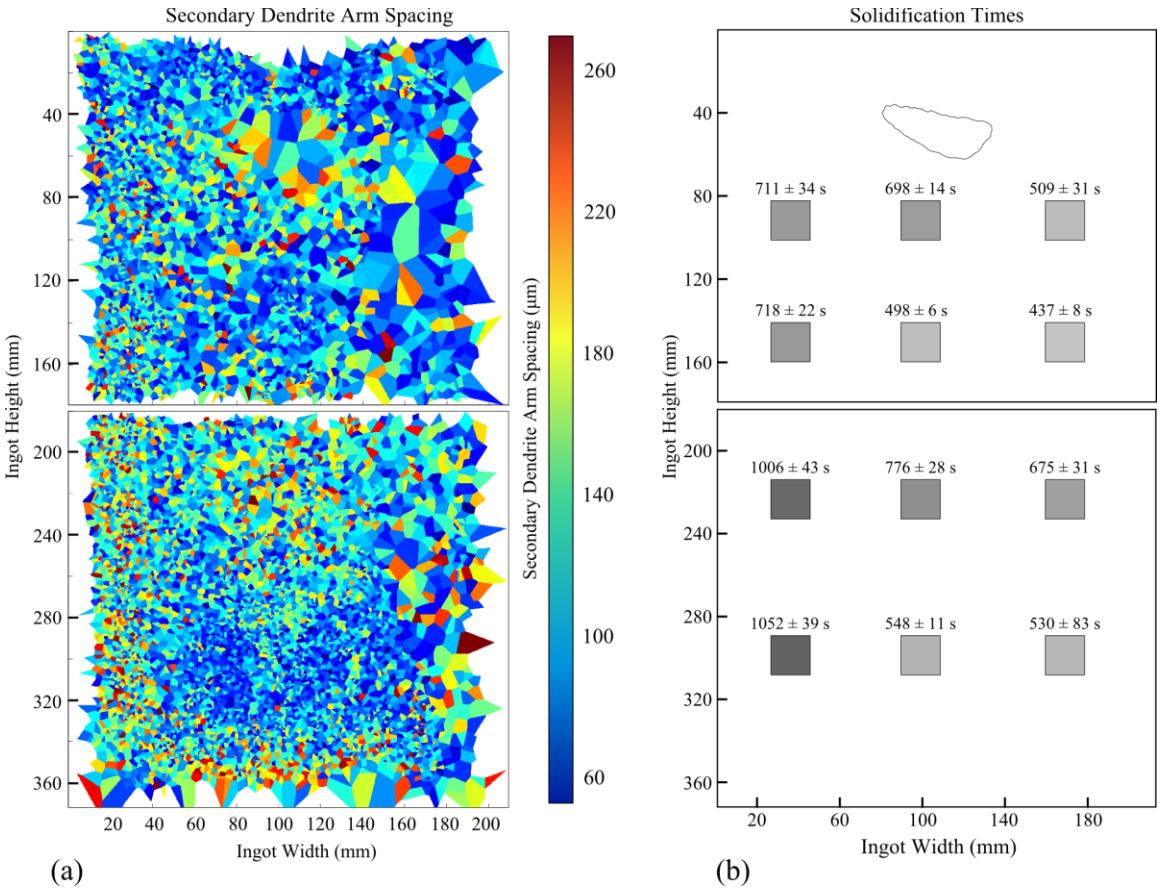

Figure 10.3: (a) Secondary dendrite arm spacing measurements from the VAR ingot are presented as a Voronoi diagram, and (b) calculated solidification times from select regions within the VAR ingot are presented. These were calculated using particle identification.

10.2. Two-point Correlation Function and Fourier Analyses

Primary dendrite arm orientations calculated from the two-point correlation technique, the associated melt pool profile estimates, and the electrode current during remelting are presented in Figure 10.4. Figure 10.4 (a) demonstrates that primary dendrite arm orientations were successfully measured throughout most of the VAR ingot. Similar to the particle identification method, three regions, each with a consistent primary dendrite

arm orientation, are identified along the left, right, and bottom of the ingot, where directional solidification occurred. The primary dendrite arm orientations in these regions are aligned with the expected heat flow during solidification. The regions of consistent primary dendrite arm orientations penetrate significantly into the ingot, almost reaching its center. Figure 10.4 (a) demonstrates that this analysis technique can detect primary dendrite arm orientations from directionally solidified microstructures, even those with weakly defined orientations near the center of the ingot. This analysis technique, however, was limited in the middle of the top slab, where primary dendrite arm orientations were not measured. Analysis failed in this equiaxed microstructural region because no preferred primary dendrite arm orientation exists.

The melt pool profile estimates are presented in Figure 10.4 (b). The melt pool profile estimates appear reasonable and exhibit a definitive change in shape from the top to the bottom of the ingot. Figure 10.4 (b) illustrates that the melt pool is "V-shaped" near the top of the ingot and flattens toward the bottom of the ingot into a "U-shape." It is not expected that this profile change was caused by fluctuations in the electrode current, but rather it is a consequence of the short height of the ingot. The transient region at the bottom of the ingot, associated with the start of the melt, alters the melt pool profile along the ingot height. Though the shape of the melt pool profile changes along the ingot height, the slope of the melt pool along the sides of the ingot does not. The slope of the melt pool was quantitatively analyzed in the left side of the VAR ingot to measure any change along the ingot height. Figure 10.5 presents the melt pool profile estimates and the measured melt pool profile slopes along the left side of the VAR ingot. The melt pool profile slopes were measured from the highlighted regions in Figure 10.5 (b). The means and standard deviations of these measurements are provided in Figure 10.5 (c) and (d). These figures illustrate that the slope of the melt pool profile remains effectively constant along the ingot

height, even toward the bottom of the ingot, near the water-cooled stool. This result suggests that the variation in the slope of the melt pool profile with height determined using the particle identification technique, as shown in Figure 10.2 (b), is a result of measurement uncertainty.

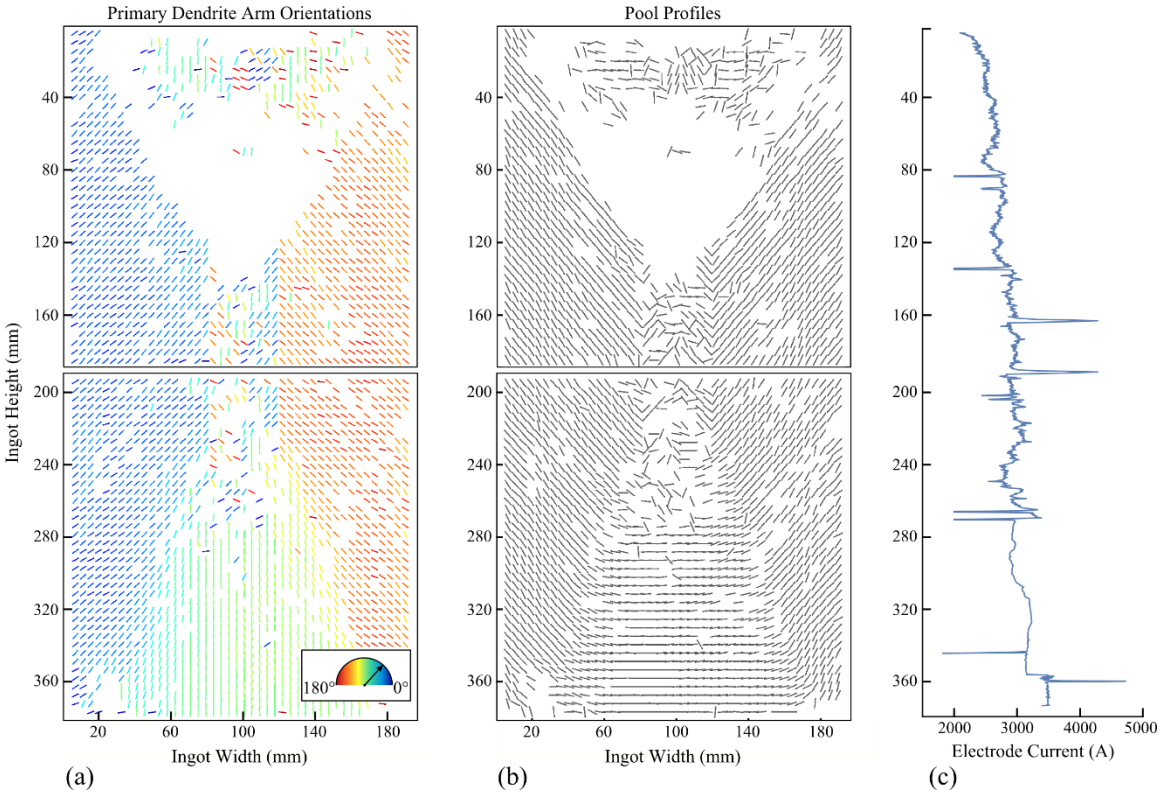

Figure 10.4: (a) The primary dendrite arm orientations used to calculate (b) expected melt pool profiles are presented. These were calculated from the two-point correlation technique. (c) The electrode current during melting is presented as a function of ingot height.

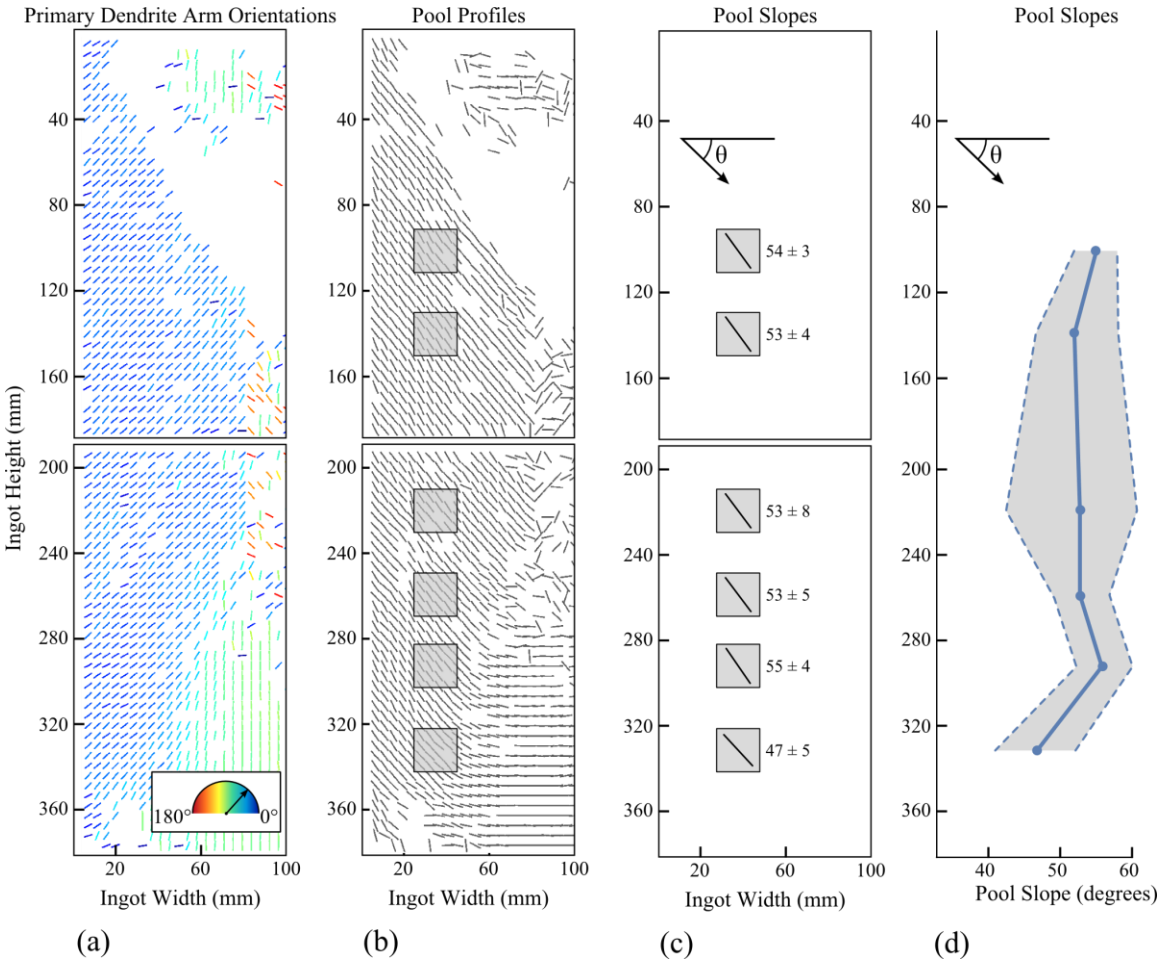

Figure 10.5: (a) Primary dendrite arm orientations from the two-point correlation technique, (b) melt pool profile estimates, and (c and d) the slope of the melt pool from the left side of the VAR ingot are presented. The melt pool slopes were calculated from the highlighted regions in (b).

Secondary dendrite arm spacing measurements acquired from the VAR ingot using the peak-counting technique for the two-point correlation function are presented in Figure 10.6. Secondary dendrite arm spacing measurements are presented in Figure 10.6 (a) using colored squares. The color of each square represents the value of the secondary dendrite arm spacing. Figure 10.6 (b) presents the means and standard deviations

of the secondary dendrite arm spacings calculated from the highlighted regions in Figure 10.6 (a).

A trend in the secondary dendrite arm spacing data is evident in Figure 10.6 (a). Spacing values are smaller along the sides of the ingot and larger in the center. Spacings are also symmetric about the vertical ingot centerline. This is supported by the measurements provided in Figure 10.6 (b). Because the VAR ingot cools more slowly at its center compared to its sides, secondary dendrite arm spacings are expected to be larger in the center. That said, because this secondary dendrite arm spacing measurement technique relies on an accurate measure of primary dendrite arm orientation, results may be misleading if that orientation is not accurately established. The uncertainty potentially introduced by this effect could not be quantified for this investigation. Solidification times were calculated from the secondary dendrite arm spacing data presented in Figure 10.6 (b). These calculated solidification times are provided in Table 10.1.

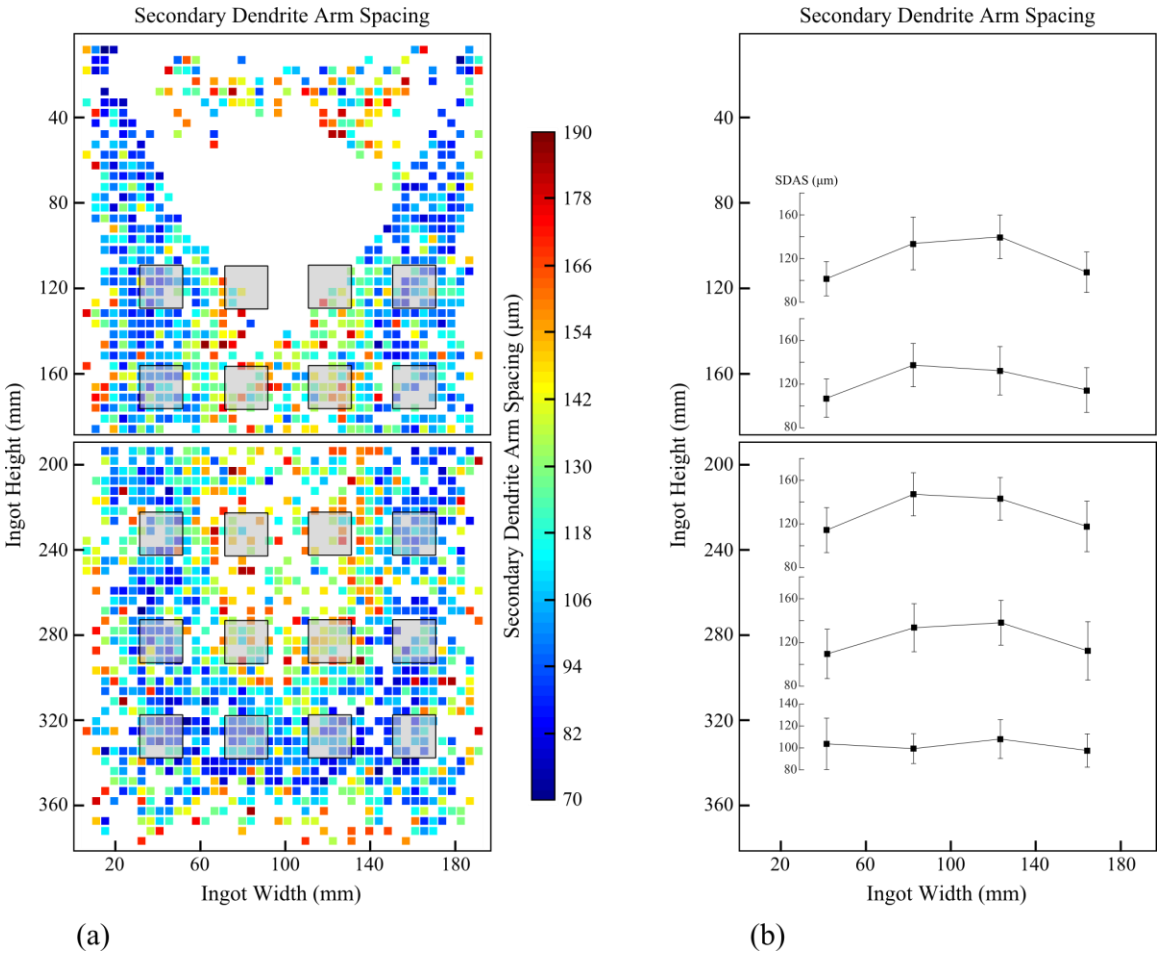

Figure 10.6: (a) Secondary dendrite arm spacings from the VAR ingot measured using the peak counting technique for the two-point correlation function are presented. (b) The means and standard deviations of secondary dendrite arm spacings measured from the highlighted regions in (a) are presented.

Table 10.1: Solidification times and secondary dendrite arm spacing measurements calculated from two-point correlation function analysis of the VAR ingot are presented. The position of each measurement is provided in distance from the top and left sides of the ingot.

Position (mm)		Secondary Dendrite Arm Spacing (μm)		Solidification Time (s)
Radial from left of ingot	Height from top of ingot	Mean	St. Dev.	Mean
40	120	101	16	306
	170	107	18	360
	230	114	21	437
	285	109	23	384
	330	103	24	325
80	120	133	24	700
	170	137	20	757
	230	147	20	931
	285	133	22	695
	330	99	14	286
120	120	139	20	801
	170	132	22	676
	230	143	20	855
	285	138	20	769
	330	108	18	368
160	120	107	19	363
	170	114	20	439
	230	117	23	476
	285	112	27	414
	330	98	15	272

10.3. Analysis Technique Comparison

Both the particle identification and the two-point correlation techniques demonstrated an ability to accurately measure primary dendrite arm orientations from the VAR ingot in regions of directional solidification. The particle detection technique was

able to identify some orientations in the equiaxed region where two-point correlation function analysis failed. The data averaging provided by the two-point correlation function produces measurements of mean primary dendrite arm orientation that are more easily interpreted and appear more consistent throughout the ingot than results of particle identification. Compare Figure 10.1 (a) and Figure 10.4 (a), for example.

Melt pool profiles were estimated throughout the VAR ingot from the primary dendrite arm orientation data acquired using both analysis techniques. The profile estimates differ slightly between the techniques. A change in shape of the melt pool with vertical position in the ingot is evident from the two-point correlation technique but is difficult to discern using the particle identification technique, as demonstrated by Figure 10.1 (b) and Figure 10.4 (b). Little change to the shape of the melt pool is detected from the particle identification technique, while the two-point correlation function technique demonstrates a clear change in melt pool profile from a "V-shape" to a "U-shape." The slopes of the melt pool profiles measured from the left side of the VAR ingot are similar for both techniques. Figure 10.2 and Figure 10.5 present an average slope of approximately 55 degrees. Much more local variation in the slope is evident from the particle identification technique than the two-point correlation technique.

Secondary dendrite arm spacing was successfully measured throughout the VAR ingot using both techniques. Spacing values acquired from the particle identification technique varied indiscriminatingly across the ingot, and no obvious trends in the data were observed. In contrast, the spacing data acquired from the two-point correlation function technique demonstrates an obvious trend. Figure 10.6 illustrates that secondary dendrite arm spacing is smaller at the sides of the ingot compared to the center. Both techniques present measurements with large uncertainties.

11. CONCLUSIONS

Solidification history was successfully reconstructed using microstructural data acquired from a laboratory-scale vacuum-arc remelted (VAR) alloy 718 ingot. Three industrial-scale electro-slag remelted (ESR) alloy 718 ingots were also successfully characterized. Melt pool profiles were estimated from primary dendrite arm orientations, and local solidification times were calculated from secondary dendrite arm spacings.

Solidification microstructures were imaged from alloy 718 cross-sectional slabs using automated macrophotography. New instrumentation was designed, constructed, and implemented to accomplish this. Montage images of each slab were then created using digital image stitching. These montage images exhibit a resolution of 9 μm per pixel, which is sufficient to resolve individual secondary dendrite arms within slab microstructures.

Microstructures were analyzed from the montage images using two techniques: particle identification and two-point correlation function analysis. The particle identification technique accurately identified primary dendrite arms as individual particles, enabling the measurement of primary dendrite arm orientations and secondary dendrite arm spacings. Primary dendrite arm orientation was measured from the geometry and positon of each particle, i.e. primary dendrite. Secondary dendrite arm spacing was measured from the change in image intensity along lines running parallel and directly adjacent to identified primary dendrite arms. Some particles that likely represent primary dendrites are missed by the identification algorithm, but a sufficient number are detected to estimate melt pool profiles.

A two-point correlation function algorithm was used to detect the orientations of primary dendrite arms and the spacing between secondary dendrite arms in the montage images. This technique generated statistically meaningful arrays representing

microstructure. Fourier analysis was then used to analyze these arrays and measure primary dendrite arm orientation and secondary dendrite arm spacing. However, applying a peak-counting technique to the original two-point correlation array was used to produce a more accurate measure of secondary dendrite arm spacing, once primary dendrite arm orientation was determined. Melt pool profiles were estimated from the measured primary dendrite arm orientations, and local solidification rates were calculated from the secondary dendrite arm spacings.

Melt pool profiles were estimated from the primary dendrite arm orientation data acquired using both analysis techniques. The profile estimates from the VAR ingot using both techniques were reasonable, but differed slightly. Little change to the shape of the melt pool with height was detected from the particle identification technique, while the two-point correlation function technique demonstrated a clear change in melt pool profile from a "V-shape" to a "U-shape" along the ingot height from top to bottom. Much more local variation in the melt pool profile was suggested by the particle identification technique than the two-point correlation technique.

Secondary dendrite arm spacings, and thus local solidification times, were successfully measured using both techniques. Spacing values acquired from the particle identification technique varied randomly across the VAR ingot, and no obvious trends in the data were observed. The random variation and lack of any clear trends are the result of measurement uncertainty associated with this technique. Spacing data acquired from the two-point correlation function technique demonstrated that secondary dendrite arm spacing is smaller at the sides of the ingot compared to the center, as expected.

This dissertation produced the following contributions to science and technology:

1) The techniques developed are the first to enable autonomous characterization of microstructural features continuously throughout an entire industrial-scale ingot.

Melt pool profiles and solidification rates can now be continuously measured throughout an ingot using specifically prepared cross-sectional slabs.

2) The techniques developed provide a new means to improve understanding of remelting processes and the solidification microstructures remelting produces.
3) The techniques developed in this dissertation provide data directly to industry for validation of new computational models of remelting.

12. FUTURE WORK

In this study, individual macrophotographs of the alloy 718 slab microstructures were acquired at a resolution of approximately 4.5 μm per pixel, but could not be stitched at this resolution to create montage images because of software limitations. Creating montage images at the full 4.5 μm per pixel resolution may improve subsequent analyses. A higher resolution may remove image artifacts created by stitching and may improve fine feature detection during analysis. Microsoft Image Composite Editor (MS ICE) is a software program potentially capable of creating new montage images. The use of this software package for image stitching in the future is recommended.

Several improvements to the two-point correlation function and Fourier analyses can be made. Primary dendritic arm orientations detected using Fourier analysis of two-point correlation function outputs might be measured more accurately if fitting techniques are improved. It is recommended that the use of other fitting routines be explored.

Analysis of the data produced by the two-point correlation function might be improved by including uncertainties calculated for primary dendrite arm orientations. For example, only one primary dendrite arm orientation is presented for each analysis region, yet in some instances, multiple orientations were detected. It is recommended to use this information in more detailed analyses of the melt pool profile.

Particle identification and two-point correlation function analysis can be used in tandem to potentially improve microstructural characterization. For example, it may be useful to inspect regions from the two-point correlation function analysis where no primary dendrite arm information was identified using particle identification. This might reduce the number of regions where no useful data is acquired.

Chemical segregation throughout slabs can be characterized using X-ray fluorescence (XRF) analysis. This chemical segregation information might then be correlated with microstructures identified using the particle or two-point correlation analysis techniques. If regions of poor chemical homogeneity are associated with specific microstructures, they might be identified from microstructure alone.

The techniques developed in this dissertation could be adapted to analyze other cast materials, as long as the material exhibits dendritic solidification.

APPENDIX A: IMAGING INSTRUMENTATION

IMAGING INSTRUMENTATION

Macrophotography was performed with a custom built linear XY stage and a Canon™ EOS 60D camera equipped with a Sigma 105mm F2.8 EX DG OS HSM macro lens. Custom software was used to control the linear motion of the XY stage and control camera functions. A list of the optical imaging equipment is as follows:

1) Vibration isolated mounting table.
2) An XY stage mounted on an optical breadboard.
3) Camera and camera mounting/adjustment equipment.
4) Computer and hardware used for image acquisition and XY stage control.

The procedure used to prepare the imaging instrumentation is described in the following:

1) The XY stage is mounted to an optical breadboard which is positioned on the vibration isolated mounting table.

2) The camera is mounted to the XY stage with a ball-head mount and a macro focusing rail. The ball mount allows the camera to be adjusted so that the lens is level relative to the surface of the optical table. Leveling was manually completed with a leveling fixture. The fixture consists of an aluminum tube machined flat at both ends and an aluminum plate machined to have two flat faces and fit to end of the tube. In order to level the lens with the specimen, the tube and cap assembly is placed on the surface of the optical table and the ball-head mount and camera height are adjusted so that the lens is flush with the flat surface of the aluminum plate. The camera is then secured in place. This ensures the lens remains level with the optical

table. After leveling, the height of the camera can be adjusted with the macro focusing rail to finely focus on a specimen at a set magnification.

3) Two stepper motors control the motion of the XY stage, one for each direction. Each motor is controlled with a stepper motor controller which is sent commands by a custom software package.

4) The custom software package controls the camera functions. This includes triggering, auto focusing, mirror-locking, and shutter movement. The custom software package records the location of the XY stage along with the date and time stamp immediately prior to capturing an image. Images are transferred to a computer and saved with the Canon™ Image acquisition software in the RAW ("*".CR2) format.

5) The camera is controlled through two inputs. One cable connects the mini-USB on the camera to the computer and one cable connects the remote shutter input on the camera to the custom software package. These cables are used to send signals to the camera and to transfer the image back to the computer to be stored.

After the imaging instrumentation was initially setup, automated imaging was performed. The autonomous image acquisition process used is described in the following:

1) Immediately prior to acquiring an image, the position of the XY stage (X, Y) and the date and time stamp are recorded in individual text files generated by the custom software package. The X and Y position is read from each stepper motor's controller. The position is given in number of steps (because the stage uses stepper

motors) away from a pre-defined home position. This home position corresponds to a XY stage position of (0, 0) and is defined by the user before imaging. The homing procedure and the home position was identical for each scan and will be described later. The position in steps is converted to position in millimeters with a conversion factor. The conversion factor was determined by measuring how far the stage traveled for a predetermined number of steps in the X and Y directions using a machinist's ruler with markings every 100^{th} of an inch. After imaging is completed, this data is combined into one text file title, "scan_#.txt", and is used to stitch the images together.

2) Once in position, the custom software is used to trigger the phase detection auto focus functionality of the camera. The focusing point is determined by the camera software. Phase detection auto focusing was necessary to account for small height variations across the imaging surface. Focusing is triggered through the remote shutter input on the camera.

3) After focusing, the custom software triggers the camera to lock the mirror in the up position. Mirror lock is triggered through the remote shutter input on the camera.

4) A 1.5 second hold time is programmed into the imaging procedure to allow for any vibrations created by the mirror locking motion to dissipate before the shutter on the camera is triggered with the custom software and a macrophotograph is taken. Lighting was supplied by two flash units mounted 60 cm away from the center of the specimen and 29 cm high on either side of the specimen. An exposure time of 1/250 seconds was used because it is the fastest possible speed at which the camera

can be synced with the strobes. Shutter movement is triggered through the remote shutter input on the camera.

5) The Canon™ imaging software records each image and saves it to a computer in the RAW format ("*".CR2). The camera is connected to the computer through the micro-USB input.

6) The custom software program sends commands to each stepper motor controller to move the camera to the next imaging location. The distance moved between pictures was pre-determined and hard-coded into the custom software so that an approximately 20% linear overlap between adjacent images occurred in both the X and Y directions. The number of images taken is predetermined by the user based upon the size of the specimen.

Photography settings used during this study:

Camera: Canon™ EOS 60D

Lens: 105mm macro lens with a circular polarizer

F-stop: 8

Exposure time: 1/250 seconds

ISO number: 100

Strobes: Paul C. Bluff AlienBees™ B400 Flash Unit

Strobe power: 3/8

The procedure used to prepare the alloy 718 slabs studied in this dissertation for imaging and the actual imaging procedure are described in the following:

1) Before imaging, specimens were cleaned with Seventh Generation™ Natural Dish Liquid and water. During cleaning, specimens were scrubbed with a stiff nylon brush, rinsed clean of any soap, and blown dry with clean dry air. After cleaning, specimens were moved to the optical imaging stage. Specimens were supported on the optical breadboard by three vibration isolating feet. Specimens were leveled with respect to the optical breadboard by adjusting the height of these feet. A small level was used to accomplish this. Note: The imaged surfaces were typically not completely flat, so the specimens were leveled as well as they could be.

2) The camera is mounted to the stage with a quick release latch. Before imaging the camera and lens are either leveled or verified to be level with respect to the optical breadboard before continuing. The Sigma 105 macro lens is set to 1:1 magnification and the camera is moved toward the center of the specimen with the XY stage for focusing. This was performed away from the edges of the specimen because they were typically less flat than the rest of the specimen. The specimen is brought into focus by adjusting the height of the camera with the macro focusing rail. The live view mode of the camera is used to determine when the specimen is in focus.

3) The home position (0, 0) for the camera with respect to the XY stage is defined by the user. Homing is completed by manually jogging the camera to the Northwest corner of the optical stage. Once there, two homing switches (one for the X direction and one for the Y direction) stop the movement of the motor. This position

is then defined as the home position in the custom software program. This homing procedure and location was used for all imaging.

4) The area to be scanned is determined by the user and programmed into the custom software program. During scanning, the image number, position of the camera (X, Y), and the date and time are recorded into individual text files and then combined into one text file. This information, combined with the home position, allows the user to easily locate and identify where an image is located in the specimen.

After imaging, the magnification at each corner of the scan area is acquired. This is completed by photographing a machinist's ruler with markings every 100^{th} of an inch at each corner of the scan area. The values measured provide measurements of pixels/mm at each corner of the scan area. These are later averaged together to produce a conversion value in pixels/mm for the entire scan area.

APPENDIX B: PARTICLE IDENTIFICATION

PARTICLE IDENTIFICATION OVERVIEW

The digital montage images of the alloy 718 slabs imaged in this study were each rotated, cropped, and scaled prior to analysis. These operations were completed with the FIJI distribution of ImageJ and Matlab™ R2015a [70, 71]. Rotation and cropping ensure that the stitched images are properly aligned with respect to each other and remove the excess area around the edges of each image, which would confuse the analysis software. Files were all scaled to a consistent magnification of 110 pixels/mm, a magnification sufficient for software feature detection in this application, so that they could be combined into a single, representative image of the entire ingot.

A contrast limited adaptive histogram equalization (CLAHE) process was applied to each stitched image. This creates a uniform histogram with intensity ranging from 0 to 255 over the entire 8-bit grayscale image. This step improves conversion to a binary image format by equalizing unevenly lighted areas. The CLAHE processed image was then converted to a binary image, wherein the valleys created during etching, which represent inter-dendritic regions, are processed into black pixels and the higher areas, which represent dendrite arms, are lighter and processed into white. In this study, images were thresholded at a value of 127, on an 8-bit scale, so that pixels below this intensity value were converted to black and those above were converted to white. The binary conversion is necessary to transform the image data into a form that the FIJI particle detection software is capable of handling. This software locates and identifies areas of continuous white pixels and labels those areas as individual particles, thus the term particle detection, and ignores regions of continuous black pixels. Because software detection of features, i.e. particles, from the as-converted binary image is poor, the binary image is further processed using morphological operations that grow and shrink regions of like-colored pixels prior to

particle detection. Experiments determined that two erosion operations sufficiently separated the pixel regions that represent dendrites for software detection to operate adequately. Erosion operations shrink regions of continuous white colored pixels. The image adjustment operations used during this study are presented in the order that they were performed. Each operation was conducted with a Dell™ Precision T3600 with an 8-core Intel™ Xeon™ E5-1620 @ 3.60 GHz processor and 32.0 GB of DDR3 RAM running Windows™ 7 Enterprise.

Note that the following sections provide a detailed description of each step of the analysis process. A brief "How to do the analysis" section will be provided at the end of this appendix for quicker referencing once the details have been presented.

IMAGE ROTATION AND CROPPING

Stitched images are often slightly askew as a result of non-perfect alignment between the specimen and camera/XY stage during imaging. Consequently, the stitched images require rotating. The images are then cropped to contain only the plate after being rotated. The rotation angle is determined by manually measuring the skewness of the plate in reference to the straightest edge (always an edge from cutting the ingot up into plates) on the plate. Rotations are applied in Matlab™ R2015a and cropping was manually performed with the FIJI distribution of ImageJ [70, 71]. The rotation method is bilinear.

Software: Fiji packaged version of ImageJ with plugins (fiji.sc)

MATLAB™ R2015a

MATLAB™ scripts: Batch_rotate.m

SCALING

Stitched images are all scaled to a magnification of 110 pixels/mm prior to processing and particle analysis. This ensures that features from plate to plate are at the identical scale and that plates can be easily stitched together to form a whole ingot image file. A magnification of 110 pixels/mm was chosen because stitched images are initially at a magnification of ~114 pixels/mm and 110 pixels/mm is a convenient round number close to that value. The magnification factor was calculated from the conversion factor in pixels/mm from the "scan_#.txt" file. The resizing method is bilinear.

Software: MATLAB™ R2015a

MATLAB™ scripts: batch_resize.m

THRESHOLD AND MORPHOLOGICAL PROCESSING

The stitched images are converted to binary images. This creates an image of white colored particles, which represent primary and secondary dendrite arms, on a black background. After converting to black and white, a series of morphological operations are applied to the image. This attempts to separate the secondary dendrite arms from the primary dendrites. The threshold procedure converts stitched, corrected, and scaled 8-bit grayscale *.tiff images to black and white *.tiff images. Two processes were performed on each slab. Erosions remove pixels from the edges of regions of continuous white pixels.

Software: MATLAB™ R2015a

MATLAB™ scripts: thresh_erode2.m

PARTICLE IDENTIFICATION

Once morphological operations are complete, the "Analyze Particles" feature contained in the FIJI distribution of ImageJ [70] is used to identify individual particles. This feature locates and identifies areas of continuous white pixels and labels all of these objects as individual particles. Once a particle is identified, FIJI fits a bounding box and an ellipse to the particle. These fits are used to calculate the following information about each particle identified:

1) Area
2) Min gray level
3) Max gray level
4) Center of mass of the bounding box (X)
5) Center of mass of the bounding box (Y)
6) Brightness-weighted center of mass (X)
7) Brightness-weighted center of mass (Y)
8) Perimeter
9) Bounding box, upper left corner (X)
10) Bounding box, upper left corner (Y)
11) Bounding box width
12) Bounding box height
13) Fitted ellipse major axis length
14) Fitted ellipse minor axis length
15) Fitted ellipse major axis orientation
16) Circularity
17) Skewness
18) Kurtosis

19) Aspect ratio

20) Roundness

21) Solidity

This process identifies all regions of continuous white particles, whether they are primary dendrite arms, secondary dendrite arms, or simply objects within the equiaxed region. Various filtering techniques, described in the "Particle Analysis and Filtering" section, are used to remove particles not likely to represent primary dendrite arms.

Software: Fiji packaged version of ImageJ with plugins (fiji.sc)

MATLAB™ R2015a

MATLAB™ scripts: find_ROI_fiji_batch.m (calls fiji_roi.m) Note that this script uses the MIJI command. This command is used to call the FIJI distribution of ImageJ through MATLAB™.

PARTICLE ANALYSIS AND FILTERING

After each particle is identified, it is analyzed to see whether or not it is likely to represent a primary dendrite. Particles not likely to be a primary dendrite are filtered out by taking into account the size and shape of the particle. A particle may be filtered out for the following reasons:

1) Particles with an exceptionally small area can be removed. During this study, this filtering procedure was not deemed necessary, so a limit value of 0 pixels^2 was chosen.

2) Particles with low aspect ratios are removed. The aspect ratio is calculated by dividing the length of the major axis of the ellipse fitted to the particle by the length of the minor axis of the ellipse fitted to the particle.
3) A particle is removed if it is deemed too short or too long to represent a dendrite. This removes small image artifacts leftover from morphological processing and large artifact particles near the edges of the plate.
4) A particle is filtered if the standard deviation of relative image intensity is large across the particle. This is calculated by drawing a line on top of the particle using the bounding box fitted to that particle. Then the image intensity is measured along that line. If the standard deviation of the image intensity is large relative to the mean image intensity of the line, that particle is removed. This removes particles that do not correlate with the original image data.

In summary, the filtering options are:

1) Small area
2) Low aspect ratio
3) Short particle length
4) Excessively long particle length
5) Relative Standard Deviation of image intensity

The settings used in this study are:

1) Small area – 0 ($pixels^2$)
2) Low aspect ratio – 5 (minimum object aspect ratio)
3) Short particle length – 22 (minimum object length in pixels)
4) Excessively long particle length – 5000 (maximum length of PDA to use in pixels)

5) RSD – 0.5 (remove lines above this relative-STD threshold)

Software: MATLAB™ R2015a

MATLAB™ scripts: matlab_batch_pda.m (calls Ingot_pda.m and tile_data.m)

The matlab_batch_pda.m script generates an ingot_*.mat file that contains all of the particle information along with some image information. The file data contains the following:

```
Area: [n x 1 single]    % Area of each particle
Min: [n x 1 single]     % Min gray level
Max: [n x 1 single]     % Max gray level
X: [n x 1 single]       % Center of mass of the bounding box (X)
Y: [n x 1 single]       % Center of mass of the bounding box (Y)
XM: [n x 1 single]      % Brightness-weighted center of mass of the bounding box
                          (X)
YM: [n x 1 single]      % Brightness-weighted center of mass of the bounding box
                          (Y)
Perim: [n x 1 single]   % Perimeter of the bounding box
BX: [n x 1 single]      % X position of the lower left corner of the bounding box
BY: [n x 1 single]      % Y position of the upper left corner of the bounding box
Width: [n x 1 single]   % Width of the bounding box
Height: [n x 1 single]  % Height of the bounding box
Major: [n x 1 single]   % Major axis length of the ellipse
Minor: [n x 1 single]   % Minor axis length of the ellipse
Angle: [n x 1 single]   % Orientation of the major axis of the ellipse
```

Circ: [n x 1 single] % Circularity of the ellipse

Skew: [n x 1 single] % Skewness of the ellipse

Kurt: [n x 1 single] % Kurtosis of the ellipse

AR: [n x 1 single] % Aspect ratio of the ellipse

Round: [n x 1 single] % Roundness of the ellipse

Solid: [n x 1 single] % Solidity of the ellipse

ROI: [n x 1 double] % Region of interest number

origin: [X Y] % Origin of the first plate loaded by MATLAB™

size: [X Y] % Size of the image

ref_range: [n x n double] % Size of individual plate images

ref_img: {1 x n cell} % Individual plate image names

Length: [n x 1 single] % Primary dendrite arm length

PDA: [n x 1 single] % Primary dendrite arm location

PDA_colors: [1 0 0] % Default color to use when plotting

PDA_err: [n x 1 single] % RSD error for each PDA

scale: 0.0091 % scaling factor

scale_units: 'mm' % units

SDAS: [n x 1 single] % Secondary arm spacing for each PDA

SDAS1: [n x 1 single] % Port side SDAS only for each PDA

SDAS2: [n x 1 single] % Starboard side SDAS for each PDA

SDAS_err: [n x 1 single] % Standard deviation for each SDAS

SDAS1_err: [n x 1 single] % Standard deviation for each SDAS (port)

SDAS2_err: [n x 1 single] % Standard deviation for each SDAS (starboard)

SDAS_xy: [n x 2 single] % (X,Y) positions for each SDAS measurement.

SDAS1_xy: [n x 2 single] % (X,Y) positions for each SDAS measurement (port)

SDAS2_xy: [n x 2 single] % (X,Y) positions for each SDAS measurement (starboard)

SDAS1_offval: [n x 1 single] % offset value (port)

SDAS2_offval: [n x 1 single] % offset value (starboard)

This completes the procedure of identifying particles contained in individual stitched images. The following processing steps are used to combine the individual plate data sets into one large data set representing the whole ingot (optional), and further filtering to remove/correct for improper primary dendrite arm identification.

FILTERING

Two filters were used to either modify or remove a particle previously identified as primary dendrite arm based upon its relative orientation with the particles near it.

The first filter used corrects for secondary dendrite arms (SDAs) being misidentified as primary dendrite arms (PDAs). Because SDAs are expected to grow perpendicularly to PDAs, if a SDA is identified during particle detection it can be rotated by ±90 degrees to create a "virtual" PDA. A particle is determined to be a SDA if it is oriented between 70 to 110 degrees of the average primary dendrite arm orientation (PDAO) in a given area. This filter calculates the average PDAO for a rectangular region 1000 pixels wide (X direction) that spans the entire height of the ingot (Y direction). Any particle oriented within ±70 to ±110 degrees from the average PDAO calculated for the rectangular filtering region is rotated -90 degrees if it is located on the left side of the ingot

and +90 degrees if it is located on the right side of the ingot. This procedure essentially creates the "virtual" PDA from the identified SDA. The filter then moves the rectangular region of interest across the width of the ingot and repeats the procedure. During this study, the filter was simultaneously run from both the left and the right side of the ingot and stopped at the center of the ingot.

The second filter removes particles that are misoriented by at least two standard deviations from the mean particle orientation for a given region. During this study a circular area with a radius of 500 pixels was used. If a particle orientation inside the radius is more than two standard deviations from the mean particle orientation within the radius, it is removed. This filter helps reduce noise by removing particles that are poorly aligned with the other particles in its immediate vicinity. Because this filter uses the standard deviation of a given region to determine if a particle should be removed, it tends to filter out more objects from areas that have a well-defined particle orientation (mid-radius region) compared to areas that have a random distribution of orientations (the equiaxed region). This reduces noise in regions where primary dendrite arms are clearly identified without significantly affecting regions without a clear PDAO.

Software: MATLAB™ R2015a

MATLAB™ Scripts: Ingot_sweep_filter.m

Ingot_filter.m (Use the 'pdao' filter option)

AUTOMATED SECONDARY DENDRITE ARM SPACING MEASUREMENT

Once the primary dendrite arms have been identified and filtered to reduce noise, secondary dendrite arm spacings (SDAS) can be calculated. Secondary dendrite arms spacing is calculated in the following manner:

1) A single PDA is chosen for analysis
2) The 8-bit grayscale TIFF image data for the plate that PDA is located in is loaded into memory.
3) A line is drawn diagonally through the bounding box fitted to that PDA. This line represents the PDA core. Lines are drawn on either side and parallel to the PDA line. These are offset by 8 pixels from the PDA line in the direction perpendicular to the PDA line. These two lines are the port and starboard SDAS lines.
4) The image intensity profile along the length of each SDAS line is measured. Peaks in the image intensity profile represent a secondary dendrite. In this approach, the peaks are determined by using a local-maximum filter on the intensity profile: A window of a specified size is moved over the profile, and if the central pixel has the largest intensity within that window it is set as a local maximum. This is subject to the additional constraints that it must not have a value of zero, and that it must not be neighboring another maximum.
5) SDAS is calculated by determining the distance between peaks. The SDAS value is assigned to the geometric center of the primary dendrite arm.
    a. If only one peak is identified, no SDAS value is recorded
    b. If only two peaks are found, the SDAS value is the distance between the peaks. The error associated with that measurement is calculated from the uncertainty of locating the center of each peak.
    c. If more than two peaks are found, the SDAS value is the mean of the calculated distances between peaks. The error associated with that measurement is the standard deviation of the calculated distances between peaks.
6) The values are stored for that particular line offset, initially 8 pixels.

7) Steps 3 through 6 are performed again for line offsets of 10, 12, 14, and 16 pixels.
8) The SDAS values for each offset line are compared and the offset line with the smallest error in SDAS is retained, the rest are discarded.
9) The SDAS values are filtered to remove poor results. SDAS measurements with a large relative standard deviation value (>= 5) were discarded.

Software: MATLAB™ R2015a

MATLAB™ Scripts: Ingot_sdas.m (calls SDAS_calc.m, tile_data.m, and Ingot_sdas_Doff.m)

Two filters were applied to the automated SDAS measurements. The first filter is the same one used to filter primary dendrite arms based upon their orientation. For filtering SDAS measurements, it removes SDAS measurements that are two standard deviations away from the mean SDAS value for a given region. During this study a circular area with a radius of 500 pixels was used.

The second filter was used to remove SDAS measurements that were excessively large and not removed by the outlier filter. Occasionally groups of large SDAS measurements were found to clump together in small regions throughout the ingot. Often no more than a dozen small clumps were observed throughout the entire ingot. However, because they were clumped together the outlier filter was incapable of removing these values. This is because the outlier filter only examines a single circular region with a radius of 500 pixels at any given time. Because of this, a low-pass filter was implemented to remove these erroneous measurements. During this study SDAS measurements greater than 270 μm were removed.

HOW TO DO THE ANALYSIS

This section gives a brief outline on how to go from stitched images to processed images and how to produced data sets of identified primary dendrite arms that have been fully filtered. Lines denoted with % are comments. All other lines are either Matlab™ commands or calls to the Matlab™ scripts provided.

Software: Fiji packaged version of ImageJ with plugins (fiji.sc)

MATLAB™ R2015a

Commands and Scripts:

```
% Convert CLAHE images into binary -> save as proc_*.tif files
thresh_erode2;

% Particle analysis -> save as MAT files
% Make sure fiji_roi.m is in the path
find_ROI_fiji_batch;

% Run Ingot_pda on each MAT file and save as Ingot_*.mat
% Make sure tile_data.m and Ingot_pda.m are in the path
matlab_batch_pda;

% Set correct origin values for each Ingot_*.mat file
matlab_origins;

% Stitch all Ingot_*.mat files into a single Ingot file
% Don't do this if you just want to analyze one ingot at a time
Ingot_stitch;
Ingot = BigIngot;

% Apply conversion from pixels to mm
Ingot.scale = 9.09e-3; % this value is only for 110 px/mm

% Apply some book-keeping information
Ingot.scale_units = 'mm'; % unit length per pixel
Ingot.Angle = -Ingot.Angle;
```

```
% Save the PDA data set
save('Ingot0_baseline','Ingot');
Ingot_plot(Ingot,'pdarms');

% Apply the filters to the PDA data set
thresh = 1.0;
Ingot_sweep_filter; % Correct for SDA'S being identified as PDA's
Ingot_filter; % Remove outliers, make sure to use the pdao option
save('Ingot1_filter','Ingot');

% Measure SDAS
Ingot_sdas;
% Remove outliers and apply the low-pass filter. Use the sdas option
Ingot_filter;
```

REFERENCES

[1] R. C. Reed, The Superalloys Fundamentals and Applications, New York, NY: Cambridge University Press, 2006.

[2] M. J. Donachie and S. J. Donachie, Superalloys: A Technical Guide, 2nd ed., Materials Park, OH: ASM International, 2002.

[3] J. a. P. J. G. Beddoes, Introduction to Stainless Steels, Materials Park, OH: ASM International, 1999.

[4] H. M. Cobb, The History of Stainless Steel, Materials Park, OH: ASM International, 2010.

[5] G. W. Meetham, The Development of Gas Turbine Materials, New York: Halsted Press, a Division of John Wiley & Sons, Inc., 1981.

[6] J. S. Peter, The History of Aircraft Gas Turbine Engine Development in the United States...A Tradition of Excellence, Atlanta, GA: International Gas Turbine Institute of The American Society of Mechanical Engineers, 1999.

[7] B. H. Kear and H. G. F. Wilsdorf, "Dislocation Configurations in Plastically Deformed Cu3Au Alloys," *Trans. Metallurgical Society of AIME,* vol. 224, pp. 382 - 386, 1962.

[8] T. M. Pollock and S. Tin, "Nickel-Based Superalloys for Advanced Turbine Engines: Chemistry, Microstructure, and Properties," *J. Propulsion and Power,* vol. 22, no. 2, pp. 361-374, 2006.

[9] J. F. Barker, "The Initial Years of Alloy 718 - A GE Perspective," in *International Symposium on Superalloys*, 1989.

[10] D. F. Paulonis and J. J. Schirra, "Alloy 718 at Pratt & Whitney - Historical Perspective and Future Challenges," in *Superalloys 718, 625, 706 and Various Derivatives*, 2001.

[11] R. E. Schafrik, D. D. Ward and J. R. Groh, "Application of Alloy 718 in GE Aircraft Engines: Past, Present and Next Five Years," in *Superalloys 718, 625, 706 and Various Derivatives*, 2001.

[12] H. Eiselstein, "Age-Hardenable Nickel Alloy". United States Patent 3046108, 24 July 1962.

[13] J. F. Radavich, "The Physical Metallurgy of Cast and Wrought Alloy 718," in *Superalloy 718 - Metallurgy and Applications*, 1989.

[14] M. C. Chaturvedi and Y. Han, "Creep Deformation of Alloy 718," in *Superalloy 718 - Metallurgy and Applications*, 1989.

[15] A. H. Jones, "An Overview of Alloy 718 in Large Structural Castings," in *Superalloy 718 - Metallurgy and Applications*, 1989.

[16] Y. Wang, W. Z. Shao, L. Zhen, L. Yang and X. M. Zhang, "Flow Behavior and Microstructure of Superalloy 718 during High Temperature Deformation," *Mater. Sci. Eng. A,* vol. 497, no. 1-2, pp. 479-486, 2008.

[17] C. Malara and J. Radavich, "Alloy 718 Large Ingots Studies," in *Superalloys 718, 625, 706 and Various Derivatives*, 2005.

[18] A. Lingenfelter, "Welding of Inconel Alloy 718: A Historical Overview," in *Superalloy 718 - Metallurgy and Applications*, 1989.

[19] S. D. Antolovich, "The Effect of Metallurgical Instabilities on the Behavior of IN 718," in *Superalloy 718 - Metallurgy and Applications*, 1989.

[20] M. J. Cieslak, G. A. Knorovsky, T. J. Headley and A. D. Romig Jr., "The Solidification Metallurgy of Alloy 718 and other Nb-Containing Superalloys," in *Superalloy 718 - Metallurgy and Applications*, 1989.

[21] J. A. Schey, Introduction to Manufacturing Processes, New York, NY: McGraw-Hill, Inc., 1997.

[22] H. Chandler, Heat Treater's Guide: Practices and Procedures for Nonferrous Alloys, Materials Park, OH: ASM International, 1996.

[23] N. A. Wilkinson, "Forging of 718 - The Importance of T.M.P.," in *Superalloy 718 - Metallurgy and Applications*, 1989.

[24] M. C. Mataya and D. K. Matlock, "Effects of Multiple Reductions on Grain Refinement during Hot Working of Alloy 718," in *Superalloy 718 - Metallurgy and Applications*, 1989.

[25] P. E. Mosser, G. Leconte, J. Leray, A. Lasalmonie and Y. Honnorat, "Metallurgical Aspects of Forge Modelling in Alloy 718," in *Superalloy 718 - Metallurgy and Applications*, 1989.

[26] A. Wagner, B. A. Shollock and M. McLean, "Grain Structure Development in Directional Solidification of Nickel-base Superalloys," *Mater. Sci. Eng. A,* vol. 374, no. 1-2, pp. 270-279, 2004.

[27] Y. Z. Zhou, A. Volek and N. R. Green, "Mechanism of Competitive Grain Growth in Directional Solidification of a Nickel-base Superalloy," *Acta Mater.,* vol. 56, no. 11, p. 26312637, 2008.

[28] R. G. Carlson and J. F. Radavich, "Microstructural Characterization of Cast 718," in *International Symposium on Superalloys*, 1989.

[29] R. M. Forbes Jones and L. A. Jackman, "The Structural Evolution of Superalloy Ingots during Hot Working," *JOM,* vol. 51, no. 1, pp. 27-31, 1999.

[30] M. C. Schneider, J. P. Gu, W. J. Beckermann, W. J. Boettinger and U. R. Kattner, "Modeling of Micro- and Macrosegregation and Freckle Formation in Single-Crystal Nickel-Base Superalloy Directional Solidification," *Metall. Mater. Trans. A,* vol. 28, no. 7, pp. 1517-1531, 1997.

[31] S. M. Jones, J. Radavich and S. Tian, "Effect of Composition on Segregation Microstructures and Mechanical Properties of Cast Alloy 718," in *Superalloy 718 - Metallurgy and Applications*, 1989.

[32] J. L. Burger, R. R. Biederman and W. H. Couts, "The Effects of Starting Condition on the Aging Response of As-Forged Alloy 718," in *Superalloy 718 - Metallurgy and Applications*, 1989.

[33] J. M. Poole, K. R. Stultz and J. M. Manning, "The Effect of Ingot Homogenization Practice on the Properties of Wrought Alloy 718 and Structure," in *Superalloy 718 - Metallurgy and Applications*, 1989.

[34] J. M. Moyer, L. A. Jackman, C. B. Adasczik, R. M. Davis and R. Forbes Jones, "Advances in Triple Melting," in *Superalloys 718, 625, 706 and Various Derivatives*, 1994.

[35] L. A. Jackman, "Specialty Metals Processing Consortium: The Perspective of Industrial Members," *JOM,* vol. 50, no. 3, pp. 26-29, 1998.

[36] A. Mitchell, "The Present Status of Melting Technology for Alloy 718," in *Superalloy 718 - Metallurgy and Applications*, 1989.

[37] F. J. Zanner, R. L. Williamson, R. P. Harrison, H. D. Flanders, R. D. Thompson and W. C. Szeto, "Vacuum Arc Remelting of Alloy 718," in *Superalloy 718 - Metallurgy and Applications*, 1989.

[38] K. O. Yu and J. A. Domingue, "Control of Solidification Structure in VAR and ESR Processed Alloy 718 Ingots," in *Superalloy 718 - Metallurgy and Applications*, 1989.

[39] J. A. Van Den Avyle, J. A. Brooks and A. C. Powell, "Reducing Defects in Remelting Proccesses for High-Performance Alloys," *JOM,* vol. 50, no. 3, pp. 22-25, 1998.

[40] W. J. Boettinger, S. R. Coriell, A. L. Greer, A. Karma, W. Kurz, M. Rappaz and R. Trivedi, "Solidification Microstructures: Recent Developments, Future Directions," *Acta Mat.,* vol. 48, no. 1, pp. 43-70, 2000.

[41] L. A. Jackman, G. E. Maurer and S. Widge, "White Spots in Superalloys," in *Superalloys 718, 625, 706 and Various Derivatives*, 1994.

[42] A. Soller, A. Jardy, R. Larue, D. Ablitzer and G. Reiter, "Behavior of Discrete White Spots Precursors in a VAR Liquid Pool," in *Proceedings of the 2005 International Symposium on Liquid Metal Processing and Casting*, 2005.

[43] F. Shved, "On the Origin of the White Spot Defect in Vacuum Arc Remelted Ingots," in *Proceedings of the 2009 International Symposium on Liquid Metal Processing and Casting*, 2009.

[44] P. Auburtin, T. Wang, S. L. Cockcroft and A. Mitchell, "Freckle Formation and Freckle Criterion in Superalloy Castings," *Metall. Mater. Trans. B,* vol. 31, no. 4, pp. 801-811, 2000.

[45] T. Antonsson and H. Fredriksson, "The Effect of Cooling Rate on the Solidification of INCONEL 718," *Metall. Mater. Trans. B,* vol. 36, no. 1, pp. 85-96, 2005.

[46] X. Wang, M. Wark, M. Jacobs and M. Barratt, "Effect of Variation in Process Parameters on the Formation of Freckle in INCONEL 718 by Vacuum Arc Remelting," *Metall. Mater. Trans. A,* vol. 39, no. 12, pp. 2981-2989, 2008.

[47] F. Zanner, R. Williamson and R. Erdmann, "On the Origin of Defects in VAR Ingots," in *Proceedings of the 2005 Internatinal Symposium on Liquid Metal Processing and Casting*, 2005.

[48] K. Morita, T. Suzuki, T. Taketsuru, D. G. Evans and W. Yang, "The Tendency for Freckle Formation in Alloy 718," in *Superalloys 718, 625, 706 and Various Derivatives*, 2001.

[49] A. Kermanpur, D. G. Evans, R. J. Siddall, P. D. Lee and M. McLean, "Effect of Process Parameters on Grain Structure Formation during VAR of Inconel Alloy 718," *J. Mater. Sci.,* vol. 39, no. 24, pp. 7175-7182, 2004.

[50] C. O'Connell, J. deBarbadillo, D. Evans, R. Minisandram, R. Smith, J. Yanke, E. Taleff, T. Ivanoff, K. Kelkar, W. Hutchison and M. Benedict, "Industrial-Scale Validation of a Transient Computational Model for Electro-Slag Remelting," in *Liquid Metal Processing & Casting Conference (LMPC 2017)*, Philadelphia, PA, 2017.

[51] R. L. Williamson, J. J. Beaman, F. J. Zanner and J. J. DeBarbadillo, "Advancing Alloy 718 Vacuum Arc Remelting Technology through Developing Model-Based Controls," in *Superalloys 718, 625, 706 and Various Derivatives*, 2005.

[52] L. A. Bertram, P. R. Schunk, S. N. Kempka, F. Spadafora and R. Minisandram, "The Macroscale Simulation of Remelting Processes," *JOM,* vol. 50, no. 3, pp. 18-21, 1998.

[53] L. Nastac, "A Multiscale Transient Modeling Approach for Predicting the Solidification Structure in VAR-Processed Alloy 718 Ingots," *Met. Trans. B,* vol. 45, no. 1, pp. 44-50, 2014.

[54] L. Nastac, "Multiscale Modelling Approach for Predicting Solidification Structure Evolution in Vacuum Arc Remelted Superalloy Ingots," *Mater. Sci. Technol.,* vol. 28, no. 8, pp. 1006-1013, 2012.

[55] L. Nastac, "Numerical Modeling of Solidification Morphologies and Segregation Patterns in Cast Dendritic Alloys," *Acta Mater.,* vol. 47, no. 17, pp. 4253-4262, 1999.

[56] L. Nastac, S. Sundarraj, K.-O. Yu and Y. Pang, "The Stochastic Modeling of Solidification Structures in Alloy 718 Remelt Ingots," *JOM,* vol. 50, no. 3, pp. 30-35, 1998.

[57] R. L. Williamson, M. E. Schlienger, C. L. Hysinger and J. J. Beaman, "Modern Control Strategies for Vacuum Arc Remelting of Segregation Sensitive Alloys," in *Superalloys 718, 625, 706 and Various Derivatives*, 1997.

[58] X. Xu, R. M. Ward, M. H. Jacobs, P. D. Lee and M. McLean, "Tree-Ring Formation during Vacuum Arc Remelting of INCONEL 718: Part I. Experimental Investigation," *Metall. Mater. Trans. A,* vol. 33, no. 6, pp. 1795-1804, 2002.

[59] X. Xu, W. Zhang and P. D. Lee, "Tree-Ring Formation during Vacuum Arc Remelting of INCONEL 718: Part II. Mathematical Modeling," *Metall. Mater. Trans. A,* vol. 33, no. 6, pp. 1805-1815, 2002.

[60] R. C. Atwood and P. D. Lee, "Multiscale Modelling of Microstructure Formation during Vacuum Arc Remelting of Titanium 6-4," *J. Mater. Sci.,* vol. 39, no. 24, pp. 7193-7197, 2004.

[61] E. N. Kondrashov, M. I. Musatov, A. Y. Maksimov, A. E. Goncharov and L. V. Konovalov, "Calculation of the Molten Pool Depth in Vacuum Arc Remelting of Alloy VT3-1," *J. Eng. Thermophysics,* vol. 16, no. 1, pp. 19-25, 2007.

[62] T. Le Roux and D. A. Wells, "An Asseement and Comparison of the Sensitivity of Various Macroetches for Alloy 718," *Superalloy 718 - Metallurgy and Applications,* pp. 109-118, 1989.

[63] W. Kurz and D. J. Fisher, Fundamentals of Solidification, Enfield, NH: Trans Tech Publications Inc, 1998.

[64] W. J. Boettinger, U. R. Kattner, S. R. Coriell, Y. A. Chang and B. A. Mueller, "Development of Multicomponent Solidification Micromodels using a Thermodynamic Phase Diagram Data Base," in *Modeling of Casting, Welding and Advanced Solidification Processes, VII*, 1995.

[65] M. Rappaz and W. J. Boettinger, "On Dendritic Solidification of Multicomponent Alloys with Unequal Liquid Diffusion Coefficients," *Acta. Mater.,* vol. 47, no. 11, pp. 3205-3219, 1999.

[66] T. J. Watt, E. M. Taleff, F. Lopez, J. Beaman and R. Williamson, "Solidification Mapping of a Nickel Alloy 718 Laboratory VAR Ingot," *Proceedings of the 2013 International Symposium on Liquid Metal Processing & Casting,* pp. 261-270, 2013.

[67] S. M. Pizer, E. P. Amburn, J. D. Austin, R. Cromartie, A. Geselowitz, T. Greer, B. t. H. Romeny, J. B. Zimmerman and K. Zuiderveld, "Adaptive Histogram Equalization and Its Variations," *Computer Vision, Graphics, and Image Processing,* vol. 39, no. 3, pp. 355 - 368, 1987.

[68] G. Bradski, *Open Source Computer Vision Library,* Dr. Dobb's Journal of Software Tools, 2000.

[69] J. Cristy, *ImageMagick,* ImageMagick Studio LLC.

[70] J. Schindelin, I. Arganda-Carreras, E. Frise and et al., "Fiji: an open-source platform for biological-image analysis," *Nature Methods,* vol. 9, no. 7, pp. 676 - 682, 2012.

[71] MATLAB R2015a version 8.5.0, Natick, MA: MathWorks Inc., 2015.

[72] C. Jung-Kuei, *The Effect of Microstructure on Cavitation during Hot Deformation in Fine-grained AA5083 Aluminum Alloy Sheet Material,* 2008.

[73] A. Tewari, A. M. Gokhale, J. E. Spowart and D. B. Miracle, "Quantitative Characterization of Spatial Clustering in Three-dimensional Microstructures using Two-point Correlation Functions," *Acta Materialia,* vol. 52, no. 2, pp. 307 - 319, 2004.

[74] A. D. Rollet, R. Campman and D. Saylor, "Three Dimensional Microstructures: Statistical Analysis of Second Phase Particles in AA7075-T651," *Materials Science Forum,* Vols. 519 - 521, pp. 1 - 10, 2006.

[75] H. Singh, A. M. Gokhale, Y. Mao and J. E. Spowart, "Computer Simulations of Realistic Microstructures of Discontinously Reinforced Aluminum Alloy (DRA) Composites," *Acta Materialia,* vol. 54, no. 8, pp. 2131 - 2143, 2006.

[76] P. J. E. Peebles, Large-Scale Structure of the Universe, Princeton, NJ: Princeton University Press, 1980, p. 435.

[77] A. M. Gokhale, A. Tewari and H. Garmestani, "Constraints on Microstructural Two-point Correlation Functions," *Scripta Materialia,* vol. 53, no. 8, pp. 989 - 993, 2005.

[78] Mathematica 10.1, Champaign, IL: Wolfram Research, Inc., 2015.

[79] P. V. C. Hough, "Method and Means for Recognizing Complex Patterns". United States Patent 3069654, 18 December 1962.

[80] R. O. Duda and P. E. Hart, "Use of the Hough Transform to Detect Lines and Curves in Pictures," *Comm. ACM,* vol. 15, no. 1, pp. 11 - 15, 1972.

[81] D. H. Ballard, "Generalizing the Hough Transform to Detect Arbitrary Shapes," *Pattern Recognition,* vol. 13, no. 2, pp. 111 - 122, 1981.

[82] J. Radon, "On the Determination of Functions from their Integral Values Along Certain Manifolds," *IEEE Trans. Medical Imaging,* Vols. MI-5, no. 4, pp. 170 - 176, December 1986.

[83] R. B. Blackman and J. W.Tukey, "The Measurement of Power Spectra from the Point of View of Communications Engineering – Part 1," Bell System Technical Journal, vol. 37, no. 1, pp. 185 – 282, 1958.

VITA

Thomas Alexander Ivanoff was born in Pennsylvania on a glorious November day in 1989. As a child growing up in Tulsa, Oklahoma he exhibited a prodigious appetite for science and engineering; he spent many a day tinkering with his toys. Through high school he sharpened his skills as a scholar and displayed quite the aptitude for history and physics. By this time he had progressed beyond his toys and began tinkering with the two noblest of steeds; the 1991 Ford Taurus SHO and the 1980's Pontiac Fiero. It was through this tinkering that Thomas unknowingly established his practical engineering expertise. For his undergraduate studies at the University of Arkansas, lamenting the career prospects behooved for a history major, he chose to study engineering and physics beginning in the fall of 2008. It was here that Thomas truly began to emerge as a scholar and first began to hone his skills as a researcher. After summer research stints at the University of Nebraska and the University of Arkansas, Thomas graduated with honors and desired more than a baccalaureate level of knowledge. His graduate studies began at the University of Texas at Austin in the fall of 2012. He shortly thereafter earned his master's degree in engineering. It was at this time he choose to seek a doctoral degree in engineering; a distinction equal to his parents and truly becoming of an Ivanoff.